UNIVERSITY OF CAMBRIDGE
INSTITUTE OF ASTRONOMY

A DISSERTATION SUBMITTED TO THE
UNIVERSITY OF CAMBRIDGE FOR THE DEGREE
OF DOCTOR OF PHILOSOPHY

PROTOPLANETARY DISC EVOLUTION AND DISPERSAL

James Edward Owen

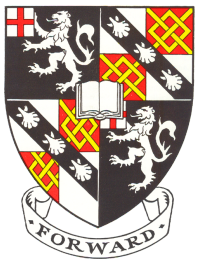

CHURCHILL COLLEGE

Submitted to the Board of Graduate Studies
June 30, 2010

UNDER THE SUPERVISION OF
PROFESSOR CATHIE J. CLARKE

For my friends and family

CONTENTS

DECLARATION

I hereby declare that my thesis entitled *Protoplanetary disc evolution and dispersal* is not substantially the same as any that I have submitted for a degree or diploma or other qualification at any other University. I further state that no part of my thesis has already been or is being concurrently submitted for any such degree, diploma or other qualification. This dissertation is the result of my own work and includes nothing which is the outcome of work done in collaboration except where specifically indicated in the text. Those parts of this thesis which have been published or accepted for publication are as follows:

- Chapter 2 is based on work that has been completed in collaboration with C. J. Clarke and B. Ercolano and has been submitted to *Monthly Notices of the Royal Astronomical Society* as:
  - Owen, J.E.; Clarke, C.J. & Ercolano, B. 'On the theory of photoevaporation'
- Chapters 3 & to 4 has been completed in collaboration with C.J. Clarke, B. Ercolano & R.D. Alexander and is based on three articles:
  - Owen, J.E.; Ercolano, B.; Clarke, C.J. & Alexander, R.D. (2010) 'Radiation-hydrodynamic models of X-ray and EUV photoevaporating protoplanetary discs', *Monthly Notices of the Royal Astronomical Society*, **401**, 1415-1428.
  - Owen, J.E.; Ercolano, B. & Clarke, C.J. (2011) 'Protoplanetary disc evolution and dispersal: the implications of X-ray photoevaporation', *Monthly Notices of the Royal Astronomical Society*, **412**, 13-25.
  - Owen, J.E.; Clarke, C.J. & Ercolano, B. 'On the theory of photoevaporation', *subm.*
- The work presented in Chapter 5 is based on work completed in collaboration with B. Ercolano and is published as:
  - Ercolano, B. & Owen, J.E. (2010) 'Theoretical spectra of photoevaporating protoplanetary discs: an atlas of atomic and low-ionization emission lines', *Monthly Notices of the Royal Astronomical Society*, **406**, 1553-1569.
- The work presented in Chapter 6 has been completed in collaboration with C.J. Clarke & B. Ercolano and is published as:
  - Owen, J.E.; Ercolano, B. & Clarke, C.J. (2011) 'The imprint of photoevaporation on edge-on discs', *Monthly Notices of the Royal Astronomical Society*, **411**, 1104-110.

This thesis contains fewer than 60,000 words.

James Edward Owen
Cambridge, June 30, 2011

ACKNOWLEDGEMENTS

There are many people to whom I am deeply indebted for their help and support, both during years at the IoA, Cambridge and long before that; I have enjoyed (almost) every minute of the last three years. Firstly, I would like to thank my supervisor, Cathie Clarke for all her hard work and support, I couldn't have asked for a better supervisor. Cathie has given me the freedom to pursue fruitful areas of research, and for indulging in many long conversation on different topics. Secondly, I must of course thank Barbara Ercolano, much of the foundations for this thesis lie in Barbara's work. Barbara has certainly gone above and beyond the call of duty; the rapid edits of her MOCASSIN code, for allowing myself to bouncing ideas of her and of course for tireless correcting my 'Yoda style' sentences.

Other people at the IoA who deserve a special mention are Mark Wyatt my second supervisor who providing his data on debris discs used in this thesis, Jim Pringle for many insightful discussion and valuable advise on getting a job, and of course Paul Hewitt for his advice on how astronomy works. Many astronomers outside the IoA have aided me either with providing help or giving me their data: Richard Alexander for introducing me to the finer points of the ZEUS code and for providing me with his OPEN-MP version, along with his expert knowledge on photoevaporation theory which has proved invaluable. Manuel Güedel, Thomas Preibisch and Jermey Drake have been invaluable in explaining the X-ray observations to myself. Thanks must also go to Ilaria Pascucci (particuarly for providing the NeII and OI data used in this work, and for involving myself in their interpretation), Al Glassgold, Eugene Chiang, Greg Herczeg, Uma Gorti, David Hollenbach, Nate Bastian, Phil Armitage and Tim Harris for the interesting discussions we have had either in person or over e-mail.

Of course I would have never made it to Cambridge or the IoA, without the support and encouragement people have provided over the years. My parents and grandparents have always encouraged me to be inquisitive and supported my career choice. Thanks must go to Tim Joliff, who encouraged me to apply to Cambridge although I was eventually lured away from Chemistry! Of course I must thank all for my year: Warrick, Amy, Jon, Alex, Becky, Stephanie, Yin-Zhe, James, Ryan, Adrian, and Dom, for entertaining coffee and tea time conversation. I am grateful to my past and present office mates: Luke, Richard, Quincy, Jayne, Stephanie, Susie, Phil, Alan and of course Hernandéz, many of whom proof read parts of this Thesis.

Finally, to Claire for your support and everything else, I would not have made it without you.

James Edward Owen
Cambridge, June 30, 2011

SUMMARY

In this thesis I have studied how discs around young stars evolve and disperse. In particular, I build models which combine viscous evolution with photoevaporation, as previous work suggests that photoevaporation can reproduce the observed disc evolution and dispersal time-scales. The main question this thesis attempts to address is: Can photoevaporation provide a dominant dispersal mechanism for the observed population of young stars?

Photoevaporation arises from the heating that high energy (UV and X-ray) photons provide to the surface layers of a disc. Before I started this work, only photoevaporation from a pure EUV radiation field was described within a hydrodynamic framework. Therefore, I start by building a hydrodynamic solution to the pure X-ray photoevaporation problem, and then extend this solution to the entire high energy spectrum. This hydrodynamic model leads me to conclude that it is the X-ray radiation field that sets the mass-loss rates. These mass-loss rates scale linearly with X-ray luminosity, are independent of the underlying disc structure and explicitly independent of stellar mass. I build a radiation-hydrodynamic algorithm, based on previous work, to describe the process of X-ray heating in discs. I then use this algorithm to span the full range of observed parameter space, to fully solve the X-ray photoevaporation problem. I further extend the algorithm to roughly approximate the heating an FUV radiation field would have on the photoevaporative flow, as well as separately testing the effect an EUV radiation field will have. These numerical tests are in agreement with the hydrodynamic model derived. Specifically, it is the X-rays that are driving the photoevaporative flow from the inner disc.

Armed with an accurate description of the photoevaporative mass-loss rates from young stars, I consider the evolution of a population of disc-bearing, young ($0.7 M_{\odot}$) stars, in order to asses photoevaporation's role as a dispersal mechanism. This study shows that the observed spread in X-ray luminosity of young stars is sufficient to drive the dispersal of the entire population of discs, reproducing both the required time-scales and the required spread in observables (disc lifetime, accretion rate). I also show that a large fraction of the observed population of 'transition' discs are consistent with being created through photoevaporation.

Having shown photoevaporation can provide a dominant dispersal mechanism for a population of discs, I attempt to describe some direct observable consequences of photoevaporation, both through gas tracers and dust emission. During this work, the first direct evidence of a photoevaporative flow emerging from a young star was obtained from TW Hya, in the NeII 12.8μm line. Therefore, I discuss this result within the framework of the X-ray photoevaporation model. Furthermore, I suggest that emission from the photoevaporative flow is the origin of the unexplained, blue-shifted, OI 6300Å line observed around all young stars that possess discs. I then described the properties of the dust particles that may be entrained within the photoevaporative flow. The total dust mass in the flow is found to be small compared to the disc, although such a region becomes observable once the disc presents as edge-on, obscuring the central star and hot inner disc. I discuss the emission from these regions and compare them to the sample of currently imaged edge-on discs.

The presented photoevaporation model reproduces all of the current observations, and I discuss some predictions it makes with regard to future observations. Finally, photoevporation may have some intriguing consequences on planet formation and dust evolution that warrant further investigation.

LIST OF TABLES

LIST OF FIGURES

NOMENCLATURE

Unless otherwise stated, it can be assumed the following symbols have this definition

Co-ordinate Systems

Cartesian $\mathbf{r} = [x\hat{\mathbf{x}}, y\hat{\mathbf{y}}, z\hat{\mathbf{z}}]$

Cylindrical Polar $\mathbf{r} = [R\hat{\mathbf{R}}, \phi\,\hat{\phi}, z\hat{\mathbf{z}}]$

Spherical Polar $\mathbf{r} = [r\hat{\mathbf{r}}, \theta\,\hat{\theta}, \varphi\,\hat{\varphi}]$

Physical Constants

Boltzmann's Constant k_b

Gravitational Constant G

Plank's Constant h

Fluid Mechanical Variables

Fluid Velocity $\mathbf{u}$

Mass Density ρ

Number Density n

Gas Temperature T

Stream-bundle Area A

Kinematic Viscosity ν

Stress Tensor $\mathbf{T}$

Length Along a Streamline l

Net Cooling Rate Λ

Energy Density e

Pressure P

Sound Speed c_s

Dynamical Viscosity η

Components of Stress Tensor T_{ij}

Accretion Disc Variables

Surface Density Σ

Accretion Rate $\dot{M}_*$

Surface Mass-loss Rate $\dot{\Sigma}_w$

Viscous 'alpha' Parameter α

Initial Disc Scale Radius R_1

Radial Pressure Scale Height H_R

Integrated Photoevaporation Rate $\dot{M}_w$

Disc Mass M_d

Initial Viscous Time t_ν

Global Viscous Time τ_ν

Vertical Pressure Scale Height H

Inner Hole Radius $R_{\rm hole}$

Radiative Transfer Variables

Wavelength λ

Frequency ν

Bolometric Luminosity $L_{\rm bol}$

Energy Density Mean Opacity κ_E

Dust Temperature T_d

X-ray Luminosity L_X

Flux f

Column N

Plank Mean Opacity κ_p

EUV Luminosity Φ_*

Miscellaneous Variables

Free fall time-scale t_{ff}

Sound crossing time-scale t_{sc}

Dust Grain Radius a

Angular Velocity Ω

Time t

Ionization Parameter ξ

Ratio of Specific Heats γ

Stellar Mass M_*

Gravitational Potential Φ

Effective Potential ψ

Stellar Radius R_*

Big O Notation (of order) $\mathcal{O}$

Telescope Names

ALMA (Atacama Large Millimeter Array) - Future Millimetre/sub-millimetre interferometer

Herschel Just launched space based MIR/FIR observatory

Spitzer In use, space based NIR/MIR observatory

Logarithms

In this thesis I use log to refer to logarithms in any base, the implied base should be clear from the context. Although for clarity: numerical values are always given in base 10; while algebraic expressions use the natural base (e).

Never lose the child-like wonder.
It's just too important.
It's what drives us.

The Last Lecture

RANDY PAUSCH (1960-2008)

1 Introduction

ONE of the ultimate goals of modern Science is understanding how our solar system, newly discovered solar systems and currently undetected solar systems are assembled. It is certainly true that the final stages of star formation and planet formation are coupled processes, with star formation setting conditions in which planet formation will begin. Currently, one can argue that how, where and when planets form is a question that is far from being answered. In fact one of the only results that the current range of planet formation models agree on, is that the initial conditions are crucial to the final result. Therefore, a detailed understanding of the physical processes, and the time-scales on which they operate will provide stringent conditions with which to begin constraining models of planet formation.

Therefore, I shall begin our discussion by describing the processes which lead to the formation of the reservoir of gas and dust from which planets will form: the protoplanetary disc. Protoplanetary discs are an inevitable outcome of star formation and their existence was postulated during the 18$^{\text{th}}$ century within the framework of the nebular hypothesis.

1.1 The origin of protoplanetary discs

In order to initiate the star formation process, the gas from which the star is going to form must satisfy a basic requirement: namely that the gravitational collapse can proceed unimpeded by the thermal pressure, which can stabilise a region against collapse. This simply means that the free-fall time must be considerably less than the sound crossing time, where $t_{ff}/t_{sc} \propto \rho^{-1/6} T^{1/2}$, meaning we need a cold, dense region. These stellar nurseries have been observationally detected and studied for many years. At the densities ($n > 10$ cm^{-3}) and temperatures ($T < 50$K) expected for these regions the gas is molecular, and these regions have been aptly named 'molecular clouds'. One property that is shared by all star forming regions is that they are slowly rotating (e.g. Figure 1.1; Myers & Benson 1983; Goldsmith &

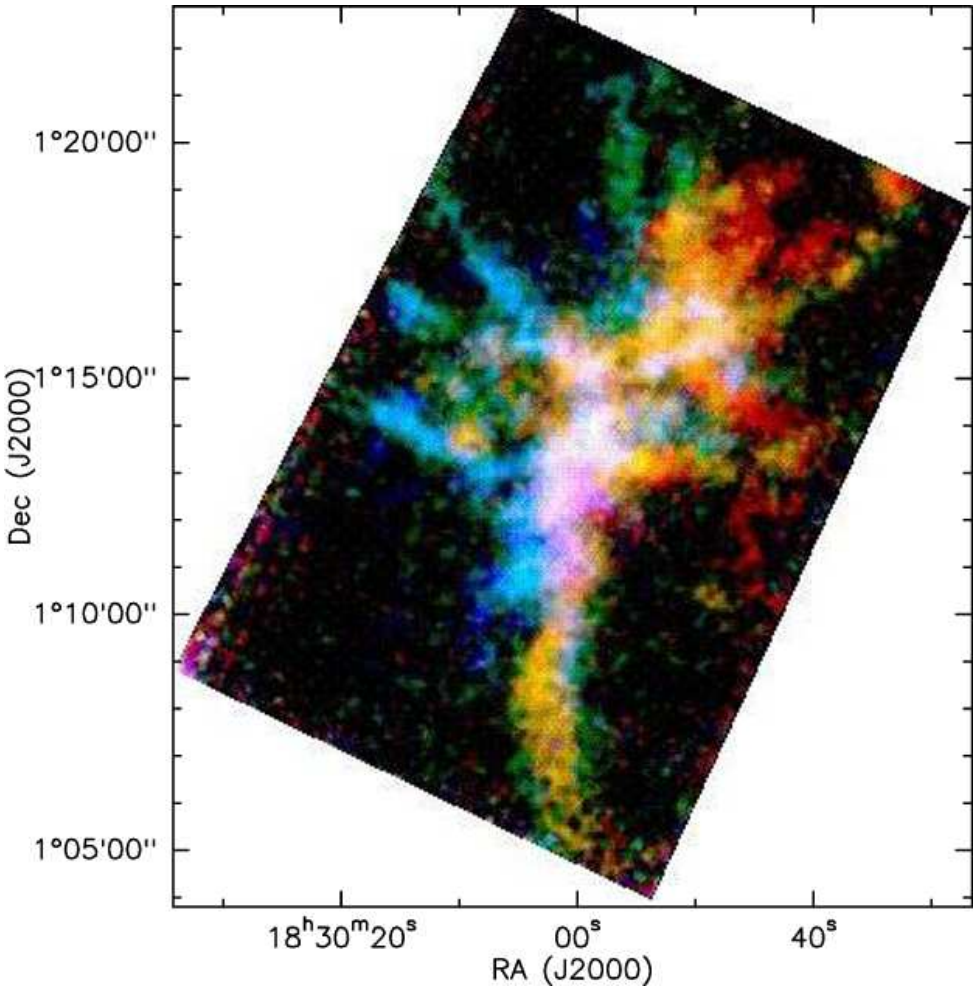

Figure 1.1: Three colour plot of the gas (traced by $C^{18}O$) in the Serpens molecular cloud, blue indicates gas moving towards the observer, green indicates gas stationary with respect to the observer and red indicates gas moving away from the observer. At a distance of 230pc, 10' corresponds to 0.6pc. The East-West velocity gradient clearly indicates that the Serpens molecular cloud is globally rotating about an axis running approximately North-South with an angular frequency of $\sim 10^{-15}$ s^{-1}. (Figure from Graves et al. 2010)

Arquilla 1985; Goodman et al. 1993; Burkert & Bodenheimer 2000), and therefore given their size (of order parsecs) the gas possesses significant amounts of angular momentum. The formation of an individual stellar system begins when an individual region within the molecular cloud becomes gravitationally unstable, and begins to collapse. When the collapse begins the gas is optically thin and it proceeds isothermally. An isothermal collapse is a runaway process, thus the collapse proceeds until the cloud becomes dense enough that it is optically thick to its own cooling radiation. The size of a region that becomes gravitationally unstable ($\mathcal{O}$ 0.1pc - the Jeans radius - Jeans 1902) can be compared to the size of a formed solar system ($\mathcal{O}$ 100 AU), i.e. the collapse proceeds through many orders in magnitude in radius. Therefore, conservation of angular momentum will result in a large increase in the angular velocity of the collapsing gas. This large increase in rotation will necessarily cause a flattening of the rotating cloud and the beginning of a disc like structure. As the collapse proceeds a centrally condensed object forms in the centre, with most of the material falling onto this object. However, gas particles in the cloud that posses significant angular velocities (resulting from the conservation of angular momentum), will be on

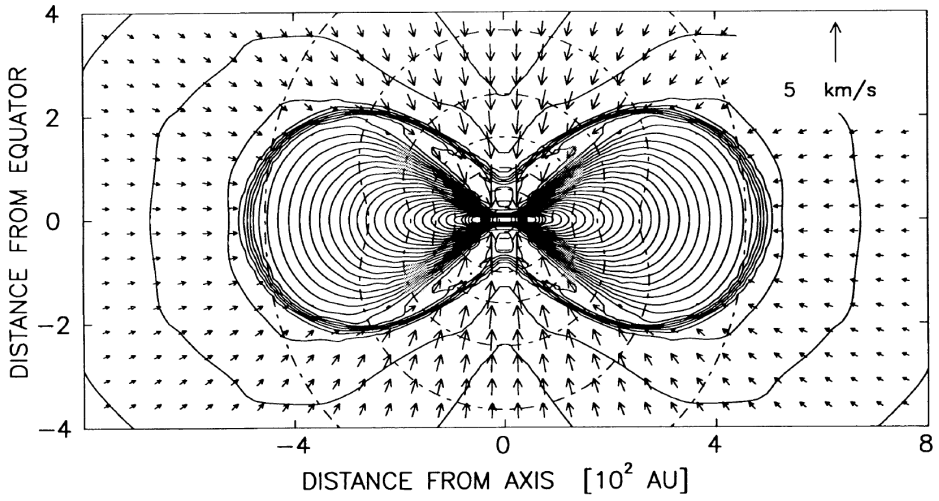

Figure 1.2: The density and velocity structure of collapsing, rotating cloud shown after 8×10^4 years. Density contours range from $\log_{10}\rho = -9.8$ to -16 at constant logarithmic steps (Figure from Yorke et al. 1999).

an orbital path that has a periapsis that will miss the central condensed structure. In an approximately symmetric collapse, any gas parcel that approaches the mid-plane[1] of the system will have an opposing gas parcel that arrives at the mid-plane at the same time, but with equal and opposite momentum. Therefore, the gas parcels will terminate their orbits at the mid-plane. This populates the mid-plane with large amounts of gaseous material, and is the origin of the protoplanetary disc. This process is shown in Figure 1.2 taken from a simulated collapse of a rotating $1\mathrm{M}_\odot$ axis-symmetric gas cloud (Yorke et al. 1999), after 8×10^4 years a $0.45\mathrm{M}_\odot$ protostar is surrounded by a stable disc structure.

Once the disc has first formed it begins to grow by accumulating material, as it grows it intercepts material at a height above the mid-plane, that may have otherwise fallen onto the protostar, or the disc at small radii. This results in a growing and expanding disc until the majority of in-falling material falls onto the disc rather than the protostar. The most basic approximation we can make is a collapsing and slowly rotating core conserves angular momentum, in this case we can write the initial disc radius as (Cassen & Mossman 1981; Lin & Pringle 1990):

$$R_d = 40\mathrm{AU}\left(\frac{\Omega_c}{1\times10^{-16}\mathrm{s}^{-1}}\right)^2\left(\frac{R_c}{0.1\mathrm{pc}}\right)^4\left(\frac{M_c}{1\mathrm{M}_\odot}\right)^{-1} \tag{1.1}$$

where Ω_c, R_c and M_c are the initial angular velocity, radius and mass of the collapsing core respectfully, although the redistribution of angular momentum through tidal torques can reduce this radius (Lin & Pringle 1990). During this disc formation phase, the central protostar is continuing to collapse, heating up from the energy realised due to the collapse. Eventually this protostar will reach the point at which it is hot enough for nuclear fusion to begin. Once this begins the protostar has formally become a star, and it will begin a process of attaining equilibrium and becoming a fully fledged main sequence star.

Of course, the description above has swept under the carpet some of the poorly understood and hotly debated issues of star formation. Perhaps the most divisive issue that remains in understanding star formation is what sets which regions of the molecular cloud collapse to form stars and which don't (the

[1]The plane that includes the centre of mass of the system and intersects the axis of rotation at a right angle

process of fragmentation), along with the final mass of the stars these collapsing regions form, and the multiplicity of the final stellar systems. A problem that is better understood is the time-scale dichotomy that must exist between the formation of low mass stars and high mass stars. In the scenario described above, there was no discussion of the effects of radiative feedback from the forming star itself on the collapse and disc formation stage itself. While this is a reasonable assumption for the formation of low mass stars, at higher masses the luminosity of the central protostar/star[2] becomes large enough that the effects from heating of the gas, and radiative feedback due to momentum transfer from photons onto dust grains and hence the gas (which becomes a dominant effect at $\sim 10\mathrm{M}_{\odot}$, e.g. Wolfire & Cassinelli 1986,1987; Sonnhalter & Yorke 2000; Edgar & Clarke 2003; Krumholz et al. 2007,2009; Kuiper et al. 2010,2011) cannot be neglected during the star/disc formation stage (e.g. Zinnecker & Yorke, 2007). No detailed, and accurate calculations of the formation of massive stellar systems have been undertaken, and the differences between the formation of low mass stars and high mass stars is unknown.

Therefore, in this thesis I will restrict my discussion to low mass stars ($M_{*} \lesssim 2\mathrm{M}_{\odot}$), where the formation of an individual disc systems is fairly well understood and in good agreement with the observations.

1.2 Observation of protoplanetary discs

We have now seen that discs are a natural outcome of the star formation process, and it is these discs which must provide the material from which planets form. Therefore, it is important to summarise the basic characteristics before we consider the more detailed aspects of their evolution. The gas cloud from which a star/disc system is born, is composed of (in terms of mass fraction) 99% gas and 1% small dust particles (with radii in the range $5 \times 10^{-3}\mu$m to 1μm, Mathis et al. 1977). Thus, observations from both the dust component and gas component will be vital to a detailed understanding of protoplanetary discs. The first observational indication of a disc around a forming star was through the detection of an excess of emission above what would be expected from a pure stellar atmosphere at Infra-Red (IR) wavelengths (Mendoza 1966, 1968; Cohen 1975). This excess was interpreted as the thermal emission arising from dust in a disc which surrounds the forming star, where the disc is colder than the forming star itself, hence the excess appearing at IR wavelengths (Adams & Shu 1986). These early indirect detections of protoplanetary discs have now been supplemented with imaging in both gas and dust. Modern observations now include a large range of broadband photometery, to study the dust emission (thermal & scattered) and emission arising from accretion, and spectroscopy to study the emission from gas phase diagnostics.

1.2.1 The Spectral Energy Distribution of Discs

One of the most widespread observational tools for studying the forming star/disc system is through analysis of its spectral energy distribution (SED), with broadband photometry ranging from the Ultra-Violet (UV), through the optical, IR to sub-millimetre and millimetre wavelengths available for many objects. Figure 1.3 shows the median SED from the Taurus star forming region (D'alessio et al. 2001). Compared to a pure stellar photosphere, the IR excess above the photosphere is clearly visible in this

[2]Due to the time-scale for stellar evolution compared to formation, the difference between a protostar and star becomes blurred as the time-scale for stellar evolution becomes comparable to the formation time-scale and a forming massive star can be considered to be an actively evolving star.

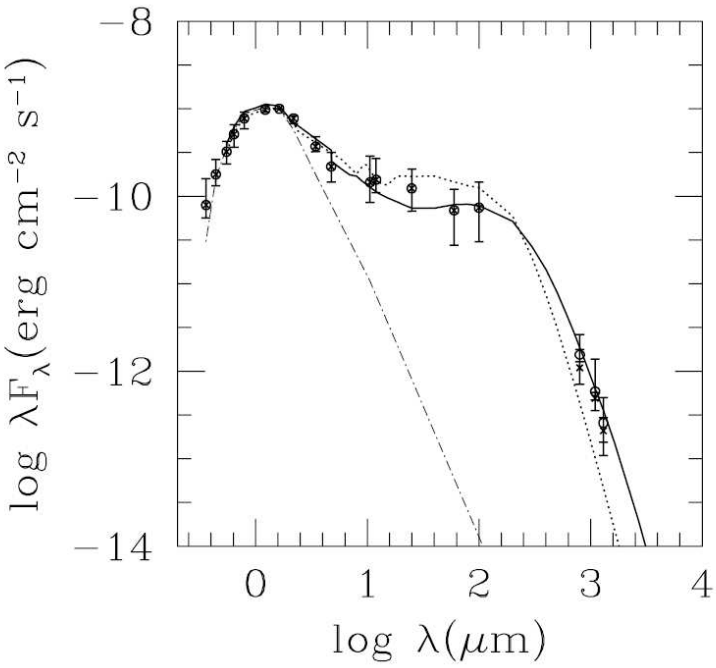

Figure 1.3: Points show the median SED observations of objects in the Taurus star forming region. The dot-dashed line shows emission arising due to a forming star, the solid line and dotted lined show the fits of various protoplanetary disc models (Figure from D'alessio et al. 2001).

plot, and its slope can be used to determine the temperature structure of the disc's photosphere. At longer wavelengths (sub-millimetre/millimetre) the disc's emission falls off rapidly, indicative of the disc becoming optically thin to its own thermal emission. If the emission is optically thin the total flux can be related directly to the total amount of opacity at these wavelengths, and hence allows for model dependant determination of (dust) disc masses. At wavelengths shorter than the peak of the stellar photosphere, the SED again shows an excess above the photosphere. This hot continuum excess is thought to arise from an accretion shock on the stellar surface, caused by gas free-falling onto the stellar surface from magnetically mediated accretion funnels (e.g Muzerolle et al. 2000). Therefore, this UV excess tell us that these protoplanetary discs are actively accreting onto the forming star, which is unsurprising, since from the discussion above a natural question to ask is: If a large fraction of the in-falling material falls onto the disc rather than the forming star, how does it accrete onto the central star? This is a question I will discuss further in Section 1.3 and relates to angular momentum transport. Furthermore, this UV excess provides a direct way to measure the rate at which material is accreted onto the forming star and is therefore crucial to discussions of protoplanetary disc evolution. Finally, the optical photometry allows us to characterise the forming star, allowing constraints to be placed on its mass and age. Therefore, the SED of a forming star is an extremely powerful tool for characterising star/disc systems allowing measurements of the accretion rates, temperature structure and mass measurements of protoplanetary discs, which have been extremely successful in constraining the basic models of disc evolution.

The SED as an indicator of Evolution

The ubiquity of SED observations has lead to their use as an observational proxy for disc evolution. The use of the SED in classifying forming stars was first used by Lada (1987) and has been updated several times since (André et al. 1993; André & Montmerle 1994). Objects are typically classified into four classes (Class 0, I, II & III) based on the slope of the SED at IR wavelengths. The physical basis for this classification is that since emission at IR wavelengths is indicative of thermal dust emission, a 'redder' SED is indicative of more dust surrounding the forming star. A Class 0 is an object is that is heavily embedded and shows very little emission in the IR but is detectable in the sub-millimetre, and is thought to represent the early stages of collapse and star/disc formation. A class I object is thought to indicate the later stages of star/disc assemblage, with in-fall onto the disc still occurring, often being associated with a molecular outflow/jet. Class II indicates an evolving star/disc system with very little in-fall occurring and Class III represents a naked photosphere/debris disk (see Wyatt 2008 for an introduction into debris disks) and is thought to indicate the by-products of the star and planet formation phase.

1.2.2 Observational tracers of gas and dust

As discussed above, most of the emission produced by the disc is thermal continuum emission, while this is important for SED modelling, and gives us an idea of roughly the temperature of the dust, it gives us relatively few specific details. However, there is a growing range of tracers that can give clues as to the properties of the gas and dust at different temperature and radial ranges within the discs. The most commonly used is strong optical emission lines from the gas (mostly commonly Hα), being optical lines they typically have very high Boltzmann temperatures and therefore trace hot gas. Furthermore, these emission lines are broad, with velocities indicative of free-fall close to the star, indicating these emission lines are tracing the hot gas falling onto the star, i.e. accretion. Methods of fitting the observed emission with multiple lines and the UV continuum have become quite sophisticated and successful, and perhaps provide the most accurate measurements of accretion rates in young stars (e.g. Muzerolle et al. 1998, 2001,2005; Natta et al 2004; Herczeg & Hillenbrand 2008).

Specifically the detectability of Hα has lead to another observational classification scheme (Herbig & Bell 1988). Young stars with strong Hα emission indicative of active accretion and are known as Classical T Tauri stars (CTTs), whereas young stars with negligible Hα emission indicative of no accretion are know as 'Weak-line' T Tauri stars (WTTs). Typically, CTTs are also Class II objects (under the SED classification scheme mentioned above) and indicative of a primordial disc, whereas WTTs are Class III objects and associated with young stars that have lost their discs. Although the mapping between the accretion classification and SED classification is not one to one, it is true in general. In recent years, these classifications have wandered away from their original meaning and some authors use CTTs/Class II/Primordial disc or WTTs/Class III/disc-less interchangeably, although throughout this thesis I will try to remain true to the original definitions.

As with the dust emission, the direct tracers of gas also occur in distinct temperature ranges, hence they probe separate radial ranges. At cold temperatures and thus large radii, the most useful probes are the rotational transitions of molecules in the gas, with CO ($1\rightarrow0$, $2\rightarrow1$ & $3\rightarrow2$) rotational transitions being the strongest (Dutrey et al. 1998; Guilloteau & Dutrey 1998; Qi et al. 2004; Hughes et al. 2008), due to the cold temperatures and low spatial resolution the information from this type of observations is

limited, other than rough bounds on the total CO mass in the disc, but should prove much more fruitful once high spatial resolution imaging with ALMA is possible. At warmer temperatures, CO ro-vibrational emission from within the inner disc has provided estimates of the inner disc masses (e.g. Brittain et al. 2007), as well as demonstrating that the inner gas disc extends inside the dust destruction radius (where the dust is so hot it evaporates) until the disc is truncated by the stellar magnetic field (e.g Edwards et al. 1994; Muzerolle et al. 2001; Calvet, 2004).

Furthermore, forbidden and low ionization lines e.g. OI 6300Å (Hartigan et al. 1995) and NeII (Pascucci & Sterzik 2009), are providing details of the upper layers of the gas discs, with many of these lines showing blue-shifts indicative of gas escaping from the surface of the disc. These higher temperature lines, along with the expected lower temperature lines expected from *Herschel* are beginning to provide a wealth of information on the upper layers of the gas disc at a range of radii.

Dust properties in the discs are even more difficult to asses than gas properties. This is because most of the disc's emission is thermal black-body emission from an optically thick dust disc, and is therefore, to first order insensitive to the dust properties of grain sizes. However, it is possible to use higher order effects to constrain certain properties from this dust emission. Of course, any dust that exists above the photosphere will by definition be producing optically thin emission, and for irradiated discs this optically thin emission is always hotter than the continuum. While small in total, this emission has been used to constrain properties about grain size and composition (Natta et al. 2000; Furlan et al. 2006), with detailed modelling by D'alessio et al. (1998,1999,2001) showing that dust has evolved from the standard ISM dust population, arguing that the dust grains must have grown in size and be settled (i.e. not well mixed throughout the entire disc). Therefore, dust is likely to be being actively processed in the disc formation and evolution stage (Dullemond & Dominik 2005; Dullemond et al. 2006). This dust processing conclusion is backed up by complementary observations of the silicate dust grains. Silicate dust grains are useful as their optical properties possess a feature at 10μm, which is sensitive to the underlying crystal structure of the grain. In the ISM silicate dust grains are almost entirely in the amorphous state; however, analysis of the 10μm silicate feature indicates that most discs possess a significant fraction of crystalline silicate dust grains (Natta et al. 2000; Furlan et al. 2006). In order to transform from the amorphous state to the crystalline state, the dust particle must undergo thermal annealing at temperatures greater than 800K. Spatially resolved observations of the 10μm feature, indicate that the crystalline fraction is significant, even at radii too large for the grains to be actively undergoing the process there (Apai et al. 2005), suggesting there must be some form of radial outward movement of crystalline silicate grains.

At sub-millimetre and millimetre wavelengths, the dust emission becomes optically thin allowing estimates of the dust mass to be made along with surface density profiles, and these are often turned into gas masses by assuming the same dust to gas mass ratio as the ISM from which the disc formed (0.01). Typical discs masses are around $\sim 10^{-2}$M$_{\odot}$, but posses an order of magnitude or larger, scatter around that value (e.g. Andrews & Williams 2005, 2007). The measurement of disc masses posses significant sources of systematic errors, the emissivity of the dust varies as the fourth power of the dust temperature (typically taken to be 10K), and small errors in the dust temperature will lead to large errors in derived dust masses. Furthermore, the observed emission is not sensitive to dust grains larger than a few mm, if the grains have been significantly processed (as suggested by IR observations) then a large mass reservoir of dust grains could be missed with this technique. Therefore, disc masses are perhaps the least well constrained of the disc's properties and may carry systematic errors as large as an order of

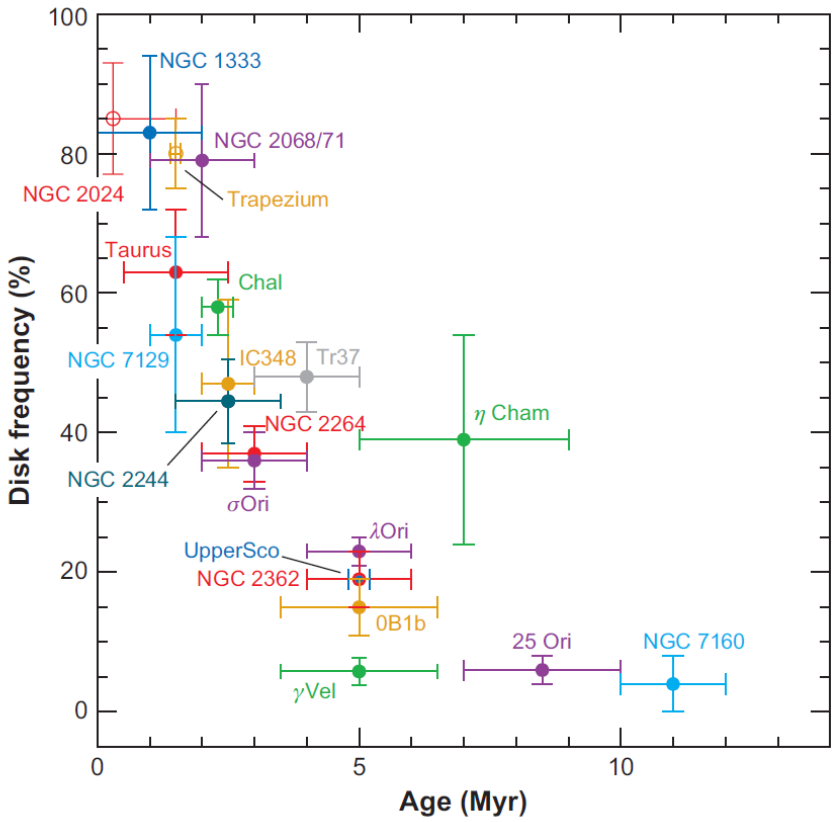

Figure 1.4: Fraction of objects in a cluster which show an NIR excess, plotted against cluster age (Figure from Wyatt et al. 2008).

magnitude. The most likely case is that the current measurements are under predictions of the actual disc mass (Andrews & Williams, 2005). While the actual values of the derived disc masses are sensitive to the assumptions made, relative comparisons are less sensitive to these assumptions. Andrews et al. (2010) used resolved sub-millimetre maps of protoplanetary discs to fit for the surface density distribution of the discs, finding the discs show a surface density profile of $\Sigma \propto R^{-0.9\pm0.2}$ at small radius, consistent with the theoretically preferred value of $\Sigma \propto R^{-1}$ which I will discuss later.

1.2.3 Observations of Disc Evolution

In this thesis I attempt to build a model for the evolution and dispersal of discs. Therefore, the observations of disc evolution should form the basis for any model I develop later and it is important to summarise the current status of the observations here. Unfortunately due to the lack of observations at Far-IR wavelengths, the current observations of disc evolution probe two different scales. Near to Mid-IR observations probe the radial scales around $\sim$ 1AU, while the sub-millimetre/millimetre observations probe radial scales around $\sim$ 100 AU, and therefore we must consider the evidence from both before making any definitive statements of global disc evolution. Perhaps one of the most important indicators of disc evolution is how long discs live around young stars. Figure 1.4 shows the fraction of young stars with masses $\gtrsim 0.2 M_{\odot}$ (Haisch et al. 2001b) in a cluster with an IR excess (JHKL bands) as function of age.

This clearly shows that at early ages $\lesssim$ 1Myr most ($\sim$ 80%) young stars are surrounded by (dust)

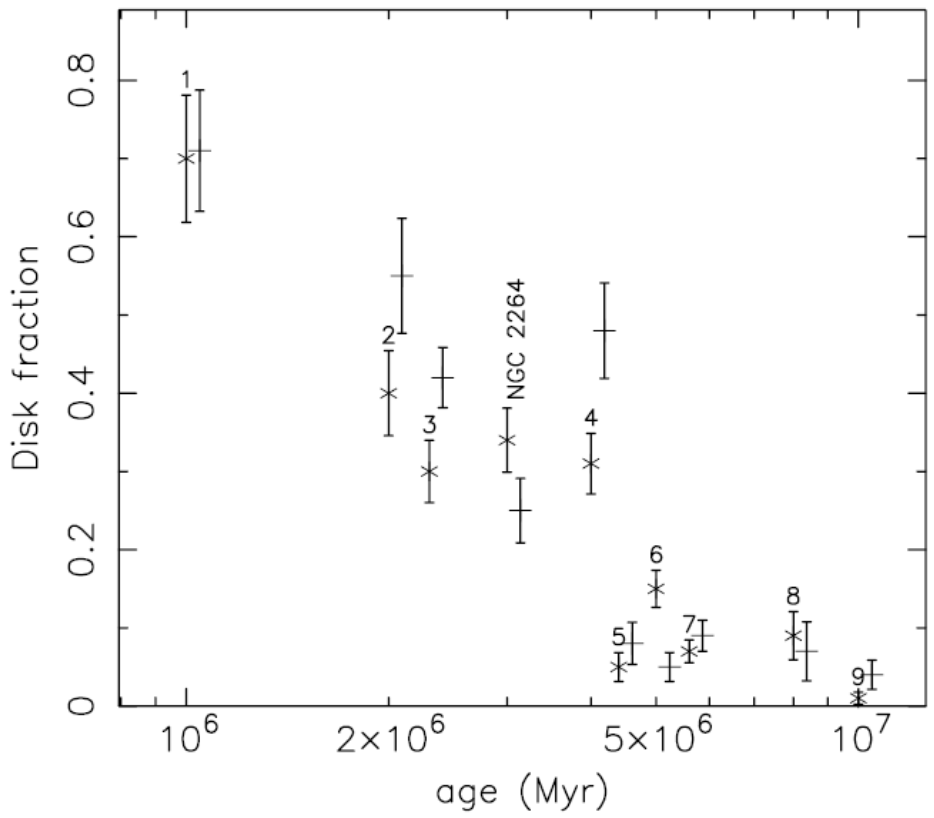

Figure 1.5: Fraction of young stars in a cluster with detectable signs of accretion as a function of cluster age. Crosses represent accreting fraction (determined from the equivalent width of Hα), where as pluses represent NIR disc fraction which are slightly offset (to the right) from the accreting fraction in age. The following clusters are shown: 1) Taurus; 2) Cha I; 3) IC348; 4) Tr 37; 5) NGC 2362; 6) OB1bc; 7) Upper Sco; 8) B1a/250ri; 9) NGC 7160 (Figure from Kennedy & Kenyon, 2009)

discs at small radii, consistent will all stars being born with discs (but some losing them due to binary truncation; e.g. Alexander & Armitage, 2009). However, over the next 10Myr of evolution the majority of stars lose their discs, with a median inner dust disc lifetime of $\sim$ 3Myr (Haisch et al. 2001b). As mentioned above we must be careful not to generalise results to all radii and to both gas and dust components. While the lifetimes of inner dust discs have been known for a long time, a lot of attention has been recently paid to whether this is indicative of the lifetime of the entire protoplanetary disc at all radii in both gas and dust. In order to study the outer disc a comparison between IR and sub-millimetre emission was employed (Duvert et al. 2000, Andrews & Williams 2005,2007). The results of these studies were quite conclusive, there is almost a one to one mapping between objects indicated as having a disc in the IR and a sub-millimetre detection and objects indicated as disc-less and no sub-millimetre detection. This indicates the destruction of a disc is spatially coordinated, the disc appears to disappear at all radii at the same time (compared to the disc's lifetime; I will discuss the interesting and special case of 'transition' discs a bit later). Furthermore, Kennedy & Kenyon (2009) performed a similar analysis, but instead of using IR observations of dust discs to indicate disc fraction, they used the fraction of discs that show signs of accretion. The results are shown in Figure 1.5, which shows an almost identical form to the decline in NIR dust discs. This indicates that the clearance of a dust disc is indicative of the clearance

of the gas and dust disc. Therefore, the observations appear to indicate that gas and dust discs around stars live on average $\sim$ 3Myr, but have a spread of around an order of magnitude, but after 10Myr almost all discs appear to be devoid of detectable dust emission in the IR and sub-millimetre, along with no detectable gas emission (Zuckerman et al. 1995). The mass dependence of this evolution is currently unknown although Ercolano et al. (2011) present a preliminary, but inconclusive attempt to understand the affect of stellar mass of disc lifetimes.

IR photometery can tell us much more than estimates of disc lifetimes, one of the most fruitful analysis is the comparison of NIR disc colours. This analysis compares the emission from different radii of the disc at the same time. Longer wavelengths probe thermal emission at lower temperature and hence larger radii. Larger values of the colours indicate 'redder' emission, i.e. more emission from colder regions of the disc and hence larger radii. In Figure 1.6 I show colour-colour plots for young stars binned by spectral type, where the colours are scaled such that a colour of 0 indicates the value expected from a pure Rayleigh-Jeans photosphere. This plot clearly shows that most discs appear in two separate regions of the parameter space, either those consistent with pure stellar photosphere (bottom left) and those consistent with optically thick primordial discs (top right). The crosses indicate the limiting case of a flat disc which is on the point of transitioning from optically thick to optically thin. This indicates that there are very few young stars that posses discs, which lie in between the point of being classified as a primordial disc and being classified as disc-less. This indicates that time-scale for the transition between a star surrounded by a primordial disc and a disc-less star is rapid, considerably shorter than the discs lifetime.

The points circled in Figure 1.6 are discs that are inconsistent with both a optically thick primordial disc and a stellar photosphere. Based on the fact these objects lie in between primordial and disc-less, these objects have been labelled as 'transition' discs, under the assertion that these discs are caught in the act of transitioning from primordial to disc-less. These 'transition' discs could fall into two categorises. They could in fact be discs that are transitioning from primordial to cleared, and by comparing the number of these objects to the number of primordial discs, an estimate of the transitional time-scale as $\sim$ 10% of the disc's total lifetime can be found (e.g. Strom et al. 1989; Skrutskie et al. 1990; Kenyon & Hartmann 1995; Muzerolle et al. 2010; Luhman et al. 2010). Or of course, these discs could be rare and long lived and uncorrelated with disc dispersal, but the evolution from primordial to disc-less must still be rapid in order to explain the gap. Furthermore, if we assume that these 'transition' discs are discs caught in the act of clearing, then the colour-colour plot indicates that this clearing must proceed from inside out, as the discs loose their excess at shorter wavelengths (smaller radii) before they loose their excess at longer wavelengths. This opacity deficit at small radii has been interpreted as evidence as an inner hole in their dust (and possibly gas) discs (e.g. Calvet et al. 2002), and that disc clearing proceeds from inside out.

One important evolutionary indicator is the accretion rate onto the star. Accretion rate measurements can be made using the UV excess above the photosphere discussed earlier, or through line emission that is thought to correlate with the UV excess (e.g. Herczeg & Hillenbrand 2007). In Figure 1.7 is an example of analysis of accretion rates. There is a clear and possibly power law decline in accretion rates over many orders of magnitude in accretion rate, with a best fitting value of $\dot{M}_* \propto t^{-3/2}$. However, for a given age there is clearly a large spread in the observed accretion rates, much larger than expected from pure random errors (Hartmann et al. 1998). At this point it is also worth pointing out that there is a

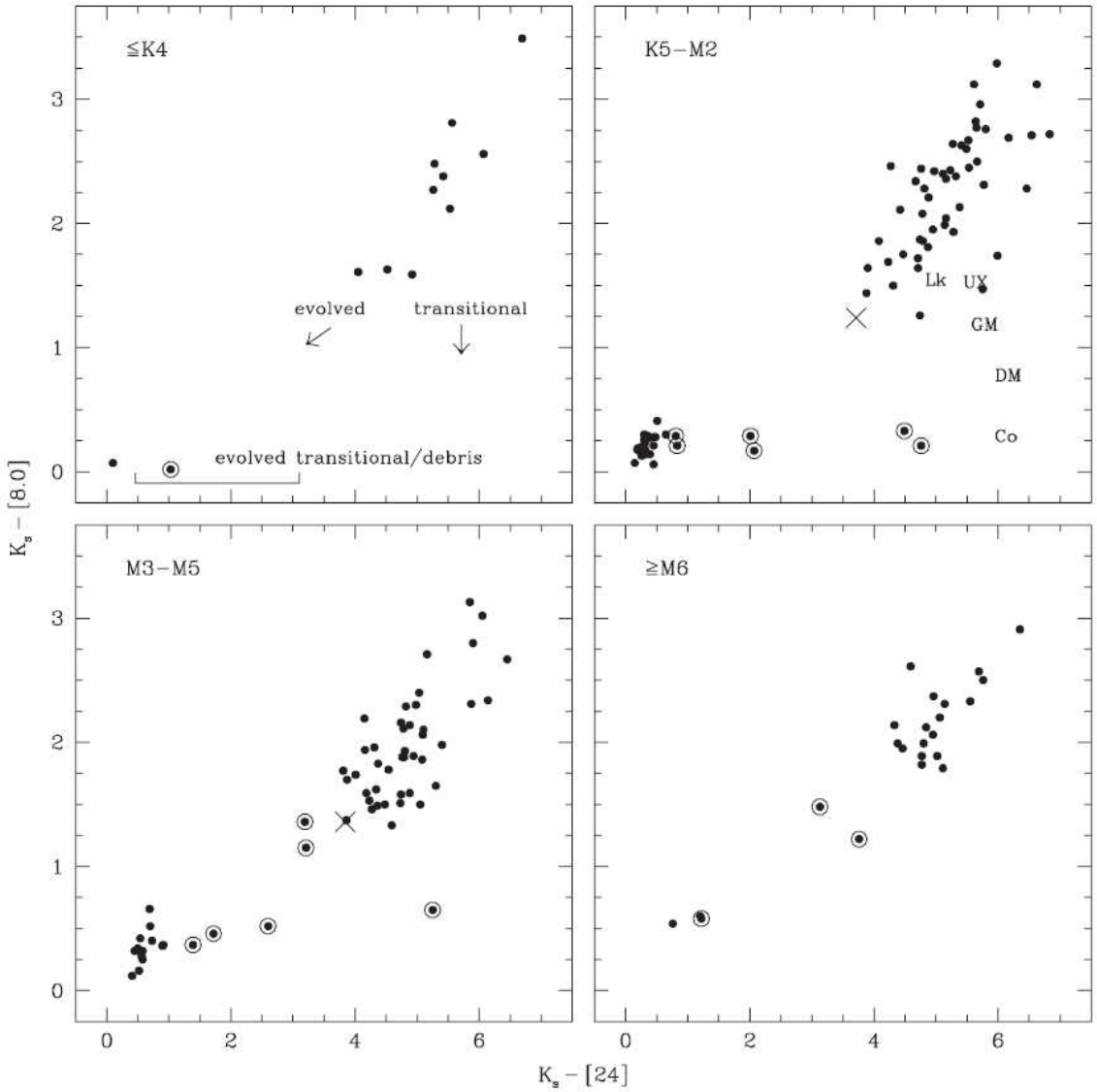

Figure 1.6: Colour-Colour plot of young stars in Taurus, shown for different spectral types. Circled points are those which are not consistent with at pure stellar photosphere or optically thick IR disc (Figure from Luhman et al. 2010).

current debate about the accurary of stellar ages, that may apply some form of transform to the x-axis of Figure 1.7 changing the exact results, but what is not in doubt is the decline with time and spread in accretion rates.

1.2.4 Properties of 'Transition' Discs

'Transition' discs are a poorly defined (both observationally and theoretically) class of objects which represent a small but important subgroup of disc-bearing systems. As mentioned above the hypothesis that these objects are discs which are transitioning from an optically thick primordial disc, to a disc-less system has placed an upper bound on the time-scale for this transition. Therefore, if these objects truly represent a set of objects caught in act of clearing, then studying their properties can provide clues as to the physical mechanism which disperses the discs. The main method for classifying objects as

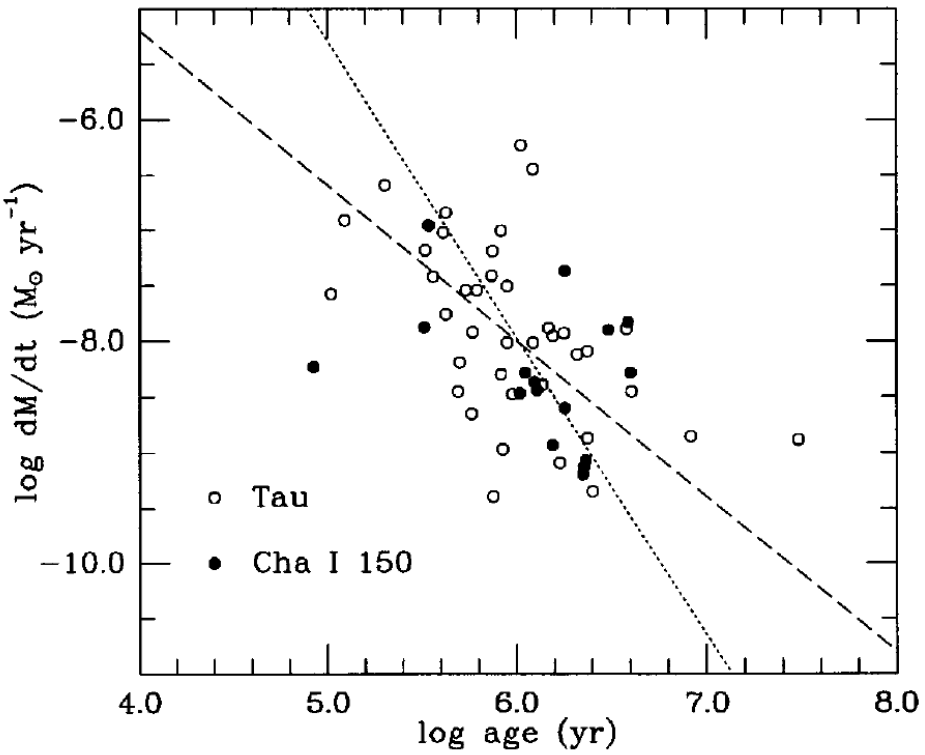

Figure 1.7: Accretion rate measurements plotted against the age of the young stars, for the Taurus and Chameleon I star forming regions. Dashed lines, least-square best-fit assuming that the error in log$t$ is 0.3, while the error in log dM_*/dt is 0.6. Dotted lines, least-square best-fit assuming that the error in both log$t$ and log dM_*/dt are 0.4. The dashed line fit is preferred because the errors in estimating accretion rates, along with the intrinsic dispersion of accretion at a given age, are likely to be larger than the differential errors in stellar ages (Figure from Hartmann et al. 1998).

'transition' discs is through the shape of their SED. An SED which shows a significant drop (compared to a primordial disc) in emission at NIR wavelengths, but then returns to the emission levels expected for a primordial disc at MIR-FIR wavelengths is the essential defining feature (e.g. Figure 1.8). However, there is no consensus of what drop in emission relative to the flux at longer wavelength constitutes a 'transition' disc and observational samples do not span the same regions of parameter space (e.g. Merin et al. 2010). This drop in emission at short wavelengths is indicative of a drop in opacity at those temperatures, and has lead to the suggestion that it represents a cleared inner hole in the dust disc. This hypothesis has been tested with resolved imaging of the largest holes, where the hole sizes estimated from the SEDs are roughly consistent with the holes seen in the resolved images (Hughes et al. 2008). Furthermore, interferometric measurements of the dust structure near the inner holes is also providing a fruitful avenue of research (e.g. Ratzka et al. 2007), although the number of resolved images or interferometric measurements of 'transition' discs remains limited, and SED fitting is still the most common and widespread method for measuring the radii of the regions of low opacity. One of the most interesting distinctions that can split the population of 'transition' discs, is whether they are accreting or not. Evidence of accretion implies that there must be a gas reservoir close to the central star and ro-vibrational CO observations (Salyk et al. 2007) have confirmed that the well know 'transition' disc GM Aur has a gas mass in the inner disc ($R < 5$AU) of $0.3 M_\oplus$, while still heavily accreting at $\sim 10^{-8} M_\odot$ yr^{-1}, with a dust inner hole radii of ~ 20AU (Calvet et al. 2005). Furthermore, Espaillat et

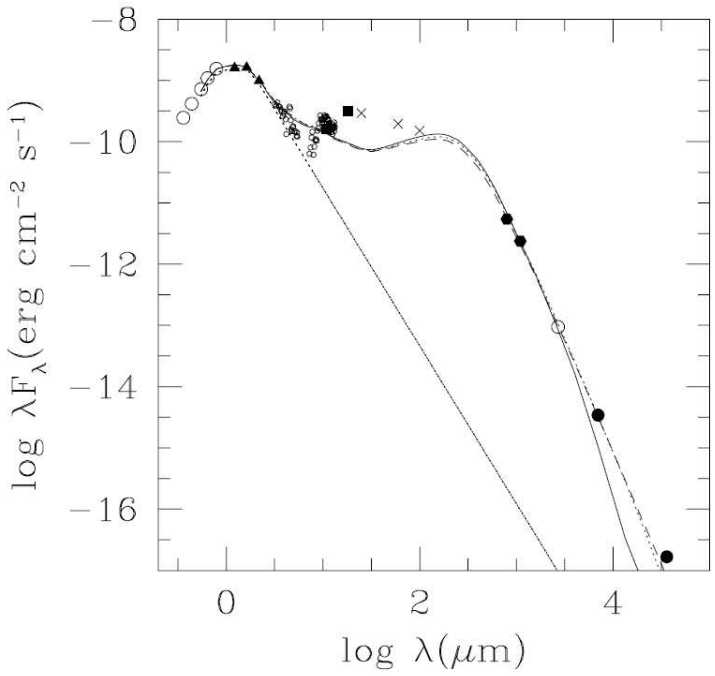

Figure 1.8: The observed SED of the 'transition' disc TW Hya shown as points, the lines represent best fit models of a pure stellar photosphere or a primordial disc (Figure from Calvet et al. 2002).

al. (2008,2010) has found evidence for optically thin dust emission from within the hole itself and the possibility of an optically thick inner dust disc at very small radii ~ 0.1 AU. All of the Espaillat et al. discs are heavily accreting $\gtrsim 10^{-8}\mathrm{M}_{\odot}$ yr^{-1}, although the significance of this inner dust disc correlated with heavily accretion has yet to be identified, as the sample only contains 4 objects.

Perhaps one of the most interesting ways to examine the properties of 'transition' discs is in the $\dot{M}_*$ - R_{hole} plane. In Figure 1.9 is a large sample of objects from the literature classified as 'transition' discs by their authors. Two things are immediately clear from this plot, the selection criterion used by one author does not in general probe the entire range of parameter space, as different selection criterion have been applied on similar regions by different authors, underlying the lack of a cast iron definition for 'transition' discs. Furthermore, the possible dichotomy in the sample between those with small inner holes $R < 20$ AU that have a wide range of accretion rate, to those with a large inner hole $R > 20$AU which either have a significant accretion rate $\dot{M}_* \sim 10^{-8}\mathrm{M}_{\odot}$ yr^{-1}or appear to be not accreting, indicating the full population 'transition' discs may not be a homogeneous one, with several possible mechanisms giving rise to their creation. While the lack of objects with large inner holes and low acccretion rates is certainly a real effect, the number of non-accreting objects with large holes is unknown and certainly something the FIR observations provided by *Herschel* should help with.

While the total statistics of the number of 'transition' discs, compared to primordial discs has placed an upper bound for the clearing time-scale of the inner disc. The fact that the 'transition' disc sample does not appear to be homogeneous, and the possibility of incompleteness at large hole sizes does not allow us to place any constraints on the speed of the inner disc clearing compared to the outer disc clearing.

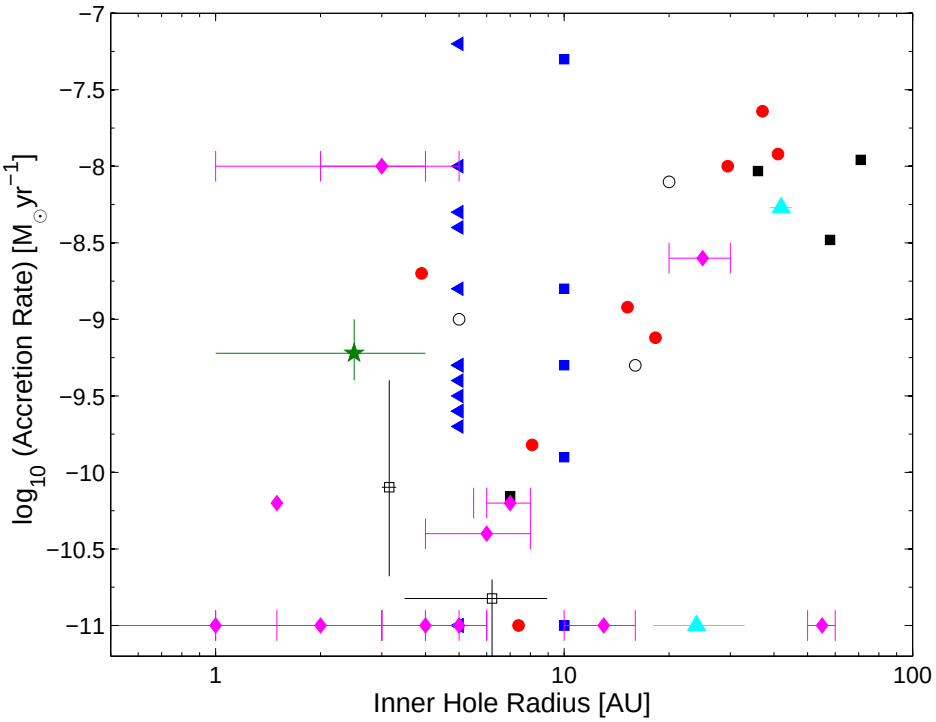

Figure 1.9: The inner hole radius and accretion rate of low-mass objects classified as 'transistion' discs by varies authors: cyan triangles (Brown et al. 2009); blue filled triangles & squares (Cieza et al. 2010); black open squares (Ercolano et al. 2009a); black filled squares (Espaillat et al. 2008,2010); black open circles (Hughes et al. 2009, 2010); red filled circles (Kim et al. 2009); magenta filled diamonds (Merin et al. 2010); green filled star (Najita et al. 2010). Where error-bars or ranges are listed they are shown. As Cieza et al. (2010) list the wavelength of the inner hole rather than the radius, I conservatively estimate an inner hole radius of < 5 AU for $\lambda_{\rm hole} < 5.8\mu$m, and < 10 AU for $8 < \lambda_{\rm hole} < 24\mu$m. Objects with no sign of accretion are placed on the plot with an accretion rate of 10^{-11}M$_\odot$ yr^{-1}, indicative of the observational detection limit.

1.3 Structure and Evolution of Discs

Now we have discussed discs from an observational point of view it is useful to consider the models of disc structure and evolution. The starting point for this discussion must be from the point of view that these protoplanetary discs are actively accreting onto their central star, i.e. they are accretion discs. Accretion discs are prevalent on all scales in astrophysics and the main problem remains the same. If the discs are actively accreting, then they must be transporting angular momentum. While very heavy protoplanetary discs (compared to the central star) may transport angular momentum in spiral density waves, through self gravitating interactions (e.g. Lodato & Rice 2005; Clarke, 2009), this is thought to be only important at the very earliest times, during the disc's assemblage and early evolution phase, thought to be closely correlated with the Class I phase. However, discs spend most of their time in the Class II phase, where the disc mass is not large enough to drive self-gravitating interactions. A viable alternative angular momentum transport mechanism is a viscosity in the disc. A viscosity will allow gas particles to diffuse radially, carrying specific angular momentum with it, allowing the disc to accrete material by diffusing its angular momentum to large radius.

The time-scale associated with this process can be roughly estimated by dividing the discs mass by

the accretion rate, which gives a time-scale $\mathcal{O}$Myrs. As we shall see this time-scale is much longer than the time-scales associated with obtaining dynamical equilibrium in the disc, therefore we can consider the structure and evolution of a protoplanetary disc as two separate problems. As the disc is primarily composed of gas then the governing equations are those of fluid mechanics. Furthermore, since the disc's mass is considerably less than the stellar mass then we can assume the gravitational potential is simply given by $\Phi = -GM_*/r$. Therefore, the governing equations of the system are continuity and mass conservation:

$$\frac{\partial \rho}{\partial t} + \nabla \cdot (\rho \mathbf{u}) = 0 \tag{1.2}$$

$$\frac{\partial \mathbf{u}}{\partial t} + \mathbf{u} \cdot \nabla \mathbf{u} = -\frac{\nabla P}{\rho} - \nabla \Phi + \frac{1}{\rho} \nabla \cdot \mathbf{T} \tag{1.3}$$

where ρ is the gas density, $\mathbf{u}$ is the gas velocity vector, P is the thermal pressure and $\mathbf{T}$ is the viscous stress tensor. The viscosity in the disc can also be a source of heating, through viscous dissipation. However, in order to match the SED observations a significant source of heating from the viscosity is inconsistent with the observations, and protoplanetary discs are closer to 'passive' discs, where the thermal structure is set by the radiation field of the star (e.g. Kenyon & Hartmann 1987; Hartmann, 2009). As the gas and dust will be in thermal equilibrium with the stellar radiation, the discs local sound speed will be considerably less than the escape velocity. In order to simplify the problem further I assume that the disc is axis-symmetric and is locally isothermal, or $c_s(R,\phi,z) \approx c_s(R)$, which is fairly robust if most of the disc's mass is either very optically thick or very optically thin to its own heating/cooling radiation.

1.3.1 Disc Structure

Radial Structure

I will first consider the radial, mid-plane structure of an axis-symmetric disc: the momentum equation in the radial direction becomes:

$$\rho \left(\frac{\partial u_R}{\partial t} + u_R \frac{\partial u_R}{\partial R} + u_z \frac{\partial u_R}{\partial z} - \frac{u_\phi^2}{R} \right) = \frac{\partial P}{\partial R} - \frac{GM_* \rho}{R^2} + \frac{1}{R} \frac{\partial \left(R T_{RR} \right)}{\partial R} + \frac{\partial T_{Rz}}{\partial z} \tag{1.4}$$

where $\{R,\phi,z\}$ describe the cylindrical co-ordinate system and u_i & T_{ij} are the components of the velocity and viscous stress tensor respectfully. So clearly, any variations are going to arise for two physical reasons: velocity adjustments due to a change in the disc's radial and hence pressure structure and velocity adjustments to viscous processes. Above I argued that the observations indicate that the time-scales associated with the viscous processes are long (comparable to the discs age). The time-scale associated with pressure variations is simply H_R/c_s, where H_R is the radial pressure scale length. For a passively heated protoplanetary disc, with a surface density profile that falls off something like $\Sigma \propto R^{-1}$, $H_R \sim 0.1R$. Therefore, the radial dynamical time-scale is considerably shorter than the time-scale associated with the viscous processes and we can separate Equation 1.3.1, into it's viscous and dynamical components, and on the time-scales associated with disc evolution can consider the disc to be in dynamical equilibrium in the radial direction. Furthermore, since $u_\phi \gg u_R$ at all radii then the equation

for dynamical equilibrium simply becomes:

$$\frac{1}{\rho}\frac{\partial P}{\partial R} = \frac{u_\phi^2}{R} - \frac{GM_*}{R^2} \tag{1.5}$$

Thus, the solution to the above equation allows us to find the azimuthal velocity in the disc. The magnitude of the pressure term on the LHS is simply $(R/H)c_s^2/R$ (where H is the vertical scale height of the disc), whereas the magnitude of the gravitational force is $v_{\rm esc}^2/R$ (where $v_{\rm esc}$ is the escape velocity), as observations tell us in order to match the SEDs of protoplanetary discs the discs sound speed is many orders of magnitude less than the escape velocity, to first order we can simply neglect the radial pressure gradient in the force balance and take the disc to be Keplerian with $u_\phi = \sqrt{GM_*/R}$. It is worth mentioning, that although this radial pressure gradient is small is has important implications for dust in discs. A slightly more detailed calculation indicates that the gases' azimuthal velocity in the disc is $u_\phi \approx [1 - \mathscr{O}(H_R/R)^2]\sqrt{GM_*/R}$ (e.g. Armitage, 2010), as dust will not be effected by the pressure gradient it will be orbiting at a Keplerian velocity and will be travelling faster than gas. Therefore, the dust particles will feel a headwind drag and begin to slowly loose angular momentum and spiral in to the star (Weidenschilling, 1977) and in some cases this drift time-scale can be as short as a couple of orders of magnitude larger than the orbital time-scale (e.g. Takeuchi & Lin 2002; Takeuchi et al. 2005), certainly shorter than the discs lifetime. While this certainly has some important issues that need to be resolved, namely the retention of mm grains in the outer disc (e.g. Alexander & Armitage, 2007), it will certainly become important when the formation of 'transition' discs are discussed.

Vertical Structure

The momentum equation in the vertical direction for the disc is:

$$\rho\left(\frac{\partial u_z}{\partial t} + u_R\frac{\partial u_z}{\partial R} + u_z\frac{\partial u_z}{\partial z}\right) = \frac{\partial P}{\partial z} + \frac{\partial}{\partial z}\left(\frac{GM_*}{r}\right) + \frac{1}{R}\frac{\partial RT_{Rz}}{\partial R} + \frac{\partial T_{zz}}{\partial z} \tag{1.6}$$

As before, this equation can be separated into the viscous components and dynamical component and assuming that u_z is small (compared to the sound speed), the disc can be considered to be in vertical hydrostatic equilibrium. If we restrict ourselves to regions close to the mid-plane, then the equation for hydrostatic equilibrium is directly integrable and we find:

$$\rho(z) \propto \exp\left(-\frac{z^2}{2H(R)^2}\right) \tag{1.7}$$

so the density profile is Gaussian about the mid-plane for an isothermal disc, where the vertical scale height is given by:

$$H(R) = \frac{c_s}{\Omega} \tag{1.8}$$

where Ω is the angular velocity. This results tell us two important results, since the sound speed is considerably less than the escape velocity, this implies that $H(R) \ll R$, nominally observations suggest $H(R) \approx 0.1R$. Thus the majority of the disc's mass is contained close to the mid-plane and the density profile derived above is to a high degree of accuracy the vertical density structure for the entire isothermal

disc. Finally, the time-scale for the disc to attain dynamical equilibrium vertically is Ω^{-1}. This time-scale is comparable to the time-scale to attain dynamical equilibrium radially. Therefore, the disc can be considered to be globally in dynamical equilibrium on time-scales longer than the disc's orbital period, thus when we are interested in the disc's evolution due to viscous processes, dynamical equilibrium arising from variations in disc structure can be assumed, and vica-versa.

1.3.2 Disc Evolution

As we have seen above the disc is thin and not radially pressure supported, allowing us to make two further simplifications when we discuss the discs evolution. The fact that the disc is thin and not radially pressure supported allows us to assume the disc is Keplerian, where the angular velocity at each radius is just given by:

$$u_\phi = \sqrt{\frac{GM_*}{R}} \tag{1.9}$$

Therefore, the continuity equation and $\mathbf{e}_\phi$ component of the momentum equation, for an axis-symmetric disc become:

$$2\pi R\frac{\partial \rho}{\partial t} + \frac{\partial}{\partial R}\left(2\pi R\rho u_R\right) = 0 \tag{1.10}$$

$$2\pi\rho u_R\frac{\mathrm{d}h}{\mathrm{d}R} = \frac{\partial}{\partial R}\left(2\pi R^2 T_{R\phi}\right) + \frac{\partial}{\partial z}\left(2\pi R^2 T_{\phi z}\right) \tag{1.11}$$

These equations can be simplified even further by integrating them over the z direction (as the disc is thin physical variables can be averaged over - weighted by mass - in the z direction), to deal with the evolution of the discs surface density rather than density. Also adopting zero shear boundary conditions at the disc's surface and the fact that $T_{R\phi} = \eta R\frac{\mathrm{d}\Omega}{\mathrm{d}R}$ for a Navier-Stokes type viscosity, where I will discuss this approximation and the origin of the viscosity in Section 1.3.3. Therefore, we can re-arrange the equations into:

$$2\pi R\frac{\partial \Sigma}{\partial t} + \frac{\partial}{\partial R}\left(2\pi R\Sigma u_R\right) = 0 \tag{1.12}$$

$$2\pi R\Sigma u_R\frac{\mathrm{d}h}{\mathrm{d}R} = \frac{\partial}{\partial R}\left(2\pi\nu\Sigma R^3\frac{\mathrm{d}\Omega}{\mathrm{d}R}\right) \tag{1.13}$$

The physical significance of these two equations is now clear, where 1.12 is just still just the continuity equation, or more physically conservation of the discs mass. Equation 1.13 is a statement of angular momentum conservation, since its of the form $\dot{m}h' = -\tau'$ where τ can be thought of as a viscous torque. Eliminating u_R from above we arrive at the 1D equation for the evolution of the disc's surface density:

$$\frac{\partial \Sigma}{\partial t} = \frac{3}{R}\frac{\partial}{\partial R}\left[R^{1/2}\frac{\partial}{\partial R}\left(R^{1/2}\nu\Sigma\right)\right] \tag{1.14}$$

This clearly has the form of a diffusion equation, consistent with our earlier assertion that viscous transport leads to the diffusion of angular momentum. Therefore, we can envisage the evolution of the an accretion disc as follows: The viscosity within the disc leads to diffusion of gas parcels, and its associated angular momentum, a disc with an initially finite outer radius will begin to spread ('viscous spreading'), taking with it the disc's angular momentum, allowing material to accrete onto the central

star. This process will continue, until eventually all the disc's mass has accreted onto the central star, and all the disc's angular momentum is at $R = \infty$ on none of the mass.

Of course, with exact knowledge of the viscosity law the solution of Equation 1.14 is trivial to determine. However, as I shall discuss in Section 1.3.3, the viscosity law is far from being determined. In the special case that ν contains no special scales then power-law similarity solutions are obtainable for Equation 1.14 and these are discussed in detail by Ruden (1993). If one assumes ν is a function of radius only, then Equation 1.14 becomes linear, and if ν is a power-law with radius, then the problem possesses the similarity solutions found by Lynden-Bell & Pringle (1974). These were discussed in detail when compared to protoplanetary disc evolution by Hartmann et al. (1998). Therefore, adopting $\nu \propto R^{\gamma}$, the similarity solution for Σ takes the form:

$$\Sigma(R,t) \propto \frac{M_d(0)}{R^{\gamma}} T^{-\frac{5/2-\gamma}{2-\gamma}} \exp\left(-\frac{R^{2-\gamma}}{T}\right) \tag{1.15}$$

where $T = t/t_{\nu} + 1$ and t_{ν} is the disc's initial viscous time. Therefore, at small radii and/or late times the surface density profile has an almost pure power law form of $\Sigma \propto R^{\gamma}$. Also even though this similarity solution implies an initial disc structure, that is unlikely to be indicative of the actual disc's initial structure, which will depend more on gravity than viscous processes. Any initial surface density profile with the same viscosity law will tend to this solution on a time-scale comparable to t_{ν}. Furthermore, we can integrate this solution to find the accretion rate onto the star and time-evolution of the disc's mass is

$$\dot{M}_* \propto T^{-\frac{5/2-\gamma}{2-\gamma}} \tag{1.16}$$

$$M_d(t) \propto T^{-\frac{1}{[2(2-\gamma)]}} \tag{1.17}$$

respectfully. The observations suggest that $\Sigma \propto R^{-1}$ and $\dot{M}_* \propto t^{-3/2}$. Both these results are consistent with the solutions discussed above if $\nu \propto R$ as argued for by Hartmann et al. (1998). Therefore, a reasonable approach is to adopt a viscosity law of $\nu \propto R$ and use the similarity solutions above. I will use the results of these similarity solutions throughout this work and therefore it is useful to summarise them here. In this case then Equation 1.14 becomes:

$$\Sigma(R,t) = \frac{M_d(0)}{2\pi R R_1} \frac{1}{T^{3/2}} \exp\left(-\frac{R}{R_1 T}\right) \tag{1.18}$$

where R_1 is the discs scale factor, or more physically the point where the discs initial (global) viscous time (t_{ν}) equals the local viscous time, which is given by:

$$t_{\nu} = \frac{R_1^2}{3\nu(R_1)} = \frac{M_d(0)}{2\dot{M}_*(0)} \tag{1.19}$$

Furthermore, we find that the evolution of the accretion rate and disc mass are given by:

$$\dot{M}_*(t) = \dot{M}_*(0)\left(1 + \frac{t}{t_{\nu}}\right)^{-3/2} \tag{1.20}$$

$$M_d(t) = M_d(0)\left(1 + \frac{t}{t_{\nu}}\right)^{-1/2} \tag{1.21}$$

At late times $t \gg t_\nu$ these become power-law functions of time, and combinations of these equations lead to useful quantities, the current disc mass divided by the current accretion rate yields:

$$\frac{M_d(t)}{\dot{M}_*(t)} \approx 2t \approx 2\tau_\nu \tag{1.22}$$

Namely, the disc's mass divided by the current age yields twice the disc's age, which is also the disc's global viscous time τ_ν, so we find that the global viscous time of the disc, i.e. the time with which the disc's evolutionary properties are changing is approximately the disc's current age. However, one important fact becomes apparent, this solution is entirely inconsistent with a rapid clearing of the disc, as observations indicate then even though the discs appear to evolve as above for their entire lifetimes, when they begin to dissipate they do so on a time-scale much less than their lifetime. In fact discs that evolve under pure viscous evolution should be observable in NIR dust observations for Gyrs (e.g. Ercolano et al. 2011a), rather than the Myrs observed. Therefore, a pure viscous model agrees very well with the evolution indicators of CTTs, provided $\nu \propto R$; however, there must be some other process that operates on a time-scale much less that the disc's global viscous time-scale in order to clear the disc rapidly out to large radius.

1.3.3 Origin of the viscosity

In the previous discussion I managed to completely ignore the origin and magnitude of the viscosity, only supposing its existence based on the requirement that the discs must be transporting angular momentum. The first most obvious source of viscosity is molecular viscosity (arising from the diffusion of molecules due to random motions of the gas particles), a simple calculation yields that the viscous time-scale molecular viscosity will produce are $\sim 10^{12}$ times too long (e.g. Armitage, 2010). Therefore, the viscosity in the disc must arise through some other mechanism. A viscosity is simply a resistance to shear (and possibly tensile stress), and a protoplanetary disc is an obvious example of a shearing flow, as each annulus of the disc is rotating at Keplerian velocity, there exists large radial velocity gradient between each of the annuli. Therefore, if there was any diffusion of gas particles between annuli, there would be a shear stress and hence a viscosity. One proposed mechanism for the transport of angular momentum is self-gravitating interactions (e.g Lin & Pringle 1987), where spiral density waves re-distribute angular momentum. While not formally a local viscous process, under the conditions found in a protoplanetary discs it can behave as an 'effective viscosity' where the torques dissipate locally (Lodato & Rice, 2004). However, for self-gravitating interactions to become important the disc need to be massive (compared to the central star) with the nominal value being $M_d/M_* > 0.1$ (e.g. Lodato & Rice 2005; Clarke 2009). Given this requirement, self-gravity cannot be the source of angular momentum transport for the majority of the disc's lifetime and certainly not the source of the angular momentum transport during the disc clearing phase we are interested in here.

One other solution would be if the disc was turbulent, then this could transport angular momentum and act as a type of viscosity. This form of the viscosity was discussed by Shakura & Sunyaev (1973) by assuming the turbulent viscosity can be parametrised in terms of a representative velocity and scale for the turbulence. Shakura & Sunyaev glossed over our ignorance of the origin of the turbulence and how it acts as a viscosity by introducing the famous α parameter, where the viscosity in this formalism is given

by:

$$\nu = \alpha c_s H(R) \tag{1.23}$$

where the scale size of the turbulence is taken to scale with the disc's scale height and the velocity of turbulence is taken to scale with the local sound speed, and the actual magnitude is described within the dimensionless α parameter. Therefore, a disc in which the viscosity scales linearly with radius and constant α parameter requires that the disc is slightly 'flared' with $H(R) \propto R^{5/4}$ in agreement with the current models of vertical disc structure (e.g. Chiang & Goldreich 1997; D'alessio et al. 1998).

While turbulence is the leading candidate for angular momentum transport in T Tauri discs, the origin of the turbulence is still a matter of debate. It is well known that a Keplerian disc is stable to pure hydrodynamic interchange instabilities (e.g. Ruden, 1993), thus we still require an instability to drive the turbulence. Lin & Papaloizou (1980) suggested thermal convective instabilities as a possible driving mechanism, with estimates of the magnitdue of the viscosity in the range required by observations (Ruden & Lin 1986; Cabot et al. 1987; Ruden et al. 1988). Although it has been pointed out that a convectively unstable disc may be unable to sustain turbulence during the disc's lifetime (Korycansky, 1992) or even transport angular momentum the correct way (e.g. Ryu & Goodman, 1992)! Currently the leading candidate is the Magneto-Rotational Instability (MRI) discovered and rediscovered by several authors, but it was Balbus & Hawley (1991) who applied it to accretion discs. In the limit of ideal MHD (where magnetic field lines are coupled to gas parcels), a rotating shear flow is unstable to linear MRI modes if:

$$\frac{\mathrm{d}\Omega^2}{\mathrm{d}R} < 0 \tag{1.24}$$

This inequality is clearly satisfied in a Keplerain protoplanetary disc, and leads to a globally turbulent accretion disc (e.g. Flock et al. 2011; Beckwith et al. 2011) and α parameters in the range $10^{-3} - 10^{-1}$, sufficient to explain the accretion rates and viscous time-scales observed. However, all these results rely on the 'Ideal' MHD approximation, where the effects from ambipolar diffusion, ohmic dissipation and the Hall effect are neglected. The most studied of these 'non-ideal' effects to date is ambipolar diffusion; the 'ideal' approximation assumes that the magnetic field lines are coupled to the gas parcels, this is true in the case of fully ionized gas. However, a protoplanetary disc is composed mainly of cold molecular gas. Low ionization levels from FUV or hard X-ray photons are possible, enough to make the regions of the disc close to the 'ideal' approximation. Though, at radii around $\sim$ 1AU (for solar mass stars) the gas is too cold for thermal ionization, and the disc's column too large to allow high ionization rates from FUV/X-ray photons. Thus, it is possible there are large regions of the disc where the gas parcels are not coupled to the magnetic field lines, and unable to drive turbulence. The idea of these 'dead zones' were suggested by Gammie (1996), and detailed calculations seem to suggest that these dead zones may exist, not allowing high accretion rates at small radii. Latests calculations by (Perez-Barker & Chiang, 2011), show that in their model the MRI is unable to sustain the full range of observed accretion rates all the way to the star.

Therefore, it appears at this stage a full understanding of the turbulence processes in the disc are far from understood and the process of converting this into a predictive viscosity law in accretion discs is a long way off, although it remains an extremely active and fruitful area of research. Therefore, in this thesis I will follow the example of many others and parametrise the viscosity in terms of $\nu = \nu_1 R/R_1$ as

indicated by observations.

1.4 Disc Clearing Mechanisms

We have seen that while the standard theory of accretion disc evolution, matches the observations of discs during the CTTs phase, it is completely unable to explain the rapid removal of disc material at late times. The two-time-scale nature of disc evolution is something that cannot be reproduced by pure viscous processes, thus in order to explain disc dispersal another mechanism must be found. When a disc disperses, there are only three things that can happen to the disc material, it can either accrete onto the central star, be removed from the disc/star system or end up in planets. While I have shown above that accreting material onto the star cannot explain the final disc dispersal stage, we are left with the final two options, either place the material in planets or remove it entirely from the system.

1.4.1 Planet Formation

Planet formation as the origin of disc destruction has an appealing closed nature to it, as planet formation which requires a disc, can also destroy the disc. Armitage & Hansen (1999) discussed planet formation as a route to disc dispersal. Placing a Jupiter mass planet in a very massive disc ($M_d = 0.1M_*$), they found that this planet was able to drive self gravitating perturbations, emphasised at the Lindblad resonances. Once the planet reaches 4-5 Jupiter masses the disc begins to fragment rapidly, forming many more planetary bodies near both the inner and outer Lindblad resonances. Figure 1.10 shows results from a numerical calculation of this process occurring, showing that these new planets could form rapidly (on dynamical rather than viscous time-scales). Planet formation as a mechanism for disc destruction, requires that one of these new planets grow large enough to begin this process again and again, until all the disc material is exhausted. The model presented by Armitage & Hansen can successfully reproduce the rapid clearing of the disc. It predicts that the resultant planetary system would consists initially of numerous massive planets on co-planar, near circular orbits, but mutual interactions would eventually leave a system with a small number of massive planets on eccentric orbits. It remains to be seen whether the observations of planetary systems are in agreement with this model for planet formation. However, it is unlikely this method could provide a dominant dispersal mechanism for planet formation since it requires the disc to be massive enough to fragment, to allow the formation of either the initial planet or secondary planets.

Origin of transition discs

The planet formation model can also account for observations of transition discs. A massive planet embedded in a gas disc will clear a gap in the gas and dust disc (Lin & Papaloizou 1979a,b), this is shown clearly in the top right panel of Figure 1.10. While it is clear that the planet provides a 'leaky' barrier to the gas, Rice et al. (2003,2006) suggested that the large radial pressure gradient present at the edge of the gap in the gas disc could trap large dust grains, preventing them form accreting across the planetary barrier and entering the inner disc, resulting in an opacity drop in the inner disc. Detailed calculations of this process have yet to be performed and it is still yet to be seen whether this opacity

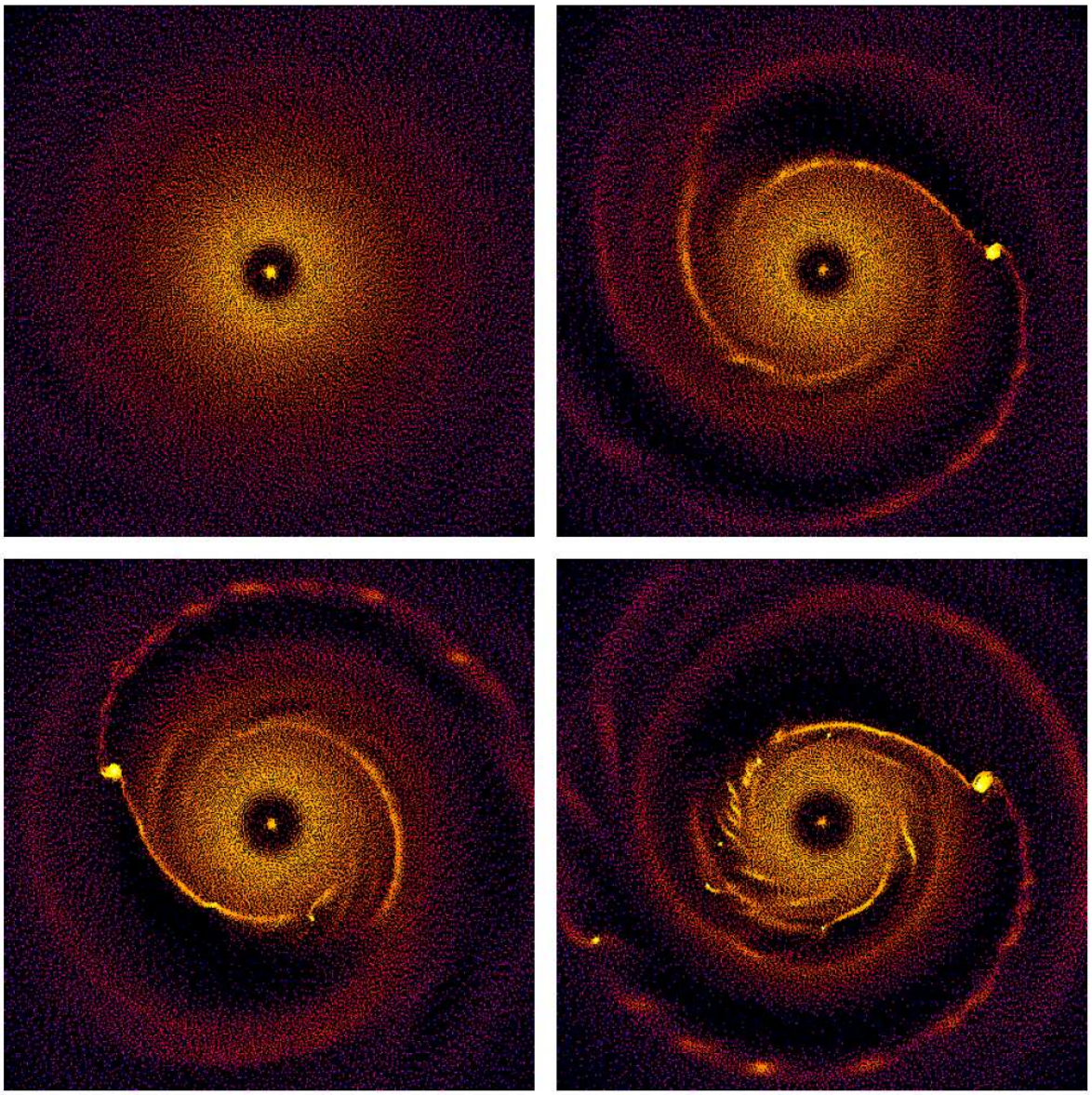

Figure 1.10: Disc surface density shown from an SPH calculation of a protoplanetary disc. The top left panel shows an isolated disc after 512 orbital period at the inner edge, whereas the top right planet shows a disc at the same time but with a initially Jupiter mass planet embedded in it. The bottom left panel indicates the time (608 orbital periods) at which the planet has reached ~ 4 Jupiter masses and is beginning to drive resonances. At 736 orbital periods (shown in the bottom right) the disc is fragmenting forming large numbers of new planetary bodies (Figure from Armitage & Hansen 1999).

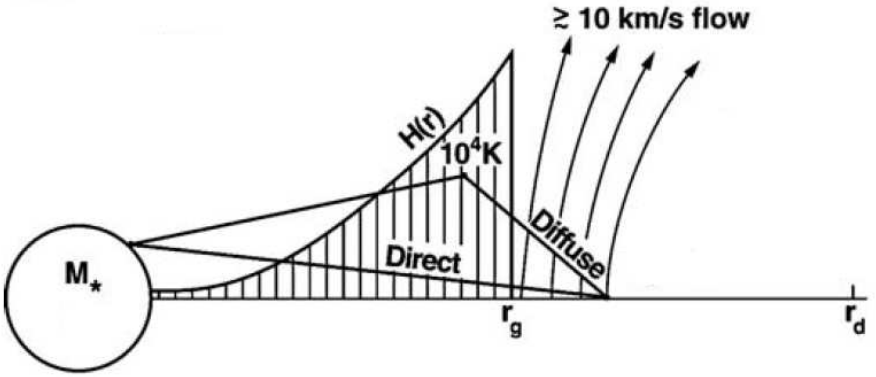

Figure 1.11: Cartoon of disc photoevaporation. Inside the radius r_g a bound atmosphere is formed, outside r_g a thermal disc wind is formed (Figure from Hollenbach et al. 2000).

drop is sufficient to explain the NIR emission in transition discs. However, it is widely believed that discs embedded with planets are the origin for some 'transition' discs.

1.4.2 Photoevaporation

In order to remove disc material from the star/disc system it must be accelerated to the escape velocity. Since, the the majority of the disc is at temperatures well below the escape temperature in order for this process to occur there must be regions close to the surface of the disc where the temperature increases and approaches the escape temperature. If the gas reaches sufficient temperatures it may drive a thermal driven wind instead of forming a bound atmosphere (similar to a stellar wind emerging from a hot corona). Such a processes has been known to occur from discs that are close enough to massive stars, where the UV luminosity can heat the surface regions of the protoplanetary discs to temperatures close to the escape temperature. This process of external disc 'photoevaporation' was invoked to explain the tailed shapes of protoplanetary discs close to the OB stars in the Orion Nebular Cluster, where gas is being stripped off the disc at such a rate that they can only survive for a short time (Johnstone et al. 1998; Clarke, 2007). Detailed radiation hydrodynamic calculations have now been performed that can match the flow morphology and low ionization lines seen from these objects (e.g. Richling & Yorke, 2000). However, external photoevaporation cannot be the origin of disc dispersal around most young stars as only $< 25\%$ of young stars will experience even mild external photoevaporation (Adams et al. 2004).

It has been known for a long time that young stars are much more active than their evolved counterparts, producing large amounts of high energy photons in the UV and X-rays. It was Hollenbach et al. (1994) who built the first self-consistent model of disc photoevaporation, driven by the central star. The Hollenbach et al. (1994) model was a pure EUV (photons capable of directly ionizing hydrogen) only model and these photons produce an approximately isothermal ($T \sim 10^4$K) layer at the disc's surface. Figure 1.11 shows a cartoon of photoevapoation driven by the central star, inside some radius labelled r_g the gas forms a bound hydrostatic atmosphere, outside this radius the gas drives a thermally driven flow. Hollebach argued that this radius would be related to the escape temperature, and when the internal energy of the gas was equivalent to the gravitational energy it would be able to escape the stars potential

in a flow. This radius can simply be calculated and is given by:

$$r_g = \frac{GM_*}{c_s^2} = 8.9 \left(\frac{M_*}{1\ \mathrm{M}_\odot}\right)\left(\frac{T}{10^4\ \mathrm{K}}\right)^{-1} \mathrm{AU} \tag{1.25}$$

Since, most of the earlier literature was only concerned with isothermal 10^4K winds, this scale radius is commonly described only in terms of mass, and for completeness I separately define $R_g = 8.9(M_*/\mathrm{M}_\odot)$AU. This simple picture of EUV disc photoevaporation has been studied in detailed by several authors, the picture was orginally described in Hollenbach et al. (1993) and Shu et al. (1993) with relation to our solar system. Hollenbach et al. (1994) then performed radiative transfer calculations based on an analytic model in order to determine the density of the base of the ionized layer. This model was then used to estimate the total mass-loss rate by assuming that the gas outside r_g had a velocity equal to the sound speed of 10km s^{-1}, this model gave a total mass-loss rate of:

$$\dot{M}_w \approx 4.4 \times 10^{-10} \left(\frac{\Phi_*}{10^{41}\ \mathrm{s}^{-1}}\right)^{1/2} \left(\frac{M_*}{1\ \mathrm{M}_\odot}\right)^{1/2} \mathrm{M}_\odot\ \mathrm{yr}^{-1} \tag{1.26}$$

where Φ_* is the total EUV ionizing luminosity in photons per second. This initial calculation was later improved by Font et al. (2004), who used the radiative transfer calculations of Hollenbach et al. (1994) as the boundary conditions for a hydrodynamic calculation. This calculation verified the basic model put forth by Hollenbach et al., while making several modifications. Firstly, it moved the inner radius from which the flow may be launched towards the star by an order of magnitude, allowing the sub-sonic launching of a wind outside $0.1r_g$, a result confirmed by Adams et al. (2004) and Alexander et al. (2008). Secondly, it reduced the total mass-loss rate by a factor of 3 and changed the profile of the mass-loss rate to one that was dominated at slightly smaller radii. It was originally thought that photoevaporation would not pay an important role in disc evolution around low mass stars as $M_d/\dot{M}_w$ yields a time-scale several orders of magnitude longer than the observed disc lifetimes.

Photoevaporation coupled with viscous evolution

It was Clarke et al. (2001), who realised that photoevaporation doesn't have to remove all the disc material to provide a disc dispersal mechanism. Instead photoevaporation can provide a cut-off in accretion rate, with most of the disc's original mass being accreted onto the star. This is suggested by the observation that there are very few discs accreting at a level below around $10^{-10}\mathrm{M}_\odot$ yr^{-1}(e.g. Muzerolle et al. 2000), similar to the limit implied by photoevaporation. Including photoevaporation into the viscous evolution described above simply involves including a sink term in Equation 1.2 and the evolution of the discs surface density is described by:

$$\frac{\partial \Sigma}{\partial t} = \frac{3}{R}\frac{\partial}{\partial R}\left[R^{1/2}\frac{\partial}{\partial R}\left(R^{1/2}\nu\Sigma\right)\right] - \dot{\Sigma}_w(R,t) \tag{1.27}$$

where $\dot{\Sigma}_w(R,t)$ describes the mass-loss rate per unit area due to photoevaporation. The implications of this extra term can be seen if we integrate Equation 1.26 over radius to find:

$$\frac{\mathrm{d}M_d}{\mathrm{d}t} = -\dot{M}_* - \dot{M}_w \tag{1.28}$$

Equation 1.28 tells us immediately that there are two phases of disc evolution: when $\dot{M}_* > \dot{M}_w$ the disc evolution is dominated by the viscous transport of angular momentum and hence associated accretion rather than the removal of gas through photoevaporation. During this stage the disc will behave in a similar manner to a standard viscously evolving disc, without photoevaportion especially when $\dot{M}_* \gg \dot{M}_w$. However, when $\dot{M}_* < \dot{M}_w$ it is now photoevaporation that dominates the evolution of the disc, opening a gap in the disc and then finally removing the remaining disc material until the disc is dispersed. As shown earlier the accretion rate of a disc evolves on the disc's global viscous time τ_ν, which is the local viscous time at the outer radius, (which is of order the disc's lifetime; e.g. Lynden-Bell & Pringle, 1974; Pringle, 1981; Ruden, 1993). The transition from a viscously evolving disc to a clearing disc occurs when a gap opens in the inner disc and the material inside the gap drains onto the central star. Since, the time-scale for the inner disc to drain is the viscous time at the point the gap opens (which is typically much less than the global viscous time of the disc), the transition from a viscously accreting disc (i.e. one that would observationally be classified as an optically thick accreting primordial disc) to one that is being dispersed, occurs on a time-scale much shorter than the disc's current lifetime (Clarke et al. 2001; Ruden 2004).

Hence, the evolution of a viscously evolving photoevaporating disc can naturally explain the observations of discs which appear to evolve under the effect of viscous transport alone, but are then rapidly dispersed. The photoevaporation process is shown occurring in the models calculated by Clarke et al. (2001) - shown in Figure 1.12 - where the inner disc rapidly drains onto the central star between the third and fourth snapshot, once the accretion rate through the disc falls below the photoevaporation rate. In the model shown above, the time-scale for the outer disc to be completely cleared is similar to the total disc lifetime. This outer disc clearing behaviour is inconsistent with the outer disc observations that show that most WTTs show no evidence of an outer disc at large radius (e.g. Duvert et al. 2000). This was corrected by Alexander et al. (2006a) who realised that the topology of the photoevapotive flow changes once the inner disc has drained onto the star and there is a large gap between the central star and the inner edge of the outer disc. Alexander et al. (2006a) performed detailed radiation hydrodynamic simulations of photoevaporation from discs with large cleared inner holes, which showed a mass-loss profile peaked at the inner edge of the disc and mass-loss rates that increased with inner hole radii. This was then used by Alexander et al. (2006b) to show that once the gap has opened and the inner disc has drained onto the central star the outer disc can be cleared very rapidly in a time-scale much less than the discs lifetime, and this evolution is shown in Figure 1.13.

Origin of transition discs

Photoevaporation provides two phases in which 'transition' discs will be created. First just after the gap opens, Alexander & Armitage (2007) showed that any dust that was present in the inner disc is rapidly accreted onto the star under the action of dust drag. This occurs on a time-scale several orders of

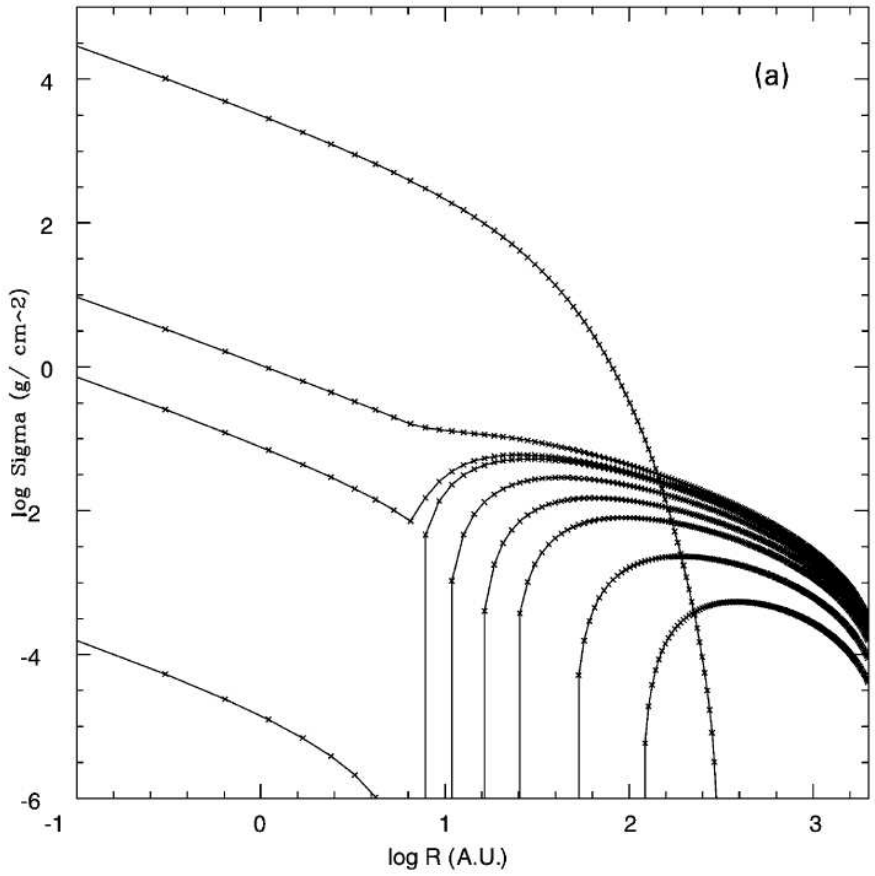

Figure 1.12: Evolution of the disc's surface density of a viscously evolving photoevaporating disc with $\Phi_* = 10^{41}$ s^{-1}. Snapshots are shown at t =0, 13.0, 14.1, 14.3, 16.0, 18.0, 20.0, 24.0 & 28.0 Myr. (Figure from Clarke et al. (2001)

magnitude faster than the time-scale for the gas disc to drain onto the star, leaving an accreting dust free (and therefore optically thin) inner gas disc. While Alexander & Armitage (2007) made some simplifying assumptions in order to perform the calculation, a rapid (almost instantaneous compared to the viscous time) drop in the NIR opacity due to dust drag is highly likely, although detailed calculations of whether this opacity drop is sufficient to explain the observed NIR emission in 'transition' discs are still required. In this work I will assume the limiting case presented by Alexander & Armitage (2007), where when dust-dust interactions are neglected the inner gas disc becomes optically thin immediately after the gap opens (when working on a time-scale comparable with viscous evolution).

The second phase is much more certain. Once the inner disc has fully drained onto the central star and the outer disc is being eroded this will lead to observations of non-accreting transition discs, where the gas and dust hole line up in radius. With the inner cavity being devoid of large amount of gas and dust emission.

Other sources of high energy irradiation

At first thoughts the EUV photoevaporation model seems to explain the observed disc clearing successfully. However, the low mass-loss rates $\sim 10^{-10}$ M$_\odot$ yr^{-1}mean it is unable to explain the majority of

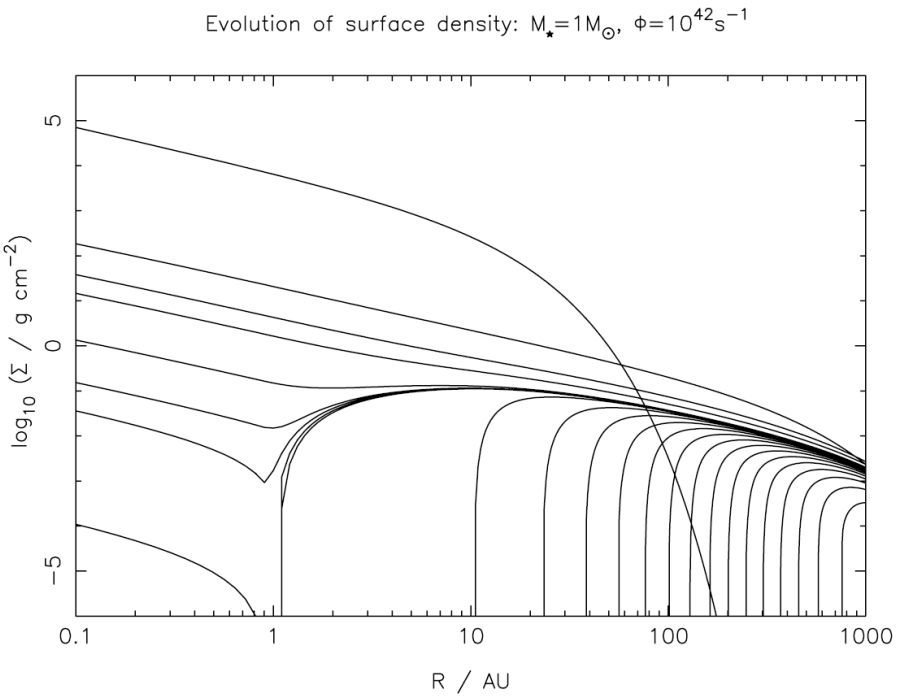

Figure 1.13: Evolution of the disc's surface density including direct EUV photoevaporation described by Alexander et al. (2006a). Snapshots are shown at t =0, 2.0, 4.0,5.9, 6.0, 6.01, 6.02, ..., 6.18Myr. Direct photoevaporation takes over when the inner disc has drained onto the star (Figure from Alexander et al. 2006b).

observed 'transition' discs. Furthermore, it has been pointed out by several authors that due to the low neutral column required to full absorb the EUV radiation $N \sim 10^{18}$ cm^{-2}, it is highly unlikely that EUV photons actually reach the surface of the disc, and therefore are unable to drive a flow (Glassgold et al. 2004, Ercolano et al. 2009b, Güdel et al. 2010).

Therefore, these problems have lead to research into other high energy photons as a possible mechanism to heat the surface layers of the disc. Young stars produce high energy photons at UV to X-ray wavelengths, where the UV is split into two regions: Far UV (FUV) are photons with energy just below 13.6eV, the photons above 13.6eV are the EUV photons we have already discussed. FUV photons are unable fully ionize the gas and heat it up to 10^4K; however, they are able provide significant heating and low levels of ionization. X-ray heating is also able provide significant heating, with gas able to reach $\sim 10^4$K and low levels of ionization. Currently, no hydrodynamic calculations of internal FUV or X-ray photoevaporation have been performed, although significant progress has been made by considering the hydrostatic structure of irradiated discs.

X-ray Heating of Discs

Young stars are extremely luminous in the X-rays with energies in the range $10^{-5} - 10^{-3}\,L_{\rm bol}$ (e.g. Guedel et al. 2007), thus they provide a significant source of energy that impinges on the disc. Alexander et al. (2004) was the first to consider the irradiation of a protoplanetary disc by X-rays. However, it was not until Ercolano et al. (2008b) that the possibility that X-rays could drive vigorous photoevaporative flows was realised, with estimates two orders of magnitude higher than the mass-loss rate from a pure

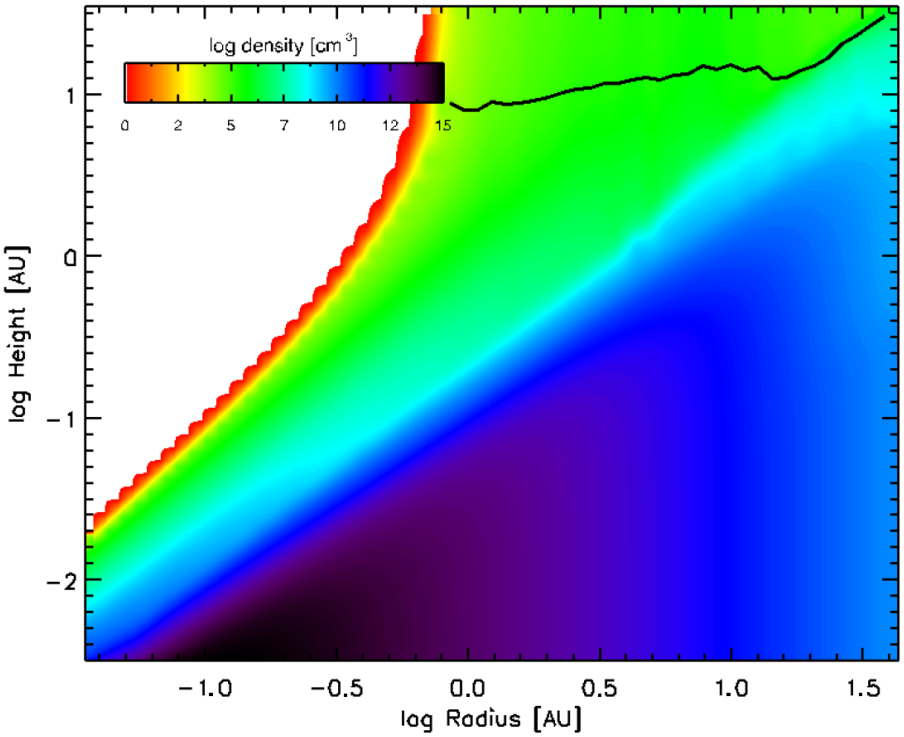

Figure 1.14: Density distribution of a hydrostatic disc heated by X-rays. The black line shows the region where the gas temperature is equal to the escape temperature (Figure from Ercolano et al. 2009b).

EUV flow obtained. In order to obtain improved estimates for the photoevaporation rates due to X-ray heating Ercolano et al. (2009b) calculated hydrostatic models of discs that included separate dust and gas radiative transfer.

In order to estimate the mass-loss rates from hydrostatic discs Ercolano et al., uses the ρc_s method, where the mass-loss rate at a given cylindrical radii is calculated by assuming at that radius the density structure is flowing at the local sound speed when the gas temperature equals the escape temperature (shown in Figure 1.14). At first thought this may seem odd, however in a pure thermally driven radial outflow the point at which the gas reaches the sonic velocity always occur at the point where the gas temperature is approximately the escape temperature (one half to be precise, Parker 1958). In reality the physical equation describing the flow is the momentum equation

$$u\frac{\mathrm{d}u}{\mathrm{d}l}+\frac{1}{\rho}\frac{\mathrm{d}(c_s^2\rho)}{\mathrm{d}l}+\frac{\mathrm{d}\psi}{\mathrm{d}l}=0 \tag{1.29}$$

whereas the equation of hydrostatic equilibrium is:

$$\frac{1}{\rho}\frac{\mathrm{d}(c_s^2\rho)}{\mathrm{d}l}+\frac{\mathrm{d}\psi}{\mathrm{d}l}=0 \tag{1.30}$$

Below the point where the temperature equals the escape temperature the $u\mathrm{d}u/\mathrm{d}l$ term in the momentum equation is smaller than or of similar magnitude to the pressure and body force terms. Therefore, the hydrostatic structure presented by Ercolano et al. (2009b) will provide a reasonable approximation to the true density and temperature structure in the flow, and the ρc_s method of calculating mass-loss rates

is certainly physically motivated, and should give a sensible order of magnitude estimate of the total mass-loss rates. Along with providing estimates of the total mass-loss rates Ercolano et al. (2009b) also investigated the implications of neutral columns close to the central star. No change in the mass-loss rates until the neutral column reached $N \sim 10^{21}\mathrm{cm}^{-2}$, or until photons with energies less than $h\nu \sim 1\mathrm{keV}$ are fully screened out. This means unlike the EUV which can only penetrate very small columns, the X-rays are able penetrate more realistic accretion columns that may form close to the star and it is 'soft' X-ray photons that provide the source of heating in the surface layers of protoplanetary discs.

FUV Heating of Discs

During the accreting phase, the accretion shock on the stellar surface produces large amount of FUV photons, with luminosities reaching as high as 10^{32} erg s^{-1} (e.g Ingleby et al. 2011). Gorti & Hollenbach (2008,2009) and Gorti et al. (2009) have investigated the affects of high energy heating on protoplanetary discs included FUV, EUV and X-ray irradiation. Again in order to simplify their calculations they solve for a hydrostatic disc structure. FUV heating is driven by photoelectric heating from dust grains and cooling from atomic and molecular lines, and in the protoplanetary disc environment the maximum gas temperatures reached by FUV heating is $\sim 1000\mathrm{K}$ an order of magnitude less than the EUV and X-rays. Furthermore, in the atmospheres of realistic discs, the Gorti & Hollenbach calculations showed that the FUV could penetrate to higher columns than the X-rays and produced a disc structure, whose temperature increased with height as near the mid-plane standard dust heating is dominant, then the FUV, then X-rays and finally EUV at the surface of the disc.

Instead of using the ρc_s method to estimate the mass-loss rates from these disc structure, Gorti & Hollenbach use a different method. The method consists of fitting an isothermal and spherical wind solution based on the model described by Adams et al. (2004) for external photoevaporation from the outer edge of discs. Since the temperature of the hydrostatic disc calculations determined by Gorti & Hollenbach vary with height, the mass-flux this solution gives also varies with height. Therefore, in order to estimate the photoevaporative mass-flux at a given cylindrical radius, Gorti & Hollenbach selects the height in the disc which the method gives the largest mass-flux. This height is then defined as the flow 'base' and the photoevaporative wind is assumed to be isothermal from this point onwards, neglecting the thermal structure above. Using this method Gorti & Hollenbach (2009) conclude that the flow begins sub-sonically in the deep within the FUV heated region of the disc, with mass-loss rates $\sim 10^{-9} - 10^{-8}\mathrm{M}_{\odot}\ \mathrm{yr}^{-1}$comparable to those found by Ercolano et al. (2008b,2009b) for X-ray heated discs.

Gorti & Hollenbach (2009) point out the use of an isothermal wind solution will lead to errors and the wind solution has come under some criticism (e.g. Ercolano & Clarke, 2010). However, it is the definition of a flow 'base' and the neglected the hydrostatic structure above this region that may provide the biggest source of error. In the photoevaporation model defining a flow base is fairly meaningless, since streamlines must ultimately originate at the discs mid-plane, where the bound disc structure/flow structure must be in dynamical equilibrium so the flow can be feed at the correct rate. Therefore, many different wind solutions (with vastly different mass-loss rates) will asymptote to this correct hydrostatic structure at low heights, and no physical reason is presented why the method of selecting the height at which this method gives the highest mass-flux, should pick out the correct solution. Furthermore, in

hydrostatic disc calculations the regions of the disc with temperatures below the escape temperature will provide a reasonably accurate (to order unity) representation of the true disc structure. By assuming an isothermal wind solution from deep within the disc the Gorti & Hollenbach method neglects the roughly correct structure of the region above. Since the temperature increases with height the true sonic surface will be lower than estimated, and may lead to errors in both the mass-loss rate and the heating mechanism (if there is one) which sets the mass-loss rate.

'Real' Photoevaporation from Protoplanetary discs

We have seen that while the pure EUV photoevaporation model is well developed and produces the require phenomenology of disc dispersal, it suffers from several issues. The main one being the fact it is unlikely that EUV photons can actually reach a protoplanetary disc's surface. There has been much work on the inclusion of X-ray and FUV heating on disc models that could drive much more vigorous flows. However, the use of simplified radiative transfer and hydrostatic disc structures is limited and has perhaps even lead to some confusion. Therefore, in order to progress a discussion of photoevaporation undergoing heating from all three heating mechanisms within a hydrodynamic framework is the only way forward.

1.4.3 Observations of Photoevaporation at Work

Before, I present the outline for the work in this thesis it is briefly worth discussing the small but growing sample of observations that attempt to probe, directly or indirectly the implications of a vigorous photoevaportive flow emerging from a protoplanetary disc, apart from the standard indicators of disc evolution. The earliest observational evidence of a photoevaporative flow was the low velocity component of the OI 6300Å line observed around many class II sources by Hartigan et al. (1995). An example of the observed line profile is shown for CW Tau, the line profile clearly shows a double peak with a peak at $\sim$ 100km s^{-1} dubbed the high velocity component and a second one at $\sim$ 5km s^{-1} dubbed the low velocity component. Hartigan et al. (1995) identified the high velocity component with a jet. However, they were unable to ascertain the origin of the low velocity component, concluding it was possibly due to a disc wind escaping from a radii of around $\sim$ 10 AU. This feature was identified around almost all class II objects observed, and could possibly be due to a photoevaporative wind, although an EUV photoevaporative wind and magnetic disc wind was ruled out by Font et al. (2004).

Another blue-shifted emission line, this time in the 12.8μm NeII was observed around several objects (Passcucci & Sterzik 2009), with the closest object TW-Hya (with a disc which is almost face on) providing direct evidence for a $5-10$ km s^{-1} disc wind, although this time the emission was consistent with the predictions from a pure EUV model (Alexander et al. 2008).

Less direct, but still interesting observations are the correlations between X-ray luminosity and accretion rate discussed by Drake et al. (2009). The observations of X-ray luminosity and accretion rates in the Orion Nebular Cluster seemed to indicate a negative correlation between these two observables, although with a large scatter. Drake et al. argued that this could arise through a process of 'photoevaporation starved accretion'. Since, photoevaporation starves the inner disc of material that would have otherwise accreted, the observed accretion rate will appear suppressed from a pure viscous model.

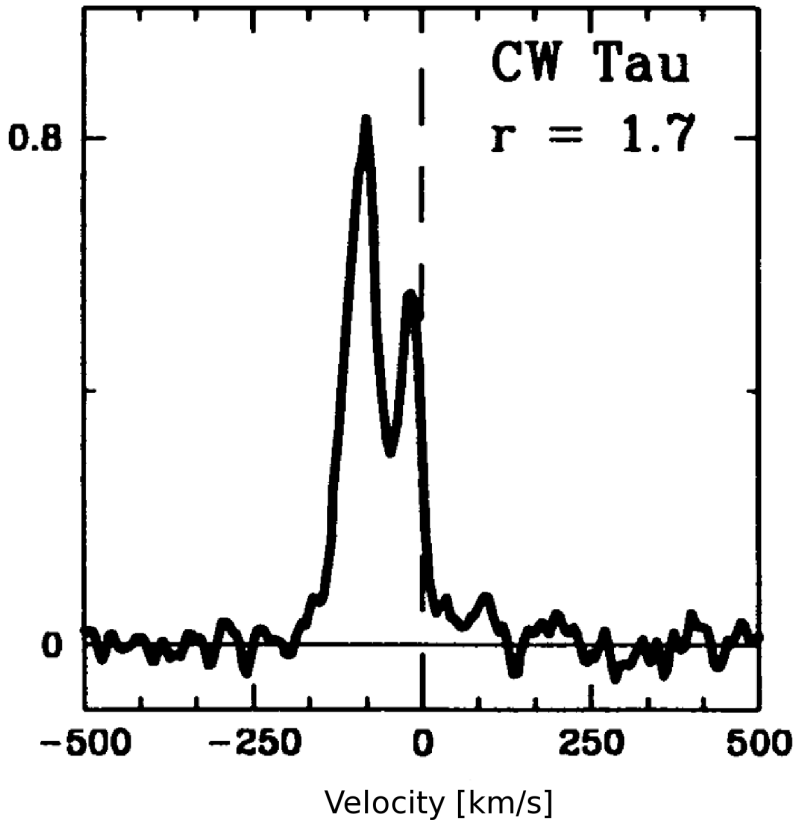

Figure 1.15: Observed OI 6300Å line profile of CW Tau (Figure from Hartigan et al. 1995)

Therefore, higher mass-loss rates driven by higher X-ray luminosities could starve the inner disc to a greater extend and provide the origin for the negative correlation.

Finally, perhaps the most tentative of indicators is the disc lifetime versus metalicity correlation reported by Yasui et al. (2009). Observations of disc populations in low metalicity environments in the extreme outer galaxy, showed lower disc fractions compared with local disc populations. While a model which relied on planet formation to clear the disc would predict a much longer disc lifetime at lower metalicities, X-ray photoevaporation rates are expected to be higher (since the opacity is lower and larger columns can be heated by the X-rays) leading to shorter disc lifetimes in agreement with the observations (Ercolano & Clarke, 2010). However, this is far from conclusive and many more observations of this type are needed before disc lifetime verus metalicity correlations are a useful test of photoevaporation models.

1.5 Thesis Outline

In this thesis I attempt to discuss whether photoevaporation can provide a dominant dispersal mechanism for discs, and what direct and indirect observational signatures can be used to test the scenario. Since, the driving mechanism for photoevaporation is still debated, in Chapter 2 I will present a hydrodynamic solution to the X-ray photoevaporation problem and then discuss hydrodynamic flows that include UV and X-ray heating. In Chapter 3 I obtained accurate mass-loss profiles by performing radiation hydrodynamic simulations of photoevaporating discs, while testing some of the predictions of the model discussed in Chapter 2: The importance of disc structure, the effects of UV luminosity and variations in stellar mass

and X-ray luminosity. In order to test whether photoevaporation can provide a dominant dispersal mechanism I build a population synthesis model of viscously evolving photoevaporating discs, in order to make statistical comparisons with current data along with making predictions for future observations. Chapter 4 describes a synthetic population of evolving discs that include both viscous evolution and photoevaportion, where the results from population is statistically compared to observations. In Chapters 5 & 6 I turn my attention to direct observational tests of photoevaporative winds, discussing gas line emission in Chapter 5 and dust emission in Chapter 6. Finally, I draw my conclusions in Chapter 7 and discuss areas where further research is required.

2

The theory of photoevaporation

PHOTOEVAPORATION is likely to play an important, if not dominant role in the evolution and dispersal of protoplanetary discs. As discussed in Chapter 1, protoplanetary discs are subject to intense irradiation by high energy photons covering a large range of energies; from FUV ($h\nu <$ 13.6eV), to the EUV (13.6 eV $< h\nu <$0.1 keV) and finally to the X-rays ($h\nu >$ 0.1keV). While basic calculations of disc heating from all three radiation fields has been carried out for protoplanetary discs (Gorti & Hollenbach 2008,2009), no one has considered the problem within the framework of radiation-hydrodynamics, which after all is important as photoevaporation is clearly a radiation-hydrodynamic problem.

As discussed previously it is the EUV-only photoevaporation problem that has been solved hydrodynamically. Therefore, if we wish to discuss the photoevaporation of real discs, in which all three high energy radiation fields will be present we must develop a hydrodynamic solution to the problem. I begin in this Chapter by presenting a hydrodynamic description of pure X-ray photoevaporation, then discuss the hydrodynamic problem of an EUV/FUV/X-ray heated protoplanetary disc. Therefore, in this work I discuss the heating of protoplanetary discs, then present the theoretical basis on which we can understand photoevaporation from real discs before we move onto detailed radiation-hydrodynamic calculations in Chapter 3.

2.1 Heating of protoplanetary discs

On time-scales much shorter than the viscous time of the disc, the equations that describe the structure of a protoplanetary disc/wind system are the classic Euler equations:

$$\frac{D\rho}{Dt} + \rho \nabla \cdot \mathbf{u} = 0 \tag{2.1}$$

$$\frac{D\mathbf{u}}{Dt} = -\frac{\nabla P}{\rho} + \nabla\psi_{\rm eff} \tag{2.2}$$

$$\frac{D}{Dt}\left(\frac{e}{\rho}\right) = -\frac{P}{\rho}\nabla\cdot\mathbf{u} + \Lambda \tag{2.3}$$

where this set of equations is closed with an ideal equation of state; D/Dt represents the Lagrangian derivative, $\psi_{\rm eff}$ is the effective potential, e is the gas' internal energy and Λ is the net cooling rate. These equations neatly hide all of the complicated physics inside the net cooling rate function, where gas heating and cooling processes are important if not dominant in setting the gas temperature. Therefore, it is important to separately discuss the main heating mechanisms in a protoplanetary discs and their role in driving photoevaporation.

2.1.1 Optical & IR heating

In terms of the overall energy budget the optical/NIR emission from the star is the dominant contribution (only for the highest accretion rates is the accretion luminosity important, e.g. Calvet & D'alessio 2011). Furthermore, as mentioned in the introduction, the SED observations indicated that the dominant heating mechanism is stellar irradiation and not viscous dissipation (Kenyon & Hartmann 1987); therefore, the dominant heating mechanism must be the optical/NIR emission from the star. At these wavelengths the opacity of the dust is many orders of magnitude larger than that of the gas, and it is the dust that is directly heated by the star. At some height above the mid-plane the dust must be optically thin to its own and the stellar radiation, and we can simply evaluate the dust's temperature by balancing absorption and emission, to find:

$$\kappa_E(T_d)T_d^4 = \kappa_p(T_*)T_*^4\left(\frac{R_*}{2r}\right)^2 \tag{2.4}$$

which for perfect black-body dust ($\kappa_E = \kappa_P$ - note in general $\kappa_p(T_*) > \kappa_E(T_d)$ - so this is a lower bound) yields:

$$T_d = 289\ {\rm K}\left(\frac{T_*}{6000\ {\rm K}}\right)\left(\frac{R_*}{1\ {\rm R}_\odot}\right)^{1/2}\left(\frac{r}{1\ {\rm AU}}\right)^{-1/2} \tag{2.5}$$

The optical depth to the central star decreases with height at a given cylindrical radius, thus the stellar flux decreases with height and the dust temperature must also decrease with height. Therefore, the mid-plane and photospheric temperature at a given R will always be less than the dust temperature in the optically thin regions shown in Equation 2.5.

While the dust absorbs most of the stellar radiation it only represents a small mass fraction of the disc, therefore the gas particles are heated indirectly by the optical/IR radiation through gas-dust collisions, where the time-scale for this process to occur is given by the dust-gas collision time-scale:

$$t_{\rm col} = \frac{1}{n_d\sigma_{dg}\bar{v}_g} \tag{2.6}$$

where $\bar{v}_g$ is the average velocity of the gas particles (since $m_d \gg m_g$) and the collision cross-section is simply given by $\sigma_{dg} = \pi a^2$ as the dust particles are much larger than the gas particles. At the high densities found close to the mid-plane this time-scale is short, thus the dust and gas temperatures are tightly coupled. However, given the approximately Gaussian fall off in density, at several scale heights

this time-scale can becomes longer allowing the dust and gas temperatures to become decoupled, provided sufficiently quick gas heating and cooling mechanisms exist. This decoupling has been studied by many authors, which show that the surface layers of the disc can be heated to temperatures above the local escape temperature. This 'extra' heating arises from FUV, EUV and X-rays, where the inclusion of these heating mechanisms has been studied either separately, or in some combination by Glassgold (1997,2004,2007); Kamp & Dullemond (2004); Gorti & Hollenbach (2004,2008,2009); Ercolano et al. (2008b,2009b); Woitke et al. (2009); Kamp et al. (2010).

2.1.2 EUV heating

EUV heating is perhaps the easiest 'extra' heating mechanism to understand. EUV photons are photons capable of directly ionizing a Hydrogen atom and as such must have an energy $\geq$ 13.6eV. Given that the interaction cross-section falls rapidly with photon energy ($\propto E^{-3}$), ionizing photons are by definition photons with energies at or just above 13.6eV. Therefore, the luminosity is measured in ionizing photons per second, with values in the range $\Phi_* = 10^{41} - 10^{43}$ s^{-1} possible from T Tauri stars (Alexander et al. 2005), in keeping with this I follow the convention of Ercolano et al. (2008b, 2009b) and take EUV photons to be in the energy range $13.6\,\mathrm{eV} < h\nu < 0.1$ keV. Since EUV photons ionize hydrogen, the main coolant for an EUV region is to emit a recombination photon, which by definition will be at 13.6eV and this recombination photon can then ionize another Hydrogen atom and so on. Therefore, an EUV heated region will result in an approximately fully ionized isothermal region with a temperature $\sim 10^4$K, where the extent of the region can be found by considering recombination balance (a Strömgren volume). Hollenbach et al. (1994) discuss two limits for EUV heating of protoplanetary discs: one where the disc's surface is directly illuminated by stellar ionizing photons at radii $R \mathscr{O} R_*$; whereas recombination photons dominate at radii $R \gg R_*$ often called the 'diffuse' limit, since it is the diffuse ionizing field that is heating and ionizing the surface layers of the disc. Due to the ease with which neutral material absorbs EUV photons, (with columns densities of $N = 10^{18}$cm^{-2} sufficient) meaning no direct measurements are yet possible (Alexander et al. 2005), several authors have questioned the ability of EUV photons to reach the outer disc (e.g. Glassgold et al. 2004; Ercolano et al. 2009b).

2.1.3 FUV heating

Young stars also emit radiation in the FUV range, i.e. UV radiation longward of $13.6eV$ and is thus unable to directly ionize hydrogen; however, it is an extremely important when one considers the heating of the upper gas layers of protoplanetary discs. FUV heating is an extremely complicated process, that is particularly sensitive to chemistry in the disc and has spawned an extensive wealth of literature that I cannot do justice here and I point the interested reader to Tielens & Hollenbach (1985a,b) and the review by Hollenbach & Tielens (1997) as an excellent starting point. However, it is important to summarise the basic principles of FUV heating here. Typical FUV luminosities of stars are in the range $10^{29} - 10^{32}$ erg s^{-1} (e.g. Ingleby et al. 2011) and for the type of environment in protoplanetary discs by far the most dominant heating mechanism is the ejection of photo-electrons from dust grains (Gorti & Hollenbach 2004), whereas the dominant cooling mechanism at higher temperatures (when the gas is predominantly atomic) are atomic forbidden line emission from SI, SiII, FeI, FeII & OI in the MIR, and molecular line emission (when the gas is predominately molecular) at cooler temperatures. Many of these cooling

lines are not optically thin and can be optically thick, furthermore when molecular lines become important, then so does the chemistry and the abundance of these molecules is sensitive to the local density, temperature and radiation field. As such very few calculations exist that have aimed to include all of the necessary physics and chemistry with the calculations by Gorti & Hollenbach (2008,2009) currently state of the art. While this complexity will prevent me from improving on these calculations, as we shall see I can use some of the main findings to investigate the photoevaporation of discs. Unsurprisingly FUV heating is unable to reach the temperatures that the EUV can reach, with a typical maximum gas temperature of around $T \lesssim 1000 - 2000$K in the T Tauri environment (e.g. Gorti & Hollenbach 2004; Bruderer et al. 2009). However, unlike the EUV, the FUV is able to penetrate much larger columns densities. Since at these UV wavelengths the opacity is dominated by dust extinction, the gas column the FUV can penetrate depends on the dust properties in the gas. For ISM type dust this penetration depth is around $N \sim 10^{21}$ cm^{-2}, although we expect protoplanetary discs to be significantly evolved away from this dust population. In particular for the dust depleted disc atmospheres argued for by D'alessio et al. (2001) based on SED modelling, the penetration column of FUV photons maybe as large as 10^{23}cm^{-2} (Gorti & Hollenbach 2009).

2.1.4 X-ray heating

Fortunately X-ray heating in protoplanetary discs is a much simpler process when compared to FUV heating. While X-rays span an extremely broad range of photon energies it is only the 'soft' X-ray photons that are important for X-ray heating (Ercolano et al. 2009b), these photons typically have an energy range of ~ 1 keV and are absorbed by large neutral columns of gas $N \sim 10^{22}$ cm^{-2}. The dominant mechanism for X-ray absorption is photoelectron generation by the K-shells of heavy metals (in order of decreasing importance: Oxygen, Carbon and Iron). Unsurprisingly this electron has a very large energy, sufficient to release a large number of 'secondary' electrons from nearby atoms, through collisional ionization of neutral gas. It is these secondary electrons which dominate the heating by thermalising within the surrounding gas. The Auger effect can also occur, however, the emitted auger electrons are significantly outnumbered by the secondary electrons produced through the photoelectric process at the expected temperature and density ranges.

Cooling of the X-ray heated gas can occur through several processes, although at the gas temperatures expected ($T_{\rm gas} \lesssim 2 \times 10^4$ K - e.g. Ercolano et al. 2008a,b) cooling due to X-ray recombination and thermal bremsstrahlung is negligible. Thus the dominant cooling mechanism is line cooling, for the densities and temperatures that will be present in an X-ray heated region of the disc the gas will always be optically thin to its own cooling radiation. Since these photons dominate the cooling and are free to escape to infinity they should provide an observational indication of X-ray heating of discs. This will be discussed further in Chapter 5, particularly in relation to the dominant cooling lines: optical forbidden line emission from OI.

All the heating and cooling mechanisms described above are purely local processes. By this I mean that the secondary electrons are thermalised on a scale considerably smaller than any other scale on which properties of interest vary (e.g. radiation field or flow scales) and the cooling radiation will not interact with the gas on distances of order (or greater than) scales of interest, giving rise to non-local heating. Furthermore, an estimation of the heating and cooling time-scales will determine whether adiabatic

heating/cooling will be an important process. The heating time-scale is simply given by the collisional time-scale of the secondary electrons with gas particles which is:

$$t_{\rm col} = \frac{1}{n_g \sigma_{e^- g} v_{e^-}} \approx 1{\rm s} \left(\frac{n}{10^7 {\rm cm}^{-3}}\right)^{-1} \left(\frac{\sigma_{e^- g}}{1 \mathring{\rm A}^2}\right)^{-1} \left(\frac{T_{e^-}}{10^7 \ {\rm K}}\right)^{-1/2} \tag{2.7}$$

whereas one can calculate the cooling time-scales using the fact these are spontaneous, collisionally excited lines. In the case the Einstein Coefficients (A_{nm}) are large, then the cooling time-scale is just set by the collisional time-scale with either neutral hydrogen or electrons, both of which are fast, as seen above. However, in the case that the Einstien Coefficients are small then the cooling rate per unit volume will be $\propto n^2$ (since the dominant cooling lines are forbidden). A detailed calculation (e.g. Figure 5 Ercolano et al. 2008b) yields cooling rates per unit volume of $10^{-14} - 10^{-12}$ erg cm^{-3} s^{-1}, which gives a cooling time of $\lesssim 1$ yr for X-ray heated gas at ~ 5000K and $n \sim 10^5$ cm^{-3}. Flow time-scales for unbound gas will be $\sim r_g/c_s$, which is ~ 10 yr for similar values, implying that $t_{\rm heat} \ll t_{\rm cool} \ll t_{\rm flow}$.

Therefore, since the heating/cooling is purely local and the thermal time-scale is much shorter than the expected dynamical time-scales (something I will verify in Chapter 3), it is a natural question to ask if the local radiation field is known can the temperature be parametrised in terms of local variables only. Fortunately it has been known for a while that X-ray ionization (and hence heating) is well described in terms of the ionization parameter (ξ) where it takes the form:

$$\xi = \frac{4\pi f_X}{n} \tag{2.8}$$

where f_X is the X-ray flux and n is the number density of the gas. It essentially scales as the available amount of X-ray energy to each atom (e.g. Tarter et al. 1969) and can characterise the ionization structure and therefore the gas temperature. Therefore, in thermal equilibrium the temperature of the X-ray heated gas can be specified in terms of the ionization parameter alone. In Chapter 3 this prescription of the X-ray heated gas is described in more detail, where its exact form is taken from the previous X-ray heating calculation of Ercolano et al. (2009). However, for the following discussion I shall assume its existence and the temperature of the X-ray heated gas is given by $T = f(\xi)$ (where the form of f is shown later), where the temperature ranges between $200 \lesssim T < 2 \times 10^4$K with ξ ranging between 10^{-7} and 10^2 erg s^{-1} cm.

2.1.5 Photoevaporation as a result of disc heating.

The much higher gas temperatures that the UV and X-ray radiation field can reach compared to the disc's mid-plane, implies that at some radii the gas temperature of the disc's atmosphere may attain a temperature that is above the escape temperature. Gas above the escape temperature is free to flow away, initiating a flow from the underlying disc (this is the process of photoevaporation). In fact thermal pressure gradients will drive a wind from sub-sonic regions, through a sonic transition and into a freely expanding supersonic wind (similar to the famous Parker wind model for a solar wind, Parker 1958). However, the process of disc photoevaporation is more complicated as the centrifugal force is non-negligible, along with no requirement that the photoevaporative wind is isothermal (unless it is a pure EUV heated wind).

As mentioned in the introduction, the pure EUV photoevaporation model is effectively a solved hydrodynamic problem (Font et al. 2004; Alexander et al. 2006a). Therefore, in this chapter I will determine the basic physics of pure X-ray photoevaporation, before discussing the photoevaporation of discs exposed to the full range of UV and X-ray radiation within a *hydrodynamic* framework.

2.1.6 Basic results of thermally driven winds

At this point it is useful to summarise some of the basic elements of thermally driven winds before going on to discuss the more detailed aspects of photoevaporation. Therefore, in this section I shall restrict the discussion to an isothermal driven wind, where the fundamental starting point is the steady state momentum equation along a streamline, given by:

$$u\frac{\mathrm{d}u}{\mathrm{d}l} = -\frac{c_s^2}{\rho}\frac{\mathrm{d}\rho}{\mathrm{d}l} - \frac{\mathrm{d}\psi}{\mathrm{d}l} \tag{2.9}$$

where l is the length along a streamline. Using continuity, we can write Equation 2.9 as:

$$\left(u^2 - c_s^2\right)\frac{\mathrm{d}\log u}{\mathrm{d}l} = c_s^2\left(\frac{\mathrm{d}\log A}{\mathrm{d}l} - \frac{1}{c_s^2}\frac{\mathrm{d}\psi}{\mathrm{d}l}\right) \tag{2.10}$$

where A is the stream-bundle area. Thus we see that in order to undergo a sonic transition, the flow requires that:

$$c_s^2 = \frac{\partial\psi}{\partial\log A} \tag{2.11}$$

at the sonic surface. While a sonic transition is not formally required, such 'weak' wind solutions, which require that the flow be in causal contact with a boundary a large radius are known to be extremely unlikely in astrophysical situations (e.g. Parker, 1958). Therefore, this requirement at the sonic surface can provide some information on the topology and structure of the flow. Two well known transonic wind solutions are the de Laval nozzle and the Parker wind.

The de Laval nozzle solution describes the topology of a transonic flow in the absence of body forces, in this case Equation 2.10 becomes:

$$\left(u^2 - c_s^2\right)\frac{\mathrm{d}\log u}{\mathrm{d}l} = c_s^2\frac{\mathrm{d}\log A}{\mathrm{d}l} \tag{2.12}$$

This tells us that when the flow is sub-sonic the flow is convergent, and when the flow is supersonic the flow is divergent, where the sonic transition occurs when the velocity divergence is zero. Therefore, in this problem the conditions at the sonic surface allow us to determine information on the topology of the flow.

Parker (1958) proposed a spherical isothermal wind as a model for the solar wind (the Parker wind). Under the assumption of a spherical outflow, Equation 2.10 becomes:

$$\left(u^2 - c_s^2\right)\frac{\mathrm{d}\log u}{\mathrm{d}l} = c_s^2\left(\frac{2}{r} - \frac{1}{c_s^2}\frac{GM_*}{r^2}\right) \tag{2.13}$$

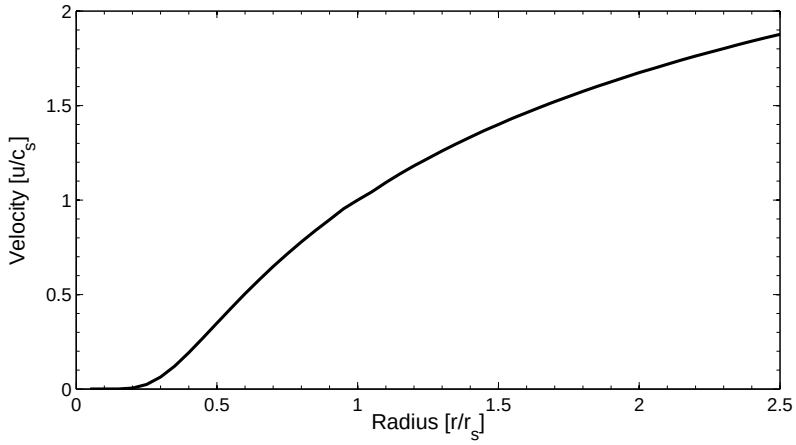

Figure 2.1: Velocity of Parker wind as a function of radius, plotted in dimensionless variables.

where in this case we find that the sonic surface must occur at a radius of:

$$r_s = \frac{GM_*}{2c_s^2} \tag{2.14}$$

thus in this case, fixing the flow topology also fixes the point of the sonic surface, where the physical significance of this radius is clear, r_s is the radius at which an ideal monotonic gas has a *total* energy of zero and has become unbound from the star (and is a factor of two smaller than the r_g defined by Hollenbach et al. 1994). It is also interesting to look at the form of the solution for the Parker wind, shown in Figure 2.1, where the velocity has a transcendental form of:

$$\left(\frac{u}{c_s}\right)^2 - 2\log\left(\frac{u}{c_s}\right) = 4\log\left(\frac{r}{r_s}\right) + 4\left(\frac{r}{r_s}\right)^{-1} - 3 \tag{2.15}$$

This shows us that it is in the sub-sonic regime that the gas gains most of its velocity, which increases rapidly as $u = c_s\sqrt{\exp(-4(r/r_s)^{-1})}$ in this regime, whereas in the supersonic regime the increase in velocity is small increasing as $u = 2c_s\sqrt{\log(r/r_s)}$ and thus the density almost falls off as $\rho \propto r^{-2}$. This form of the velocity is easy to understand, since most of the acceleration must have occurred sub-sonically as the wind is accelerated by the pressure gradient, which is fairly ineffective at accelerating super-sonic gas.

Furthermore, we can now see that in general flow geometries (non-spherical), if your flow becomes super-sonic at radii smaller than r_s, then Equation 2.11 tells us it must do so at a temperature higher than the escape temperature. Therefore, we can use this argument to reverse this principle and use the gas temperatures obtainable by the different high energy heating mechanisms to estimate the approximate *minimum* radius at which the flow may transition from sub-sonic to super-sonic. So for a solar mass star, the EUV has a minimum radius at ~ 10 AU, $\sim 10-100$AU for the X-rays and $\gtrsim 100$AU for the FUV.

2.2 The theory of X-ray Photoevaporation: scaling relations

In this section I develop the theory of X-ray photoevaporation from discs, with a view to understanding how photoevaporation rates vary. I assume that the gas is heated by optically thin X-ray radiation and is in

thermal equilibrium, where the gas temperature can be described in terms of the ionization parameter. In qualitative terms, the flow starts highly sub-sonically at the base of each streamline and is then accelerated by a mixture of pressure gradients and the effective gravity, $\mathbf{g}_{\rm eff}$ (i.e. the combined effects of the gravity of the central star and a centrifugal force). It is assumed that viscous effects are negligible over the flow, thus the specific angular momentum of each fluid element is conserved, being the Keplerian value at launch (cylindrical radius R_b) with value $h = \sqrt{GM_* R_b}$. Now, writing the specific energy of a gas parcel as:

$$\varepsilon = \frac{1}{2}v^2 + \Phi + \frac{e}{\rho} = \frac{1}{2}(u_R^2 + u_z^2) + (\Phi + \frac{1}{2}u_\phi^2) + \frac{e}{\rho} \tag{2.16}$$

where the term in the second brackets on the far right hand side can be identified as the effective potential ($\Psi_{\rm eff}$), now using $u_\phi = h/R$ and $\mathbf{g}_{\rm eff} = -\nabla\Psi_{\rm eff}$ we find:

$$\mathbf{g}_{\rm eff} = -\frac{GM_*}{r^2}\hat{\mathbf{r}} + \frac{GM_* R_b}{R^3}\hat{\mathbf{R}} \tag{2.17}$$

In a steady state ($\partial\rho/\partial t = 0$), the continuity equation (2.1) becomes:

$$\nabla\cdot(\rho\mathbf{u}) = 0 = \frac{\mathrm{d}}{\mathrm{d}l}(\rho u A) \tag{2.18}$$

where the second result can be recast as:

$$\frac{\mathrm{dlog}\rho}{\mathrm{d}l} = -\frac{\mathrm{dlog}u}{\mathrm{d}l} - \frac{\mathrm{dlog}A}{\mathrm{d}l} \tag{2.19}$$

Now starting from the steady state ($\partial u/\partial t = 0$) momentum equation (2.2) we can expand the convective derivative to find:

$$\frac{1}{2}\nabla u^2 - \mathbf{u}\times\nabla\times\mathbf{u} = -\frac{\nabla(\rho c_s^2)}{\rho} + \mathbf{g}_{\rm eff} \tag{2.20}$$

where I have introduced the sound speed through $P = \rho c_s^2$. Now taking the dot product of Equation 2.20 with $\mathbf{u}$ the term including the Lamb vector disappears by orthogonality. Furthermore, using $\mathbf{u}\cdot\nabla = u\frac{\mathrm{d}}{\mathrm{d}l}$ and Equation 2.19 we can re-write Equation 2.20 as:

$$\left[\left(\frac{u}{c_s}\right)^2 - 1\right]\frac{\mathrm{dlog}u}{\mathrm{d}l} = \frac{\mathrm{dlog}A}{\mathrm{d}l} - \frac{\mathrm{dlog}c_s^2}{\mathrm{d}l} + \frac{\mathbf{g}_{\rm eff}\cdot\hat{\mathbf{l}}}{c_s^2} \tag{2.21}$$

Therefore, as described above a flow will undergo a sonic transition at the point where the right hand side of Equation 2.21 is equal to zero. However, the present case is much more complicated, since we do not know the flow geometry *a priori* and because g_{eff} is non-negligible at all radii and, to further compound the problem, c_s is not constant. Although it is possible to solve for $u(l)$ (and hence $\rho(l)$ and $c_s(l)$) for a fixed streamline topology, there is no guarantee that such a solution would satisfy the steady state momentum equation perpendicular to the streamlines. This is the reason that there is presently no analytic solution for the structure of a 2D disc wind, even in the simplest isothermal case. Instead the steady flow structures are computed through time-dependent hydrodynamical simulations (e.g. Proga et al. 2000; Richling & Yorke, 2000; Font et al. 2004; Alexander et al. 2006a).

At first sight these observations appear to preclude further analytic arguments, but in fact we can make useful progress through the use of *scaling relations*. Take the case where we have obtained a

self-consistent steady state flow structure (via a hydrodynamical simulation) for a given set of input parameters, and we then change some parameter of the flow and obtain a new structure. We can then ask whether there are circumstances where one case is simply a scaled version of the original case.

Suppose that every streamline in the first case can be identified with a topologically identical streamline in the second case, which differs only in an over all geometrical scaling. We can also assume that the variation of flow variables along a streamline in the second case can be scaled to the variation along the original streamline, i.e. we write all variables in the form $u = u_0\tilde{u}(\tilde{l})$ where $\tilde{l}$ is the distance along the streamline scaled to the radius at the base of the streamline (R_{b0}) and u_0 allows for a simple re-scaling of the velocity between the two streamlines. In this case we can write Equation 2.21 as:

$$\left[\left(\frac{u_0}{c_{s0}}\right)^2\left(\frac{\tilde{u}}{\tilde{c}_s}\right)^2 - 1\right]\frac{\mathrm{dlog}\tilde{u}}{\mathrm{d}\tilde{l}} = \frac{\mathrm{dlog}\tilde{A}}{\mathrm{d}\tilde{l}} - \frac{\mathrm{dlog}\tilde{c}_s^2}{\mathrm{d}\tilde{l}} + \frac{GM_*}{R_{b0}c_{s0}^2}\frac{\tilde{\mathbf{g}}_{\rm eff}\cdot\hat{\mathbf{l}}}{\tilde{c}_s^2} \tag{2.22}$$

where

$$\tilde{\mathbf{g}}_{\rm eff} = -\frac{1}{\tilde{r}^2}\tilde{\hat{\mathbf{r}}} + \frac{1}{\tilde{R}^3}\tilde{\hat{\mathbf{R}}} \tag{2.23}$$

Now in order to obtain a consistent, self-similar solution we require that the above equation should contain only scaled variables, i.e. should not depend on the parameters R_{b0}, u_0 and c_{s0} which vary from case to case. Examining the left hand side of Equation 2.22 requires that $u_0 = c_{s0}$ (i.e. we require that the Mach number of the flow is the same for the two scaled streamlines at given $\tilde{l}$). Furthermore the individual values of u_0 and c_{s0} are the same for both streamlines: if c_{s0} were different then the temperature at given $\tilde{l}$ would be different between the two streamlines (by a constant factor) and the density would also be different, according to the parametrisation of temperature against ionisation parameter. Since this relation is not a simple power law scaling (there is no reason to expect it to be as the heating and cooling rates depend on specific ionization fractions and temperatures, this is confirmed in Chapter 3) then the density variation along the streamlines would not be self-similar, in contradiction with our assumption. Therefore, for streamlines to map onto one another in a self-similar way, we must have the *same velocity and temperature structure* as a function of $\tilde{l}$.

Turning now to the right hand side of Equation 2.22 we see that in order that this does not contain variables that differ from case to case, we must have $R_{b0} \propto M_*$. Or more physically, the problem is scalable in terms of escape temperature, if there is no scale to the problem, since $T_{\rm esc} \propto M_*/r$. Namely, streamlines can be topologically identified in terms of the escape temperature at some (scaled) point along the streamline.

2.2.1 Primordial discs

I apply the above description to the case of 'primordial' discs; those that, having mid-plane variables which have no intrinsic scale (i.e. discs which are well described by the Lynden-Bell & Pringle similarity solutions - as suggested by observations - e.g. Andrews et al. 2010). Therefore, primordial discs appear to be good candidates for yielding self-similar solutions when the input parameters are varied:

Variation of L_X at constant M_*

We have seen above that strict self-similarity requires that $R_{b0} \propto M_*$. Thus for fixed M_*, R_{b0} is the same and each streamline simply maps onto itself, with the same temperature and velocity variation along the streamline, when L_X varies. Since the temperature is a function of ionisation parameter, it follows that as one varies L_X, the density scaling along each streamline must simply vary uniformly with L_X. The mass flux along each streamline is the product of streambundle area, velocity and density. As the velocity and area are unchanged from case to case and the density scales with L_X, then the mass flux is simply $\propto L_X$. Therefore, I conclude that primordial discs which differ only in their values of incident L_X should be topologically identical, with identical velocity and temperature structure. But with a mass weighting on each streamline that scales with L_X. This agrees with the result of Ercolano et al. (2008b), whose hydrostatic calculations indicated that the mass-loss rate may scale linearly with X-ray luminosity.

Variation of M_* at constant L_X

In this case, $R_{b0} \propto M_*$ implies the streamlines from discs around one mass should map onto those with a different value of M_* by a simple geometrical scaling in proportion to M_* (i.e. a streamline rooted at 10 AU with $M = 1M_\odot$ should simply map on to a streamline rooted at 1 AU when $M = 0.1M_\odot$). As before, we require that the two scaled streamlines should have the same variation in velocity and temperature as a function of distance along the streamline normalised to the radius of the streamline base, i.e. the same variation of ionisation parameter. Since $\xi = L_X/nr^2$, it follows that a radial scaling $\propto M_*$ results in a scaling with density of $\propto M_*^{-2}$. The mass-loss from the streamline is proportional to the product of the density ($\propto M_*^{-2}$), the local velocity (constant) and the area of the streambundle ($\propto M_*^2$): i.e. the mass loss rate along each streamline is the same as the mass loss rate over its scaled equivalent. Therefore (provided the disc is sufficiently radially extended that it encompasses the whole region from which significant mass loss occurs in all cases), I conclude that, at constant L_X, the mass flux in the wind is *independent of* M_*.

It is of course important to note, that even though there is no explicit mass dependence on photoevaporation rates from discs, there will of course be a strong implicit variation with mass through the variation of X-ray luminosity and mass. Observations suggest this approximately $M_* \propto L_X^{3/2-5/3}$ (e.g. Preibisch et al. 2005, Guedel 2007).

2.2.2 Discs with inner holes

Here the truncated density profile of the disc introduces a particular radial scale ($R_{\rm hole}$) into each underlying disc . However, if one fixes $R_{\rm hole}$, then the above arguments for L_X and M_* are still applicable. For fixed M_* and $R_{\rm hole}$ then as one varies L_X the density must also vary as $n \propto L_X$, resulting in a total mass-loss rate that varies linearly with X-ray luminosity. Furthermore, if one varies M_*, then one can simply map one solution with an inner hole radius to the equivalent inner hole around another mass using $R_{\rm hole} \propto M_*$. This means that the mass-loss profile should be scalable in mass in terms of R_g. However, as described above the temperature-ionization parameter relation doesn't permit scalable solutions in temperature. The only choice to obtain an exact similarity solution - $c_{s0} \propto M_*/R_{\rm hole}$ - is not commensurable with this requirement. Therefore, while photoevaporation from discs with inner holes provides scalable

solutions in mass and X-ray luminosity a complete similarity solution that encompasses mass, X-ray luminosity and inner hole radius does not exist. Therefore, in Chapter 3 I will use the numerical methods to perform a full parameter study in mass, X-ray luminosity and inner hole radius, in order to describe the variation of mass-loss rate with inner hole size.

Summary

I have argued that the flow from primordial discs is expected to be self-similar (when L_X and M_* are varied) and predict that the mass loss rate should scale linearly with L_X and be independent of M_*, and the mass-loss profile should be scale-free when considered in terms of R/R_g. Furthermore, I have demonstrated that the photoevaporation rate from discs with inner holes should scale linearly with L_X, and the profiles can be scaled in terms of stellar mass. However, no general similarity solution exists for discs with inner holes and will require simulations to describe the mass-loss rate as a function of inner hole radius and stellar mass.

2.3 The theory of X-ray photoevaporation: absolute flow rates

In order to make further progress in predicting the mass-loss from X-ray photoevaporation, I consider the case of a primordial disc and obtain an estimate of the total mass loss rate by integrating over the sonic surface:

$$\dot{M}_w = 2\int_0^\infty 2\pi R n_s(R) c_s(R) \mathrm{d}R \tag{2.24}$$

where n_s and c_s are the values of the number density and sound speed at the sonic surface. Note that the true mass loss flux will differ from this by a factor of order unity due to the fact that the flow is not purely vertical at the sonic surface.

We can use Equation 2.21 to write the condition for the sonic surface as:

$$c_s^2 = \frac{GM}{2R} \times \frac{R}{r} \times \frac{f_g}{f_A} \tag{2.25}$$

where

$$f_g = \frac{-\mathbf{g_{eff}} \cdot \hat{\mathbf{l}}}{GM/r^2} \tag{2.26}$$

and

$$f_A = \frac{\frac{\mathrm{dlog}A}{\mathrm{d}l} - \frac{\mathrm{dlog}c_s^2}{\mathrm{d}l}}{2/r} \tag{2.27}$$

The first two terms equate the temperature at the sonic surface to the usual expression for a spherical Parker wind; f_g takes into account the different component of the effective force along the streamline compared with the Parker case (both due to the centrifugal term and the non-spherical geometry), while f_A takes into account the different divergence of non-spherical flows and also the fact the flow is not isothermal. If f_A and f_g are both of order unity and if r is $\not\gg R$ (i.e. if the height of the sonic surface at radius R is $\not\gg R$) then we would expect that the sound speed at the sonic surface is given approximately by the Parker wind expression, i.e. $c_s \approx (GM/2R)^{1/2}$. Certainly, the numerical calculations in the next Chapter will verify if this condition holds in the case of primordial disc photoevaporation. However,

there are several factors that indicate that this may be a reasonable assumption, the non-spherical nature of a photoevaporative wind primary arises from the centrifugal force. Given the centrifugal force falls away quickly ($\propto R^{-3}$), if the sonic surface occurs at a cylindrical radius significantly larger than R_{b0} then the flow is likely to be approximately spherical. Furthermore, to attain the high gas temperatures required at the sonic surface, it must occur in a region that is optically thin to X-ray radiation. Thus there is likely to be a sufficient height of X-ray heated gas below the sonic surface, meaning gas parcels experience a region that is hot enough to thermally drive it to larger radii, while not hot enough to undergo a sonic transition, and the inclusion of extra heating mechanisms below the X-ray heated region (e.g. FUV heating - Gorti & Hollenbach 2009) mean the size of the transonic region will be larger, making the likelihood of a spherical flow at the sonic surface even more likely.

All these factors create the expectation that the wind temperature at the sonic surface should be within a factor of order unity of the corresponding Parker value at each cylindrical radius, i.e. we may write:

$$c_s^2 = \beta \frac{GM}{2R} \tag{2.28}$$

where β is a factor of order unity. Given that we can estimate the sound speed as a function of R at the sonic surface via Equation 2.28 and that the temperature-ionisation parameter relationship fixes the density at given r and T we can then write the mass loss integral in the form:

$$\dot{M}_w = \int_0^\infty 4\pi R n\{\xi_s(R)\}\sqrt{\frac{GM_*}{2R}}\mathrm{d}R \tag{2.29}$$

Now taking the temperature ionization relation to be given by $T = f(\xi)$, and using the definition of $\xi = L_X/nr^2$, at the sonic surface we may approximately write[1] $n_s(T_s) = L_X/R^2 f^{-1}(T_{\rm esc}/2)$. Therefore, if we change the variable of integration in Equation 2.29 from cylindrical radius R to escape temperature we find:

$$\dot{M}_w = L_X\sqrt{\frac{8k_b\pi^2}{3\mu m_h}}\int_0^\infty \frac{T_{\rm esc}^{-1/2}}{f^{-1}(T_{\rm esc}/2)}\mathrm{d}T_{\rm esc} \tag{2.30}$$

$$\approx 8\times10^{-9}\left(\frac{L_X}{1\times10^{30}\,\mathrm{erg\ s^{-1}}}\right)\mathrm{M_\odot\,yr^{-1}} \tag{2.31}$$

where k_b is Boltzman's constant, μ is the mean molecular weight, m_h is the mass of a hydrogen atom and L_X is the X-ray luminosity of the central star. The second result comes from evaluating the integral out to an escape temperature of 1000K, or a radius of $\mathcal{O}$100AU for a solar mass star (indicative of the outer radius of the disc). As I will discuss in Section 2.4 this is also the region out to which we expect the photoevaporation to be important for disc evolution. This again demonstrates the mass and X-ray luminosity scaling determined above, along with obtaining reasonable estimates of the mass-loss rate which we can compare to numerical models. Furthermore, Figure 2.2 shows the surface-mass loss rate predicted by the analytic calculation at the sonic surface for a $0.7\mathrm{M_\odot}$star and X-ray luminosity of $L_X = 1\times10^{30}\mathrm{erg\ s^{-1}}$. This shows that the mass-loss profile of X-ray photoevaporation is likely to be broad, with the total mass-loss dominated at large radius, rather than small radius as a pure EUV model yields. These values are in agreement with the surface mass-loss rates obtained from the previous static

[1] where $f^{-1}\circ f = 1$

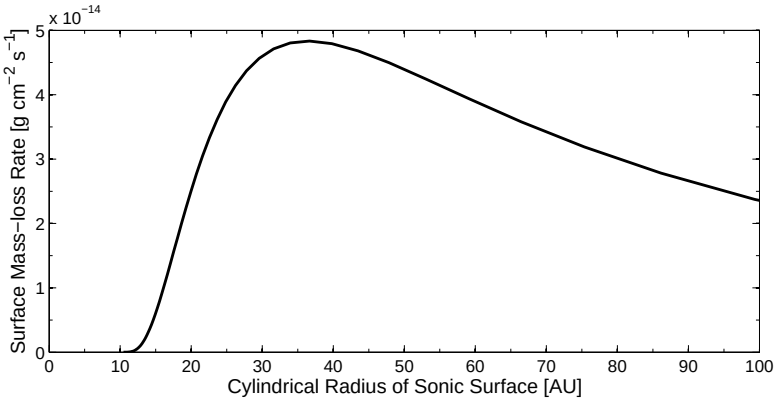

Figure 2.2: Analytic predictions of the mass-flux through the sonic surface plotted against cylindrical radius, for a $0.7M_{\odot}$ star with an X-ray luminosity of $L_X = 1 \times 10^{30}$erg s^{-1}.

calculations of Alexander et al. (2004) and Ercolano et al. (2008b,2009b) indicating that the model described above provides a good physical basis of the X-ray photoevaporation model.

2.3.1 Role of the sonic surface

It is important not to underestimate the implications of Equation 2.28, where in the case of X-ray photoevaporation we are free to write down the temperature at the sonic surface *a priori* as a pure function of mass and cylindrical radius. As shown, this means that the mass-flux at the sonic surface is fixed by the shape of the temperature-ionization parameter relation and X-ray luminosity alone. Equation 2.21 tell us that the conditions at the sonic surface must be satisfied in order to attain a steady state, thermally driven wind. Therefore, since mass flux is conserved, the mass flux in the wind must be identical to that at the sonic surface. This means that whatever the underlying disc structure/temperature it *must* feed the sonic surface at the desired rate.

This is far more restrictive than the similarity solution described in Section 2.2, as we don't need to make any assumptions about the properties of the underlying disc structure. Therefore, provided the flow satisfies: (i) the sonic surface occurs at $z \not\gg R$; (ii) the sonic surface occurs in a region where the centrifugal force is small, or $R_s \gg R_{b0}$, the photoevaporation rate is exclusively set by the X-ray physics alone. Therefore, we can be confident that the mass-loss rates are independent of our original choice of underlying disc structure and any heating mechanism that may or may not operate below the X-ray heated region, since the disc must adjust itself to feed the flow with the required mass-flux rather than the mass-flux adjusting itself to changes in disc structure. Obviously, such a physical description of X-ray photoevaporation, along with the degree to which these conditions are satisfied is something the numerical models presented in Chapter 3 will test.

2.3.2 Importance of Numerical Results

Given we can obtain the mass-loss rates without reference to running hydrodynamic simulations, it is worth briefly addressing their crucial importance to disc evolution models. The above result ultimately only tells us about the total mass-loss rates, not the mass loss rates from the surface of the disc ($\dot{\Sigma}_w(R)$). Of course we could extract an estimate of the surface mass-loss rates by differentiating Equation 2.30

with respect to $T_{\rm esc}$. However, this will only give an estimate of $\dot{\Sigma}_w$ at the sonic surface (which is shown in Figure 2.2), as described above, we expect the sonic surface to be at a distance far from the bound disc. Therefore, without running hydrodynamical models it is impossible to quantitatively predict how this sonic surface links with the bound disc and obtain an accurate $\dot{\Sigma}_w(R)$, which is crucial to the behaviour of the disc during the final clearing stages, i.e. the point at which a gap may open in the disc, and the speed at which the clearing may proceed through a depleted outer disc.

2.4 Theory of UV & X-ray Photoevaporation

Now I have developed the physics behind X-ray heated flows from protoplanetary discs we may turn our attention to photoevaporation from discs around stars emitting the entire spectrum of high energy radiation from the FUV, through the EUV to the X-rays.

2.4.1 EUV and X-ray heated flows

The calculations of Ercolano et al. (2009b) also included an EUV component, of equal luminosity to the X-rays in their input spectrum. Based on their hydrostatic disc calculations they argued that the EUV had negligible impact on photoevaporation, since it was the X-rays that were dominating the heating in the region where the gas was likely to undergo a sonic transition. The order of magnitude estimate in the chapter can be used to estimate the radius the EUV may penetrate to using the fact $\dot{M}_w \propto n \times R^2 \times c_s$. Therefore an X-ray driven wind with a mass-loss rate of $\sim 10^{-8}$M$_\odot$ yr^{-1} out to $R \sim 100$ AU at a sound speed of $\sim$ 5km s^{-1} for a solar mass star, yields a penetration depth of approximately 1AU for the EUV based on absorbing column of 10^{18}cm $^{-2}$ (Ercolano et al. 2009b). This penetration radius is approximately the radius at which the heated disc's surface transitions from a bound atmosphere to a flow (Font et al. 2004; Alexander, 2008). Thus it is likely that an X-ray driven photoevaporation flow is too optically thick to allow EUV photons to reach the disc's surface, where it could drive a photoevaporative flow. Certainly such a hypothesis is easy to test using numerical methods, once the X-ray flow solution is obtained and I perform this analysis in Chapter 3.

2.4.2 FUV and X-ray heated flows

Gorti & Hollenbach (2008,2009) considered the combined effect of UV and X-ray heating in setting the hydrostatic disc structure and then used their static structures to predict resulting flow rates. However, it is a most precarious step to predict flow solutions from a hydrostatic density structure since a variety of solutions (whether static or flowing) asymptote to the same (nearly hydrostatic) structure at small z. Although the results of Gorti & Hollenbach still represent the state of the art in terms of the thermal and chemical structure of X-ray and FUV irradiated discs, the implications of these studies for the resulting mass loss rate are currently unclear. In Chapter 3 I explore this further by using a simple parametrisation of FUV heating in radiation hydrodynamic simulations. Firstly, however I discuss the general theoretical framework for combined FUV and X-ray heated flows. As noted above, X-ray heating is effective up to a total hydrogen column of around 10^{22} cm^{-2} (independent of the dust properties of the gas). For models using depleted dust in the disc atmosphere (e.g. Gorti & Hollenbach 2004,2008,2009), FUV heating extends to significantly higher columns. This means that travelling along a line from the star to a point

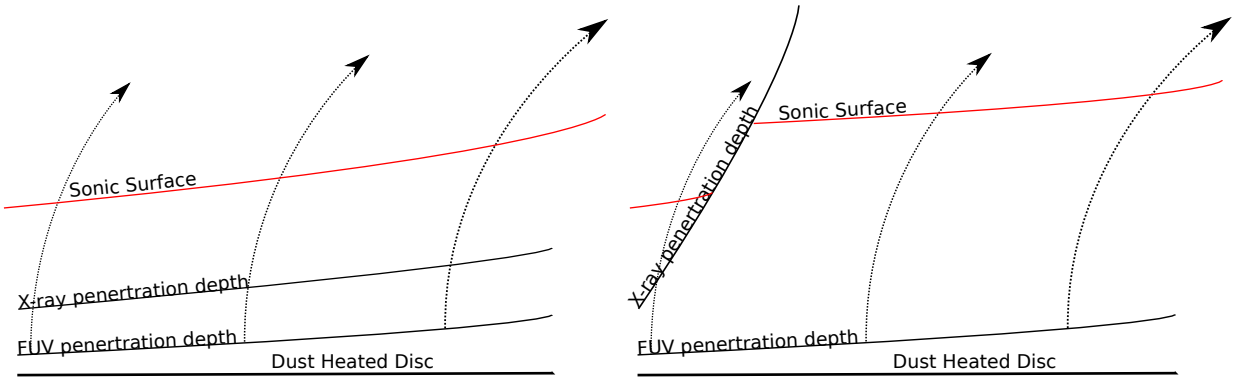

Figure 2.3: Figure showing a cartoon sketch of photoevaporation from a disc exposed to UV and X-ray irradiation. The flow begins in the FUV heated region, but at some height the flow transitions to the X-ray heated region and then passes through the sonic surface in the X-ray heated region. Left shows X-ray dominated, and right shows FUV dominated.

in the disc, one first traverses gas that is exposed to both X-rays[2] and FUV, then to FUV only and then to neither. Within $\sim$ 100 AU (for a solar mass star) the X-rays dominate the heating in the regions that are exposed to both X-rays and FUV. Therefore, in this region, the sequence (as one proceeds away from the star) is X-ray heated, FUV heated and then heated by neither - in reality heated by coupling to the dust - as mentioned earlier.

Though we expect this sequence of X-ray heating followed by FUV heating as one proceeds away from the star, there are still two topologically distinct possibilities which are illustrated in Figure 2.3. The left hand figure is a schematic illustration of the case where the flow in the FUV heated region never exceeds its local sound speed for any of the streamlines shown and the sonic transition occurs in the X-ray heated region. In this case we can use the arguments contained in Section 2.3.1 to argue that the sound speed at the X-ray heated sonic surface is simply given by Equation 2.28 with β of order unity as before: in other words the temperature at the sonic surface is simply a function of cylindrical radius. Since this also fixes the density at the sonic surface (via the ionisation parameter) this implies that the mass flux is just a function of R and X-ray luminosity. In other words, whatever the detailed physics of the heating and cooling processes in the X-ray dark region, they must combine to drive a flow that is able to deliver the required mass flux to the X-ray sonic surface. Therefore, one would expect that if the geometry is as shown in the left hand panel, the photoevaporation rate is entirely controlled by X-ray heating.

On the other hand, the right hand panel shows three streamlines where the two at larger radius undergo a sonic transition within the FUV heated region. Where the FUV is driving a flow that is optically thick to X-rays photons (c.f. the EUV and X-ray case described above). In this case the flow has to self-adjust to deliver the required conditions at the FUV sonic surface; in other words it is the structure of the FUV heated region that controls the mass flow rate. Although in principle gas flowing out in this FUV heated wind could become X-ray heated at some point, this region would not be causally connected to the flow base, the two regions being separated by a shock. As is the case in the offset ionisation fronts created when EUV radiation interacts with an FUV wind in the case of externally illuminated proplyds

[2]In this case the X-rays I am explicitly referring to the X-ray photons that provide significant thermal heating, with a maximum energy of 1-2KeV and not those at higher energies that can penetrate larger columns but provide insignificant heating (see Ercolano et al. 2009b).

(see Johnstone et al 1998). However, it is unlikely that an FUV driven wind would ever be significantly heated by X-rays from the central star. This is because we require the condition at the sonic surface in the FUV heated region to satisfy Equation 2.28. Given that FUV heating does not generally attain temperatures in excess of $\sim 1000 - 2000$K, this implies that the schematic FUV sonic surface shown in the right hand panel of Figure 2.3 must lie at radii of $\gtrsim 100$ AU where X-rays are incapable of heating the gas to greater temperatures than the FUV.

I therefore conclude, although FUV driven winds may be significant at radii > 100 AU, if the flow topology at smaller radii is as shown in left hand panel of Figure 2.3 then the photoevaporation rate is set entirely by the X-rays. The only situation in which FUV heating could control mass loss from much smaller radii is if the streamlines crossing the FUV sonic surface at > 100 AU actually originated at small radii Naturally, I need to perform a radiation hydrodynamical simulation with FUV heating to assess this possibility (Chapter 3) though I note in advance that it would require the gas to move sub-sonically in the FUV heated region over a much larger radial range than seen in our previous calculations, with exceedingly large mass fluxes.

2.5 Discussion

The hydrodynamic framework of photoevaporation discussed in this Chapter starkly disagrees with the arguments Gorti & Hollenbach (2009) present for UV and X-ray heated discs. While the suggested thermal structure of the disc does not differ from their state of the art calculations, it is how this disc structure drives a photoevaporative flow that is in disagreement with the model presented in this Chapter. Here I suggest that the density-temperature coupling at a fixed radius (arising from the temperature-ionization parameter coupling for X-ray heated gas) fixes the photoevaporation rate at the sonic surface in the X-ray heated region. Whereas Gorti & Hollenbach assume that the mass-flux is fixed by the density structure deep within the sub-sonic FUV heated region and ignore the thermal structure above in estimating the mass-loss rates. Although both models suggest that the EUV radiation field will have negligible impact on photoevaporation arising from its lack of penetration.

Therefore, the question that needs to be discussed to understand this discrepancy is: Does the sonic surface adjust to the structure below, or does the structure below adjust to the sonic surface? In the case where X-ray heating is dominant at the sonic surface, I have shown the answer is quite clear: the disc structure below must adjust itself to feed the sonic surface at the required rate. This is because, to first order one can write down the temperature at the sonic surface as approximately the Parker value. Since to attain the required temperatures it must occur in a region optically thin to the stellar X-rays, and thus is likely to be a significant distance from the regions of the disc where the gas parcels originate, meaning the centrifugal force is small and the flow is likely to be approximately spherical. If at a given cylindrical radius we know the temperature, then we know the density through the temperature - ionization parameter coupling and thus we know the mass-flux at the sonic surface. Thus everything is determined at the sonic surface and the sub-sonic FUV heated region below must adjust itself in order to maintain this mass-flux.

However, this does not preclude a flow where the gas reaches the FUV sonic surface before it becomes heated by the X-rays, I argue that such a scenario is unlikely to be important for disc evolution since this sonic surface must occur at a radius $\gtrsim 100$AU. As the FUV is only capable of heating the gas to temperatures much lower than those possible by the X-rays, at these large radii the available mass

reservoir in the disc means it is unlikely to be important for the evolution of the inner disc, where the observational indicators of disc evolution come from. Obviously, this does not preclude a situation where the FUV drives an extremely powerful photoevaporation at small radii up to a sonic surface at a height of $\sim$ 100AU (for a solar mass star) meaning the X-rays are unable to reach the discs surface. However, this seems unlikely given the only order of magnitude difference in the penetration depths of the FUV and X-rays and their similar luminosities.

Therefore, the hydrodynamic model of disc photoevaporation presented in this Chapter indicates that it is the X-ray physics that is likely to be controlling the photoevaporation from the majority of the disc, and that the disc structure adjusts itself to feed the flow at the rate required by the X-ray sonic surface. In this case I have shown that the mass-loss rates are explicitly independent of stellar mass (although not implicitly since the X-ray luminosity is a strong function of stellar mass), the mass-loss rates for all discs scale linearly with X-ray luminosity and that the mass-loss profiles should scale linearly with escape temperature (or stellar mass). Obviously, while this discussion provides a firm physical basis for understanding photoevaporation, this will be useless unless it is backed up with detailed numerical calculations both to thoroughly test the basic principles, underlying scalings and simplifying assumptions made, as well as determining the correct mass-loss profiles. Where the following assumptions have been used in this discussion and need to be verified explicitly by the numerical models:

- The sonic surface occurs predominately in the X-ray heated region.
- The sonic surface occurs in a region where the centrifugal force is small compared to gravity.
- The sonic surface occurs at a height $z \not\gg R$.

At this stage, the simple analytic calculations do not provide knowledge of the mass-loss profile from the surface of the disc which I will need to follow the evolution of a disc's surface density. Furthermore, the mass-loss scaling from discs with larger inner holes is yet to be characterised. To this end, the next chapter is dedicated to performing detailed numerical simulations that aim to capture X-ray heating accurately of physical disc structures, along with physically motivated tests of the impact of EUV and FUV irradiation.

2.6 Conclusions

In this Chapter I have described photoevaporation from protoplanetary discs, that are irradiated by the full spectrum of high energy radiation present in isolated young star/disc systems. In particular I have presented a simple model for X-ray driven photoevaporation, and discuss the implications of FUV and EUV irradiation. The main findings are summarised below:

1. X-ray photoevaporation from primordial discs can be characterised by an as yet undetermined similarity solution that is a function of the X-ray luminosity and $\mathbf{r}/R_g$ only, provided suitable scale free boundary conditions are present (namely a scale free structure to the underlying bound disc).
2. X-ray photoevaporation rates scale linearly with X-ray luminosity and are explicitly independent of stellar mass.

3. X-ray photoevaporation is extremely vigorous, with possible total mass-loss rates in the range $10^{-11} - 10^{-8} M_{\odot}$ yr^{-1} for the observed X-ray luminosities of young stars.

4. A similarity solution does not exists for discs with large inner holes, and simulations will be needed to describe the variation of mass-loss rate with inner hole radii.

5. In the case that the X-rays dominate the heating at the sonic surface, then the mass-loss rate is determined by the X-ray physics while the FUV heated region must adjust itself to the required rate.

6. The EUV may be unable to provide heating at the radii important for photoevaporation as it is unable reach the disc's surface at these radii.

7. The FUV maybe responsible for photoevaporation at large radii from the disc $R \gtrsim 100$ AU, but this cannot be important for the disc clearing indicated by the observations.

3

Numerical Radiation-Hydrodynamic Models of Photoevaporating Protoplanetary Discs

THE simple theoretical arguments presented in the previous Chapter have given us estimates of the total mass-loss rates, along with demonstrating that these mass-loss rates should be independent of all parameters except the X-ray luminosity (e.g. disc structure, stellar mass, incident UV flux). However, these simple calculations can only get us so far, they do not provide an accurate representation of the mass-loss profile, or demonstrate the physically motivated assumptions hold true for the full range of observed parameter space. Therefore, in this section I will use a numerical radiation-hydrodynamic approach, to accurately solve the problem, which will also allow testing of the predictions made in the previous chapter, indicating whether the approach described encompasses the correct physics.

3.1 Methods

I undertake 2D hydrodynamic calculations, in which - under the assumption that the gas is in radiative equilibrium - I parametrize the gas temperature as a function of local variables. This parametrization is based on the results of 3D Monte Carlo radiative transfer calculations using MOCASSIN (Ercolano et al. 2003,2005,2008a). In Chapter 2 I argued that the gas will be in radiative equilibrium, based on an estimation of the heating and cooling time-scales compared to estimates of the dynamical time-scale. However, these calculations will allow us to verify *a posteriori* that the thermal time-scale is less than the flow time-scale, justifying our assumption of radiative equilibrium.

3.1.1 Radiative Transfer

Ercolano et al. (2008b,2009b) employed the 3D Monte Carlo photoionization and dust radiative transfer code MOCASSIN, to calculate the temperature and ionization structure of a typical T Tauri disc, which was irradiated by chromospheric X-ray and EUV flux. MOCASSIN uses a stochastic approach to the transfer of radiation and allows for arbitrary geometries and density distributions. The version of the code used to calculate the Ercolano et al. (2009b) models was modified by Ercolano et al. (2008a), and I refer to this article for a detailed description of the code and model setup. For clarity I summarise some of the basic elements of MOCASSIN next.

The MOCASSIN *code*

The MOCASSIN code is a publicly available radiative transfer code, originally created by Barbara Ercolano to study the photoionization of planetary nebulae as part of her PhD thesis (Ercolano et al. 2003). Since then it has gone through two major modifications: MOCASSIN V2 included dust radiative transfer along side the gas radiative transfer, allowing for the coupled solution of both the gas and dust temperature (Ercolano et al. 2005); MOCASSIN V3 was updated to include the radiative affects arising from a high energy spectrum, which stretches all the way from the optical to the gamma rays (Ercolano et al. 2008a). Although it was primarily designed for calculations with an X-ray radiation field. It is a fully 3D dimensional radiative transfer code and can use an arbitrary spaced Cartesian grid with multiple radiation sources, which are free to be placed at any point in the domain.

The fundamentals of the Monte-Carlo radiative transfer code is based on the algorithm described by Lucy (1999). The code stochastically follows the evolution of 'energy-packets' through multiple processes of absorption and re-emission (assumed to be instantaneous processes) until they leave the grid. Furthermore, whenever an energy packet traverses a grid cell (whether it is absorbed/scattered or not) its contribution to the local energy density is calculated and stored. This then enables the calculation of the gas and dust temperature without requiring a large number of energy packets, particularly in optically thin regions. Since the (gas) opacities are dependant on temperature then an iterative procedure is employed: at each iteration, a large number of energy packets ($\gtrsim 10^7$) are allowed traverse the region of interest. Then the gas and dust temperatures as well as ionization structure (under the assumption of local ionizational balance) are calculated. The opacities are then updated to account for the current thermal structure and the iteration procedure is repeated again and again until convergence. Furthermore, MOCASSIN V3 included an extra step that allows the current structure to be iterated into hydrostatic equilibrium, using the procedure set out in Alexander et al. (2004). Typically the Ercolano et al. (2008b,2009a) calculations took 10-30 iteration steps to reach an equilibrium state, and approximately 1000-10000 CPU core hours. Under the assumption that the thermal and hydrodynamical time-scales are decoupled, a coupling of the MOCASSIN code with a hydrodynamical code is trivial in principle. It simply consists of feeding the density fields produced by the hydrodynamical code into MOCASSIN to calculate gas temperatures that are then in turn fed back to the hydrodynamical code. While conceptually easy, this type of coupling is obviously computationally prohibitive (one would require a radiative transfer step time-scale of $\ll 1$ CPU core hour) and we must construct a different method for including radiative transfer within a hydrodynamic calculation.

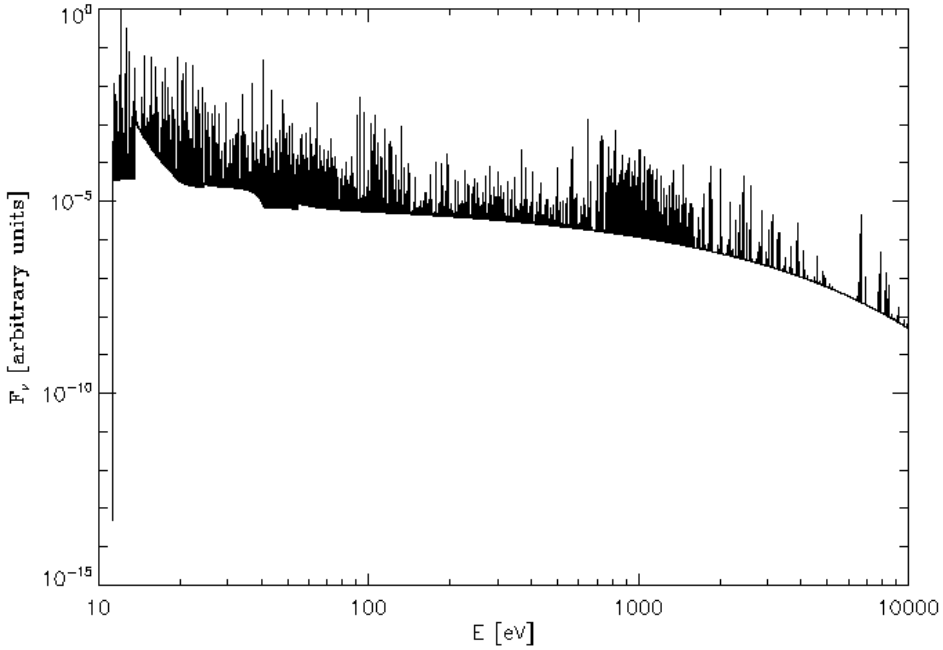

Figure 3.1: Input spectrum used in MOCASSIN calculation, for the hydrostatic calculations by Ercolano et al. (2009b) (Figure adapted from Ercolano et al. 2009b).

The ionization parameter - temperature relation

As described previously, the temperature of X-ray heated gas in radiative equilibrium can be parametrised in terms of the ionization parameter. Therefore, in order to determine this relation I make use of the previous calculations of X-ray irradiation of hydrostatic discs preformed in Ercolano et al. (2009b). The model used is the FS0H2Lx1 calculation of Ercolano et al. (2009b) and I summarise here the input parameters here. The initial density structure is of a protoplanetary disc surrounding a 0.7 $M_\odot$ star (T_{eff} = 4000 K, R_* = 2.5 $R_\odot$) taken from the D'alessio et al. (2001) set and was developed as a model that best fit the median SED in Taurus. This model is in vertical hydrostatic equilibrium in the case that the dust temperatures are set by irradiation from the central star, and under the assumption of full thermal coupling between the gas and dust. The total mass in the disc is 0.026 $M_\odot$ with an outer radius of 500 AU.

This disc structure, which provides the starting density distribution, employs a bimodal dust distribution, where atmospheric dust follows the standard MRN model (Mathis et al. 1977) but with a low dust to gas mass ratio (2.5×10^{-5} for graphite and 4.0×10^{-5} for astronomical silicates) and interior dust consists of larger grains with a size distribution still described by a power law of index -3.5, but with a_{min} = 0.005 μm and a_{max} = 1 mm and a dust-to-gas mass ratio of 3.1×10^{-2} for graphite and 5.0×10^{-2} for astronomical silicates. The transition between atmospheric and interior dust occurs at a height of 0.1 times the mid-plane gas scale height.

This initial disc was then irradiated by a synthetic coronal spectrum of X-ray luminosity $L_X = 2\times10^{30}$erg s^{-1} (see Figure 3.1) and total ionizing luminosity of $L_{TOT} = 4\times10^{30}$erg s^{-1} by Ercolano et al. (2009b). This synthetic spectrum was a thermal spectrum generated by Ercolano et al. (2008b,2009b) using the plasma code of Kashyap et al. (2000); the emission measure distribution is based on that derived for

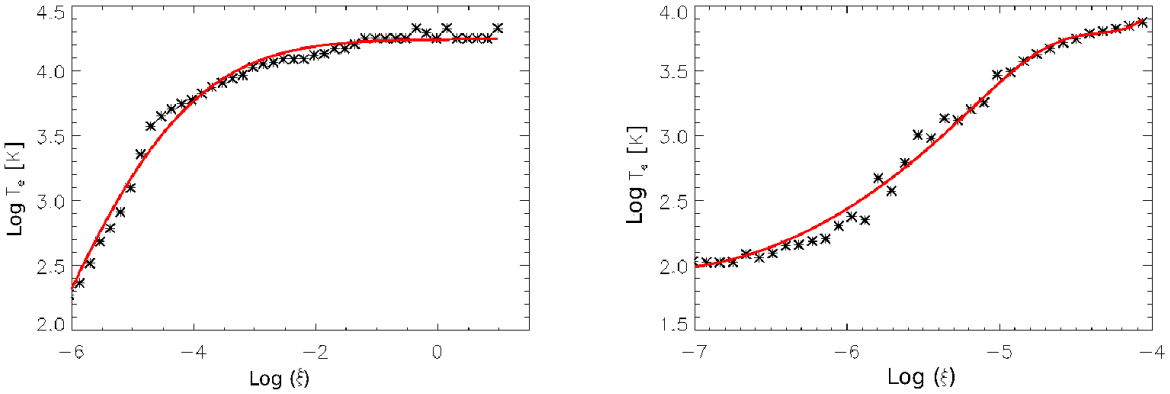

Figure 3.2: Plot of Temperature as a function of ionization parameter obtained using MOCASSIN with a numerical parametrization shown in red. The black asterisks show the mean temperature in the ionization parameter bins obtained from MOCASSIN, with a scatter about the mean of ~ 0.3 dex. The left hand panel is for a primordial disc and the right hand panel is for a disc with an inner hole at $\sim$ 16AU

RS CVn type binaries by Sanz et al. (2002) and fits to Chandra spectra of T Tauri stars by Maggio et al. (2007) (which peaks at around $\log T = 7.5$K). The use of the input spectrum shown in Figure 3.1 implies that there is no column of neutral material close to the source. As described in Ercolano et al. (2009b), the disc temperatures are updated in response to irradiation by the high energy spectrum and the density structure is updated so as to attain a situation of hydrostatic equilibrium for this updated temperature profile. These temperature and density distributions are then updated iteratively until a situation of both thermal and hydrostatic equilibrium is attained. It is these converged hydrostatic models that form the basis of the parametrization described below, even though the hydrodynamical calculation will evolve away from this initial static structure towards a steady flow solution. However, I will check retrospectively that the parametrization also applies to the evolved structure.

In order to render the calculation tractable, I exploit the fact that the wind will be optically thin to high energy photons. Figure 3.2 shows the mean relations between ionization parameter and temperature in the X-ray heated region of the hydrostatic models of Ercolano et al. (2009b), where I define the X-ray heated region as comprising gas for which the absorbing column to the central star is less than 10^{22} cm^{-2} (roughly the penetration depth of 1 keV photons). The scatter of the MOCASSIN grid cells about the relation shown is small (~ 0.3 dex), thus confirming that the ionization parameter is indeed a good determinant of the gas temperature. This confirms the central importance of X-ray heating in determining the thermodynamics of the heated atmosphere (note that a tight relationship between ionization parameter and temperature would not be expected in general in the case of heating dominated by EUV radiation). I will also consider the case of photoevaporation from discs containing inner holes, for which I need to make sure our parametrization in the lower temperature regime is still applicable. The right hand panel of Figure 3.2 depicts the result of a similar calculation of a disc which is truncated at an inner radius of $\sim$ 16 AU. This also provides a good fit to models with different inner hole sizes and hence I use this relation in all the hydrodynamic models. Also, note the similarity of the relations for the identical ionization parameter range, this implies that it is the direct field that is dominating in both cases. Therefore, I can be confident that the simple model of X-ray heating outlined in Chapter 2 provides an accurate description of the physical processes occurring in protoplanetary discs. Furthermore, I can combine the

two temperature ionization parameter relations to a range that will span all possible ranges expected in photoevarporation models. Thus, at the most basic level I assume that this temperature ionization parameter relation is independent of all physical parameters considered in this study (X-ray luminosity, mass and disc structure). Since, these relations show that the gas temperature varies monotonically with ionization parameter in the X-ray heated regime, it can be used to prescribe the gas temperature for regions lying at columns of $< 10^{22}$ cm^{-2} from the central source. For columns larger than 10^{22}cm^{-2} Ercolano et al. (2009b) found that the gas and dust were thermally coupled. Hence, I use the dust temperatures of D'alessio et al. (2001) to fix the gas temperatures for columns greater than 10^{22}cm^{-2}. In order to check that our temperature parametrization is appropriate for the final converged flow solution, this density field will be feed back into MOCASSIN to compare the temperatures obtained.

3.1.2 Radiation-Hydrodynamic Methods

In order to accurately determine the mass-loss rates and the kinematic and morphological structure of the evaporative flow, I need to compute the temperature distribution in the flow and feed this into a hydrodynamic code.

The ZEUS *Code*

The hydrodynamic codes I have chosen to use are the publicly available ZEUS set of hydrodynamical codes. The ZEUS code was originally the brain child of Michael Norman in the 1970's, as a hydrodynamical scheme to study star formation, but has evolved significantly over the years to include extra physics and optimizations to modern supercomputer architectures. However, the underlying hydrodynamic algorithms are essentially the same. The method for intergrating the hydrodynamic equations are described in detail by Stone & Norman (1992a,b) for the ZEUS-2D code and its extension to 3D and MPI in Hayes et al. (2006) in the ZEUS-MP/2 code. Therefore, here I mainly summarise the basic outline of the integration method. The ZEUS code employs a staggered finite difference grid. In this setup the hydrodynamic equations are naturally differenced on the grid using central volume differencing, allowing fluxes to be conserved to approximately machine precision. Vectors are stored and updated on cell faces, while scalars are stored and updated at cell centres, and differencing is performed using a covariant formalism. This differencing allows the code to switch between various coordinates systems efficiently, with caretesian and cylindrical & spherical polars having been implemented.

The ZEUS code integrates the hydrodynamic equations using an operator splitting technique. The equations are split into two parts, source terms (i.e. non-advective terms) and transport terms (advective terms). At each time-step the source terms are used to update the hydrodynamic variables first, and then the advective terms are calculated from these updated values, and used to calculate the fluxes to transport across the grid. Then the new time-step is calculated using the Courant condition, where I choose a Courant number of 0.5 to ensure numerical stability. I have modified the ZEUS suite of hydrodynamic codes (Stone et al. 1992a,b; Hayes et al. 2006) (both ZEUS-2D and ZEUS-MP/2) to include the heating from X-ray radiation, by writing a new module that calculates the gas temperature. This temperature is

Table 3.1: Primordial Disc models

Stellar Mass [$M_\odot$]	$\log_{10}(L_X)$ [erg s^{-1}]	Code	Radial range [AU]
0.7	28.3	ZEUS-2D	[0.33,100]
0.7	28.8	ZEUS-2D	[0.33,100]
0.7	29.3	ZEUS-2D	[0.33,100]
0.7	29.8	ZEUS-2D	[0.33,100]
0.7	30.3	ZEUS-2D	[0.33,100]
0.7	30.8	ZEUS-2D	[0.33,100]
0.1	28.3	ZEUS-MP/2	[0.03,46]
0.1	28.8	ZEUS-MP/2	[0.03,46]
0.1	29.3	ZEUS-MP/2	[0.03,46]
0.1	29.8	ZEUS-MP/2	[0.03,46]
0.1	30.3	ZEUS-MP/2	[0.03,46]

then used to update the internal energy density of gas (e) in the wind via the ideal equation of state:

$$e = \frac{k_B}{\mu m_h(\gamma-1)}\rho T \tag{3.1}$$

The mean molecular weight is fixed in the flow, to a value of $\mu = 1.37125$. The internal energy is only required to update the pressure needed for evaluation of the momentum equation. The pressure is thus determined again from the ideal gas law, via:

$$p = (\gamma-1)e \tag{3.2}$$

and hence the procedure is independent of choice of γ. This thermal update is done during both the source step and transport step in order to minimise the time to a converged solution.

I assume azimuthal and mid-plane symmetry and therefore adopt a 2D axis-symmetric grid. Since, I expect a photoevaporative flow to be approximately spherical at large radius, I use a spherical grid and neglect magnetic fields and self-gravity. The rotation option in ZEUS is enabled, which introduces the necessary pseudo-forces arising from rotating frames. The inner and outer radial boundaries are set to outflow, while the angular boundaries are given the appropriate symmetry boundary conditions.

3.2 Primordial Discs

In order to determine the flow structure for the disc for the majority of its standard viscously accreting phase, I calculate hydrodynamic models for two masses and the range of X-ray luminosities observed for young stars, the details of these simulations are summarised in Table 3.1.

3.2.1 Numerical Method

The grid is chosen to be in the range $\theta = [0, \pi/2]$ and the radial range is shown in Table 3.1, I adopt a radial range out to 100AU in the case of simulations around $0.7M_\odot$ stars, since previous calculations around stars of this mass indicate that the majority of the mass-loss occurs inside 50AU (Alexander et al.

2004; Ercolano et al. 2008b,2009b). For the case of a $0.1M_{\odot}$ star no such previous calculation exists, although the theoretical model in Chapter 2 indicates that I could simply scale the $0.7M_{\odot}$ result and use an outer boundary of ~ 15AU, I urge on the side of caution and use and outer boundary of 46AU. The inner boundary is chosen to be well inside $0.1R_g$, where the disc transitions from a bound X-ray heated atmosphere to an X-ray driven wind, and is at small enough radii not to interfere with the flow. Grid cells are logarithmically spaced in the radial direction, so that there is adequate resolution at small radius: in particular I ensure that the onset of the flow, and the scale height of the bound X-ray 'dark' disc is resolved. For calculations performed with the ZEUS-2D code I use 100 cells in the angular direction and 250 in the radial direction. The calculations performed with the ZEUS-MP/2 included the added complication that in order to use the distributed memory architecture of the DARWIN supercomputer (for maxium efficiency and cost!) the number of grid cells needed to be divisible by multiples of 4. Therefore, accounting for this and the increased radial range of the $0.1M_{\odot}$simulations I use 144 angular cells and 288 logarithmic radial cells.

Initial Conditions

The vertically hydrostatic density and temperature structures generated by (D'alessio et al. 2001) are taken as the underlying structures for both the 0.1 & 0.7 $M_{\odot}$star. The $0.7M_{\odot}$disc structure is the same as described previously for the calculation of the temperature-ionization parameter and the $0.1M_{\odot}$disc model is a $3\times10^{-3}M_{\odot}$ disc around a star with $T_*=3000$K and $R=0.8R_{\odot}$. These disc structures were then allowed to evolve hydrodynamically using the numerical method, with the gas temperatures being updated at every time-step, until a 'steady-state[1]' disc/wind system was obtained. It should be noted that the density structure of the X-ray 'dark' regions is also allowed to evolve hydrodynamically, i.e. it is not reset to the original density structure at every time-step (compared with previous EUV hydrodynamic simulations e.g. Alexander et al. (2008); Font et al. (2004) which - since they did not model the EUV 'dark' disc - reset the base density of the flow to its original value at each time-step). I emphasise that the mass loss over the duration of the simulation is much less than the initial disc mass, and the obtained wind structures are close to a steady state.

3.3 Inner Hole Flows

As was discussed previously, photoevaporation combined with viscous evolution results in a gap opening in the primordial disc. The inner disc then drains onto the star leaving the outer disc exposed to direct irradiation by the central star. The flow expected from such a system is of course different from a primordial disc's photoevaporative flow, and in this section I set out the methods used to calculated mass-loss rates from discs with inner holes.

3.3.1 Numerical Method

In order to describe the variation of mass-loss rate with inner hole radii, I have run several models with inner holes at different radii, out to a radius beyond which disc holes become hard to detect observation-

[1]Where the term 'steady-state' strictly means quasi-steady-state or more formally $\dot{M}_w \times t \ll M_{\rm disc}$.

ally (i.e. at around $\sim 10-100$ AU depending on the stellar mass). I used a regularly space spherical grid in order to maximise resolution while minimising computational effort (see Alexander et al. 2006a). The grid was constructed with 400 cells in the radial direction and 200 cells in the angular direction, again sufficient to resolve the onset of any flow and the scale height of the 'dark' disc at all radii. All other ZEUS parameters were kept the same as above and table 3.2 summarises the input parameters used. As starting points for the calculations, the hydrodynamic primordial disc models were cut a radius close to the desired inner hole radius (Note: the inner hole radius will be set by dynamical balance with the flow, hence the final inner hole radius will be slightly different to this value). Then the density profile was smoothed over four pressure scale lengths at inner edge, where the angular velocity was adjusted to match the new imposed radial pressure gradient. In most cases the model was then allowed to evolve hydrodynamically until it attained a steady flow solution. However, as we shall see when we come to the results, the simulations around the $0.1M_{\odot}$ star with the largest inner holes ~ 5 AU violate the 'quasi-steady state' regime discussed above due to vigorous mass-loss rates and low disc surface densities. This is exactly the situation encountered by Alexander et al. (2006a), even though the time integrated mass-loss rate over the simulation was comparable to the mass reservoir in the initial bound disc. One can argue that since the sound crossing time-scale of the flow is much shorter than the expected erosion time for the inner-edge of the disc, then the simulations may attain a very rough 'steady-state', which will presumably vary on the disc's dynamical time-scale. However, given I don't expect the disc structure to be important for determining the mass-loss rates then the effect of a disc structure that varies on it's dynamical time-scale to be small. Therefore, I can extract a run of the mass-loss rate as a function of inner hole size as the inner edge of the disc is eroded to larger and larger radius as in Alexander et al. (2006a). In addition, just to be sure that I can trust these mass-loss rates I take the wind/disc structure from a time-step when the system has reached this rough steady state and perform a simulation where the density of the X-ray 'dark' mid-plane is reset at every time step in order to attain an exact steady state solution to compare with the rough steady state results.

3.4 Results

The systems were found to have converged after $\sim$4-6 orbital time-scales at the outer boundary. The flow structure after 10 orbital time-scales at the outer boundary is used in the analysis. All simulations yield a well defined photoevaporative flow and bound disc, and find that the presence of a photoevaporative flow above the bound disc, causes very few changes to the structure of the underlying bound discs calculated by D'alessio et al. (2001), which is reassuring since these hydrostatic disc structures were calculated in order to fit the dust observations of protoplanetary discs.

3.4.1 Primordial Discs

In Figure 3.3 I show the velocity and density structure for a X-ray photoevaporating disc around a $0.7M_{\odot}$ star with an X-ray luminosity of 2×10^{30} erg s^{-1}, with the mass-loss rate for this system found to be $1.4\times10^{-8}M_{\odot}$ yr^{-1}, in good agreement with the analytic prediction derived in Chapter 2. As expected that the mass-loss profile is broad extending over many 10's of AU, but is roughly complete by 50-60AU, I also find as expected that the sonic surface occurs at height well above the X-ray 'dark'/'bright' tran-

Table 3.2: Inner Hole Models

Mass [$M_\odot$]	$\log_{10}(L_X)$ [erg s^{-1}]	R_{in} [AU]	Code	Grid range [AU]
0.7	30.3	8.3	ZEUS-2D	[1.33,90]
0.7	30.3	9.7	ZEUS-2D	[1.67,90]
0.7	30.3	11.7	ZEUS-2D	[3.35,100]
0.7	30.3	14.2	ZEUS-2D	[3.35,100]
0.7	30.3	17.7	ZEUS-2D	[3.35,100]
0.7	30.3	21.1	ZEUS-2D	[3.35,100]
0.7	30.3	30.5	ZEUS-2D	[3.35,100]
0.7	30.3	64.5	ZEUS-2D	[10,450]
0.7	30.3	86.9	ZEUS-2D	[15,500]
0.7	28.8	5.4	ZEUS-2D	[0.45,93]
0.7	28.8	10.5	ZEUS-2D	[0.45,93]
0.7	28.8	19.6	ZEUS-2D	[0.45,93]
0.7	28.8	62.3	ZEUS-2D	[1.0,448]
0.7	29.8	5.7	ZEUS-2D	[0.45,93]
0.7	29.8	11.2	ZEUS-2D	[0.45,93]
0.7	29.8	20.3	ZEUS-2D	[0.45,93]
0.7	29.8	65.0	ZEUS-2D	[1.0,448]
0.7	30.8	6.0	ZEUS-2D	[0.45,93]
0.7	30.8	12.1	ZEUS-2D	[0.45,93]
0.7	30.8	22.7	ZEUS-2D	[0.45,93]
0.7	30.8	71.8	ZEUS-2D	[1.0,448]
0.1	30.3	0.6	ZEUS-MP/2	[0.05,20]
0.1	30.3	4.7[1]	ZEUS-MP/2	[0.29,30]
0.1	29.3	0.7	ZEUS-MP/2	[0.05,20]
0.1	29.3	4.5[1]	ZEUS-MP/2	[0.29,30]

sition indicating the assumption of an optically thin X-ray wind is a good one. In Figure 3.3 I show the total mass-loss rates obtained for all primordial disc simulations compared to the theoretical model calculated in Chapter 2, this figure indicates that the two major results of the model are correct: the mass-loss rates scale approximately linearly with X-ray luminosity and they are roughly independent of stellar mass, along with showing good agreement with the order of magnitude calculations performed previously. One of the major starting points of the model is that the thermal structure of the flow should be set by the mass of the central star and scale with the escape temperature, meaning that the thermal structure of the flow should be invariant when considered in terms of radii scaled by R_g, this means that the density structure should scale as M_*^{-2} for a fixed r/R_g, and the mass-loss profile should be fairly self-similar when also considered in terms of R/R_g. In Figure 3.5 I compare the thermal, density and velocity structures of two models with masses of $0.1M_\odot$ and $0.7M_\odot$. This shows clearly that the thermal structure of the flow is indeed invariant when considered in terms of r/R_g and the sonic surfaces roughly follow the same loci, along with the density structure and flow topology roughly scaling as expected. We can look in more detail at the self-similarity of the mass-loss profile by looking at cumulative mass-loss rate as a function of cylindrical radius, which are shown in Figure 3.6, the model predicts that this should be approximately self-similar and this is what is found for variations in stellar mass (when one considers it in terms of R/R_g) and X-ray luminosity. The profile is very broad with approximately 50%

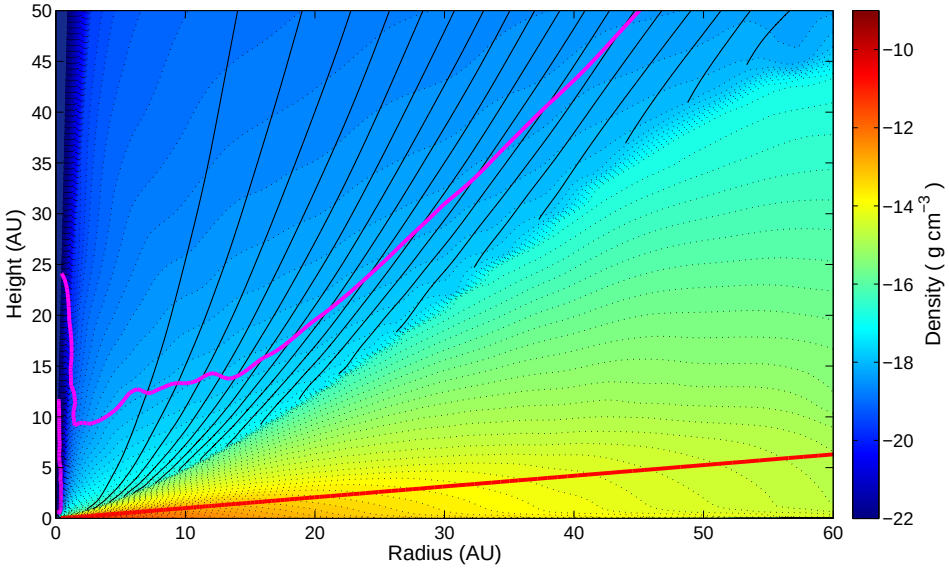

Figure 3.3: The density structure of the flow solution for a primordial disc around a $0.7M_{\odot}$star with and X-ray luminosity of 2×10^{30} erg s^{-1}. The red line indicates the $\tau = 2/3$ surface from the central star, while the magenta line shows the sonic surface. The streamlines are plotted at 5% intervals of the integrated mass-loss rate.

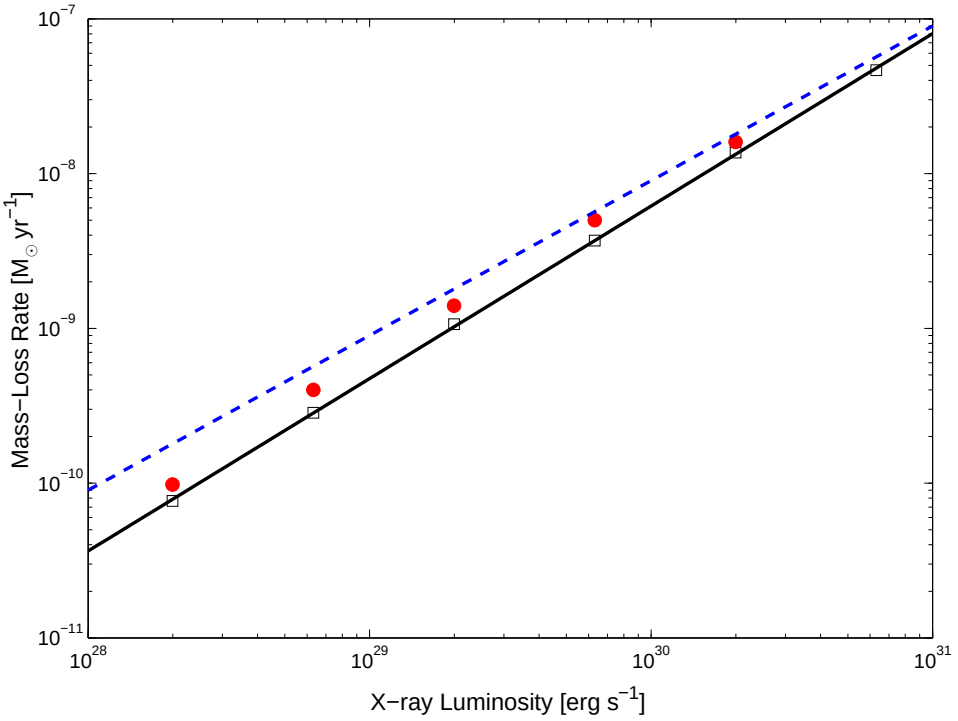

Figure 3.4: Mass-loss rate plotted against X-ray luminosity, the open squares show the simulations results for a $0.7M_{\odot}$star, the filled circles show the simulation results for a $0.1M_{\odot}$star. The solid line show the numerical fit I will use for solar type stars in Chapter 4 to conduct a population synthesis study, the dashed line shows the order of magnitude estimate obtained in Chapter 2.

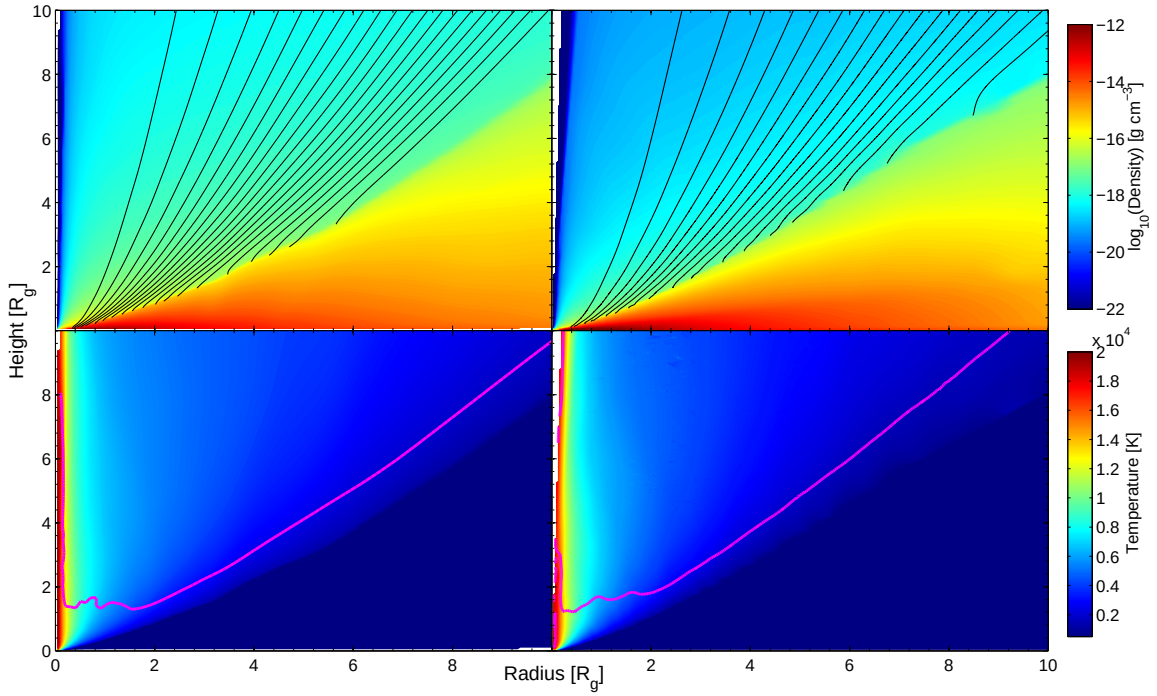

Figure 3.5: Figure showing the flow topology around a 0.1 (left panels) and 0.7 (right panels) $M_\odot$ star for an X-ray luminosity of 2×10^{29} erg s^{-1}. The top panels show the density structure with streamlines plotted at 5% intervals of the integrated mass-loss rate. The lower panels show the temperature structure of the flow, where the solid line show the sonic surface.

of the mass-loss occurring inside $20AU$ for a $0.7M_\odot$star and the remain 50% occurring outside and very little mass-loss occurs outside 60-70AU. The profiles also become broader with increasing X-ray luminosity, although this broadening is very small when considered in terms of the entire radial range of the photoevaporative flow.

3.4.2 Inner Hole Flows

The mass-loss rates are found to be approximately insensitive to the inner-hole size. Furthermore, as expected they scale linearly with X-ray luminosity. In Figure 3.7 I show the mass-loss rates as a function of inner hole size and X-ray luminosity for discs around a $0.7M_\odot$star and in Figure 3.8 for a $0.1M_\odot$star.

Figure 3.9 shows the flow topology from a disc around a $0.7M_\odot$star with an X-ray luminosity of 2×10^{30} erg s^{-1} and an inner hole at $\sim$18 AU, in all cases the first streamline is sub-sonically driven radial inwards, at a radius of $R \sim R_{\rm hole}/2$ the gas has obtained an azimuthal velocity equal to the break up velocity and gas escapes vertically passing through the sonic surface at a height of $z \sim R_{\rm hole}$ and a temperature around $\sim$ 6000K considerably higher than the escape temperature, accounting for the non-spherical velocity divergence and magnitude of the centrifugal force. The model described in Chapter 2 demonstrated that no similarity solution exists and this is what is found, as the mass-loss profiles cannot be described as function R/R_g. However, I do find that the solution is scalable in X-ray luminosity and the profile is scalable in terms of escape temperature, demonstrating the basic ideas of the model.

Figure 3.10 shows the evolution of the 'quasi steady-state' simulation with time, during the first 300 years of evolution the photoevaporative flow slowly strips of gas from the inner edge of the disc

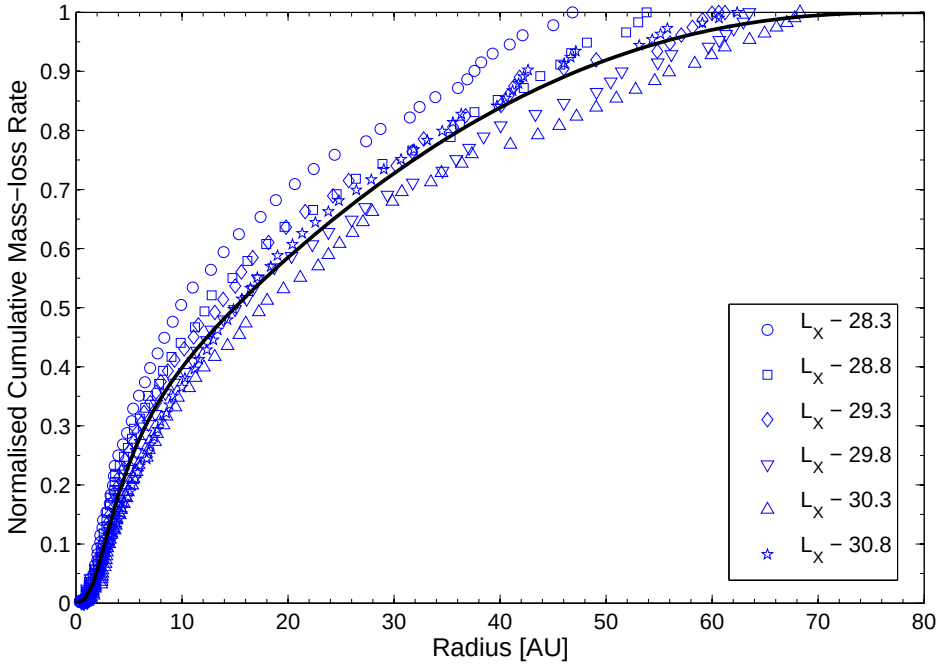

Figure 3.6: Cumulative mass-loss profiles for discs around a $0.7M_{\odot}$star with various X-ray luminosities, (the profiles for $0.1M_{\odot}$also agree with those shown when considered in terms of R/R_g but are not shown for clarity). The points represent the individual simulations, where the solid line shows a numerical fit used later in Chapter 4

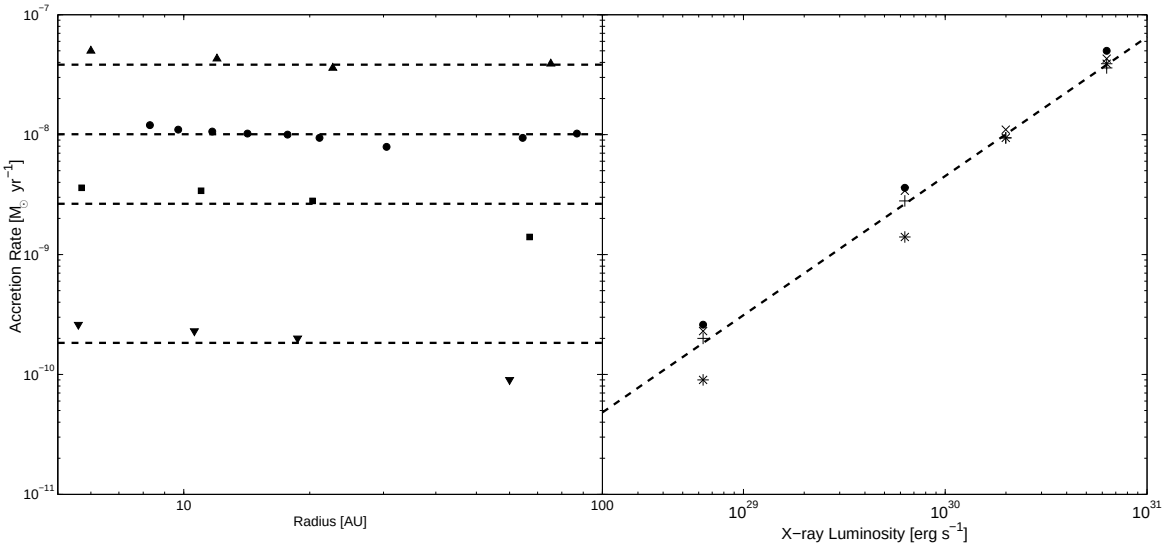

Figure 3.7: Mass-loss rate as a function of inner hole radius (left panel), the points show the results from the simulations (upright triangles - $L_X = 30.8$; circles - results taken from Owen et al. 2010 for $L_X = 30.3$; squares - $L_X = 29.8$; downward triangles - $L_X = 28.8$) and the dashed line shows the fit used throughout this work. The right panel shows the mass-loss rate as a function of X-ray luminosity ($\bullet$ - $\approx$ 5AU; $\times$ - $\approx$ 10AU; $+$ - $\approx$ 20AU; $*$ - $\approx$ 70AU) with the dashed line showing the fit used in Chapter 4.

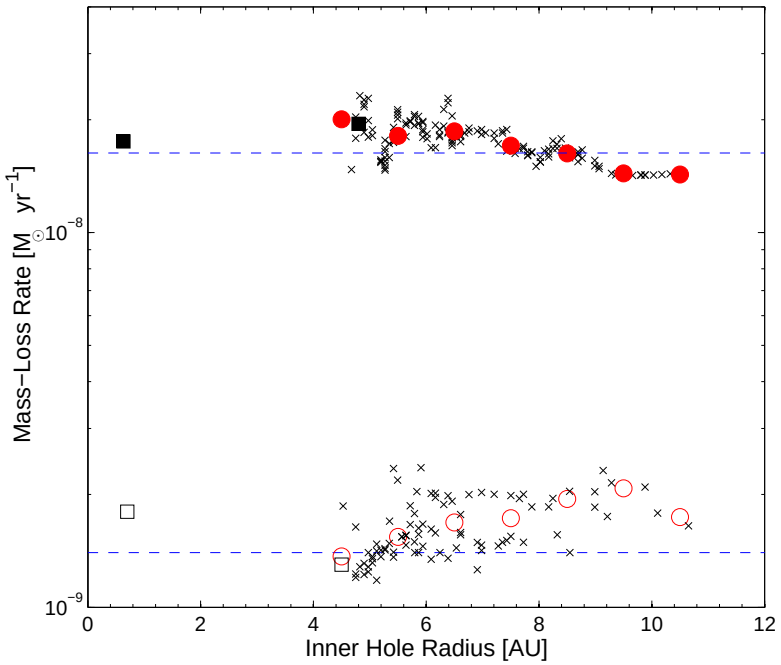

Figure 3.8: Figure showing the mass-loss rate as a function of inner hole size for discs around a $0.1M_{\odot}$star. The filled points are those for an X-ray luminosity of 2×10^{30} erg s^{-1} and the open points are those for and X-ray luminosity of 2×10^{29} erg s^{-1}. The crosses are the mass-loss rates calculated from the eroded inner hole models, while the circles are the moving average calculated from these mass-loss rates. The dashed line shows the mass-loss rates for primordial discs with the same X-ray luminosity.

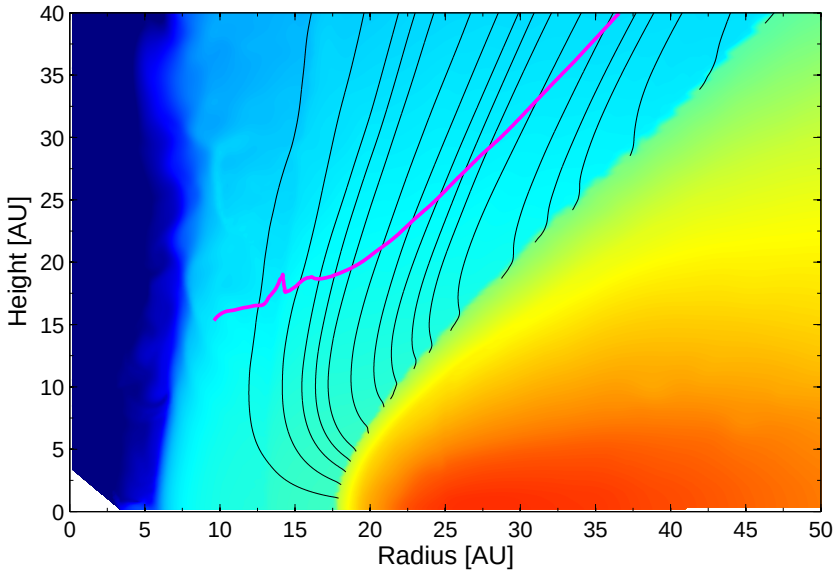

Figure 3.9: Flow structure from a disc with an inner hole of 17.7AU, around a $0.7M_{\odot}$star with an X-ray luminosity of 2×10^{30} erg s^{-1}. The streamlines are plotted at 5% intervals of the integrated mass-loss rate, and the magenta line shows the sonic surface.

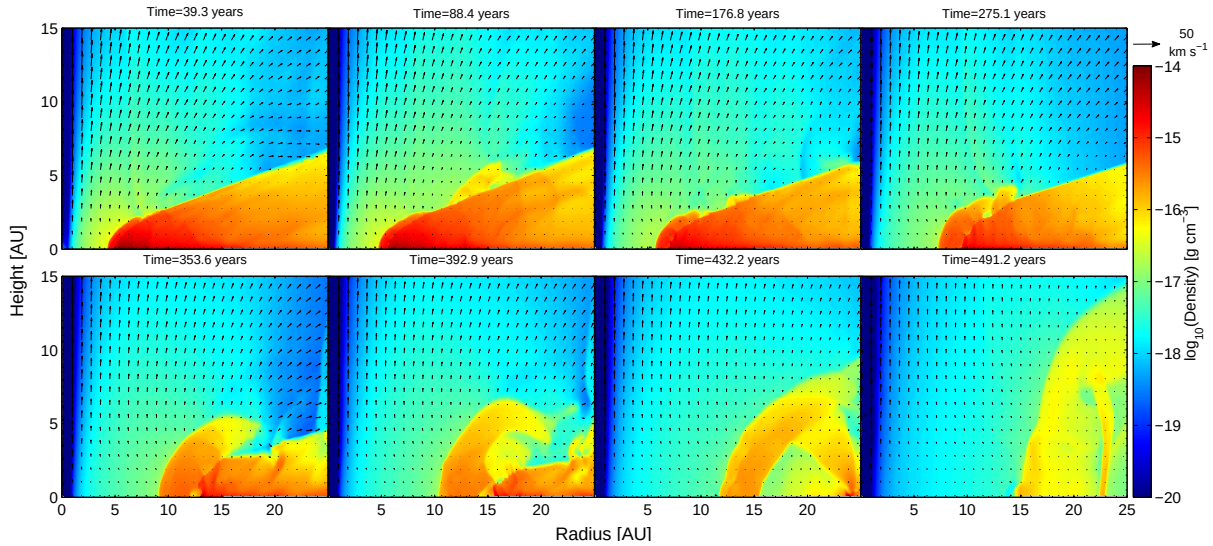

Figure 3.10: Time evolution of 'quasi steady state' simulation of a disc with an inner hole and an X-ray luminosity of 2×10^{30}erg s^{-1} around a $0.1 M_{\odot}$star. The colour map shows the density structure and the arrows indicate the velocity structure. Each panel indicates a snapshot of the flow structure.

(note: that as there is no viscosity in the disc that the inner disc region is not resupplied with material and the erosion time-scale is quicker than would be expected from a viscous disc model). As the hole grows the layer of warm bound X-ray heated gas grows in size. Once the hole size grows to $R_{\rm hole} \sim 10$AU, this region becomes large enough that it can clear the remaining disc, which is completely cleared on the dynamical time-scale ($\sim$100 years at 10AU). This was not seen in the simulations calculated for the $0.7 M_{\odot}$star, the reason for this is since I have moved to lower masses the column in the disc mid-plane has become considerably lower and reached the point where the size of the X-ray heated bound disc has become of order the radial pressure height of the disc. If I had the computational resources to calculate inner hole models around solar type stars with very large radii we would have seen exactly the same process occurring.

Understanding the Inner hole Scalings

Examination of the streamline topology for various inner hole radii (over a factor of ~ 2) suggests that the topology of the innermost streamline is approximately scale free (i.e with an over all radial scale that varies with $R_{\rm hole}$) and as a consequence the variation of temperature and velocity along this streamline (as a function of distance along the streamline scaled to $R_{\rm hole}$) is approximately the same in each simulation (see Figure 3.11). This alludes to the possibility of constructing an approximate scaling argument even though in Chapter 2 I demonstrated an exact similarity solution does not exist. Nevertheless, if we use the *empirical* numerical result (i.e. that the flow topology of the innermost streamlines simply scales with $R_{\rm hole}$ and that the velocity and temperature variation along the streamline is the same in scaled distance units) then we can derive the origin of the found mass-loss scaling law. The constancy of temperature at given $\tilde{l}$ implies constancy of ξ and hence a density scaling as $R_{\rm hole}^{-2}$. Then the mass flux along the streamline (at fixed $\tilde{l}$) scales with density ($\propto R_{\rm hole}^{-2}$), velocity (constant) and area of streamline bundle ($\propto R_{\rm hole}^{2}$). Therefore, the mass-flux along this streamline is invariant of inner hole radius.

The origin of a scalable innermost streamline is likely to originate from the fact that unlike primordial

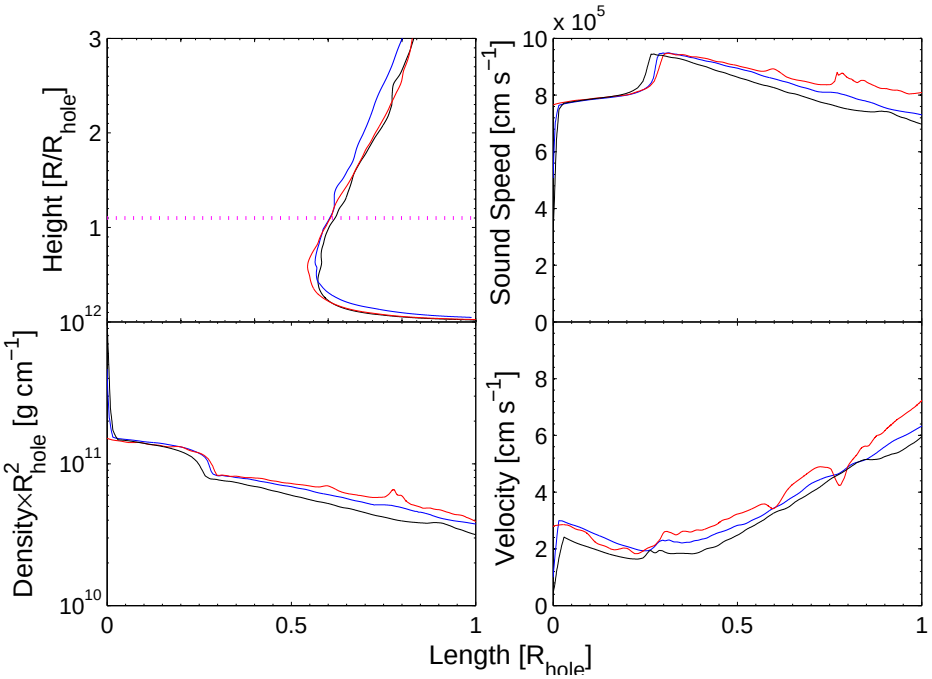

Figure 3.11: Figure showing the streamline topology and density, sound speed and velocity along the sub-sonic section of the streamline. The streamline topology is shown in the top left hand panel scaled in terms of $R_{\rm hole}$, with the sonic surface shown as the dotted line. Then bottom left panel show the density $\times R_{\rm hole}^2$, the top right show the sound speed and the bottom right show the velocity, where all are scaled in terms of $l/R_{\rm hole}$. The black lines are for a hole of 14 AU, the blue line for a hole of 21AU and the blue for an inner hole of 30 AU.

discs, where the thermal pressure is dominant in determining the streamline topology it is the centrifugal force that dominates. The streamlines emerging from the inner edge of the disc move towards the central star meaning (see Figure 3.9) the centrifugal force quickly becomes dominant. As the form of the effective potential is scalable in terms of $R_{\rm hole}$, in the limit of negligible pressure the streamline topology would also be scalable in terms of $R_{\rm hole}$, and this 'strong' body force limit is the most likely origin of the scalable streamline topology. Provided the total mass-flux is dominated from the inner hole region - as the simulations indicate - then the total mass-loss should scale in a similar fashion to the mass-flux on the innermost stream-bundle, resulting in a total mass-loss rate that is approximately independent of the inner hole radius.

3.5 Numerical tests

The photoevaporation model presented in Chapter 2 made some rather strong predictions regarding the variation (or non-variation) of the mass-loss rate with physical parameters. While the predicted scalings with X-ray luminosity and stellar mass can be tested using the simulations discussed above, it is important to asses the prediction that the underlying disc structure and FUV heating will have almost no affect on the derived results. This is obviously important since the surface density of a disc, optical properties of the central star and FUV luminosity can vary by large factors over the millions of years of evolution expected during the disc's lifetime. In order to test the role of disc structure and FUV heating I restrict

the calculations to one stellar mass and X-ray luminosity, a simulation with $M_* = 0.7\mathrm{M}_\odot$ and $L_X = 2 \times 10^{30}\mathrm{erg\ s}^{-1}$.

Variations in disc structure

Perhaps the easiest way to vary the disc's underlying structure along with generating very different thermal and density structure, is to instead of coupling the X-ray 'dark' disc to the dust temperature allow it to evolve adiabatically. Obviously, such a situation has no physical basis but it easily generates some different disc structures, which can be changed simply by varying the adiabatic index in the ZEUS code (Note: as described above the X-ray heated region evolves independently of the choice of γ). Such tests should clearly show up if the disc's structure plays an important role in photoevaporation. Therefore, I perform simulations with $\gamma = 1.10,\ 1.33,\ 1.41,\ 1.67$ using exactly the same parameters as the $0.7\mathrm{M}_\odot$ primordial disc calculations described above.

In order to consider some more realistic variations in disc structure, I have performed a further set of simulations where the disc structure is varied in a more physical manner, namely due to variations in the disc's surface density and the (total) luminosity of the central star. Therefore, one simulation has been performed with a disc mass that is 10% of the original calculation (i.e. $M_d = 2.6 \times 10^{-3}\mathrm{M}_\odot$). Furthermore, in order to account for variations in the thermal structure of the disc due to luminosity variations I have increased and decreased the dust temperature by a factor of $\sqrt{2}$. Since the X-ray 'bright'/'dark' transition occurs in a region where the dust is optically thin, then this is just effectively a change in the stellar luminosity by a factor of 4. These simulations are performed on the same grid range as the original calculation, although I switch to the ZEUS-MP/2 code and adopt the more efficient grid resolution of $N_r \times N_\theta = 288 \times 144$.

Effects of FUV radiation

In Chapter 2 I argued that since X-ray heating can heat the gas to higher temperatures than the FUV, then the mass-loss rate will be set by the X-ray physics. In order to test this, I perform some simulations that roughly aim to include the effect of extra-heating below the X-ray dominated region. If FUV heating was important to the calculation of photoevaporation rates then one would require a detailed calculation of X-ray and FUV heating and cooling, along the lines of combing the X-ray algorithm with an FUV algorithm (e.g. Richling & Yorke, 2000). While such a calculation would be necessary to predict line emission from the warm atomic and molecular layer, the theoretical framework described above predicts it is unimportant when photoevaporation rates are what is required. Therefore, a full X-ray + UV calculation is unnecessary and beyond the scope of this thesis. Thus, in order to test the model predictions I simulate the affect FUV heating by adding an extra heating source to the X-rays at the level expected from FUV heating.

Therefore, I calculate the FUV flux throughout the disc/wind system in an identical manner to Richling & Yorke, (2000) including opacity only from dust extinction (e.g. I ignore opacity arising from the ionization of Carbon and Sulphur -a second order effect- overestimating the flux and gas temperature). I then turn the attenuated FUV flux into a temperature using a parametrisation of the external FUV photoevaporation calculations performed by Richling & Yorke (2000) and internal disc heating calculations of

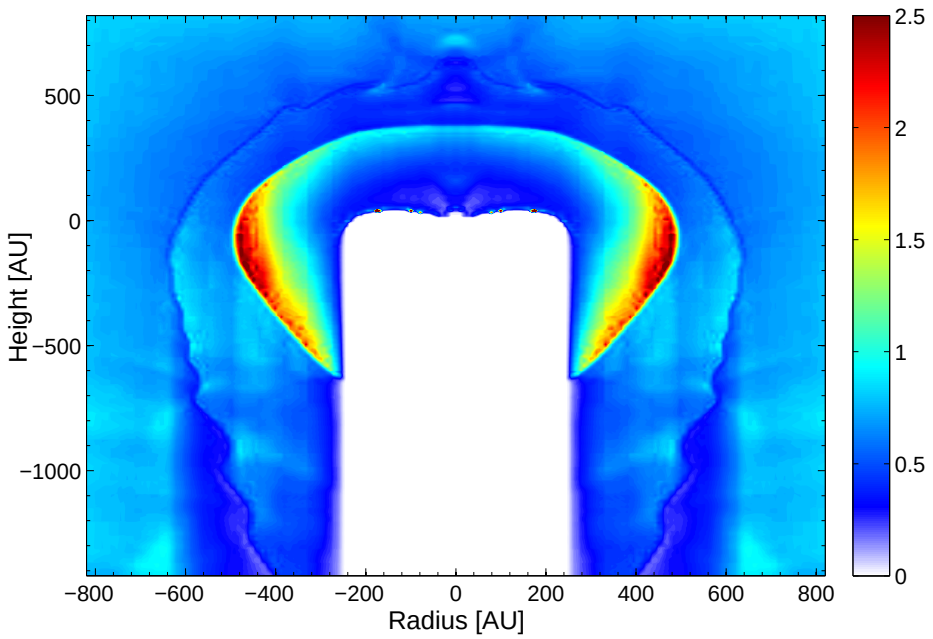

Figure 3.12: Comparison of gas temperature from the external photoevaporation calculation of Richling & Yorke, (model A) compared with the temperature given by the parametrisation shown above, the colourmap shows the ratio of the two temperatures $T_{\rm param}/T_{\rm actual}$, this shows the parameterisation reproduces the temperature to within a faction of ~ 2. The white region shows those which are optically thick to the direct FUV field and are therefore excluded from our comparison as I can neglect the diffuse FUV field to first order in our problem (internal photoevaporation).

Gorti & Hollenbach (2008). The parametrisation:

$$T_{\rm FUV} = 1400{\rm K}\left(\frac{f_{\rm FUV}}{300\ {\rm erg\ s^{-1}\ cm^{-2}}}\right)^{0.35}\left(\frac{n}{5\times 10^{6}{\rm cm^{-3}}}\right)^{-0.25} \tag{3.3}$$

reproduces the temperature structure of the region directly irradiated by FUV in Richling & Yorke (2000) calculated (labelled model A) as shown in Figure 3.12, and the temperature structure listed for the 'launching point' of the Gorti & Hollenbach (2008) calculation to within a factor of 2. I perform a simulation with a very large FUV luminosity of 1×10^{31}erg s^{-1} and choose a depleted (from ISM type dust) value of the FUV extinction of 300 cm^2 g^{-1} used by Richling & Yorke (2000) and a extinction that is depleted by a further factor of 10. Furthermore, since the conclusions of Gorti et al. (2009) indicate that disc structure affects the FUV mass-loss rates, where more depleted discs drive more efficient winds, I calculate a model that would indicate if this effect was real and important. This model uses the mass depleted disc described earlier (with a $M_d = 2.3\times 10^{-3}$ M$_\odot$), along with assuming the disc's atmosphere is very settled with a low dust to gas mass ratio, and therefore a FUV extinction of 2 cm^2 g^{-1} (approximately half that of the settled disc described by D'alessio et al. 2001), in this case the mass fraction of the disc penetrated by the FUV is likely to be an over-estimated.

At every point in the disc/wind system I choose the heating mechanism X-rays, FUV or dust that produces the highest temperature. I emphasis this is no attempt to calculate the self-consistent thermal structure of a disc heated by FUV/X-rays, but purely an investigation into the effect FUV type heating will have on the photoevaporation. I demonstrating this further by running calculations in which I vary

the parametrisation, while this of course has no physical basis it is a simple way to demonstrate that are our results are not being driven by our underlying choice of temperature parametrisation, but rather the physics of the problem i.e. the flow being mediated by the conditions at the X-ray heated sonic surface. To do this I calculate an extra 4 models for the model with an FUV extinction of 30 cm^2 g^{-1}, where I vary the power law indices (in all four possible combinations) of the flux and density variation by factors of one-half and two and find no significant differences from the calculations presented below.

3.5.1 Results

I have performed a large set of tests. Including those in which I have neglected certain physical processes (e.g FUV irradiation), and those I have been required to make on order to make the numerical calculations tractable (e.g. use of ionization parameter - temperature relation), along with the standard issues that exist with numerical models (e.g. convergence), so that we can be confident that the solutions obtained are accurate and are unaffected by the assumptions discussed above.

Numerical Convergence

With calculations that rely on numerical methods, such as the ones used in this work, we must always be sure that the results obtained are the ones we set out to obtain, i.e. the issue of numerical convergence. In the case of photoevaporation calculations, I must ensure that our flows are adequately spatially resolved. In order to test this I have repeated one calculation with double resolution (the $0.7M_{\odot}$, $L_X = 2 \times 10^{30}$ erg s^{-1} model) and find the flow is converged to $\lesssim 5\%$. In order to calculate photoevaporation rates I require that the flow is in steady state; while I physically motivated this by waiting until after 10 dynamical-time scales at the order edge of the disc (the longest time-scale in the system) to extract information, I go one step further to ensure a true steady-state. To do this I calculate the Bernoulli potential in the rotating frame[2] noting that this will be constant in a steady flow. For each streamline I determine the enthalpy term by parametrizing the run of pressure and density as a baratropic relation (i.e. $P(\rho)$) along the streamline, then integrating along the streamline. I note that the flow is not strictly baratropic or irrotational and thus don't expect the Bernoulli potential to the same for different streamlines. Figure 3.13 shows that the Bernoulli constant is conserved along the streamlines to within 3-4% for the $0.7M_{\odot}$, $L_X = 2 \times 10^{30}$ erg s^{-1} indicating our simulations are extremely close to a true steady state.

Numerical Simplifications

In order to make any detailed calculation numerical tractable, simplifications must always be made. In this case the main simplification was the coupling of the radiative transfer to the numerical fluid mechanics. This was done by assuming that the thermal structure can be described in terms of local variables only, (i.e. the ionization parameter and neutral column) and that the flow was in radiative equilibrium. In order to be confident the parametrization of X-ray heating is correctly reproducing the temperature structure in the flow I have re-calculated the gas temperatures of the steady-state solution using MOCASSIN. Figure 3.14 shows a comparison between the temperatures determined by the radiation-hydrodynamic

[2]This is also known as the Jacobi potential

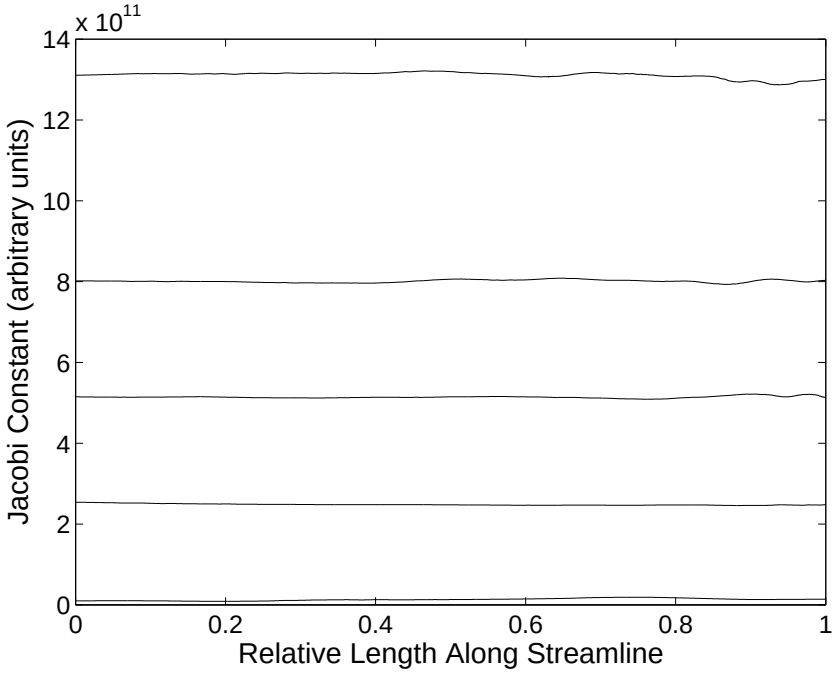

Figure 3.13: Plot of the Bernoulli potential along various streamlines in the range 2-50AU, plotted against the normalised streamline length. The variation in the mean value along each streamline is $\sim 3\%$

algorithm and those obtained using MOCASSIN. This shows that the errors are $<15\%$ for 50% of the grid and errors $<40\%$ for 95% of the grid. In Figure 3.15 I show the comparison between the gas temperatures determined using the algorithm and those obtained using MOCASSIN at various cuts in cylindrical radii. It shows good agreement throughout the grid especially in the launch region of the flow (region of large temperature gradient) and in the regions of the flow which are subsonic (red regions) where the thermal pressure gradient can be a first order effect. Note that the disagreement between the temperatures in the flow/disc transition region is an artifact of MOCASSIN, which imposes a hard transition between the molecular and atomic zones (see discussion in Ercolano et al. 2009b), hence the errors quoted can be considered an overestimate.

Throughout the modelling I assume that the gas is always in thermal equilibrium with the radiation. This assumption can be tested by comparing the gained energy flux of the wind to the ionizing luminosity. Figure 3.16 shows a plot of specific energy for a primordial disc around a $0.7 M_{\odot}$ star with an X-ray luminosity of 2×10^{30} erg s^{-1}. Considering the streamlines around the median mass-loss value (launching from 15-20AU) the total change in specific energy along these streamlines from launch (with a *negative* specific energy of $\sim 10^{11}$ erg g^{-1}) to exit from the grid (with a *positive* specific energy of $\sim 5 \times 10^{11}$ erg g^{-1}) is $\sim 6 \times 10^{11}$ erg g^{-1}. Given the grid boundary is far from the sonic surface this can be considered close to the maximum gained energy flux of the wind. In order to compare with the input energy rate (L_{tot}), I can compute the mechanical luminosity of the wind using $L_{mech} \approx \dot{M}_w \times \Delta e/\rho$, which evaluates to $\sim 10^{29}$ erg s^{-1}. Thus it is clear that the energy gained in the wind is much less than the input energy from the X-rays (2×10^{30} erg s^{-1}). For all flows (both the primordial and inner-hole flows) I explicitly calculate the gained energy flux in the wind and find that its $\ll L_{\rm X}$ ($\lesssim 8\%$). Hence, the assumption of thermal equilibrium is valid in this case and since the mass-loss rate scales linearly with X-ray luminosity and is roughly self-similar then it is valid in all cases considered.

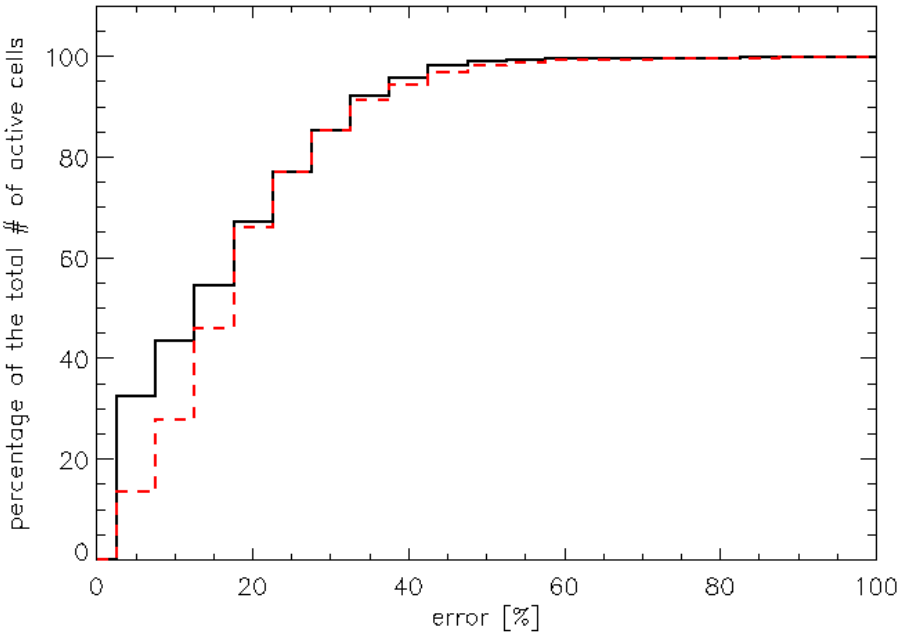

Figure 3.14: Histogram of cells with temperature errors less than a given value. Black solid line refers to errors in cells in entire grid, red dashed line to errors from cells that are locally sub-sonic (in the rotating frame).

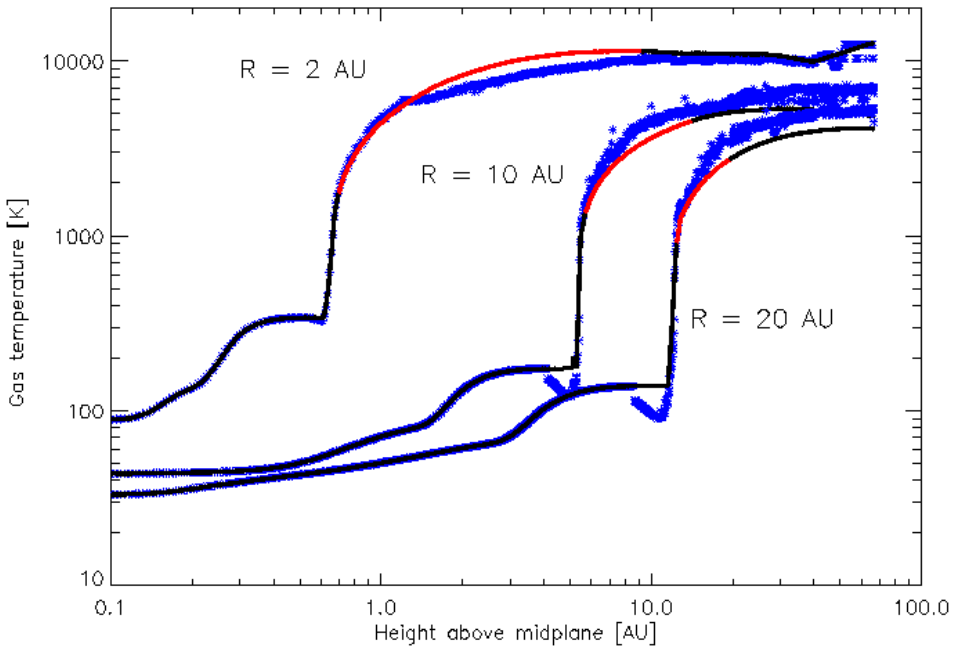

Figure 3.15: Radial cuts showing temperature comparison for R=2,10,20AU. Solid line indicates temperatures calculated by the ZEUS-2D algorithm, where the red solid line indicates where those cells are locally subsonic (in the rotating frame) and in the photoevaporative flow. Blue stars represent the temperatures determined by MOCASSIN.

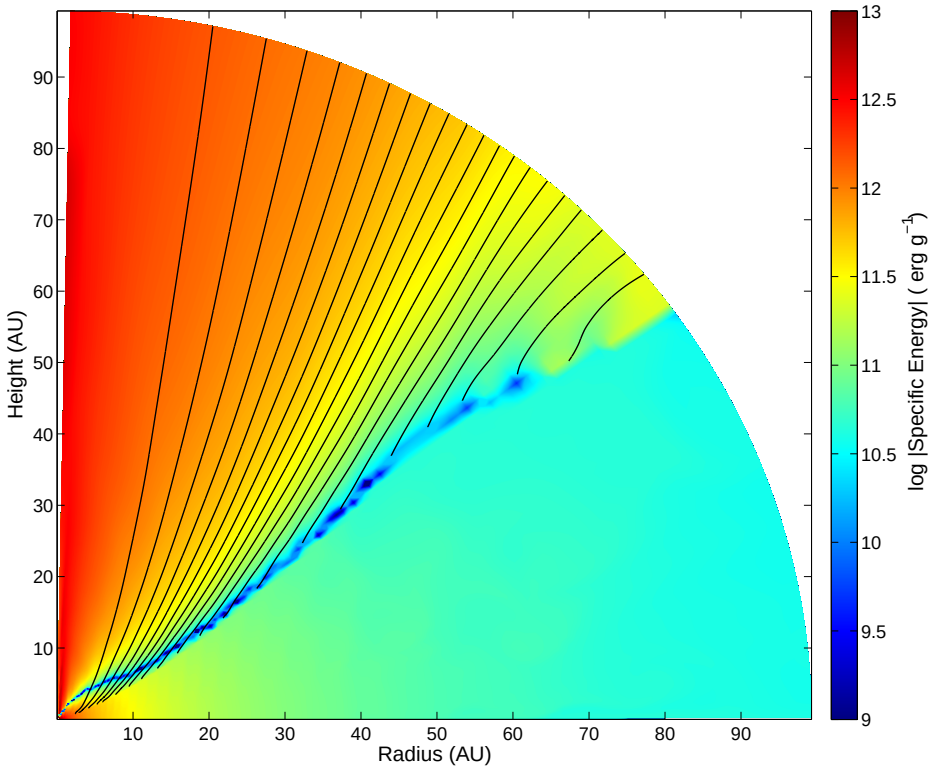

Figure 3.16: Figure showing the specific energy of gas particles throughout the grid. Streamlines are plotted at 5% of the total mass-loss rate. The dark blue lane indicates the transition between a overall negative specific energy (bound gas) and an overall positive specific energy (unbound gas). This clearly shows that the total energy gained by gas launched into the wind is less than L_X with a total efficiency $\sim 8\%$ compared to the input X-ray energy.

Physical assumptions and model tests

Based on the theoretical understanding gained in Chapter 2, I will make some further assumptions about the photoevaporation rates when I consider the disc's evolution as a function of time. Namely, that the photoevaporation rates are fixed by the X-ray luminosity rather than the evolving disc structure below, and that I can neglect the EUV and FUV radiation fields. Given the theoretical description of the flow predicts that the sonic surface controls the mass-flux, In Figure 3.17 I show the temperature at the sonic surface as a function of cylindrical radii, compared to the temperature the simple model predicts from that radius. Furthermore, I can understand why inside $1R_g$ the temperature at the sonic surface is below the expected value and above at radii greater than $1R_g$. As the maximum temperature to which the X-rays may heat the gas is $T_{\rm gas} \sim 2 \times 10^4$ K, which is below the escape temperature inside $1R_g$ the sonic surface occurs at a height of $\sim 1R_g$ irrespective of the radius it is launched from. While the simple models assume that the centrifugal force is completely negligible by the sonic surface, Figure 3.5, shows that this assumption becomes worse as the cylindrical radii increases, and explains why at radii greater than $1R_g$ the sonic temperature is slightly higher than the predicted value. However, these results indicate that the model described in Chapter 2 describes the basic physics necessary to understand X-ray photoevparotion and its scalings with physical parameters. Figure 3.18 shows the density and velocity structure of calculations for identical physical parameters but with varying disc structures, I note that all models models where I vary the disc structure, either by forcing the discs to be adiabatic or

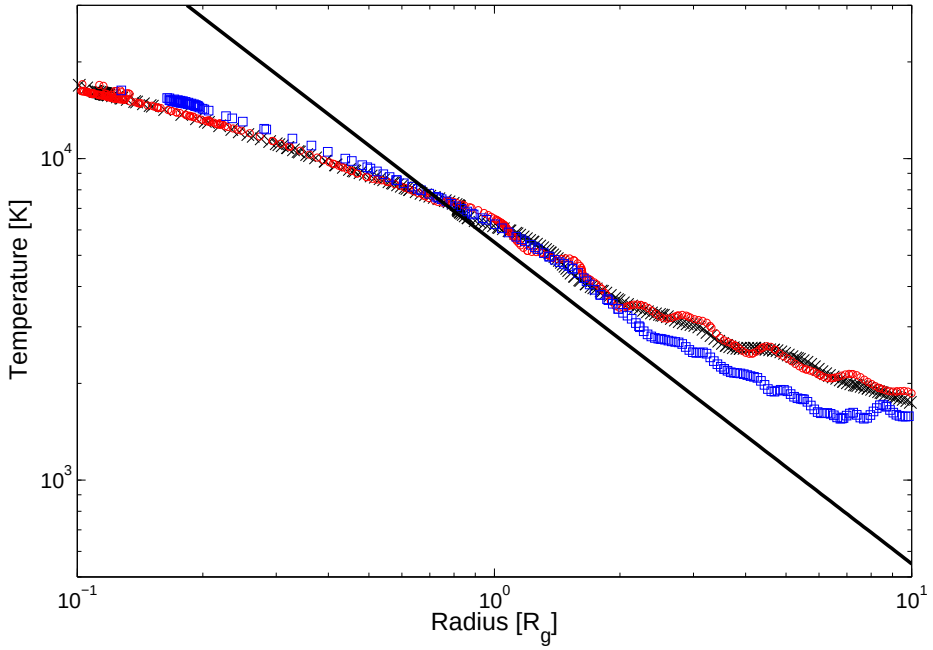

Figure 3.17: The temperature at the sonic surface as a function of cylindrical radii (scaled by R_g) for 3 models with two different stellar masses (0.1 & 0.7$M_\odot$) and X-ray luminosities of (2×10^{29} & 2×10^{30} erg s^{-1}). The open squares show the original 0.7$M_\odot$, 2×10^{30}erg s^{-1} calculated by Owen et al. (2010), the black crosses are those of the 0.1$M_\odot$, 2×10^{29}erg s^{-1} and the open circles are for the 0.7$M_\odot$, 2×10^{30}erg s^{-1} model calculated with at disc depleted in mass by a factor of 10 from the original calculation. The black line shows the temperature expected from the order of magnitude calculations performed in Chapter 2. I note all primordial disc calculations have sonic temperatures that follow the same loci.

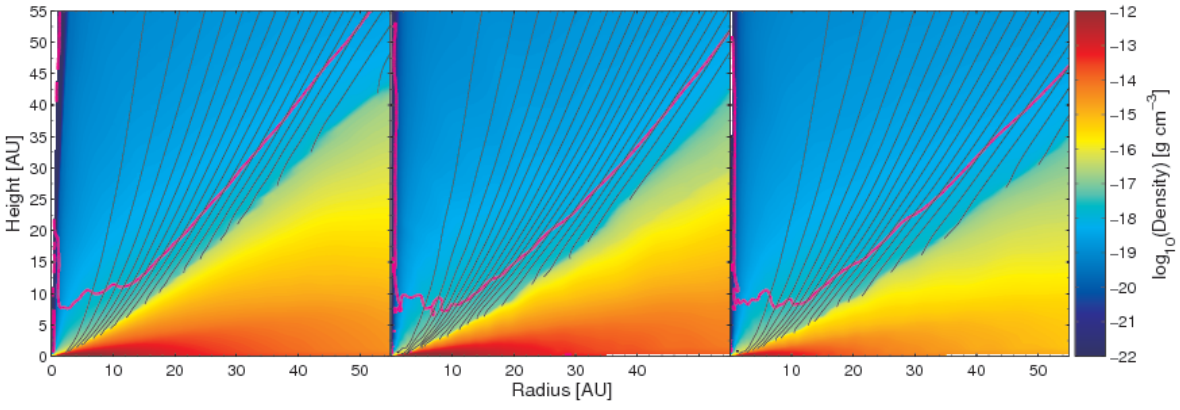

Figure 3.18: Density and velocity structure for photoevaporative winds with same stellar parameters ($M_* = 0.7M_\odot$, $L_X = 2\times10^{30}$ erg s^{-1}) but varying disc structures. From left to right: Original calculation by Owen et al. (2010); a reduction in dust temperature by $\sqrt{2}$; a reduction in the disc mass by a factor of 10. All figures shows very similar velocity and density structures in the wind.

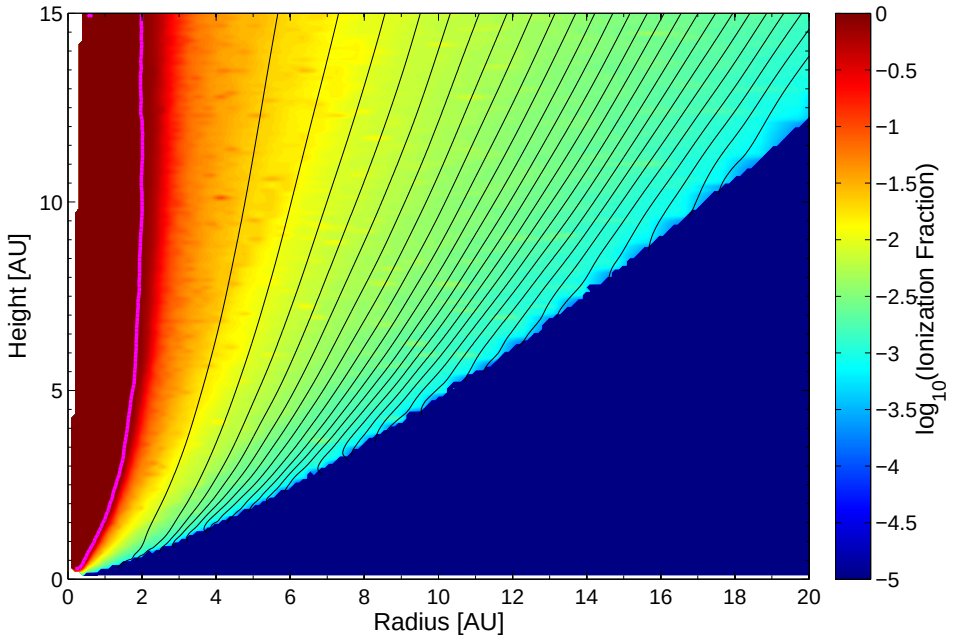

Figure 3.19: Ionization structure of the X-ray wind around a $0.7 M_{\odot}$star with an X-ray luminosity of 2×10^{30}erg s^{-1}, the streamlines are equispaced in 2% of the cumulative mass-loss rate and the magenta contour shows the region of 98% ionization fraction (i.e. roughly the penetration depth of EUV photons). This shows that an X-ray driven wind is itself entirely optically thick to EUV photons and prevent them from reaching the disc surface.

varying the D'alessio et al. disc structures used in the calculations show very similar behaviour and flow topologies. Furthermore, the total mass-loss rates and profiles are fairly invariant to dramatic changes in disc structure (including the adiabatic discs and more realistic variations) with total mass-loss rates that range between $0.9 - 1.7 \times 10^{-8} M_{\odot}$ yr^{-1}compared to the original $1.4 \times 10^{-8} M_{\odot}$ yr^{-1}for a X-ray luminosity of 2×10^{30} erg s^{-1}.

Impact of EUV radiation

As mention at the begining of this Chapter the input spectrum includes an EUV component. While the initial radiative transfer calculations indicated that it was X-ray heating that dominates at the radii important for photoevaporation, the approximation that the heating is exclusively controlled by the X-rays can be checked using radiative transfer calculations. Therefore, using MOCASSIN to determe the ionization structure will highlight regions where the EUV is important. This result is shown in Figure 3.19, which clearly indicates that the X-ray wind drives a flow that is itself optically thick to EUV photons. Therefore, if the EUV was able to reach the disc then so would the X-rays. Thus the X-ray driven flow will always prevent the EUV from driving a photoevaporative flow, and it is the X-rays that control the heating and hence mass-loss rate from the surface of a disc iradiated with an EUV and X-ray spectrum.

3.5.2 Inclusion of 'FUV' heating

Our calculations using this extra 'FUV-type' heating does not affect the mass-loss rates obtained with a value of $1.2 \times 10^{-8} M_{\odot}$ yr^{-1}for the initial calculation with the same depleted FUV extinction coefficient

as Richling & Yorke (2000), a value of $1.1 \times 10^{-8} M_{\odot}$ yr^{-1}for the calculations with the very depleted FUV extinction coefficient, and a value of $1.3 \times 10^{-8} M_{\odot}$ yr^{-1}for the mass depleted disc. In all simulations the sonic surface occurs in the X-ray heated regions and therefore confirms the simple ideas presented in Chapter 2, as well as demonstrating that the photoevaporation rates are only set by the X-ray physics alone and independent of extra FUV heating, as well as large changes in the underlying disc structure. Figure 3.20 shows the density, velocity structure the maximum FUV penetration model (i.e. the mass depeleted disc) including 'FUV-type' heating. This shows as, expected that the sonic surface occurs in the X-ray heating region, while the FUV heated flow is confined to a layer between the bound dust heated disc and the X-ray heated flow. Furthermore I find that even though the density and temperature structure of the 'FUV' heated region varies between model runs, in all cases the thermal structure of the sonic surface is as shown in Figure 3.17. Therefore, the FUV layer must be adjusting its structure in order to 'feed' the X-ray heated region with the correct mass-flux, and satisfy the hydrodynamical conditions at the sonic surface. Therefore, extra heating below the X-ray heated region has little affect on the photoevaporation rates in the range $R \sim 1 - 100 AU$.

The structure of the disc shown above does allow a possibility of driving an FUV flow at large radii. Since the height of the extra heated region increase with radius, I cannot rule out a thermally driven flow through this 'wedge' below the X-ray heated region. Such a flow could then escape at large radius, and undergo its sonic transition when the temperature of the X-ray and FUV heated region become comparable. While this will have no effect on the X-ray heated flow and hence photoevaporation rates from this region, simple estimates based on the column of FUV heated gas at $R \sim 100$ suggest mass-loss fluxes through this wedge of $\sim 10^{-8} M_{\odot}$ yr^{-1}are sustainable. While the simulations show no 'wedge' flow at small radius, gas does leave the grid sub-sonically in the FUV heated region. Due to the use of outflow boundary conditions on this grid boundary, it is impossible to tell if this flow is real or an artefact of outflow boundary conditions (which are only exact for super-sonic flow). Therefore, further conjecture on the role or possibility of these FUV 'wedge' flows is not possible without a more detailed investigation.

3.6 Discussion

As described below, in order to make these calculations feasible I have needed to make a series of simplifications. In the previous section I described in detail the tests performed in order to ensure the the model described in Chapter 2 provided an accurate description of the underlying physics of the problem, as well as ascertaining the accuracy to which I may trust the numerical results presented in this calculations. These test have shown that model provides an accurate description of the physics of photoevaporation, namely that the sonic surface occurs in the X-ray heated region and that the X-ray physics determines the mass-flux through the sonic surface. Therefore, variations in disc structure and inclusion of extra heating mechanisms should not affect the mass-loss rates to first order and this is indeed what is found. Dramatic variations in disc structure only resulted in a maximum variation of $\sim 35\%$ in the mass-loss rates. Furthermore, I have shown that the numerical simplifications do not effect the derived mass-loss rates and are confident that the results are accurate enough (i.e. error in the mass-loss for an individual X-ray luminosity is much less than the expected spread in mass-loss rates for the entire X-ray luminosity range) for the study disc evolution and I can proceed with freedom in following

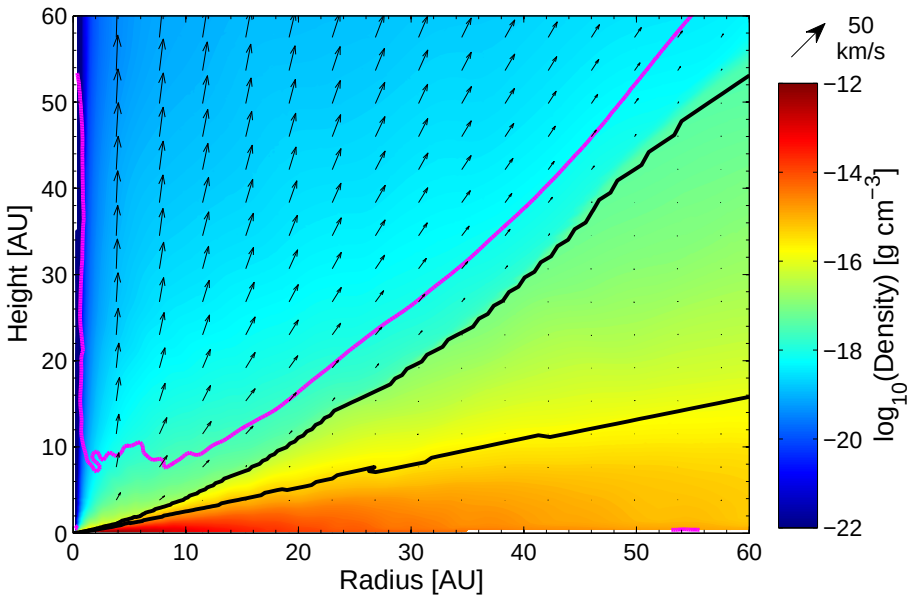

Figure 3.20: Velocity and Density structures of winds including an extra 'FUV' like heating mechanism, the arrows show the velocity in the wind and the black lines show regions where the extra heating mechanism is dominating over the X-rays and dust and the majenta contour shows the sonic surface. The model shown is the depleted disc with the extremely low FUV extinction allowing for maximum penetration of the underlying disc.

the evolution of discs undergoing photoevaporation.

3.6.1 Final Clearing of the Disc

Figure 3.10 shows the evolution of the 'quasi steady-state' simulation with time, during the first 300years of evolution the photoevaporative flow slowly strips of gas from the inner edge of the disc (I note again that as there is no viscosity in the disc, so that the inner disc region is not resupplied with material, and the erosion time-scale is quicker than would be expected from a viscous disc model).

Since the inner streamline topology for inner hole flows is fixed, there is no requirement that the total column density along the mid-plane to the bound disc is 10^{22} cm^{-2}, in fact the column in the flow scales as $R_{\rm hole}^{-1}$ and is always much less than 10^{22} cm^{-2}. Therefore, the X-ray absorbing column is a warm, bound X-ray heated layer (typically at $T \sim 200-400$K) behind the flow, separated by an entropy discontinuity (which can be thought of as a contact discontinuity) and can be identified in all the simulations with inner holes in the disc. However, in the case of simulations around the $0.1M_{\odot}$ star this region eventually dominates the dynamics. In these simulations, as the hole grows the layer of warm bound X-ray heated gas grows in radial thickenss, Δ. Once the hole size grows to $R_{\rm hole} \sim 10$AU, this region becomes large enough that it can push the remaining disc out to large radii, and is completely cleared on the dynamical time-scale ($\sim$100 years at 10AU). This was not seen in the simulations calculated for the $0.7M_{\odot}$ star; the reason for this is since the disc has a lower mass and lower temperature for the low mass case, the pressure in the disc's mid-plane is considerably lower than the higher mass case. Thus the density in the warm bound region is correspondingly lower, meaning that the warm bound region needs a larger Δ in order to maintain a column density of 10^{22} cm^{-2}.

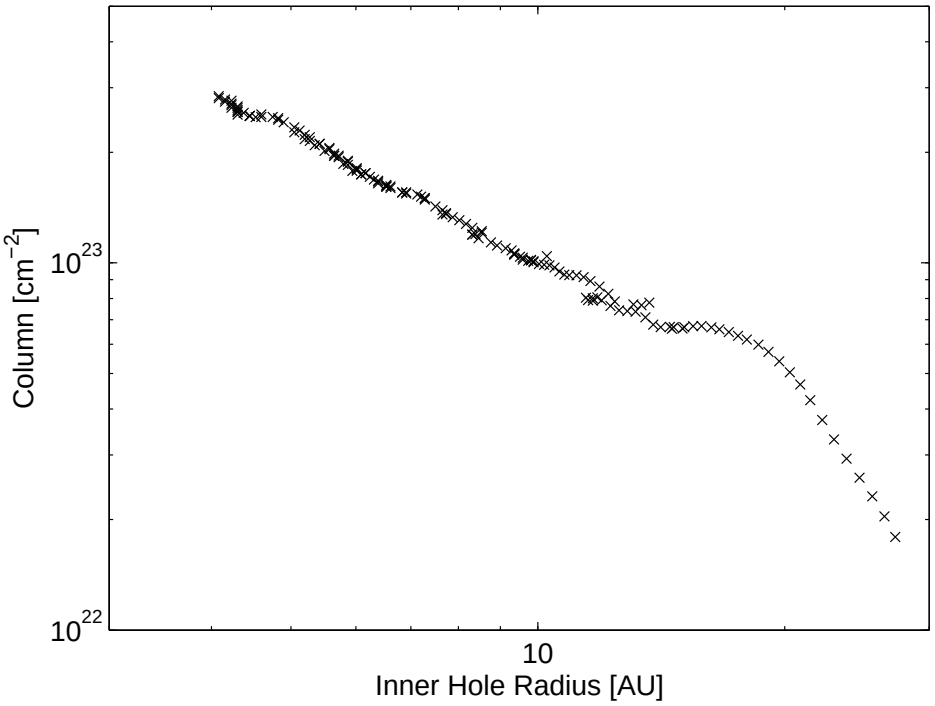

Figure 3.21: Column density from the central star to the edge of the grid along the disc's mid-plane, as a function of radius to the X-ray 'dark' disc.

For the disc to become dynamically unstable and be pushed out by this warm, bound X-ray heated region, we simply require that the radial pressure gradient in this region grows to become similar in size to gravity (i.e. $\nabla P/\rho \sim GM_*/R^2$), which is simply stating $H_R \sim R$ where H_R is the radial pressure scale length of the X-ray heated disc. This is a necessary, but not sufficient condition as the pressure gradient in this X-ray bound region will be large whatever its size. When this X-ray warm, bound region is small it must be in dynamical balance with the photoevaporative flow and the dust heated disc. The time-scale on which it can obtain this equilibrium is the sound crossing time of the region $t_{\rm sc} \approx \Delta/c_s$. When $\Delta/H \ll 1$, this region can adjust to dynamical equilibrium quickly and the disc/flow system is stable, even though the pressure in the region is significant. However, at the point when $\Delta \sim H$ this region cannot rapidly obtain dynamical equilibrium. Therefore, this region will expand vertically on the same time-scale. This vertical expansion can clearly be seen in the time series plots, and as it expand the mid-plane density drops resulting in higher temperatures. Once, the temperature of the mid-plane is increasing on the same time-scale as this expansion a runway process will occur. As the disc cannot adjust rapidly to the increasing mid-pane temperature and will continue to expand, and increase its temperature further. Eventually, a high pressure region develops at the edge of the dust heated disc that pushes the remaining disc material away rapidly on the dynamical time-scale. The fact we have seen this process only in a couple of simulations, with the same initial disc structure, mass, but different X-ray luminosities does not allow us to generalise the situation to all masses and disc structures. However, plotting the column from the central star to the edge of the simulation grid (which will be identical to the column to infinity, since the disc's column in dominated at small radii), shown in Figure 3.21 is instructive. This shows the disc transitions from slow photoevaporative erosion, to rapid hydrodynamical clearing at a total column of $N \sim 10^{23}$ cm^{-2}, ten times larger than the penetration depth of the X-rays, this is indicative that this

processes relates to the fraction of the disc penetrated by the X-rays. Since all the $0.7M_{\odot}$ disc possess high mid-plane pressures $\Delta < H$ in all cases, and there is no evidence of this process beginning in any simulations. Furthermore, the simulations which differ by an order of magnitude in X-ray luminosity show the same processes of clearing at the same time-scales, indicating that the process may be directly insensitive to X-ray luminosity.

It is worth mentioning that while the simulations have allowed us to gain a macroscopic understanding of this process, because the simulations were designed to study the photoevaporative process (which occurs in optically thin X-ray heated gas) whereas this process occurs in the gas that is transitioning from the optically thick to thin regime, a column cut-off will not accurately reproduce the thermal structure of this region. Furthermore, as the gas is considerably cooler (hundreds to thousands rather than thousands to tens of thousands K as in the photoevaporation calculations) I cannot neglect the affect molecular cooling will have, along with the added affect of FUV heating (which may or may-not be important depending on the dust properties at the mid-plane of the disc at large radii). A disc with dust that is ISM like at the mid-plane will be heated by X-rays first; however, if the dust is significantly depleted this process may begin earlier than the X-ray alone calculations predict as the FUV may penetrate larger columns of dust depleted gas than the X-rays. Furthermore, the heated regions appear to be unstable to large scale convective modes and therefore, full 3D calculations that include X-ray and FUV radiation along with dust evolution would be required to accurate study the evolution of such a process and are certainly beyond the scope of this work.

3.6.2 Comparison with previous work

Solutions to the photoevaporative flow problem have evolved over the years and while this work has shown that it is predominately driven by the X-rays, it is worth discussing the differences between the new solutions presented in this work and the previous calculations. Either with pure EUV or X-ray radiation, or with Ercolano et al. (2009b) who considered the combined effect of X-EUV radiation. The predicted mass loss rates due to pure EUV photoevaporation have been accurately determined as $1.1 \times 10^{-10} M_{\odot} yr^{-1}$ (Font et al. 2004) for a $0.7M_{\odot}$ star and an ionizing flux of $10^{41} s^{-1}$. Also Alexander et al. (2006a) found that when the inner hole first forms, the mass loss rate rises by about a factor ten and then increases mildly as the hole grows according to $R_{\rm hole}^{1/2}$.

As discussed in Chapter 1, previous estimates of X-ray photoevaporation rates to be found in the literature are qualitatively different from the values presented in the present work since they are not based on hydrodynamic calculations. Alexander et al. (2004) estimated mass-loss rates per unit area at ~ 20 AU which were similar to those obtained in this work. Ercolano et al. (2009b) argued for similar surface mass-loss rates as those of Alexander et al. (2004), but estimated a much larger launching regions (i.e.over a region 5-50AU). They therefore concluded that X-ray photoevaporation would dominate over EUV photoevaporation at all but the lowest of X-ray luminosities. The estimates of Gorti et al. (2009) suggested much lower mass loss rates than the EUV case, implying that X-rays would only have an indirect effect on disc dispersal. However, as discussed in Chapter 1 this result is a consequence of the rather unusual and certainly unphysical method for estimated photoevaporative mass-loss rates.

The mass loss rate of $1.4 \times 10^{-8} M_{\odot} yr^{-1}$ that I obtain from our radiation hydrodynamical calculations can be compared to the estimate of Ercolano et al. (2009b) for the same input parameters

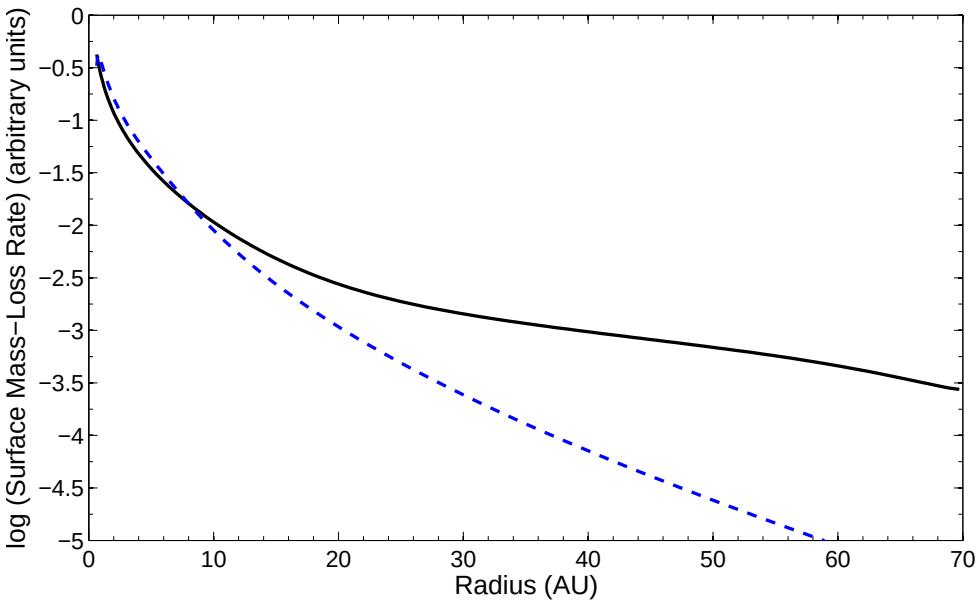

Figure 3.22: The surface mass-loss rate for the X-EUV wind (solid black line) obtained in this work compared to the EUV wind (dashed blue line) (Font et al. 2004). I have scaled the peaks of the profile to be the same value in order to compare the relative broadness of the different profiles. Clearly this shows the X-EUV profile is much broader than the EUV profile.

(model FS0H2Lx1 of ECD09) of 6.7×10^{-9} $M_{\odot}yr^{-1}$ and the theoretical prediction in Chapter 2 of $8 \times 10^{-9}M_{\odot}$ yr^{-1}. This difference arises from the fact that Ercolano et al. (2009b) assumed that the gas escaped at the sound speed at the point at which the internal energy of the gas was equivalent to the escape potential. It is nevertheless reassuring that these values are of a similar order of magnitude. I also find that the mass-loss occurs over a large radial range of 1-70AU, in contrast to the EUV case where it is steeply peaked about one characteristic radius (for a $0.7M_{\odot}$ star this would be 6.2AU). Given the mass loss rates obtained and the monotonic temperature-ionization parameter relations found (see Figure 3.2), it is clear in this case that X-ray photoevaporation will be a dominant effect in disc evolution.

3.7 Conclusion

In this Chapter I have performed detailed radiation-hydrodynamic calculations, in order to determine accurate photoevaporative mass-loss profiles and rates, along with testing the physical model presented in Chapter 2. I have found that as described in Chapter 2 it is the sonic surface in the X-ray heated region and the theory presented in Chapter 2 provides an accurate picture for understanding the underlying physics involved in photoevaporation from discs around young stars. The main findings of this Chapter are:

1. The algorithm described in this Chapter provides an accurate and computationally feasible method for including X-ray heating of protoplanetary discs in a hydrodynamic scheme.

2. The derived mass-loss rates scale approximately linearly with X-ray luminosity and are independent of the mass of the central star.

3. The mass-loss rates are insensitive to changes in disc structure and the inclusion of extra 'FUV' type heating as well as EUV and X-ray radiation fields and it is the X-ray properties at the sonic surface alone that to first order determine the mass-loss rates.

4. The mass-loss profiles from primordial discs are very broad, including mass-loss over a large radial range $0.1 - 10R_g$, much broader than the previous EUV only calculations.

5. The mass-loss rates from discs with inner holes are approximately independent of inner hole size and mass and scale linearly with X-ray luminosity.

6. Once the radial pressure scale height of a disc with an inner hole becomes optically thin to X-ray irradiation the disc becomes dynamically unstable and is rapidly swept from inside out to large radius by the thermal pressure gradient resulting from the X-ray heating inner rim of the disc.

   In this and the previous Chapter I have set out the underlying physics of photoevaporation from discs exposed to high energy radiation that includes X-rays, alone with performing accurate numerical calculations that have determined the mass-loss profiles as well as total mass-loss rates. I have confirmed that these are insensitive to the changes in disc structure that will occur during the Myrs of disc evolution and therefore are ready to proceed to calculations of disc evolution that include photoevaporation in the next Chapter.

4

Protoplanetary disc evolution and dispersal

IT is now time to turn our attention to the evolution of protoplanetary discs, which are undergoing the dual action of viscosity and photoevaporation. As I have argued throughout Chapters 2 & 3, the photoevaporative mass-loss from a primordial disc will be approximately independent of the current disc structure, and set by the X-rays. Therefore, I use the mass-loss profiles derived from the numerical calculations of X-ray photoevaporation described in the previous Chapter. In the introduction, I argued that viscous evolution coupled with photoevaporation was one of the currently preferred ideas for the destruction of protoplanetary discs, at its most basic level reproducing the two-time-scale phenomenology and concept of inside out clearing indicated by observations of 'transition' discs. In this work, I have been able to characterise the mass-loss from discs in the full range of parameter space observed. Therefore, a natural question arises: is photoevaporation the dominant mechanism for disc destruction?

This is the question I set out to discuss in this Chapter. To do this I will follow the evolution of a synthetic population of evolving discs, which can then be compared to the observations. Even though the theory of photoevaporation can be extended to all masses, at the current time the observations of disc evolution at lower masses are not complete enough to make a good comparison at this stage, and there is still much debate as to their interpretation (see Ercolano et al. 2011a,b and Currie & Sicilia-Aguilar 2011, for contrasting views). Therefore, I shall restrict the discussion to those observations which are best understood, i.e. solar type stars (using observations in the range 0.5-1.0$M_\odot$ to give a roughly even spread about the 0.7$M_\odot$ photoevaporation models calculated earlier), and only discuss observations from this range of stellar mass.

4.1 X-ray Luminosity Function

As described previously, the X-ray luminosity (L_X), is the crucial input for the photoevaporation model, where I take the X-ray luminosity to span the range $0.1 - 10$keV. Since the choice of L_X fully describes

the mass-loss rate due to photoevaporation in a given system, we must describe how the X-ray luminosity of stars varies within a population of young stars.

It has been known for some time that there is a large scatter in the X-ray luminosity of T Tauri stars for a given stellar mass (and bolometric luminosity). While there have been no long term studies into X-ray variability around young stars, they are known to 'flare' both as CTTS (Feigelson & DeCampi 1981) and WTTS (Walter & Kuhi 1984); however, the activity-rotation relationship is similar to other active stars indicating that the scatter is intrinsic rather than solely arising from variability (Güdel et al. 2004). Therefore, I have used the data for the Taurus cluster (Güdel et al. 2007) and the Orion Nebular cluster (Preibisch et al. 2005) to build cumulative X-ray luminosity functions[1] (XLFs) for all pre-main sequence stars (including both CTTs and WTTs) in the 0.5 to 1 $M_{\odot}$ range. The data for these two regions shows good agreement at low luminosity, but they differ at high luminosities, in the sense that the Orion data contains a higher fraction of sources with high L_X. The difference is most probably *not* intrinsic to the X-ray properties of these two regions, but due to the different treatment of strong flares in the two samples. Strong flares were excluded in the Taurus data, in contrast to the Orion sample where luminosities were averaged over the whole observational period. Strong flares are relatively rare (although not sufficient to account for the different luminosity functions), and Albacete Colombo et al. (2007) found that non-flaring sources have a median $k_bT = 2.1 \pm 0.3$KeV, compared to flaring sources with $k_bT = 3.8$KeV. Therefore, due to their higher X-ray temperature flares tend to emit most of their radiation in the hard X-ray region (as shown by observations of objects in a 'flare' state compared to in a 'quiescent' state, e.g. Imanishi et al. 2001), where the thermal impact is low. For this reason, the Taurus sample is the most appropriate for use in the photoevaporation model, since it should provide a better approximation of the quiescent, and therefore softer X-ray luminosity. Therefore, I adopt the Taurus XLF for the use in the population synthesis model. I assume that the X-ray luminosity function remains invariant throughout the stars' pre-main sequence evolution. While it is known that the median of the stellar X-ray luminosity function does in fact decrease with age due to stellar spin down (e.g. Hemplemann et al. 1995; Güdel et al. 1997; Güdel 2004), the evolution of the X-ray luminosity during the disc dispersal phase is much smaller (Güdel 2004) and a recent study of the evolution of X-ray luminosity as a function of time (Ingelby et al. 2011) concluded that there was no evidence for a decrease in X-ray luminosity for the first 10Myr. Certainly, any evolution of the X-ray luminosity for ages up to several tens of Myrs is smaller than the observed spread in X-ray luminosities at $\sim$ 1Myr. Furthermore, there is observational evidence that the X-ray luminosities of CTTs and WTTs are systematically different, with WTTs in general being more luminous than CTTs (e.g. Neuhauser et al 1995; Stelzer & Neuhauser 2001; Flaccomio et al. 2003; Preibisch et al. 2005). This has lead to a discussion of X-ray emission being 'disturbed' by accretion, in terms of either X-ray absorption in accretion columns (Gregory et al. 2007) or confinement of the X-ray producing corona in accreting systems (Preibisch et al. 2005). As discussed in the introduction, Drake et al. (2009) suggested that X-rays may modulate accretion through photoevaporation (something they called 'photoevaporation starved accretion'). Such a scenario may be able to account for the difference in the observed X-ray luminosities of CTTs and WTTs since more luminous stars will lose their discs first, and is something I will aim to test within the framework of this population synthesis model. Therefore, in order to assess the effect of 'photoevaporation starved accretion' in explaining the X-ray observations I

[1]Where the X-ray luminosity is taken to be in the range 0.3-10keV for the Taurus sample and 0.5-8keV for the Orion sample, consistent with my definition which includes both the 'soft' and 'hard' component.

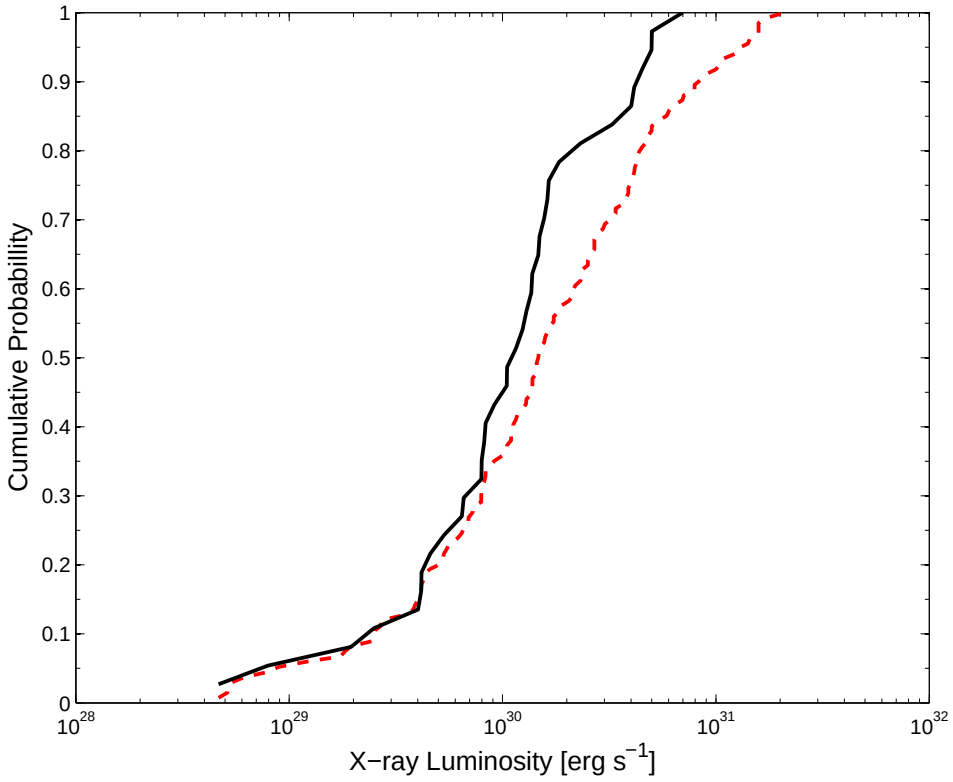

Figure 4.1: Cumulative X-ray luminosity functions for the Taurus (black solid line) and Orion (red dashed line) clusters for solar type stars with mass in the range [0.5,1.0] $M_{\odot}$, including both WTTs and CTTs.

adopt the null stance: the X-ray luminosity of an individual young stellar object (YSO) remains constant in time as individual disc models evolve from CTTs to WTTs.

4.2 Photoevaporating Viscous Discs

As shown in the introduction, the evolution of the surface density of a photoevaporating and viscously evolving disc can be described in one dimension, using the formalism of Lynden-Bell & Pringle (1974):

$$\frac{\partial \Sigma}{\partial t} = \frac{3}{R}\frac{\partial}{\partial R}\left[R^{1/2}\frac{\partial}{\partial R}\left(\Sigma \nu(R) R^{1/2}\right)\right] - \dot{\Sigma}_w(R,t) \tag{4.1}$$

where ν(R) describes the viscosity term and $\dot{\Sigma}_w(R,t)$ represents the mass-loss due to photoevaporation calculated by differentiating a functional fit[2] to the cumulative mass-loss profile, shown as the black line in Figure 3.6. In the introduction I argued that the combination of viscous evolution (first term on the RHS of Equation 4.1) and photoevaporation (second term on the RHS of Equation 4.1) naturally reproduces a two time-scale clearing, with clearing beginning when the accretion rate through the disc becomes comparable to the mass-loss rate due to photoevaporation. While much of this thesis has been dedicated to the detailed evaluation and understanding of the photoevaporation term $\dot{\Sigma}_w$, little attention has been paid to the magnitude of the viscosity term. The magnitude, scaling, and in some regions of the disc perhaps even the origin of the viscosity is still poorly understood. At first sights it might seem

[2]The form of the fits is shown in Appendix A

like we are doomed to fail, since without this theoretical understanding how can we proceed? However, since photoevaporation has little effect on disc evolution when the mass-loss rate is below the accretion rate, the disc's evolution is entirely controlled by the viscosity. Thus as we shall see below, if we restrict ourselves to a single mass it is possible to use the current observations to construct a model *dependent* description of the viscosity, which I can use to follow the evolution of the disc population.

4.2.1 Viscosity Law and Initial Conditions

In order to proceed in determining the magnitude of the viscosity I must first make some observationally and theoretically motivated assumptions. As mention above, during the majority of the disc's evolution we can consider the effects of photoevaporation to be negligible. Hartmann et al. (1998) showed that the observations of the accretion rate as a function of time were consistent with a viscosity law that scaled linearly with radius, i.e. $\nu \propto R$. Therefore, currently a simple power law description is the best we can do for the viscosity law, and as discussed in the introduction, observations indicate I should adopt a viscosity law of the form $\nu = \nu_0 R$, where $\nu_0 = \alpha c_s^2/\Omega$, where I always evaluate α at 1AU. Furthermore, I adopt the zero-time similarity solution of Lynden-Bell & Pringle (1974), for which the initial surface density distribution takes the form:

$$\Sigma(R,0) = \frac{M_d(0)}{2\pi R R_1}\exp(-R/R_1) \tag{4.2}$$

These initial conditions, together with the viscosity parameter α and the X-ray luminosity fully determine the evolution of the disc through Equation 4.1.

In order to determine a model dependant viscosity parameter it is necessary to construct a 'null model' of viscous evolution without photoevaporation, that when combined with the observed X-ray luminosity function can explain the observed decline in disc fractions with age. In effect I am asking whether there is a universal set of disc parameters which can explain the variation in disc lifetime from cluster to cluster, purely in terms of the observed spread in X-ray luminosity. As discussed above, the basic principle of all photoevaporation models is that discs should evolve viscously, hardly noticing the effects of photoevaporation, until the mass accretion rates in the discs have fallen to a value that is comparable to the photoevaporation rate, at which point the remaining disc material is rapidly cleared.

Viscous evolution alone with $\nu \propto R$ predicts that accretion rates evolve as:

$$\dot{M}_*(t) = \dot{M}_*(0)\left(1+\frac{t}{t_\nu}\right)^{-3/2} \tag{4.3}$$

where t_ν is the viscous time-scale at R_1. This evolution should therefore be observed in discs before photoevaporation sets in. We can equate the fraction of disc-bearing pre-main sequence stars at a given time (f_d), with the fraction of stars in the X-ray luminosity function that have luminosities less than a cut-off X-ray luminosity $L_c(f_d)$. In order for objects with X-ray luminosities equal to L_c to be about to lose their discs, the viscous accretion rate must be equal to $\dot{M}_w(L_c)$ at this point. Therefore, for each cluster shown in Figure 4.3 (the sample compiled by Mamajek 2009), this method determines the lowest possible accretion rate a star can have without loosing its disc by photoevaporation (at that time). Or for a single set of initial conditions this method will extract the accretion evolution of a star that is evolving under the action of viscous evolution alone, with no photoevaporation i.e. the 'null' model allowing the determination of the viscous initial conditions. The result is shown in Figure 4.2, where

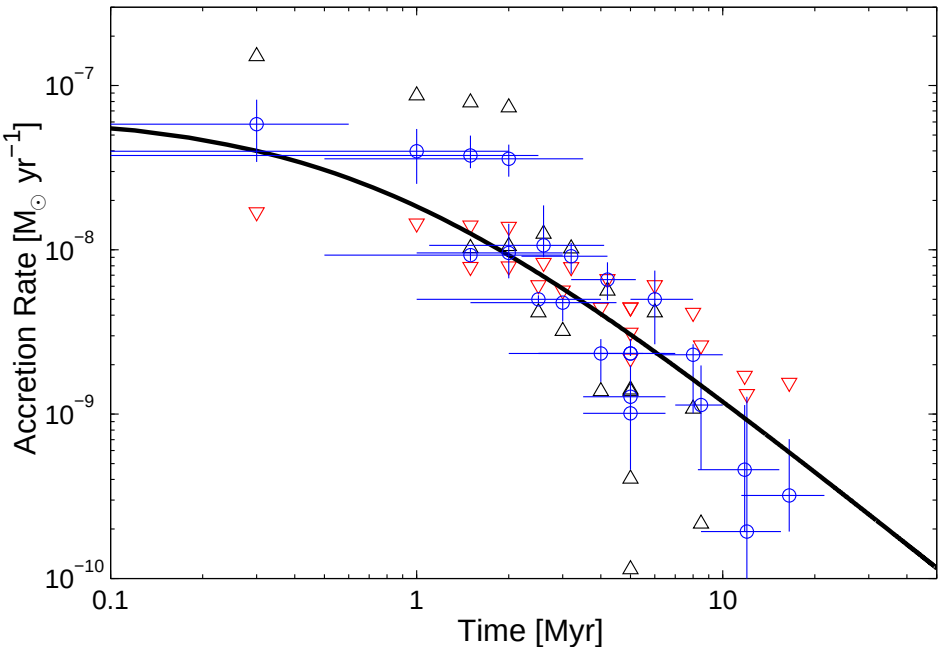

Figure 4.2: Accretion rates as a function of time for the 'null' disc model shown as the blue open circles. The errors in accretion rate are estimated from the $\sqrt{N}$ errors in the disc fractions. The solid line shows a fit of Equation 4.3 used to determine suitable values of $M_d(0)$ and t_ν. The triangles show the results for a X-ray luminosity function with a spread about the median 5 times larger (black 'up') and 5 times smaller (red 'down') than observed.

each point represents the current accretion rate cut-off in a cluster implied by X-ray photoevaporation. The results for the disc fractions are scaled assuming an initial close binary fraction of 14% (consistent with the observational value of 10-20% Kraus et al. 2009), by considering that the 0.3Myr old cluster NGC 2024 (Haisch et al. 2001a), which shows a disc fraction of 86%, is too young for any disc to have been destroyed by photoevaporation or planet formation (e.g. Alexander & Armitage, 2009), but only through binary interactions. The solid line in the plot represents a suitable fit of Equation 4.3 to the data, from this fit we can extract an initial accretion rate of $\dot{M}_*(0) = 5 \times 10^{-8} \mathrm{M}_\odot\ \mathrm{yr}^{-1}$and a viscous time of $t_\nu = 7 \times 10^5 \mathrm{yr}$. From these two values we can calculate an initial disc mass of $M_d(0) = 0.07 \mathrm{M}_\odot$, which is similar to the canonical value (10% of the stellar mass) at which viscous angular momentum transport takes over from self-gravity.

Along with giving us appropriate initial conditions for our disc population model, the above also provides a stringent test of the hypothesis that X-rays are key to disc evolution and dispersal. If the X-rays were not the dominant dispersal mechanism, there is no a priori reason to expect a 'null' model (constructed only using knowledge of the X-ray luminosity function and observed disc fractions) to reproduce a plausible evolution of the accretion rates seen in CTTs, both in terms of the time exponent (in Equation 4.3) and its initial value. In fact, increasing or decreasing the spread about the median of the Taurus X-ray luminosity function by a factor of $\sim$5 or greater makes a fit of Equation 4.3 to the 'null' model difficult, as shown in Figure 4.2. Although this agreement could be fortuitous, it is reassuring that the X-ray luminosity function, disc lifetimes and accretion histories are consistent with the hypothesis.

Furthermore, in order to uniquely specify the viscous evolution we must pick suitable values of α

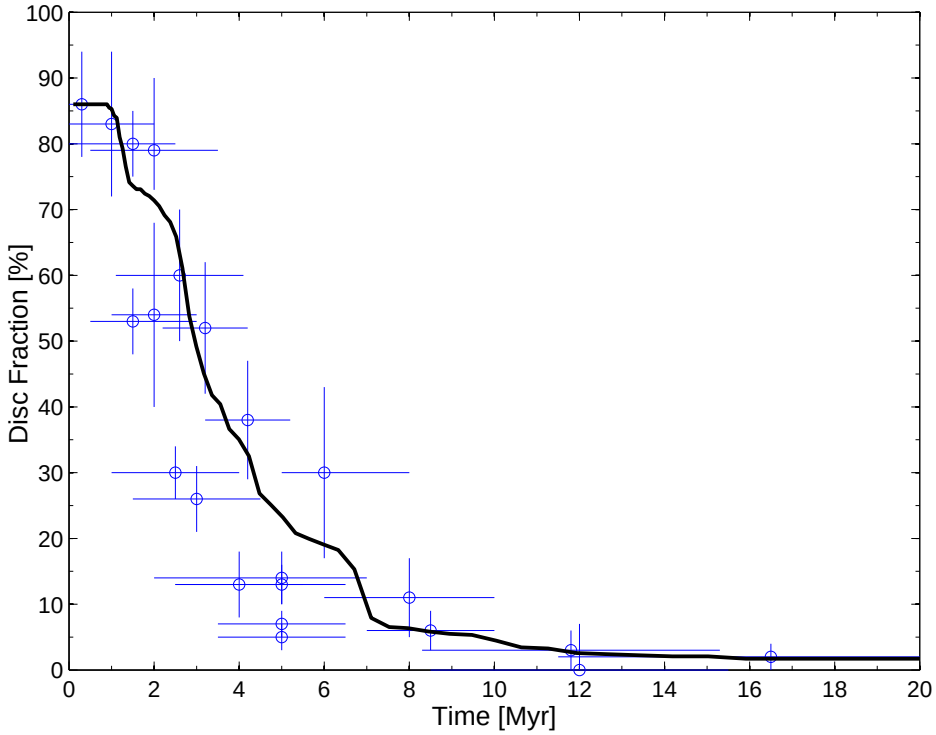

Figure 4.3: Primordial disc fraction as a function of time (solid black line) from our XPE population calculated using 500 disc models with the mass-loss rate determined by randomly sampling the Taurus X-ray luminosity function, all discs evolve from a single set of initial conditions. The points are observed disc fractions compiled by Mamajek (2009). Model disc fractions have been scaled to account for disc destruction by close binary interaction. Note that the structure of the black line reflects the structure in the X-ray luminosity function.

and R_1, which in turn specifies ν_0. While any combination of R_1 and α that give the required viscous time will reproduce the same 'null' viscous model (i.e. non-photoevaporating), a disc evolution model that includes photoevaporation mildly breaks this degeneracy. By performing a fit (by eye) of a viscously evolving photoevaporating disc population to the disc fractions used to derive the 'null' model I obtain values of $\alpha = 2.5 \times 10^{-3}$ and $R_1 = 18$AU, although due to the large scatter in the disc fractions and only mild breaking of the α, R_1 degeneracy, errors on these values are estimated to be around a factor of 2-3. Figure 4.3 shows the result of this exercise compared to the disc fractions compiled by Mamajek (2009), where the synthetic disc population used the single set of initial conditions: $M_d(0) = 0.07\mathrm{M}_\odot$, $\alpha = 2.5 \times 10^{-3}$ and $R_1 = 18$AU, and shows excellent agreement with the observations.

4.3 A population of viscously evolving, photoevaporating discs

I have used initial conditions derived in the previous section to construct a population synthesis model for the evolution of discs dominated by viscosity and photoevaporation. In order to produce a population with sufficient statistical accuracy to compare to observations, I calculate the evolution of 500 discs, where the X-ray luminosity is the only variable between each model, which is determined by a random sampling of the Taurus X-ray luminosity function.

Computing the disc's evolution

Since Equation 4.1 is a linear inhomogeneous diffusion equation, it is in principle easy to construct an analytic solution to the problem using a Green's function method. Such an approach involves indefinite integrals of uncommon transcendental functions (which would need to evaluated numerically), and is therefore much more uninstructive than would first be imagined. As such, it is much simpler to just solve Equation 4.1 numerically from the outset, a method adopted by Clarke et al. (2001) and Alexander et al. (2006b). I integrate the diffusion equation forward in time using a standard first order explicit scheme, on a grid uniformly spaced in $R^{1/2}$, with 1000 grid cells in the range [0.0025,2500] AU, sufficient to resolve the disc's evolution (e.g. Alexander et al. 2006b). In order to ensure strict flux conservation, I use central differencing where fluxes are evaluated on cell boundaries and scalars are evaluated at cell centres. I use zero torque boundary conditions (i.e. set $\Sigma = 0$ in the boundary cells), and in order to ensure numerical stability in time, I use a time-step of:

$$\Delta t = \min\left[\left(\frac{1}{4}\right)\frac{R\Delta R}{3\nu}\right] \tag{4.4}$$

which is half the time-step formally required for stability (von-Neuman time-step). Furthermore, since the addition of the photoevaporative sink term can, in practice, allow the numerical solution to become negative, I use a numerical base surface density of $\Sigma = 1 \times 10^{-20}$ g cm^{-2}. The numerical fits to the photoevaporation profiles are shown in Chapeter 3 and I switch between the primordial and inner-hole profile after the gap has opened and the mid-plane column of the inner disc reaches a level lower than 10^{22} cm^{-2}.

I use this method to follow the evolution of each disc. The evolution of the surface density for the median model (model with median L_X) is shown in Figure 4.4. All discs show qualitatively similar behaviour to this disc. The disc evolves unaffected by photoevaporation for the majority of its life. However, when photoevaporation becomes important it begins to flatten the surface density in the region of $R \sim 10$AU indicating photoevaporation is starving the inner disc of material. Once the accretion rate is no longer capable of sustaining a flow all the way to the star, a gap rapidly forms. While the inner disc drains, the inner edge of the outer disc is slowly eroded to larger and larger radii. Once the inner disc has entirely drained the outer disc is exposed to direct photoevaporation and eroded to larger and larger radii.

4.4 Results and Discussion

As mentioned above the qualitative evolution of all discs is identical: viscous evolution followed by gap opening and inner disc draining, then outer disc clearing. While this phenomenological aim was the basis of constructing the photoevaporation model, the calculation of a population synthesis allows much more direct comparison with disc evolution indicators. In the previous section I showed conclusively that the spread in X-ray luminosities (and hence photoevaporation rates) was sufficient to explain the spread in disc lifetimes, without the need for large variations in initial conditions.

One of the other arguments for a spread in initial conditions is the spread in accretion rates seen for a given age (e.g. Hartmann et al. 1998). In Figure 4.5 we show the predicted evolution of accretion rate

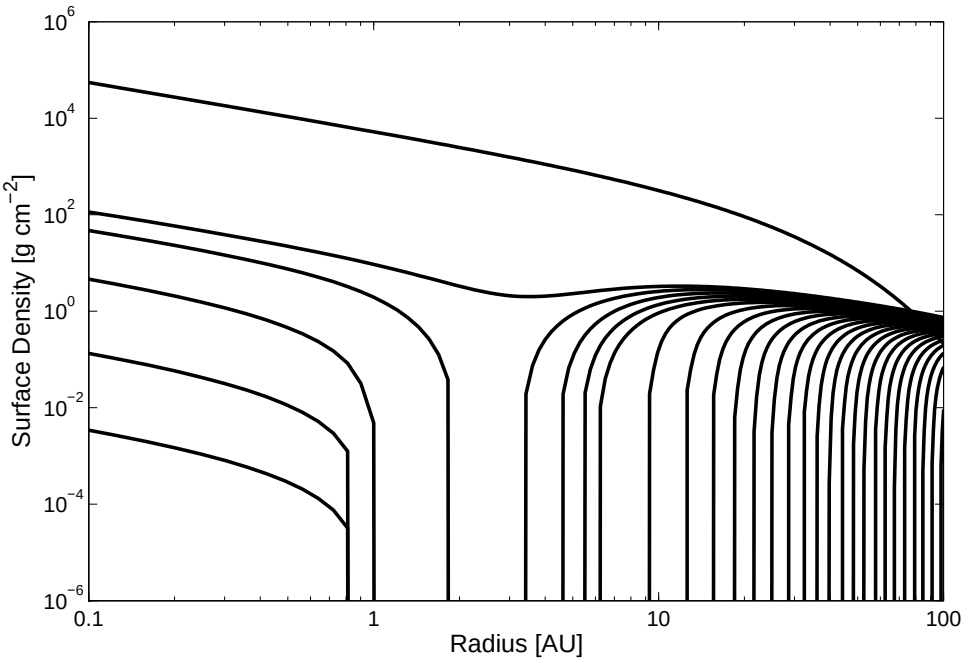

Figure 4.4: The evolution of the disc's surface density during the disc clearing phase. The first line shows the zero time surface density profile, the next shows the profile at 75% of the discs lifetime ($\sim$ 3.5Myr) and the remaining lines show the surface density at 1% steps in disc lifetime.

with time for individual disc models (each line shows the evolution of accretion rate with time for one disc model, for a given value of the X-ray photoevaporation rate). This clearly shows that a spread in accretion rates at late times $>$ 1Myr does not necessary require a spread in initial conditions, as some authors have suggested is necessary outside this framework (e.g. Armitage et al. 2003; Alexander & Armitage, 2009). However, there is observationally a spread in accretion rates seen at early times $<$1Myr. This variability cannot be fit with a single set of initial conditions, since photoevaporation has had no time to act on the disc. The failure to match the spread in accretion rates at early times $<$ 1Myr may not be surprising, since at early times the angular momentum transport mechanism may be dominated by self-gravity and accretion may be episodic (e.g. Lodato & Rice, 2005). In reality the zero time point in our models corresponds to the point at which the transition from a self-gravitating to a viscous disc occurs, as indicated by the determination of $M_d(0) = 0.1M_*$. This may explain, why our initial accretion rate is significantly lower than some of the accretion rates measured for the youngest objects (Hartmann et al. 1998).

Furthermore, better agreement at early times could easily be obtained by assuming a range of initial surface density profiles. Indeed our choice of a self-similar surface density distribution at zero time has no physical basis, only convenience (in fact it would be extremely surprising for discs to be born with the surface density distribution of the zero time similarity solution of Equation 4.1 given viscous angular momentum transport is not a key process during the disc formation stage). I emphasise that any initial surface density distribution with the same initial viscous parameters $M_d(0)$, t_ν and α will tend to the same evolution after a few viscous times (e.g. Lynden-Bell & Pringle, 1974). For this reason, I do not attempt to explain disc evolution at early times here, since we are mainly interested in the question of disc dispersal, for which only the viscous evolution phase at $>$ 1Myr is relevant.

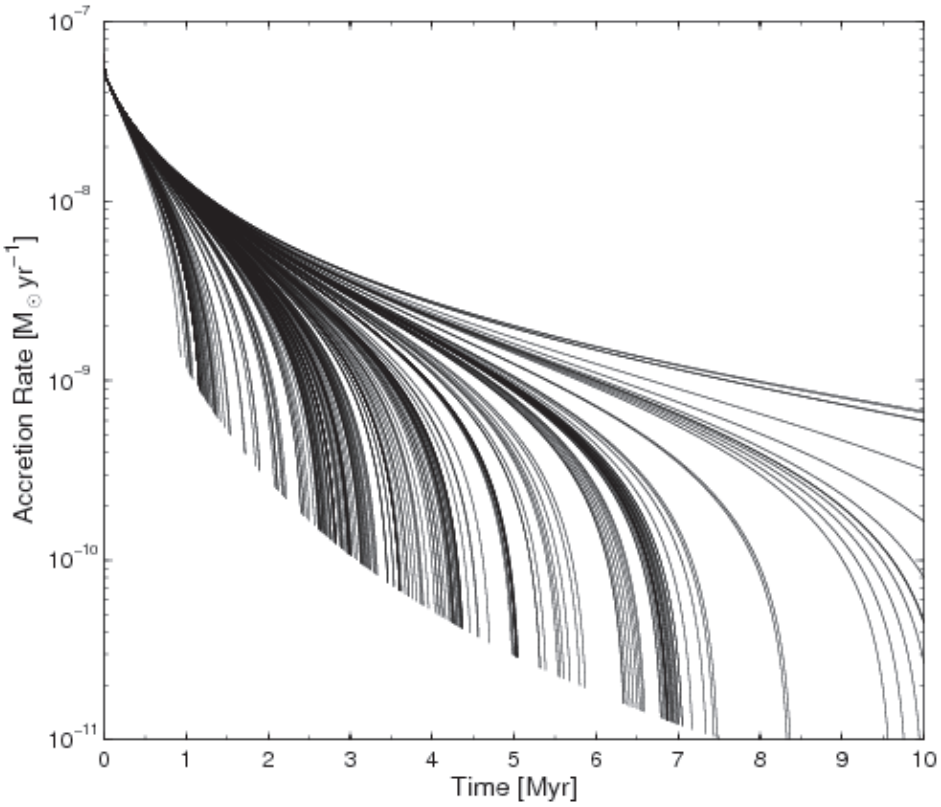

Figure 4.5: Each solid line represents the evolution of accretion rate as a function of time for an individual disc model undergoing X-ray photoevaporation. All models have the same initial conditions, the X-ray luminosity is the only variable.

Certainly it is somewhat implausible to expect there to be no spread in initial conditions; however, we can certainly rule out the large spreads in initial conditions (>1dex) as required by some other models. Furthermore, the agreement between the disc fractions and spread in accretion rate is certainly a good indication that the dominant dispersal mechanism is indeed photoevaporation. The accuracy of the 'null' model is certainly reassuring in supporting this hypothesis. However, the most direct tests of the photoevaporation model will come from comparing X-ray luminosities to disc evolution parameters, since if X-rays had no implications on disc evolution, then there is no explicit reason for X-ray luminosity to correlate with disc evolution parameters.

4.4.1 Photoevaporation starved accretion

As discussed in the Introduction, Drake et al. (2009) suggested that coronal X-rays suppress the accretion flow onto young solar-type stars through the driving of a photoevaporating wind. This photoevaporation starved accretion phase can explain the tentative negative correlation between mass accretion rate and stellar X-ray luminosity reported by Drake et al (2009). Moreover the reduction in disc lifetime in strong X-ray sources can explain the observation that the X-ray luminosities of accreting T Tauri stars are systematically lower than those of non-accretors.

The median photoevaporation model in Figure 4.4 clearly shows that there is indeed a phase in the disc evolution (before the opening of the gap) where the effects of this 'starving' are apparent in the radial

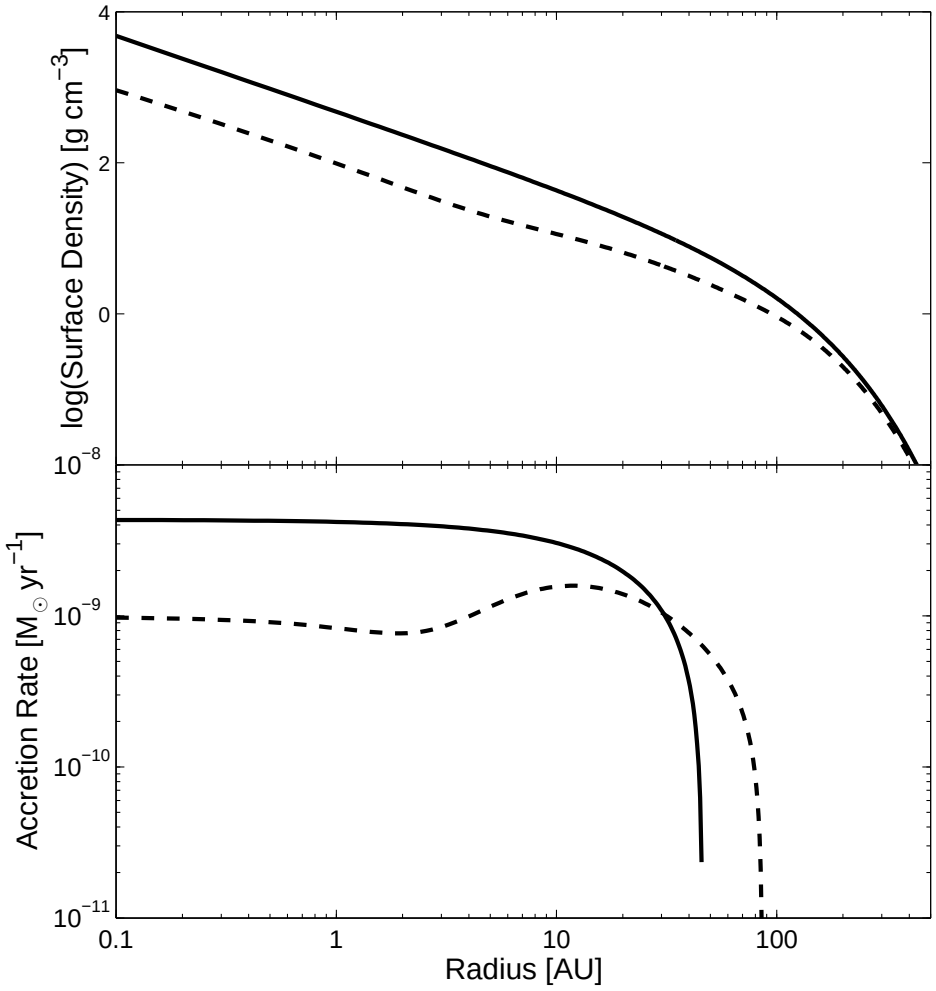

Figure 4.6: Surface density (top) and accretion rate (bottom) radial profiles. The solid line represents a disc undergoing no photoevaporation and the dashed line represents the median disc model ≈ 0.5Myr before a gap opens in the disc due to XPE.

dependence of the surface density, and hence the accretion rate. In Figure 4.6 we compare the accretion rate and surface density profiles of the median disc model undergoing photoevaporation, 0.5Myr before the gap opens against those of a disc which is only subject to viscous evolution. Inside 70 AU the accretion rate drops before it reaches the star compared to the standard case where the accretion rate tends to a constant value throughout the entire disc. The photoevaporation starved accretion lasts for $\sim$20-30% of the disc lifetime in the X-ray model, with significant consequences for global disc evolution.

The negative $\dot{M}$-L_X correlation reported by Drake et al (2009) is a simple consequence of the fact that discs with higher X-ray luminosities produce more vigorous winds, causing the disc's accretion rates to be lower than those for discs with less vigorous winds. Thus, a negative $\dot{M}$-L_X correlation is expected for clusters with a relatively narrow age range. However, this effect is counteracted by the fact that discs with lower X-ray luminosities take longer to evolve, spending more time at lower accretion rates compared to high luminosity objects. Therefore, if the X-ray luminosity was compared to accretion rates for the entire population's lifetime, in clusters with very large age spreads, a positive correlation

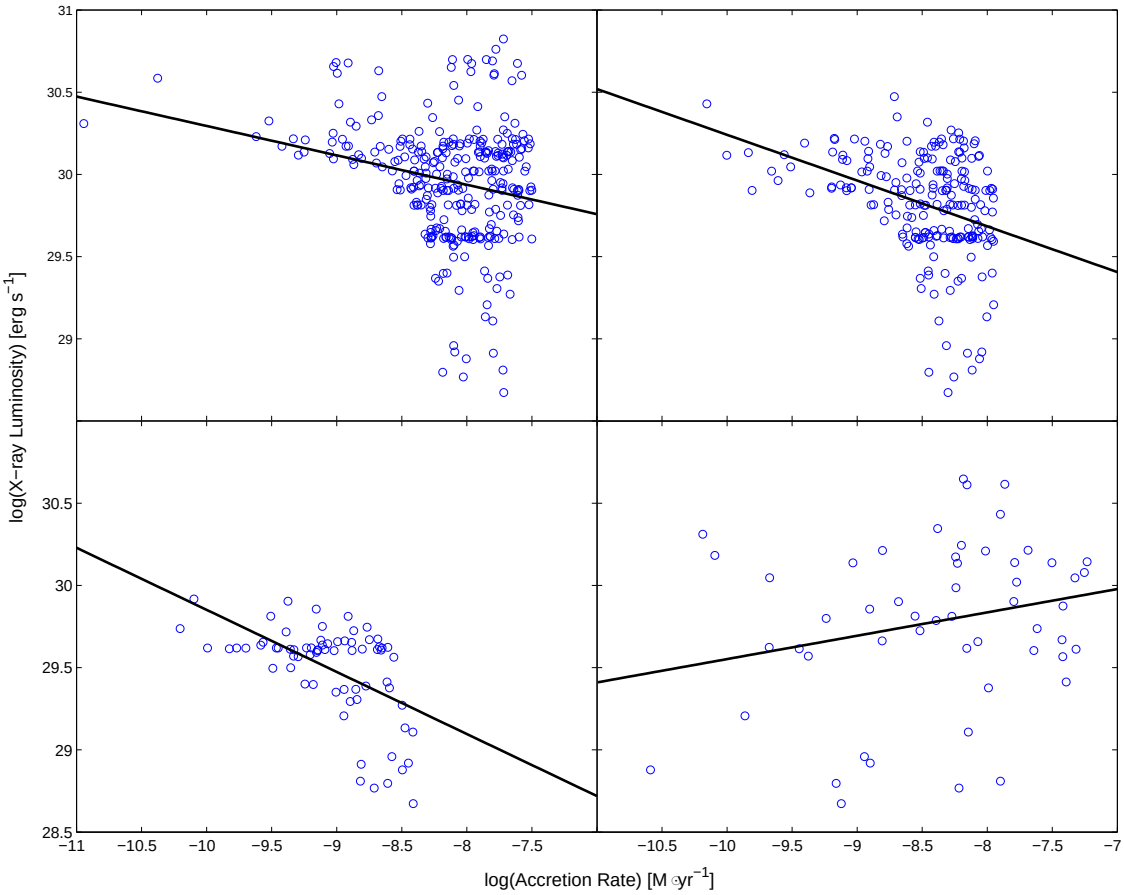

Figure 4.7: Synthetic observations of X-ray luminosity and accretion rates of clusters with a uniform age spread, the synthetic observations are shown as points while a linear fit to the data is shown as the solid line. The top left and right panels and the bottom left panels represent young clusters with uniform age spreads of 0.5-3.5Myr, 1.5-4.5Myr and 4-8Myr, respectively. The bottom right panel represents the disc population observed over the entire evolution.

might be expected. In Figure 4.7 I show plots of $\dot{M}$-L_X for synthetic 'cluster' members, selected to give clusters with various 'observationally sensible' age ranges of 3-4Myr (e.g. Palla & Stahler 2000, Haisch et al. 2001ab; as indicated by the luminosity spread in the H-R diagram), along with the plot of the total disc population (bottom right panel). I note that the interpretation of luminosity spreads as age spreads is currently under debate, with the spread in luminosities possibly arising from accretion history (e.g. Ballesteros-Paredes & Hartmann 2007; Baraffe et al. 2009) and much smaller age spreads ($< 1Myr$). While an large age spread will wash out any $\dot{M}_* - L_X$ variation, I will see if the large age spreads predicted from pure luminosity spreads are sufficient to remove the expected correlations, or it persist as indicated by observations (Drake et al. 2009).

As expected, the photoevaporation model predicts a positive $\dot{M}$-L_X correlation for clusters with large age spread and a negative correlation for clusters with a narrow age spread. As a comparison, the age spread in Orion is roughly 2-3Myr (Haisch et al. 2001b), which explains the observation of a negative correlation by Drake et al. (2009).

The observation of systematically higher X-ray luminosities of non-accreting TTs (WTTs) compared to accreting TTs (CTTs) can also be explained by the model in terms of photoevaporation starved accretion. Figure 4.8 shows the time evolution of the median X-ray luminosity of the CTTs (solid line) and

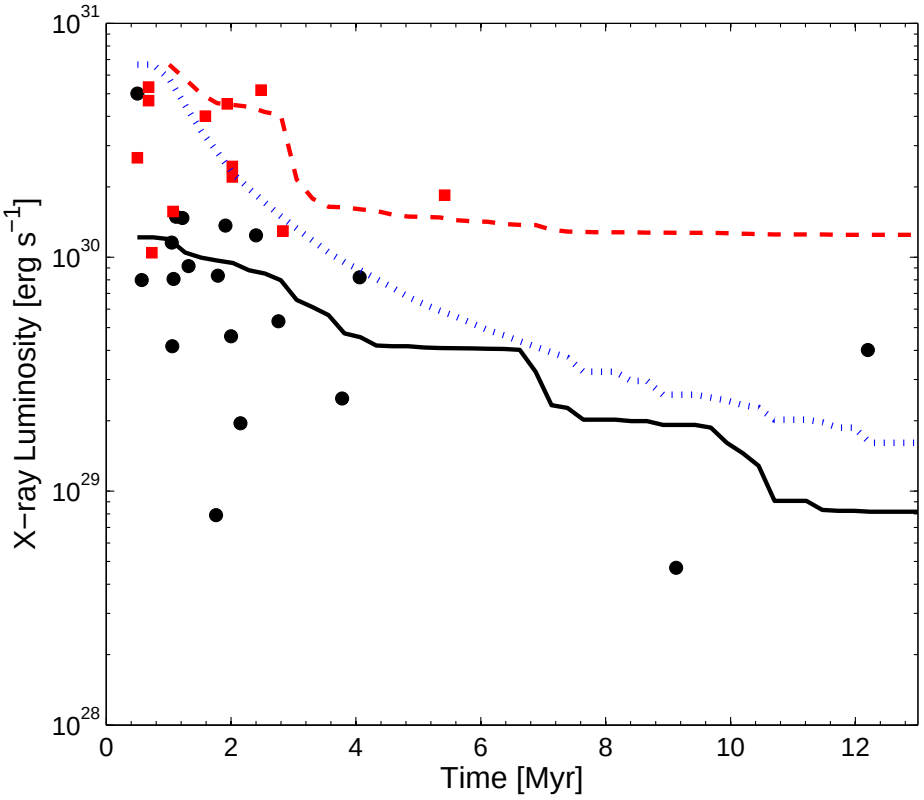

Figure 4.8: Time evolution of the median X-ray luminosity in the synthetic cluster for CTTs (solid line) and WTTs (dashed line). The dotted line represents the transition X-ray luminosity between a CTTs and a WTTs as a function of time. The data points are taken from the compilation of Güdel et al. (2007) in the Taurus cluster, filled circles refer to CTTs and filled squares refer to WTTs.

WTTs (dashed line) populations for our model compared to the data compiled by Güdel et al. (2007) for the Taurus cluster (black circles and red squares). The dotted line represents the critical X-ray luminosity as a function of time which in our model separates CTTs and WTTs, and corresponds to the X-ray luminosity of objects which have just opened a gap and have begun the clearing phase. The number of anomalous objects (i.e. CTTs above the line and WTTs below the line) is small at ages $\gtrsim$ 1 Myr. Given uncertainties in age determinations from isochrone fitting (particularly at $<$ 1 Myr; Mayne & Naylor 2008; Baraffe et al. 2009) the agreement between the median X-ray luminosities for the CTTs and WTTs populations at Taurus' median age of 2 Myr is very encouraging.

4.4.2 The nature of transition discs: accreting and non-accreting

The recent observations of a class of 'transition' discs with residual gas inside the inner dust radius and a signature of accretion, has prompted some authors to question the viability of photoevaporation as the formation mechanism for the inner hole in some sources (e.g. Cieza et al 2010). Previous EUV-driven photoevaporation models (e.g. Alexander & Armitage 2009) indeed predicted that at the time of gap opening the surface density of the gas in the inner disc and the accretion rates due to the inner disc draining onto the star should be undetectable. However, this is not the case when X-rays are included, mainly due to the fact that the wind rates can be two orders of magnitude higher than the EUV-driven rates. This means that at the time of gap opening the mass of the draining inner disc, and the accretion rate remains

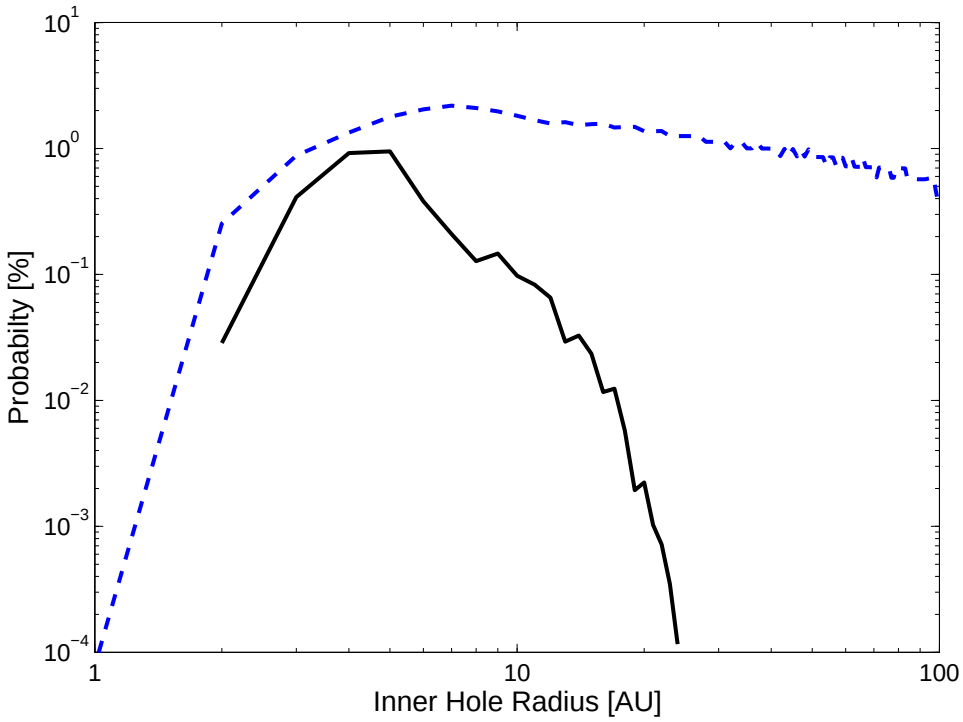

Figure 4.9: Probability distribution function of accreting (solid line) and non-accreting (dashed line) transition discs with inner hole radius. They are both scaled so that the integrated sum of both distributions is 100%.

detectable for a non-negligible amount of time. For the disc population generated in this work, Figure 4.9, shows that the accreting inner holes and non-accreting inner-holes ($\dot{M} < 1 \times 10^{-11} \mathrm{M}_{\odot}\ \mathrm{yr}^{-1}$) are, in general, equally likely out to a radius of $R_{in} \sim 5$AU. Clearly as the disc is further photoevaporated and its inner radius moves out, the accretion signatures onto the star become less evident and non-accreting inner holes dominate at radii larger than 20 AU. The total integrated ratio out to 10AU (the radius probed by 24μm emission around solar-type stars) is found to be 25% accreting and 75% non-accreting for the entire population. Although, I caution that this is *not* equivalent to the observed fraction of accreting to non-accreting objects in a individual cluster, where the cluster age should also be accounted for. In young clusters, the transition disc population is dominated by high X-ray luminosity objects which give rise to a considerably longer accreting inner hole phase. In contrast this ratio is much lower in old clusters where the transition disc population is dominated by low X-ray luminosity objects that have very short accreting inner-hole phases.

It is perhaps worth noting at this point that the detection of a 'transition' disc observationally is made through observation of the dust continuum spectral energy distribution (SED). As mentioned in the introduction, Alexander & Armitage (2007) examined the behaviour of dust in a photoevaporating disc finding that, under the action of dust drag, the time-scale for dust grains to drain onto the star is of order 10^3yrs after the gap opens. This dust removal time-scale is approximately two order of magnitudes faster than the gas draining time-scale. Therefore, an observer would certainly see a significant drop in opacity in the inner disc immediately after a gap has opened, while the gas will still linger in the inner dust disc for the duration of its viscous draining time-scale of $\sim 10^5$yrs.

I have used the population synthesis model to investigate the accretion rate versus inner hole size

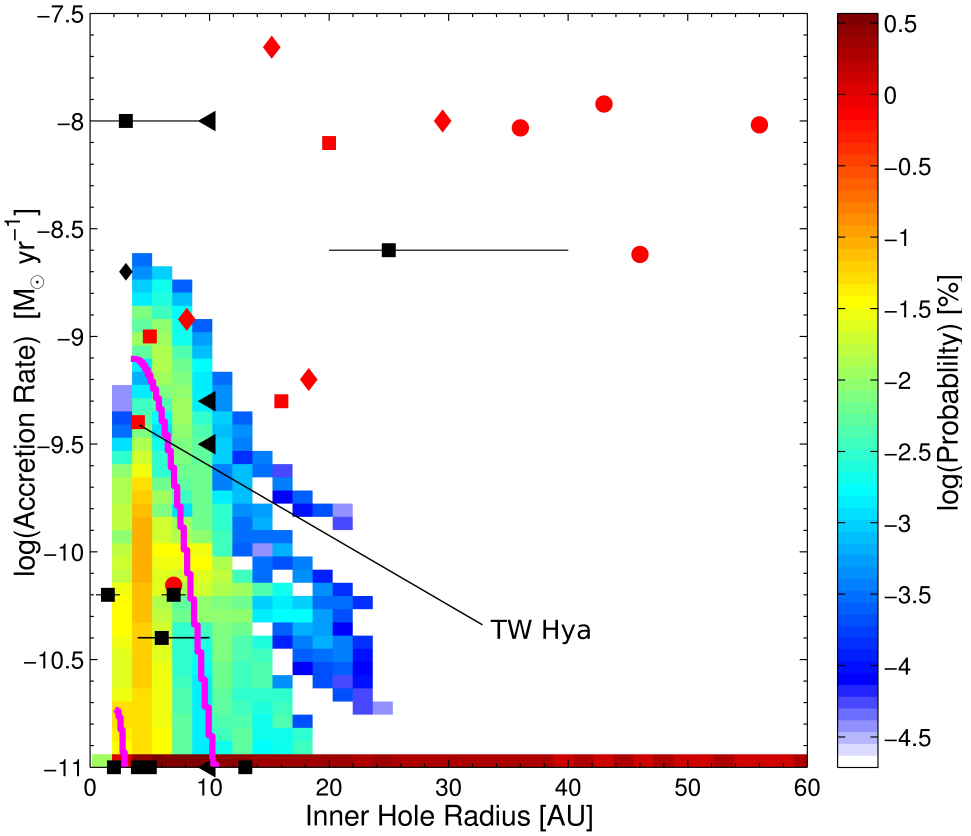

Figure 4.10: Transition disc probability map in the $\dot{M}$-R_{in} plane. We have applied an observational cut-off of 10^{-11}M$_\odot$ yr^{-1}in accretion rate and objects below the cut-off are all shown at the bottom of the diagram. We show a representative sample of solar-type objects classified as 'transition' discs; data from taken from Espaillat et al. (2007a,b,2008,2010) - Red Circles, Hughes et al. (2009,2010) - Red Squares, Kim et al. (2009) - Red Diamonds, Calvet et al. (2005) - Black Diamonds, Merín et al. (2010) - Black Squares and Cieza et al. (2010) - Black Triangles, where error-bars are given in the literature they are shown. We also show two model tracks corresponding to a 1dex spread in X-ray luminosities about the median model in magenta.

evolution for transition discs created by XPE under the assumption of immediate dust clearing at the time of gap opening. Figure 4.10 shows the probability distribution of the disc models in the $\dot{M}$-R_{in} plane. The symbols represent a sample of observations of solar-type objects classified as 'transition' discs by Espaillat et al. (2007a,b,2008,2010) - Red Circles, Hughes et al. (2009,2010) - Red Squares, Kim et al. (2009) - Red Diamonds, Calvet et al. (2005) - Black Diamonds, Merín et al. (2010) - Black Squares and Cieza et al. (2010) - Black Triangles (Although Cieza et al. 2010 do not fit for the inner-hole radius they list as transitional sources those discs that have a deficit of emission in the *Spitzer* IRAC bands; therefore we conservatively estimate an inner hole radius of $<$ 10AU for all their sources).

It is immediately clear from the figure that there is a population of large inner hole, strongly accreting transition discs that cannot have been created by photoevaporation. Gap opening by a giant planet or grain growth is perhaps the most plausible explanation for these objects. However, there is a significant number of discs ($\approx 17/28$) with inner holes that are consistent with a photoevaporation origin.

Since the observations of 'transition' discs by their nature are rare, we are plagued by low number statistics and observational uncertainties. A quick look at Figure 4.10 indicates that different selection criterion applied by different authors on similar data sets probes different regions of this parameter space.

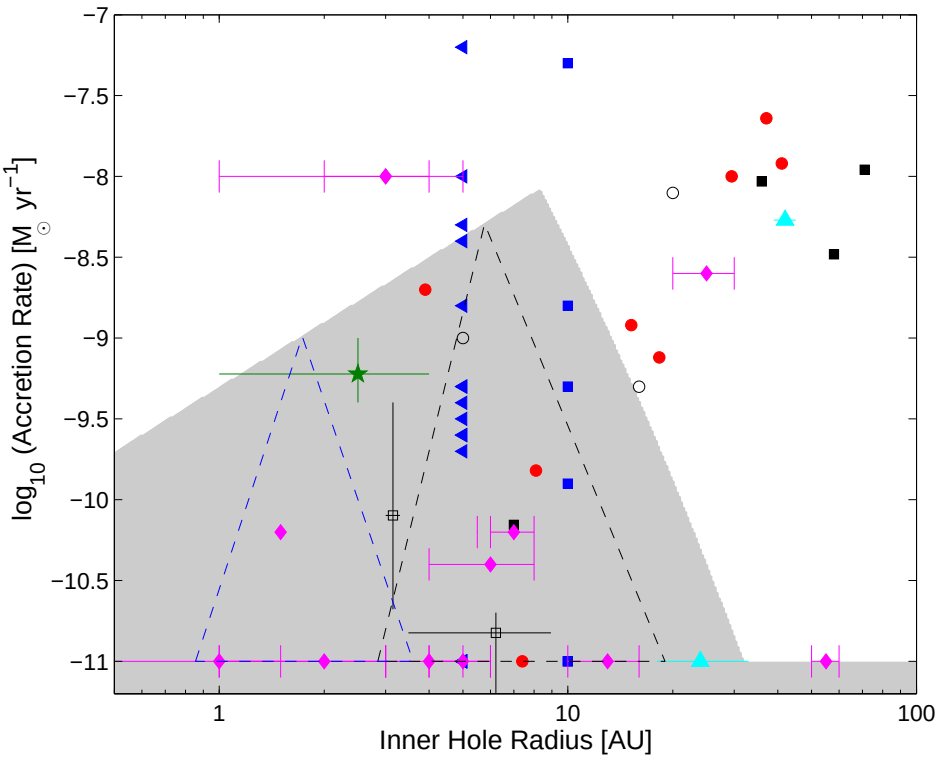

Figure 4.11: The inner hole radius and accretion rate of low-mass objects classified as 'transistion' discs by various authors: cyan triangles (Brown et al. 2009); blue filled triangles & squares (Cieza et al. 2010); black open squares (Ercolano et al. 2009); black filled squares (Espaillat et al. 2008,2010); black open circles (Hughes et al. 2009, 2010); red filled circles (kim et al. 2009); magenta filled diamonds (Merin et al. 2010); green filled star (Najita et al. 2010). Where error-bars or ranges are listed they are shown. Any object classified as non-accreting is placed on the plot with an accretion rate of 10^{-11}M$_\odot$ yr^{-1}. The grey region represents the region of parameter space where the objects are consistent with gaps created by photoevaporation. The blue and black dashed regions represent those regions for a 0.3 and 1 M$_\odot$ star respectfully, calculated using the similarity solutions (for mass dependence) described in Chapter 2, see text below for details.

Therefore, in order to improve our low number statistics I have built an extended version of Figure 4.10, shown in Figure 4.11 which includes the full mass spectrum of observations.

Using the photoevaporation theory developed in Chapter 2 we can fully describe the region of 'transition' disc parameter space in which transition discs with a photoevaporative origin would lie. Since the radial scale of the photoevaporative flow scales linearly with mass, the radius at which the gap opens will obviously scale linearly with mass too. Furthermore, the gap opens when the accreation rate falls below the photoevaporation rate, then the stellar mass is not important in determining the accretion rates of transition discs, other than through the implicit mass dependence on the photoevaporation rate through the X-ray luminosities variation with stellar mass. In Figure 4.11 I show the region in which photoevaporating transition discs are expected (with individual regions for 1M$_\odot$and 0.3M$_\odot$stars shown separately), over-plotted with all current observations[3]of discs classified as transition discs: cyan triangles (Brown

[3]Several other types of astrophysical objects are found to enter these samples (e.g. AGB star or debris disk) in these cases we follow the definitions of the authors and only plot objects that are classified as protoplanetary discs with a gap/hole in its dust disc.

et al. 2009); blue filled triangles & squares (Cieza et al. 2010); black open squares (Ercolano et al. 2009); black filled squares (Espaillat et al. 2008,2010); black open circles (Hughes et al. 2009, 2010); red filled circles (kim et al. 2009); magenta filled diamonds (Merin et al. 2010); green filled star (Najita et al. 2010). I note that as Cieza et al. (2010) do not fit for an inner hole radius but rather list the *Spitzer* band of the inner hole I split the sample into two: the objects with a $\lambda_{\rm turnoff} \leq 5.8\,\mu$m the inner hole is conservatively set to be less than 5AU, for $\lambda_{\rm turnoff} = 8\,\mu$m I again conservatively set an inner hole of 10AU (since the inner-hole must occur in the temperature range $\lambda = 8$ – $24\,\mu$m); I add that these are safe overestimates based on simple temperature structures of protoplanetary discs. It is also worth noting that at very low masses $\sim 0.1{\rm M}_{\odot}$ Ercolano et al. (2009a) showed that current observations are not good enough to determine the presence of holes smaller than ~ 1 AU arising from a lack of contrast between the disc and the stellar photosphere. The photoevaporation region is constructed by using the fact that the photoevaporation profile is self-similar when the radius is scaled in terms of R_g. (i.e. if the gap opens at 1AU around a $1{\rm M}_{\odot}$ star it would open at 0.1AU around a $0.1{\rm M}_{\odot}$ star) and I use an X-ray luminosity scaling of $L_X \propto M_*^{3/2}$ (Priesch et al. 2005, Guedel et al. 2007) to extend the region calculated in Figure 4.10 to the full mass range ($M_* \lesssim 1.5{\rm M}_{\odot}$), thus the left-hand slope of the grey region maps the $L_X \propto M_*^{3/2}$ and scales as $R_{\rm hole}^{3/2}$. The right-hand slope of the grey region and steeper slopes of the dashed triangles are obtained by fitting power laws to both sides of the photoevaporation region shown in Figure 4.10 and scaling the radii linear with mass as the model predicts. Unsurprisingly, this again shows that the observations can be separated into two groups, those with small inner-holes $\lesssim$ 20AU and small accretion rates $\lesssim 10^{-8}$ M$_{\odot}$ yr^{-1} that are consistent with a photoevaporative origin, and those discs with large accretion rates and large holes that cannot have a photoevaporative origin.

In both cases I note the lack of objects with large holes and low accretion rates, this could be due to observational biases, as the longest IR wavelength observation in most cases is the 24μm (MIPS1) *Spitzer* band, which constitutes a radius of roughly $10-20$AU for solar type stars. However, we can be fairly sure that there is not a large number of undetected, heavily accreting objects ($\gtrsim 10^{-11} - 10^{-10}){\rm M}_{\odot}$ yr^{-1} objects. Certainly *Herschel's* sensitivity in the FIR, will probe this region of parameter space definitively and should provide much better statistics of the speed of inner disc clearing, compared to outer disc clearing.

One obvious consequence of an X-ray photoevaporation mechanism is that the properties of transition discs should be correlated with the X-ray luminosity, something no other model of photoevaporation or 'transition' disc origin would predict. In Figure 4.12, we show two such correlations namely the inner hole radius (left panel) and accretion rate (right panel) against X-ray luminosity, considering only accreting 'transition' discs (i.e. those with an accretion rate $> 1 \times 10^{-11}{\rm M}_{\odot}$ yr^{-1}). The plots have been generated by a random sampling (in time) of the accreting transition phase of each disc model several times, and should therefore provide a reasonable estimate of both the general form of the correlation plus the associated scatter. Clearly, since discs with higher X-ray luminosities open gaps earlier and at higher accretion rates a strong positive correlation between L_X and $\dot{M}$ would be expected and is reproduced by the models as shown.

Furthermore, I also recover a positive correlation between inner hole radius and X-ray luminosity for *accreting* transition discs as shown in Figure 4.12. We can understand this by remembering that while the inner disc is still draining, the inner hole radius is also being eroded outwards as shown in Figure 4.4. For more X-ray luminous objects the region being eroded is more depleted due to photoevaporation starved

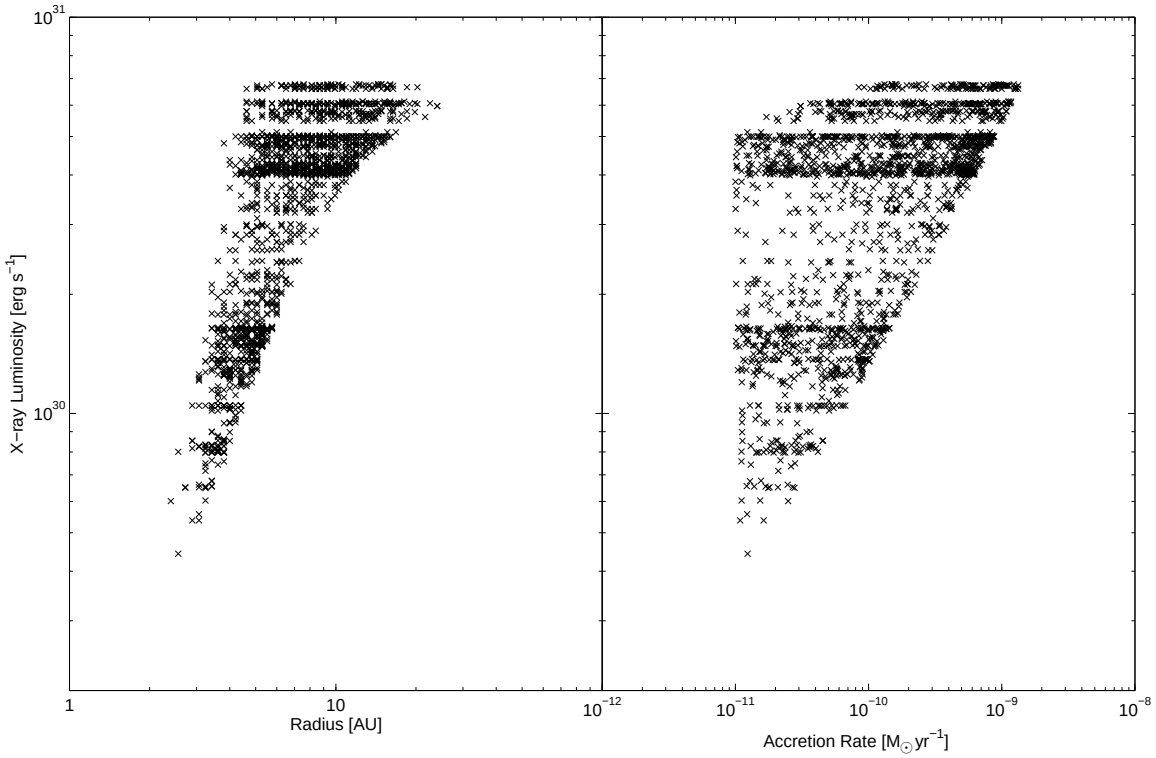

Figure 4.12: Simulated observations of *accreting* 'transition' discs. The left hand panel shows X-ray luminosity plotted against inner-hole radius. The right hand panel shows X-ray luminosity plotted against accretion rate where an observational cut-off of 10^{-11}M$_\odot$ yr^{-1}has been used.

accretion and the magnitude of the mass-loss is higher. Thus, the inner-hole radius is able to be eroded to larger radius during the accreting phase. This explains the positive slope of the right hand extent of the symbols in the left panel of Figure 4.12.

Consequences of a different X-ray luminosity function

The X-ray luminosity function is a crucial input into the XPE model. In this work I have used the Taurus X-ray luminosity function as this best represents the quiescent X-ray flux the disc sees throughout its lifetime. However, here I discuss the consequences of a different X-ray spectrum that may be incident on the disc. If the incident spectrum the disc sees is systematically harder than the one used (through attenuation of the X-ray spectrum by large neutral columns close to the star) or softer than the spectrum used, the qualitative behaviour of the disc population would remain the same, since one can vary the initial condition to fit. Therefore, it is important to assess the qualitative changes to some of the predictions relating to transition discs. As discussed previously it is only the soft X-rays (0.1-2keV) that have any thermal impact, then the result of a changing spectrum can just be considered to be a change in the soft X-ray luminosity incident on the disc. Therefore, overall mass-loss rates can simply be scaled to this new harder/softer spectrum.

In Section 4.1 I argued that any X-ray luminosity function with a similar spread can have a 'null' model constructed to fit the observations of disc fraction. Thus, a harder or more attenuated spectrum would result in lower-mass loss rates, which would require a lower initial accretion rate, compared to a

softer spectrum, which would require a higher initial accretion rate to explain the observed disc fractions. Provided this effect is systematic across all values of L_X (i.e. it doesn't change the spread of X-ray luminosities) then the consequences for the predicted 'transition' disc population can be considered. For the harder/more attenuated spectrum a lower initial accretion rate is required implying a lower initial disc mass, and therefore a smaller population of accreting transition discs, with lower accretion rates and smaller inner holes. The converse is true for a softer spectrum which requires a higher initial accretion rate and hence larger initial disc mass, giving rise to a larger population of accreting transition discs, with higher accretion rates and larger holes.

4.4.3 Final clearing of the disc

As discussed in Chapter 3, the numerical models have demonstrated a further phase in disc dispersal, the rapid removal of disc material due to a 'thermal sweeping' period. However, without knowledge of how it generalises to all masses, disc structures and X-ray luminosities I cannot accurately estimate its implications for the evolution of the disc population. Without this knowledge I am unable to terminate the evolution of the disc due to 'thermal sweeping' at the correct time, and instead stop the evolution when $R_{\rm hole}$=100 AU, when the IR indicators of a protoplanetary disc have almost disappeared and the observational constrains on clearing through this region are sparse. While the total columns of these 'relic' discs are small ($\lesssim 10^{23}$ cm^{-2}) suggesting that many may have already gone through this 'thermal sweeping' process, it is important to discuss the implications of their continued existence in case the 'thermal sweeping' does not occur until much later times around solar type stars.

Therefore, if we ignore the 'thermal sweeping' period we can estimate the remaining clearing time by dividing the disc mass by the photoevaporation rate (since it is expected to be approximately independent of inner hole radii). Such a calculation shows that in about 10% of cases (discs irradiated by a low X-ray flux) the final clearing time-scales would exceed 10Myr, resulting in a population of long lived discs with large inner holes. These objects will certainly survive for a long enough time for their dust continuum emission to be observed. The spectral energy distribution (SED) of these cold massive discs should be similar to that of young debris discs, where a debris disc model is normally considered to be a single temperature belt of optically thin dust (thought to be constantly replenished by collisions between planetesimals) at a given radius from the star (Wyatt 2008). This suggests that some of the sources that are currently classified as debris discs could in fact be photoevaporation 'relics'.

In order to asses this I have used the radiative transfer code of Whitney et al. (2003a,b) to calculate the SED of a typical relic using the standard input disc structure and dust properties of the code. The properties of these relics were taken from the end point of the lowest X-ray luminosity (and hence the longest lived) model. While such a disc is likely to be settled in the dust, I computed three models: a flat dust distribution, a fully mixed dust distribution and a disc where $H_{\rm dust} = 0.1H$. Figure 4.13 shows a plot of the fractional excess of the disc compared with the stellar photosphere at 24μm and 70μm, where the models are compared with observations of objects classified as young debris discs around solar-type stars (Wyatt 2008). It is clear from this figure that the relics with a degree of dust settling share the same space in the excess-excess plot as sources currently classified as young debris discs. The fully-mixed discs show a 70μm excess which is probably too large to be classified as a debris disc, although it is extremely unlikely that any disc could survive for $>$ 10Myr without undergoing dust settling. I also note

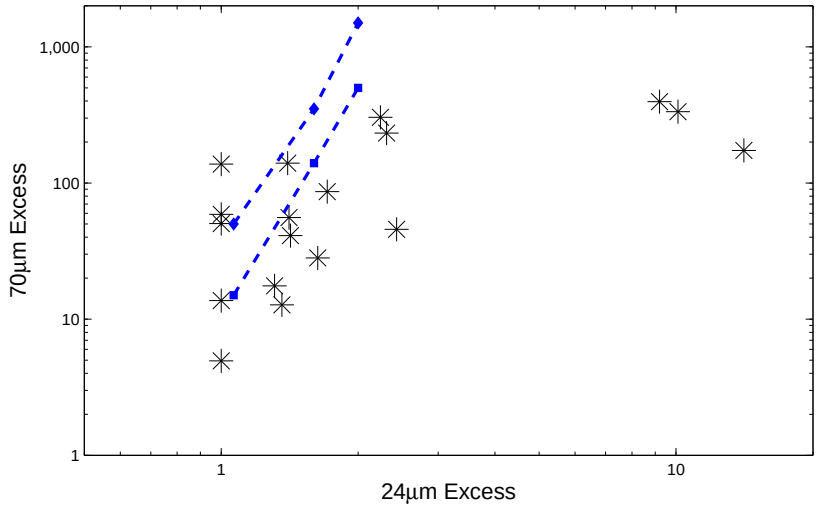

Figure 4.13: Plot of 70μm excess above the photosphere against 24μm excess for disc models with a large inner hole (100 AU) and low X-ray luminosities and therefore a predicted remaining lifetime $>$ 10Myr. The squares show discs close to edge-on and increasing 24μm excess represents the evolution from a flat to fully mixed dust distribution. Similarly the diamonds show the disc models close to face-on. Also shown as data points are observations of young solar-type stars ($<$ 100Myr) with IR excesses classified as debris discs, taken from (Wyatt 2008).

that the predicted 850μm emission from the evolved relics falls below the current detection limits at 50 pc (Andrews & Williams 2005), and thus these relics would not contradict previous sub-mm observations of WTTs which show that most are devoid of emission out to 500 AU (Duvert et al 2000). Only ALMA will be able to separate these large massive discs from canonical debris discs, and hence confirm or dismiss the existence of this proposed class of objects.

However, I emphasise that such objects may not exist at all, as they may be cleared by the 'thermal sweeping' process seen around lower mass stars in the previous Chapter. Certainly, further work on this process around solar type stars is needed before any definitive statements on the existence or non-existence of 'relic' discs is made.

4.5 Conclusions

I have coupled the numerical radiation-hydrodynamic models of X-ray photoevaporation perfomed in Chapter 3 to a viscous evolution model to construct a population synthesis model, with which we have studied the physical properties of primordial and transition discs. The initial conditions and viscosity law are constrained using recent observations of disc fractions in nearby clusters (Mamajek 2009). The model requires a viscosity coefficient of approximately $\alpha = 2.5 \times 10^{-3}$ to match the observational constraints. The main conclusions are as follows:

1. X-rays play a major role in the evolution and dispersal of discs around solar-type stars, driving vigorous photoevaporative winds.

2. I have constructed a 'null' accretion disc model using only knowledge of the observed disc fractions and X-ray luminosity functions under the assumption that discs are dispersed through X-ray

photoevaporation. This 'null' model shows very good agreement with observed accretion rates in YSOs as well as their evolution with time, providing further independent confirmation of the viability of X-ray photoevaporation as a dominant dispersal mechanism.

3. X-rays suppress accretion by preventing accreting material from reaching the star, since this material is removed through photoevaporation. This 'photoevaporation starved accretion' (Drake et al 2009) produces a negative correlation between X-ray luminosity and accretion rate for clusters with a relatively narrow age spread, in agreement with the observational correlation reported by Drake et al. (2009) in the Orion data.

4. The model successfully reproduces the observation that WTTs are systematically brighter in X-rays than CTTs. Whereas this has previously been interpreted as modification of X-ray emission or detectability by the presence of discs, our models support Drake et al. (2009) in reversing the causal link - i.e. that disc lifetimes are regulated by photoevaporation and hence disc-less stars are on average those with higher L_X.

5. A large fraction ($\gtrsim 50\%$) of observed transition discs can be easily explained by X-ray photoevaporation. There is however a population of strongly accreting transition discs with large inner holes (> 20AU) that lie outside the $\dot{M} - R_{in}$ region predicted by the models, suggesting that alternative mechanisms are responsible for their inner hole (e.g. binary interaction, grain-growth and/or planet formation).

5

Detecting the wind I: theoretical spectra of photoevaporating discs

In order to provide more direct tests of the photoevaporation model I will discuss emission from the wind itself. In particular, I will discuss emission lines from the gas, which through resolved spectroscopic measurements can provide direct evidence for a photoevaporative wind, and be used to test the ionization and kinematic structure of the wind. Currently, observations of resolved gas emission lines from the upper disc and photoevapoartive flow are sparse, with quality data only available for the complicated 'transition' disc TW Hya. Therefore, in this Chapter I will discuss predictions for several observable gas emission lines, along with an analysis of the observational data, particularly for TW Hya.

5.1 The status of current observations

While gas line emission has proved a successful test of the external photoevaporation model (e.g. Richling & Yorke 2000), these diagnostics have only recently begun to be used to constrain the intrinsic photoevaporation model. Perhaps the earliest indications of a direct detection of a photoevaporative wind were the observations by Hartigan et al. (1995) of the optical lines: OI 6300 & 5577Å, SII 6731Å and NII 6583Å. The original aim of their work was to study jet emission from young stellar objects and contained a large sample of 42 T Tauri stars. However, most objects showed line profiles with two components. These multi-component line profiles were split into two regions: the high velocity component (HVC - $|v| > 60$ km s^{-1}) and the low velocity component (LVC - $|v| < 60$ km s^{-1}). While the HVC was found to be well described by jet models, it was the LVC that was not consistent with any of the availble models and it is this component I discuss here. The LVC emission lines showed blue-shifts in the range $\sim 5 \pm 2$km s^{-1}, line widths of $\mathscr{O}10$km s^{-1} and luminosities around 10^{-5}L$_{\odot}$ with a $\sim$ 1dex spread, where

the LVC was best resolved (compared to the HVC) in the OI 6300Å line, and was always present when the young star had an NIR excess (i.e. a primordial disc). Furthermore, a comparison of the line ratios indicated that the LVC arises in a region with a significantly different temperature and density from the HVC (or jet), and that the variation of the blue shift with the critical density indicates that the emitting region is 'accelerating' towards regions of lower densities. In fact Hartigan et al. hypothesised that the most likely origin is a (at least) partially ionized disc wind emanating from somewhere in the radial range 0.1-20AU. With the most startling fact was the one to one correspondence between an NIR excess and LVC blue-shift, and this is what a photoevaporative wind would predict. However, Font et al. (2004) showed conclusively that while an EUV photoevaporative wind is capable of producing suitable blue-shifts, the predicted luminosities only reached $\sim 10^{-7}\mathrm{L}_{\odot}$ which is inconsistent with the observations. This incompatibility is easy to understand, since to produce OI emission, neutral oxygen atoms need to be present in the flow and EUV photons fully ionize the region. Furthermore, Gorti et al. (2011) recently discussed OI emission within the framework of the FUV photoevaporation, and conclude that while the observed line fluxes can be matched (through non-thermal OI emission, via OH dissociation), an FUV flow is necessarily cooler (thus slower) and is unable to reproduce blue-shifts of $\sim$ 5km s^{-1} Therefore, an EUV driven wind is simply too ionized and an FUV wind too slow to match the observations. While the Hartigan et al. observations provided an excellent sample of line observations, the low resolution and confusion with the HVC component mean that comparisons of line profiles are not possible with the sample.

It was not until observations by Pascucci & Sterzik (2009) of the NeII 12.8μm from 4 young stars, that direct evidence for photoevaporation was presented, with TW-Hya (which presents with an almost edge on disc) being the closest showing a well resolved, blue shifted and non axi-symmetric profile. This was followed up in detail in Pascucci et al. (2011) and was supplemented with observations of several optical forbidden lines, including the OI 6300Å. In this case the NeII line profile was also shown to be consistent with an EUV photoevaporative origin (Alexander, 2008). The NeII line profile shows a clear blue shift of 6 ± 1km s $^{-1}$ and a FWHM of $\sim$ 14 km s^{-1}, which is wider than expected from pure thermal and Keplerian broadening indicating its production in an hydrodynamic disc wind. Unfortunately, TW Hya is not a simple primordial disc but an accreting transition disc (which is consistent with a photoevaporative origin), with an inner hole in the range $1-4$AU (Calvet et al. 2002, Ratzka et al. 2007), and unlike the disc bearing Hartigan et al. (1995) objects, the LVC components of the optical lines are not blue-shifted, indicating they may not be tracing a flow.

In this Chapter I will use the results of radiative transfer post-processing of the numerical models calculated in Chapter 3 to produce theoretical line profiles and luminosities, these can then be compared to the current observations as well making predictions for future observations. While this method is flexible to produce line-profiles and luminosities for any required line, I will restrict my discussion to those lines which have attracted previous attention from observers, to either compare with current data or make predictions for currently observable lines.

5.2 Radiative transfer post-processing

In order to calculate the line emission from the radiation-hydrodynamic models calculated in Chapter 3, the solutions must again be run through a radiative transfer code. While the algorithm accurately deter-

mined the thermal structure, and thus dynamical structure of a photoevapoartive wind, the algorithm does not calculate the ionization structure and level populations of the species we are interested in, which are necessary for computing line fluxes and profiles. While the information calculated during the radiation-hydrodynamic algorithm is sufficient to compute these quantities, it is easier to use a radiative transfer post-processing of the temperature and density structures generated by the hydrodynamic calculations.

In order to do this, the structures are fed back into MOCASSIN, which then calculates the ionization structure of the region and the level populations of all the species. Once MOCASSIN has obtained these quantities it can then compute the emissivities of any desired line. The calculations were carried out using the input spectrum shown in Chapter 3 (the same spectrum used to determine the temperature-ionization parameter relation) The atomic database included opacity data from Verner et al. (1993) and Verner & Yakovlev (1995), energy levels, collision strengths and transition probabilities from Version 5.2 of the CHIANTI database (Landi et al. 2006, and references therein) and the improved hydrogen and helium free-bound continuous emission data of Ercolano & Storey (2006). However, there are several missing quantities that are worth pointing out: excitation rates of Ne^{+} by collisions with neutrals are not known, therefore theoretical calculations of this line, including this work, only account for collisions with electrons. This is likely to result in the NeII 12.8μm line flux being underestimated by a factor of $\lesssim$2 (Glassgold et al 2007). Furthermore, the collisions with neutral hydrogen and oxygen (which are likely to dominate as in the case of the OI 6300Å line) are not included in the calculation for the $^1S_0$ level due to the unavailability of the collision rates. This will lead to underestimates for the OI 5577Å line, although it will not affect the calculation of the OI 6300Å line. The following elemental abundances are used in the calculations, given as number densities with respect to hydrogen: He/H = 0.1, C/H = 1.4×10^{-4}, N/H = 8.32×10^{-5}, O/H = 3.2×10^{-4}, Ne/H = 1.2×10^{-4}, Mg/H = 1.1×10^{-6}, Si/H = 1.7×10^{-6}, S/H = 2.8×10^{-5}, these are solar abundances (Asplund et al. 2005) depleted according to Savage & Sembach (1996). The dust model of D'alessio et al. (2001) used for the initial condition of the disc is adopted for the final flow structure.

I perform this analysis for models of a 0.7 $M_\odot$ star, where the X-ray luminosity spans the observed range for T Tauri stars of this mass ($2\times10^{28} \leq L_X \leq 2\times10^{30}$ erg s^{-1}). Furthermore, I consider the disc at different stages of dispersal, by considering discs with cleared inner holes of sizes ($R_{\rm hole}$ = 8.3 AU, 14.2 AU and 30.5 AU) for an X-ray luminosity of 2×10^{30} erg s^{-1}. While the temperature and ionization structure in the X-ray heated region is accurately known, as described in Chapters 2 & 3, it is expected that the FUV is important between the X-ray heated region and dust heated region. The ionization structure, temperature and level populations are highly dependent on chemistry occurring in the disc in this region, something MOCASSIN is currently unable to treat. Therefore, I only consider the line emission to be well constrained from within the X-ray heated region and do not discuss the predictions from the model for emission that occurs in the upper regions of the bound disc.

5.2.1 Calculation of the line profiles

The two-dimensional maps of emissivities (calculated using the MOCASSIN post-processing described above) and gas velocities (taken form the radiation-hydrodynamic calculation) were used to construct a three-dimensional model of the disc and calculate the line-of-sight emission profiles for a number of transitions. The emissivities are calculated using 120 radial points ($N_R = 120$) and 1500 height points

($N_z = 1500$). By assuming azimuthal symmetry about the z-axis, and reflection symmetry about the disc mid-plane the resultant 3D grid has dimensions $N_R \times 2N_z \times N_\phi$. I take a value of $N_\phi = 130$ and checked that this was large enough to fully resolve the profiles. For the chosen emission lines the disc atmosphere is optically thin and therefore I assume that the line contribution of each parcel of gas can escape freely along the line of sight, provided that this does not intercept the mid-plane (e.g. Alexander 2008, Schisano et al. 2010). Although, when I consider discs with cleared inner holes, this cleared inner hole region is taken to be optically thin to the line; therefore, lines of sight that intercept the bound disc's mid-plane are taken to be optically thick to the lines. This means that for discs with inner holes, certain lines of sight will be able to 'see' both the blue shifted and red shifted components of the photoevaporative flow. Furthermore, for almost edge-on inclinations escape columns are large enough for dust attenuation to start playing a role. Therefore, comparisons with objects at high inclinations is not yet possible.

The line luminosity is then computed by including a Doppler broadening term in each cell. Hence the line luminosity at a given velocity v is computed by evaluating the following integral by direct summation.

$$L(v) = \int_V \mathrm{d}^3 r \frac{\ell(r)}{\sqrt{2\pi v_{\rm th}(r)^2}} \exp\left(-\frac{[v - v_{\rm los}(r)]^2}{2v_{\rm th}(r)^2}\right) \tag{5.1}$$

where $\ell(r)$ is the volume averaged power emitted at a point r, $v_{\rm los}(r)$ is the projected gas velocity along the line of sight and $v_{\rm th}$ is the local thermal velocity of the emitting atom given by

$$v_{\rm th} = \sqrt{\frac{k_b T(\mathbf{r})}{\mu_i m_{\rm H}}} \tag{5.2}$$

with μ_i the mean molecular weight of the required atom. The resolution of the velocity array is 0.25 km s^{-1}. I have evaluated the profiles of the OI 6300Å, the NeII 12.8μm, as these are the only lines for which high resolution data is currently available for comparison.

5.3 Results

Tables 5.1 & 5.2 list the emission line luminosities for the models. I note only a small subset of all the lines calculated are listed in the tables (a full set is listed in Ercolano & Owen 2010), however these are the lines that have been currently observed. The tables are organised as follows: Table 5.1 lists the luminosities for the primordial disc models with varying X-ray luminosity ($\log(L_X/\mathrm{erg\ s^{-1}})$ = 28.3, 29.3 and 30.3) while Table 5.2 show the results for the inner hole models irradiated by $\log(L_X/\mathrm{erg\ s^{-1}}) = 30.3$ with varying hole sizes.

A simple inspection of these tables immediately reveals that the integrated line luminosities are not very sensitive (factors of 2-5 at most) to the size of the inner hole. However, inner hole models do produce, in most cases, lines that are approximately a factor of two more luminous than those of a primordial disc with the same X-ray luminosity. This is due to the different physical conditions in inner hole regions, that are less dense and most importantly on average warmer than primordial disc winds.

In general, line luminosities are correlated with X-ray luminosity. However, the response of different lines to changes in L_X is different for different transitions, and depends on how sensitive to changes in luminosity a line's emitting region is, and on the dependence of a given emission line to temperature,

Table 5.1: Primordial disc models with varying X-ray luminosity.

Species	Wavelength	Line Luminosity [$L_\odot$]		
	[Å]	$\log(L_X)$=28.3	29.3	30.3
OI	6302.030	2.83E-07	1.93E-06	1.25E-05
OI	5578.890	5.22E-09	7.83E-08	9.12E-07
NeII	128155.8	9.25E-08	5.51E-07	5.41E-06
NeIII	155545.2	1.01E-08	1.16E-07	1.06E-06
SII	4069.760	2.23E-07	1.64E-06	1.22E-05
SII	6732.690	2.08E-07	1.16E-06	1.08E-05
MgI	4573.180	6.11E-08	8.21E-07	1.08E-05

Table 5.2: Inner hole disc models with varying hole size.

Species	Wavelength	Line Luminosity [$L_\odot$]		
	[Å]	$R_{\rm hole}$=8.3 AU	14.2 AU	30.5 AU
OI	6302.030	4.51E-05	4.48E-05	3.59E-05
OI	5578.890	1.47E-07	9.13E-08	5.16E-08
NeII	128155.8	1.21E-05	1.16E-05	1.04E-05
NeIII	155545.2	2.43E-06	2.90E-06	3.44E-06
SII	4069.760	2.43E-05	1.99E-05	1.49E-05
SII	6732.690	2.78E-05	3.07E-05	3.14E-05
MgI	4573.180	1.12E-06	9.13E-07	6.66E-07

density or ionisation structure. A number of factors are relevant in determining which region contributes to the emission of a given line. The ion's abundance is important; collisionally excited lines of NeII and OI require Ne^+ and O^0, along with colliding particles such as electrons and/or neutral hydrogen. Collisionally excited lines depend exponentially on the gas temperature through the Boltzmann factor and therefore preferentially trace the hotter regions. In the case of collisionally excited lines in the IR, this temperature dependence is weakened by the fact that the gas temperature is generally much higher than the line excitation temperature, causing the Boltzmann term to tend to unity. Gas density also influences the emissivity of collisionally excited lines through the critical density, above which the line emission is suppressed.

It should also be noted that increasing the X-ray luminosity not only affects the ionisation rate of the wind, but also affects its density. Higher luminosities drive a more vigorous (denser) wind, with a linear correlation between L_X and gas density in the wind as shown in Chapter 2.

5.3.1 Line profiles

Figure 5.1 shows the normalised profiles of the NeII fine structure line at 12.8μm and the OI forbidden line at 6300 Å for the primordial disc model with $\log(L_X/\mathrm{erg\ s^{-1}})$ = 28.3 (left), 29.3 (middle) and 30.3 (right). Figure 5.2 shows the same line profiles for inner-hole models with $\log(L_X/\mathrm{erg\ s^{-1}})$ = 30.3 and inner hole radii of 8.3 AU (left), 14.2 AU (middle) and 30.5 AU (right). Profiles are computed for ten inclination angles from 0^o to 90^o in steps of 10^o. The profiles were degraded to an instrumental resolution of R = 100,000, typical of the best ground based facilities.

Figure 5.3 shows emissivity maps of the primordial disc (left panels) and inner-hole models (right panels), with velocity vectors overlain. The models from top to bottom are for increasing X-ray lumi-

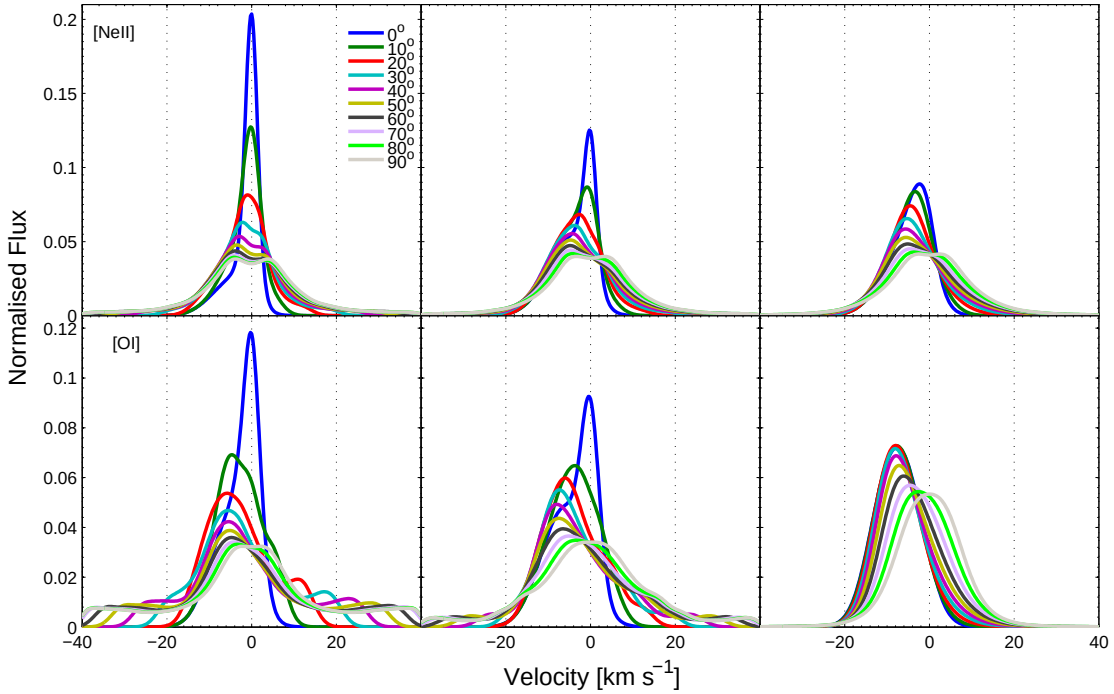

Figure 5.1: Line profiles for (from the top) NeII 12.8μm, OI 6300Å and a generic hydrogen recombination line. The left, middle and right panels are for primordial disc models irradiated by $\log(L_X/\mathrm{erg\ s^{-1}})$ = 28.3, 29.3 and 30.3, respectively. These line profiles are all normalised, such that $\int_{-40}^{40} L[v/(\mathrm{km\ s^{-1}})]\ \mathrm{d}v = 1$. The profiles are colour-coded according to their inclination angle, a colour legend in given in the top-left panel.

nosities (left) and increasing inner hole radii (right). The magenta and yellow contours delineate the region containing 85% of the emission for the NeII 12.8μm and the OI 6300Å, respectively. The noisy appearance of some of the emitting regions are due to Monte-Carlo fluctuations and the imposition of a hard cut-off to draw the contours.

The OI 6300Å line (yellow contours) originates in the wind, or in the primordial disc case, the wind and the very inner (hot and bound-$R < 1$ AU) region of the disc which is where the temperatures are high enough to populate its upper level. The bound disc compared to wind contribution varies with the X-ray luminosity, as the X-ray luminosity increases the density in the wind increases, and therefore so does the wind's contribution which dominates at the highest X-ray luminosity, However, at the lower luminosities the line profiles shows increasing complexity with the multi-component nature of the profile. Therefore, it is the contribution from the bound hot inner disc that produces the 'winged' profiles (resulting from the high Keplerian broadening) for the OI 6300Å clearly seen in the lower luminosity primordial models.

The NeII mid-infrared (MIR) lines can arise in much cooler regions and therefore, while still predominantly produced in the wind, they are not confined to the hot inner layers, but span over a larger region. The NeII emitting region (magenta contours in Figure 5.3) and line profiles vary significantly with X-ray luminosity, tracing the highest electron density regions since $L(\mathrm{NeII}) \propto n_e^2$.

The reason why inner hole models produce very small or no blue-shifts is that at low inclinations both the blue and red-shifted components of the wind are visible through the hole, resulting in only a

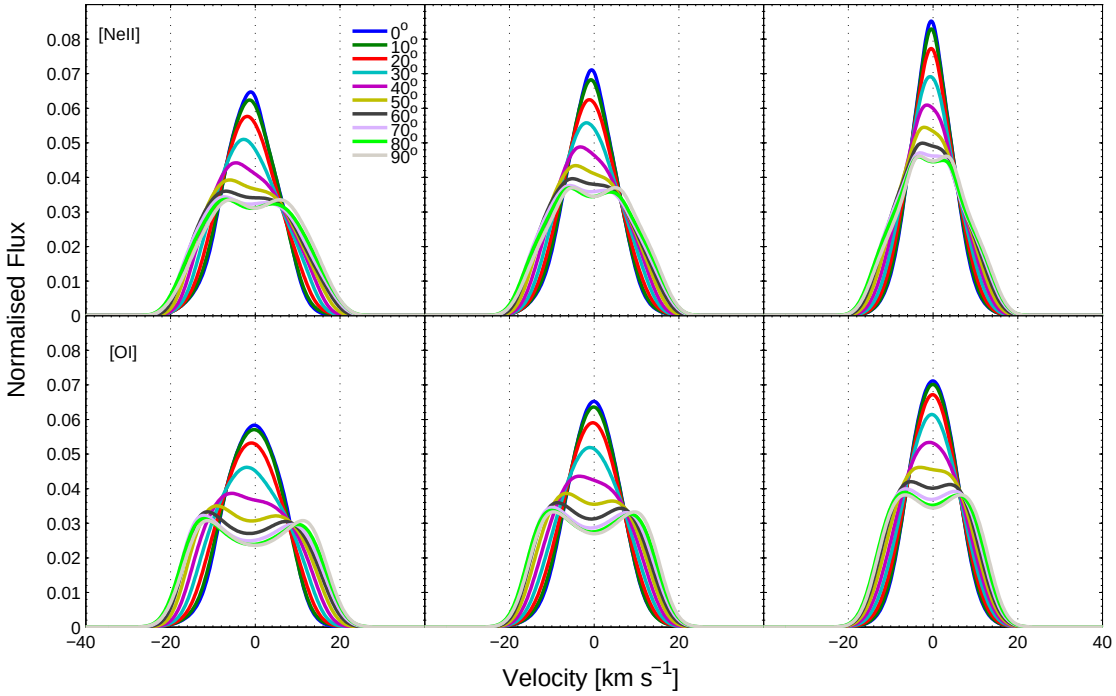

Figure 5.2: Line profiles for (from the top) NeII 12.8μm, OI 6300Å and a generic hydrogen recombination line. The left, middle and right panels are for inner-hole disc models irradiated by $\log(L_X/\mathrm{erg\ s^{-1}})$ = 30.3, with inner holes of radius 8.3, 14.2 and 30.5, respectively. These line profiles are all normalised, such that $\int_{-40}^{40} L[v/(\mathrm{km\ s^{-1}})]\ \mathrm{d}v = 1$. The profiles are colour-coded according to their inclination angle, a colour legend in given in the top-left panel.

small, often undetectable, blue-shift. At higher inclination the lines are Keplerian and no blue-shift is expected anyway. I will discuss the significance of this result in the next section, when comparisons are made with observations, but note at this point that this is only true if the winds are optically thin to the lines in question.

The main profile characteristics are summarised in Tables 5.3 and 5.4. These include the velocity of the peak(s), v_{peak}, the full-width-half-maxima (FWHM) and the profile "type". Where the line profiles have been classified as shown in Figure 5.4. Type "A" is a single peaked profile that could be well approximated by a Gaussian. Type "B" is a single peaked Gaussian-like profile, but with large wings. This is generally produced when there is both a wind and bound disc contribution to the line and/or the emission region is spread over a large radial domain. Type "C" is a double peaked profile, in this case the two values of v_{peak} are given. Type "D" are profiles where two clear peaks are not resolved, yet the profile is broad, flat-topped or significantly asymmetric; in this case the value at the centre of the line (i.e. the middle of the FWHM segment, horizontal dashed red line in Figure 5.4) is given; strictly speaking, this is not the location of the 'peak' however I keep the label v_{peak} for simplicity.

5.3.2 NeII 12.8μm and OI 6300Å radial profiles

The model's radial intensity profiles of the NeII 12.8μm and of the OI 6300Å line are shown in the left and right panels of Figure 5.5. The top panels show the response of the radial intensity profiles of these

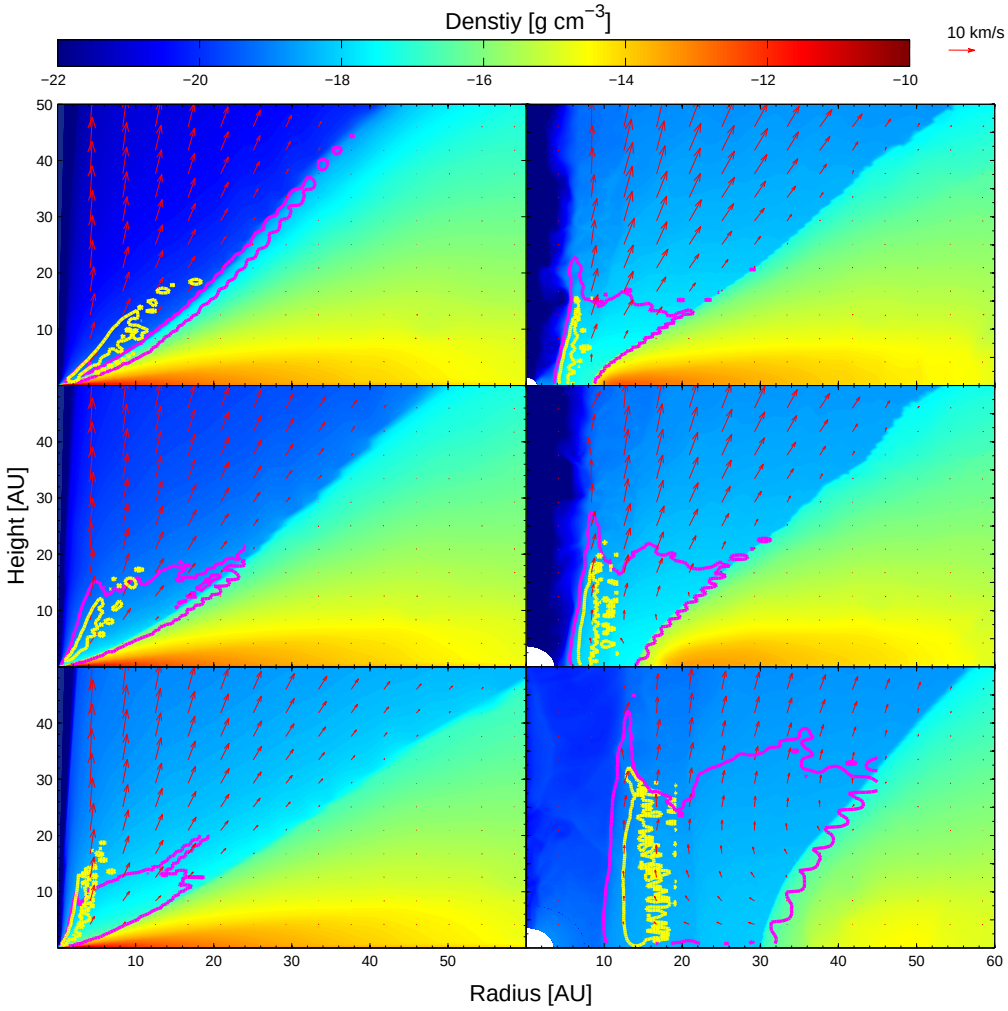

Figure 5.3: Density maps showing the location of the 85% emission region of HI recombination lines (black contour), OI 6300Å line (yellow contour) and NeII 12.8 μm line (magenta contour). The velocity field is represented by the red arrows. *Left:* Primordial disc models irradiated by $\log(L_X/\mathrm{erg\ s^{-1}})$= 28.3 (top), $\log(L_X/\mathrm{erg\ s^{-1}})$ = 29.3 (middle) and $\log(L_X/\mathrm{erg\ s^{-1}})$ = 30.3 (bottom). *Right:* Inner hole models irradiated by $\log(L_X/\mathrm{erg\ s^{-1}})$ = 30.3 with inner hole radii of R_{hole} = 8.3 AU, 14.2 AU and 30.5 AU

lines to changes in the X-ray luminosity. Wider profiles are expected for lower X-ray luminosities since these drive a wind that is less dense than in the higher X-ray luminosity case, meaning that the emission region is more extended. The bottom panels of Figure 5.5 show the radial intensity profiles for discs irradiated by the same X-ray luminosity (2×10^{30}erg/sec), with the black line representing a primordial disc and the red, green and blue lines representing discs with inner holes of size 8.3, 14.2 and 30.5 AU, respectively. Both the NeII and OI lines show a very clear sequence with inner hole size suggesting that spectro-astrometry (e.g. Pontoppidan et al 2009) may perhaps be used to infer the evolutionary states of gaseous discs in the clearing phase. One clear testable fact is that the peak of the emission in all inner-hole cases is at radii smaller than the dust inner radius of the disc. This is obvious by looking at the structure of the wind and the location of the emission region (see Figure 5.3). So the presence of gas in the inner hole of these objects is simply due to gas that is being photoevaporated from the inner edge

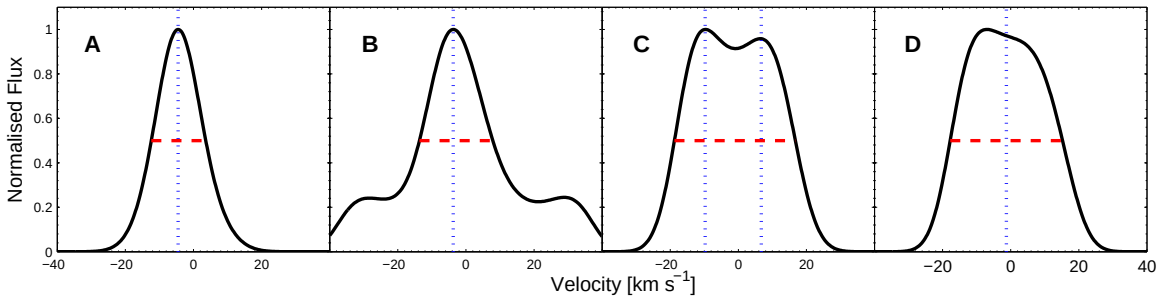

Figure 5.4: Representative shapes for the line profile shapes calculated from our models. Profile A (left) can be well approximated by a Gaussian. Profile B is a Gaussian with large wings. Profile C is a double peaked profile and profile D are profiles where two clear peaks are not resolved, yet the profile is broad, flat-topped or significantly asymmetric. The blue vertical dots show the location of $v_{/rmpeak}$ as given in Table 5.3 and the red horizontal dashed line shows the FWHM for the given profiles.

of the disc.

5.4 Discussion: The emission line spectra

5.4.1 Oxygen

The OI 6300Å forbidden line deserves special attention. As mentioned earlier, this line was detected by Hartigan et al. (1995), blue-shifted by ~ 5 km s^{-1} for all T Tauri with an NIR disc. Detection of this line in T Tauri stars has been reported by various other authors including White & Hillenbrand (2004) and Mohanty et al (2005). The OI 6300Å line profiles reported by Hartigan et al. (1995) all showed a LVC, (also seen also in other forbidden lines, such as OI 5577 Å, and SII 6731 Å), which was interpreted by these authors as being produced in a slow moving disc wind. This was further demonstrated by the fact that blue-shifts were largest for forbidden lines of lowest critical density, suggesting that the emitting region accelerates away from the surface of the disc.

While Hartigan et al. did not ascertain the nature of the disc wind, a photoevaporative wind origin is a natural solution. The EUV calculations of Font et al. (2004) failed to reproduce the observed OI 6300Å line luminosities; a result of the fact that an EUV-driven wind is, by construction, fully ionised. The OI 6300Å line can only then be produced in a thin layer at the bottom of the photoevaporating (ionised) layer. However, an X-ray driven photoevaporation process, yields a disc wind that is predominantly neutral, thus allowing abundant production of the OI 6300Å line. Indeed the model predict luminosities of a few 10^{-5} L$_\odot$ for $L_X = 2\times10^{30}$erg/s, roughly two orders of magnitude higher than the value predicted by Font et al. (2004) and in the range of values reported by Hartigan et al. (1995). Figure 5.6 shows a comparison of equivalent widths observed in the LVC of OI 6300Å by Hartigan et al. (black histogram) with those predicted by the models (red and blue line). The red line represents the primordial disc models irradiated by X-ray luminosities between 2×10^{28} and 2×10^{30} erg s^{-1} and the blue line corresponds to inner hole sources with hole sizes between $\sim$8 and $\sim$30 AU irradiated by an X-ray luminosity of 2×10^{30} erg s^{-1}. The higher equivalent widths shown on the histogram are lines where even the LVC velocity range (-60 to 60 km s^{-1}) is saturated by emission from a jet (the x-axis is truncated in this plot and could go up to 7Å). However, I note that the range of X-ray luminosity, mass and hole size that I have

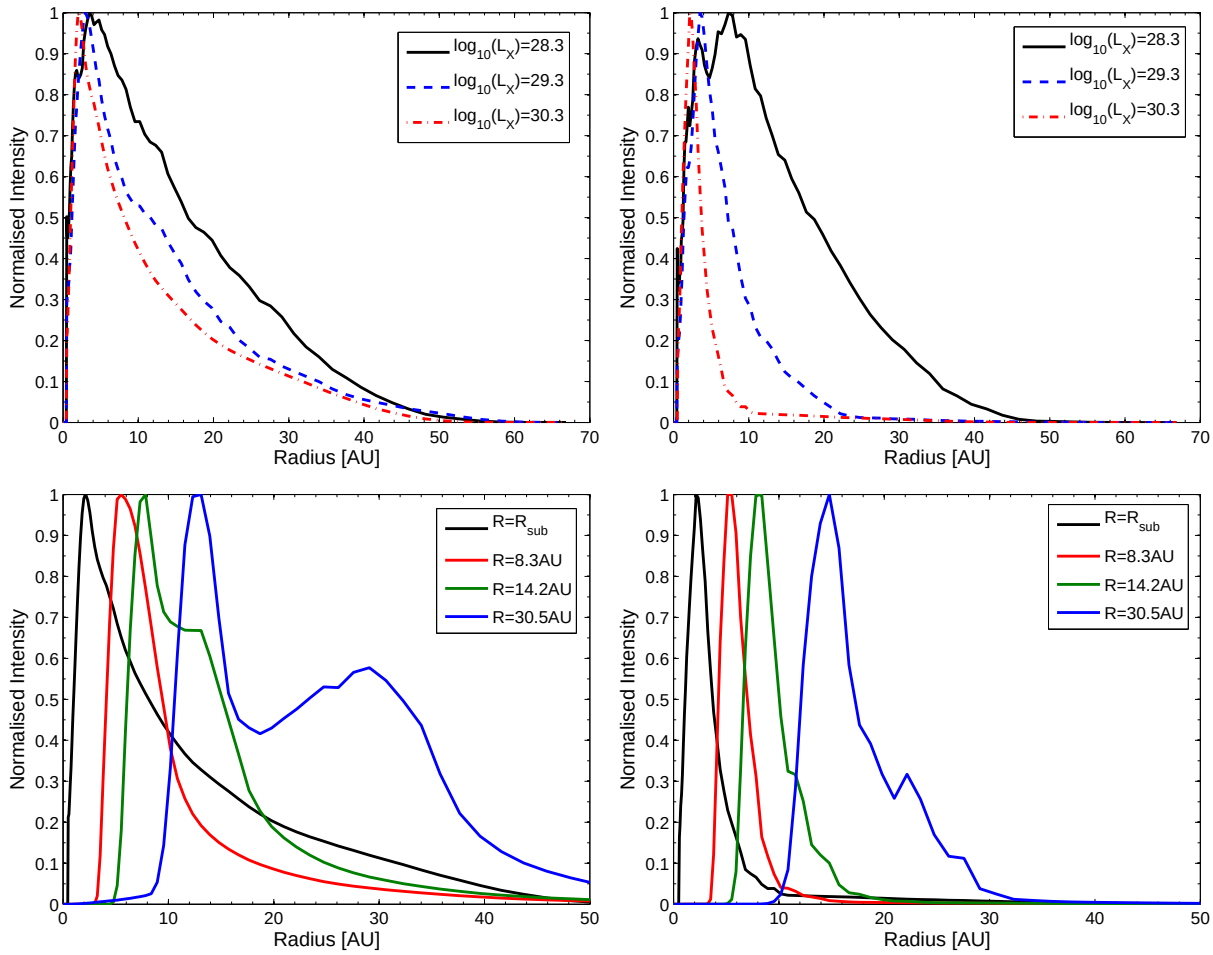

Figure 5.5: Radial intensity profiles of NeII 12.8μm (left panels) and OI 6300Å (right panel). The top panels show how the profiles respond to variations in the X-ray luminosity in the case of a primordial disc, while the bottom panels show the response to different hole sizes (R_{hole}). R_{sub} is the dust sublimation (destruction) radius. All models shown in the bottom panels are irradiated by an X-ray luminosity of 2×10^{30}erg/sec.

investigated is restricted, and detailed modelling of individual sources will provide the ultimate test for an X-ray photoevaporative explanation to the OI problem.

The luminosity of the OI 5577 Å is under predicted by the models compared to the Hartigan et al. (1995) observations. However, this is not a cause of concern, since this is most likely due to the fact that collisions with neutral hydrogen (which are important for the OI 6300Å line) are not available for all levels for the OI 5577 Å line as mentioned above, and it is at this stage not possible to predict the errors in the calculated luminosities for this line.

5.4.2 Neon

Since the prediction by Glassgold et al (2007) and the first detections of the NeII 12.8 μm line in T Tauri discs (Pascucci et al 2007; Espaillat et al 2007; Lahuis et al 2007; Herczeg et al 2007), this line has received a lot of attention in the literature, both observationally (Güdel et al 2010; Pascucci & Sterzik 2009; Najita et al 2009; van Boekel et al 2009; Flaccomio et al 2009) and theoretically (Meijerink et al,

Table 5.3: Line profiles from primordial discs irradiated by $\log(L_X/\mathrm{erg\ s^{-1}})$= 28.3, 29.3 & 30.3. The table lists the velocity of the peak, the full-width-half-maximum (FWHM) and the type of the profile (see Figure 4 for details), for ten inclinations from 0^o to 90^o. The profiles were degraded to an instrumental resolution of R = 100,000.

	NeII 12.8μm								
	$\log(L_X)$= 28.3 erg/s			$\log(L_X)$= 29.3 erg/s			$\log(L_X)$= 30.3 erg/s		
i^o	v_{peak} [km/s]	FWHM [km/s]	Profile	v_{peak} [km/s]	FWHM [km/s]	Profile	v_{peak} [km/s]	FWHM [km/s]	Profile
0	0	3.7	B	-0.25	5.0	B	-2.25	10.2	A
10	-0.25	6.0	A	-0.75	10.8	B	-3.25	10.6	A
20	-1	10.1	A	-2.75	13.9	A	-4.5	11.9	A
30	-1.25	13.6	D	-3.75	15.4	A	-5.25	13.4	A
40	-3/+1.75	15.9	C	-4.25	16.6	A	-5.5	15.0	A
50	-3.5/+2	17.6	C	-4.75	17.6	A	-5.5	16.5	A
60	-3.75/+2.5	18.9	C	-2.25	18.6	D	-5	17.8	A
70	-4/+3	19.8	C	-4.75/+0.75	19.4	C	-4.5	19.0	A
80	-4/+3.5	20.4	C	-4.25/+1.75	20.0	C	-3.75	19.8	A
90	$\pm$3.75	20.8	C	$\pm$3.25	20.6	C	$\pm$2.5	22.6	C
	OI 6300 Å								
	$\log(L_X)$= 28.3 erg/s			$\log(L_X)$= 29.3 erg/s			$\log(L_X)$= 30.3 erg/s		
i^o	v_{peak} [km/s]	FWHM [km/s]	Profile	v_{peak} [km/s]	FWHM [km/s]	Profile	v_{peak} [km/s]	FWHM [km/s]	Profile
0	-0.25	6.4	A	-0.5	10.0	B	-7.5	13.3	A
10	-4.75	14.0	A	-3.75	15.0	B	-7.75	13.0	A
20	-5.75	15.9	B	-6	15.2	B	-8	12.6	A
30	-5.5	16.0	B	-7.25	14.6	B	-8	12.6	A
40	-5.5	16.2	B	-8	16.0	B	-7.75	13.1	A
50	-5.25	17.0	B	-7.5	18.0	B	-7.25	13.9	A
60	-4.75	17.8	B	-6.5	20.1	B	-6	15.0	A
70	-4.25	18.5	B	-5	21.7	B	-4.5	16.0	A
80	-3.5	19.1	B	-3.25	22.7	B	-2.5	16.7	A
90	0	19.5	B	0	23.1	B	0	17.0	A

2008; Schisano et al. 2009; Alexander 2008; Hollenbach & Gorti 2009); it was originally proposed as a probe of X-ray irradiation of T Tauri discs. The large scatter in the L(NeII) for stars of a given L_X may be due to differences in the irradiating spectrum or the disc structure (Schisano et al 2009), variability, or for the higher L(NeII) cases to stellar jets (Hollenbach & Gorti 2009; Shang et al. 2010).

The L(NeII) calculated from the models are in the range of those observed and show a roughly linear dependence with X-ray luminosity. However, what the models show is that this line is produced almost exclusively in the photoevaporating wind, as clear from the blue-shifted profile for non edge-on inclinations (Table 5.3 and Figure 5.1). It is also clear that a clean linear relationship with L_X is not expected (or found) given that the wind structure and the NeII emitting region change in response to different X-ray luminosities. In this perspective it is easy to understand the scatter in the L(NeII)-L_X relation noticed by Güdel et al (2010) even for the non-jet sources.

The NeIII to NeII line ratio for our models is never lower than $\sim$0.1, while observations generally indicate lower values, e.g. $\sim$0.06 (Lahuis et al 2007), $\sim$0.045 (Najita et al 2010), although in the case of WL5 a value of $\sim$0.25 is reported by Flaccomio et al (2009). Unfortunately few detections of this line are

Table 5.4: Line profiles from inner-hole discs irradiated by $\log(L_X/\mathrm{erg\ s^{-1}})$ = 30.3 erg/s, with inner hole radii of 8.3, 14.2 and 30.5 AU. The table lists the velocity of the peak, the full-width-half-maximum (FWHM) and the type of the profile (see Figure 4 for details), for ten inclinations from 0^o to 90^o. The profiles were degraded to an instrumental resolution of R = 100,000.

				NeII 12.8μm					
	R_{hole} = 8.3 AU			R_{hole} = 14.2 AU			R_{hole} = 30.5 AU		
i^o	v_{peak} [km/s]	FWHM [km/s]	Profile	v_{peak} [km/s]	FWHM [km/s]	Profile	v_{peak} [km/s]	FWHM [km/s]	Profile
0	-1	15.0	A	-0.5	13.3	A	-0.5	10.9	A
10	-1.25	15.4	A	-0.75	13.9	A	-0.5	11.2	A
20	-2	16.7	A	-1.25	15.2	A	-0.5	12.1	A
30	-2.75	19.7	A	-1.75	17.6	A	-0.75	13.7	A
40	-1.5	23.3	D	-1	20.8	D	-1.5	15.9	A
50	-1.5	26.2	D	-1	23.5	D	-0.5	18.2	D
60	-1.5	28.4	D	-1.25	25.8	D	-0.75	20.0	D
70	-7.25/+2.5	29.8	C	-5.75/+2.25	27.2	C	-3/+1.5	21.3	C
80	-7/+4.25	30.2	C	-5.75/+3.75	27.8	C	-3.25/+2.25	21.7	C
90	$\pm$5.75	30.1	C	-5/+5	27.5	C	$\pm$3.25	21.3	C
				OI 6300 Å					
	R_{hole} = 8.3 AU			R_{hole} = 14.2 AU			R_{hole} = 30.5 AU		
i^o	v_{peak} [km/s]	FWHM [km/s]	Profile	v_{peak} [km/s]	FWHM [km/s]	Profile	v_{peak} [km/s]	FWHM [km/s]	Profile
0	-0.25	17.1	A	0	14.7	A	0	13.5	A
10	-0.25	17.2	A	0	15.0	A	0	13.6	A
20	-1	18.6	A	-0.25	16.2	A	0	14.2	A
30	-2	22.4	A	-1	19.1	A	-0.25	15.7	A
40	-0.75	26.9	D	-0.5	23.3	D	-0.75	18.5	A
50	-9/+5	30.1	C	-6.5/+4.25	26.6	C	-0.25	21.5	D
60	-11.25/+7.25	32.4	C	-8.75/+6.25	28.9	C	-5.25/+4	23.8	C
70	-12.25/+8.75	34.0	C	-9.75/+7.75	30.5	C	-6.25/+5.25	25.3	C
80	-12/+10.25	34.9	C	-10/+8.5	31.4	C	-6.75/+5.75	26.2	C
90	$\pm$11.25	35.0	C	$\pm$9.5	31.6	C	$\pm$6.5	26.5	C

currently available and it is therefore hard to draw statistically significant conclusions. To make matters worse this ratio is quite uncertain in theoretical models due to the lack of neutral collision rates, as mentioned above, and uncertainties in the charge exchange coefficients. In view of the current observational and theoretical difficulties with this line ratio, its diagnostic power cannot yet be harnessed.

5.4.3 Sulphur

The models predict SII 6717Å and 6731Å lines in the range observed by Hartigan et al. (1995) for the LVC. The ratio of the 6731Å to the 6717Å, which is a useful density diagnostic, is approximately two in the models, and it compares well with the value reported for most of the sources in Hartigan et al. (1995). A ratio of two at $\sim$7000 K corresponds to an *electron* density of just below $10^4 \mathrm{cm}^{-3}$, again consistent with a wind origin for this line. Furthermore, all of the detections for the LVCs of these lines in Hartigan et al. (1995) where the source presents with an NIR disc show a small blue-shift, reinforcing the conclusion that all discs show evidence of a wind which can be produced by photoevaporation. The OI

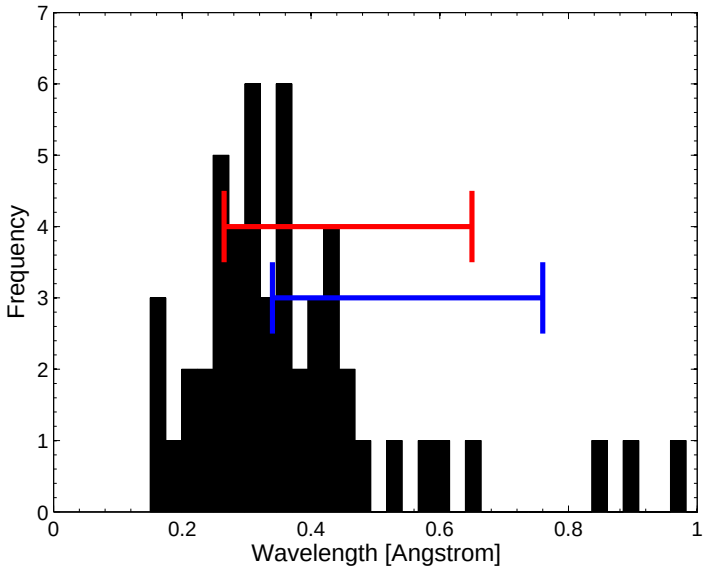

Figure 5.6: OI 6300 Å equivalent width histogram for the LVC sources in HEG95 compared to the model predictions for primordial discs (red line) irradiated by X-ray luminosities between 2×10^{28} and 2×10^{30} erg/sec, and compared to inner hole sources (blue line) with hole sizes between $\sim$8 and $\sim$30 AU irradiated by an X-ray luminosity of 2×10^{30} erg/sec. The error in the equivalent widths is around the 10-20% level.

to SII ratios also compare favourably, when the OI line luminosities observed are in the range predicted by the model (i.e. $< 10^{-4}L_{\odot}$). However, I note that this ratio can be as large as one order of magnitude for the higher OI luminosities detected, these detections correspond to objects where the jet emission has saturated the LVC and are associated with large equivalent widths in the LVC OI line (e.g. CW Tau, DQ Tau and HN Tau).

5.4.4 Magnesium

The models predict a rather strong MgI line at 4573 Å ($\sim10^{-5}L_{\odot}$ for $L_X = 2\times10^{30}$erg s^{-1}). This line has been detected to date, in four young low mass stars, namely VY Tauri (M0; Herbig 1990), XZ Tau B (M1; White & Ghez 2001) and very recently in the low-mass variable TWA 30 (Looper et al 2010) and TW Hya (Pascucci et al. 2011). Detection of this line in M-stars is rendered possible by the much lower stellar continuum in the B-band compared to higher mass stars and the strength of this line indicates that it should be target for resolved spectroscopic measurements, providing complementary observations to the OI 6300Å line, particularly around lower mass stars.

5.5 A direct comparison: TW-Hya

The recent observation of a blue-shifted NeII 12.8μm line profile by Pascucci & Sterzik (2009) in a few well known YSOs with discs, including TW Hya, has been interpreted as the first direct evidence for photoevaporation. Unlike the blue-shifted OI 6300Å line, the NeII 12.8μm profile for the pure EUV wind (Alexander, 2008) is consistent with the observed profile from TW Hya. Furthermore, Pascucci et al. (2011) supplemented the NeII observations with optical forbidden lines in Oxygen and Sulphur. The

EUV model can successfully reproduce the NeII line (Alexander, 2008), although as discussed above, the EUV model cannot explain the luminosities of the OI line observed in all T Tauri stars with NIR discs by Hartigan et al. (1995), and as described in Chapter 3 the EUV field in the presence of the X-rays, is unable to reach the disc's surface. Therefore, the TW Hya observations need to be considered within the framework of the X-ray photoevaporation model, which as I have discussed in this thesis, best describes the true photoevaporation flow from discs.

TW-Hya is a $0.7M_{\odot}$ star (Muzerolle et al. 2000) at a distance of 51 ± 4pc (Mamajek et al. 2005), with an X-ray luminosity of 1.4×10^{30} erg s^{-1}(e.g. Kastner et al. 1999). Therefore, the most appropriate model to use for a first analysis is the $0.7M_{\odot}$, $L_X = 2 \times 10^{30}$ erg s^{-1} calculated in this work. Furthermore, TW-Hya is a disc that presents at very low inclinations, with estimates in the range 4–8^{o}, thus effects from absorption along the line of sight through the disc's atmosphere can be considered a minimal effect (e.g. Schisano et al. 2010). The first comparison that can be performed is the measured line fluxes; the observed line flux in NeII is $4.5 \pm 0.3 \times 10^{-14}$ erg s^{-1} cm^{-2} compared to a predicted line flux of $6.6 \pm 1 \times 10^{-14}$ erg s^{-1} cm^{-2} for the $L_X = 2 \times 10^{30}$erg s^{-1}, and therefore a simple scaling to the observed X-ray luminosity of TW-Hya means that the predicted line luminosity is consistent with the observations. In order to compare the theoretical line profiles to the observed profiles they are scaled to the same total flux and I use the 6^{o} model as it lies in the middle of the current estimates for the inclination of the inner disc (Although at low inclinations the line profile is not a particularly strong function of inclination and cannot be used to further constrain the inclination). This comparison is shown in Figure 5.7, which shows excellent agreement with the observations. Thus it is clear that while the NeII line provides clear evidence for a photoevaporative flow emerging from the disc, it is unable to constrain the mass-loss rate, Since the line can be matched by a $10^{-10}M_{\odot}$ yr^{-1} pure EUV flow, or a $10^{-8}M_{\odot}$ yr^{-1} X-ray driven flow. This can be understood since the NeII line traces electron density and the EUV flow and X-ray flow have very similar electron density structures. The EUV flow has an ionization fraction of unity, while the X-ray flow has an ionization fraction of approximatively ~ 0.01 in the region of NeII emission. Therefore, the two order of magnitude in mass-loss rate is counteracted by a two order of magnitude difference in ionization fraction.

As both the EUV- and X-ray model produce a good match to the NeII data, it seems that this particular diagnostic cannot be used to discriminate between them. Therefore other diagnostics are required such as the OI 6300Å line discussed previously, that only the X-ray driven photoevaporation model which predicts a largely neutral wind has been able to reproduce the observed luminosities and blue-shifts. Towards this aim Pascucci et al. (2011) also considered the emission from optical forbidden lines in OI, SII and MgI with non-detections presented in a few other optical lines (NII, OII). However, unlike the observations of Hartigan et al. (1995) these optical lines show no blue-shifts, but with luminosities (in solar units) in OI 6300Å of 1.1×10^{-5}, OI 5577Å of 1.5×10^{-6}, SII 4067Å of 1.4×10^{-6}, a SII 4077Å upper limit of $< 4.8 \times 10^{-7}$ and MgI 6.4×10^{-7}. While the Oxygen line flux is roughly consistent with the model predictions (note again the model prediction for the OI 5577Å line is a lower limit as the model does not include the collision rates with neutrals), it over predicts the Sulphur and Magnesium lines. Pascucci et al. (2011) suggested that the low luminosities could arise from a depletion of sulphur in the disc, something suggested by Lamzin et al. (2004) who argued that refractory elements are depleted in the TW Hya gas disc. This emphasises the problem that elemental abundances will always be an issue of in these calculations leading to an additional sources of uncertainty. Or as we discuss below if there is

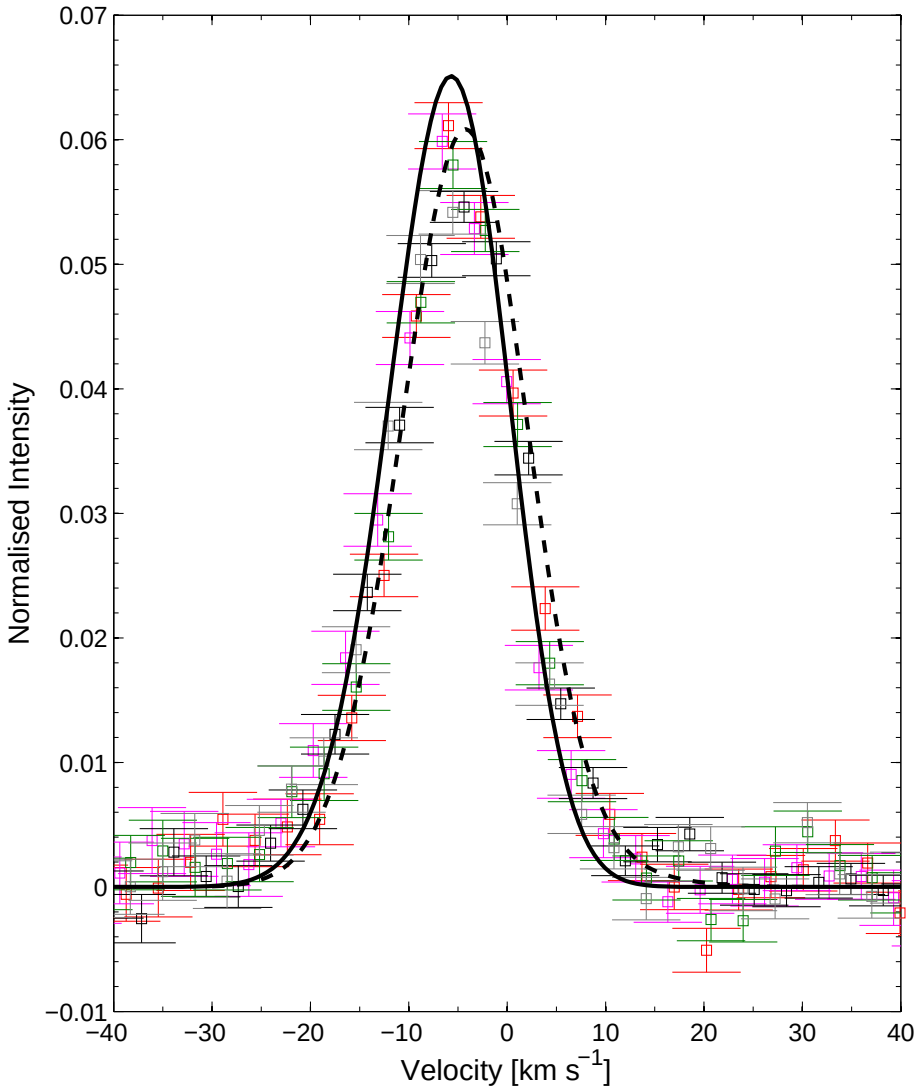

Figure 5.7: Theoretical NeII profile for primodial disc (solid) and preferred 'gap' disc (dashed) discussed below, compared to the observed spectrum of TW Hya at six different PAs: green - 0^o, magenta - 90^o, black - 180^o, red - 270 ^{o} and grey - 333^o.

a gap in gas disc that corresponds to the dominant emission region then these lines will be observed with significantly lower luminosities.

However, the most curious aspect of these observations is the fact that they are not blue-shifted. This is curious as the optical lines have higher Boltzmann factors and thus are preferential emitted from gas that is hotter than the NeII emitting gas. This is clearly shown in Figure 5.3, where the OI emission traces the hot $\gtrsim 10^4$K gas at small radii, whereas the NeII emission traces the flow at larger radii. This means that while there is a photoevaporative flow emerging from the disc at radii $\gtrsim$ 4AU, there is no overall blue-shifted flow emerging from inside a few AU. Since TW Hya has been classified a 'transition' disc (e.g. Calvet et al. 2002), this may provide an explanation for this observation as the inner disc is optically thin to optical and IR photons.

As mentioned at the start of this Chapter, TW Hya is an accreting 'transition' disc consistent with a

photoevaporative origin. Thus there are several possible inner gas disc structures depending on which mechanism created the inner dust hole. I will now discuss the implications of these structures for the observed optical emission lines.

5.5.1 The structure of TW Hya's inner gas disc

In the Introduction I outlined several mechanisms which are thought to give rise to an observed accreting 'transition' disc: photoevaporation, a planet embedded in the disc (Rice et al. 2003) and grain growth (Dullemond & Dominik, 2005). For TW Hya to still be an accreting 'transition' disc there must be an inner gas disc that is being accreted by the star. However, in the case of grain growth the gas disc is unchanged from a primordial one, and the flow topology will be identical to a primordial disc. An embedded planet creates a gap in the gas disc, where this gap has size that depends on the mass of the planet. For a small planet the gap will be much smaller than the scale of the photoevaporative flow ($\mathscr{O} r_g$), and the photoevaporative flow will be unchanged from the primordial one. However, a massive planet/binary companion could open a gap larger than the photoevaporative flow scale, and thus create a gap in the flow itself. Therefore, like a transition disc created through grain growth, a transition disc created by a small embedded planet will have a photoevaporative flow almost identical to the photoevaporative flow from a standard primordial disc. Although, with an opacity hole inside the inner edge of the outer gas disc, due to the removal of dust opacity. However, in the case of a gap opened by photoevaporation it can be much larger, and in the case of TW Hya possible extend from ~ 0.6AU ($\sim 0.1 r_g$) to $\sim 2-4$ AU where the inner edge of the dust disc is found (e.g. Calvet et al. 2002, Razak et al. 2007). Therefore, the photoevaporative flow structure may well be different to the primordial flow near the gap. These scenarios are schematically shown in Figure 5.8, with the possible flow structures and emission regions for the optical lines and the NeII line. The case of a standard primordial disc is shown for instructive purposes at the top, where the OI emission arises from around 1AU, whereas the NeII emission arises at slightly larger radii ~ 5 AU. For a transition disc created by a small planet or by grain growth, the flow structure and emission regions are unchanged, the only difference is the inner 2-4AU of the disc are optically thin in the line. In the final case there is a large gap in the disc, with an inner optically thin (in dust and the line) gas disc extending out to $\sim 0.1 R_g$ and an outer gas and dust disc starting at 2–4AU. In this case the OI emission only arises from the bound atmosphere of the inner disc and the NeII emission arises from a photoevaporative flow being driven of the outer disc, and there is no emission from within the gap.

In all cases the non blue-shifted optical lines can be understood, since TW Hya is at very low inclination then the line of sight will see both sides of the flow and hence the red-shifted flow will counterbalance the blue-shifted flow leaving a total line profile that is centred on the stellar velocity.

In order to investigate these possibilities, I use the primordial disc model calculated earlier to estimate the OI 6300Å line profiles from the type of disc structures expected. I note that since the NeII emission is dominated at radii larger than the inner hole the line profile shown in Figure 5.7 is unaffected. When the flow topology is primordial disc-like (grain growth or small planet); to represent a dust hole in the gas disc the disc's mid-plane is made optically thin to the line, thus any lines of sight that go through this dust hole 'see' both sides of the wind. In the case of a photoevaporation created transition disc it is much harder to develop a model; to do so properly would require a new hydrodynamic calculation, since

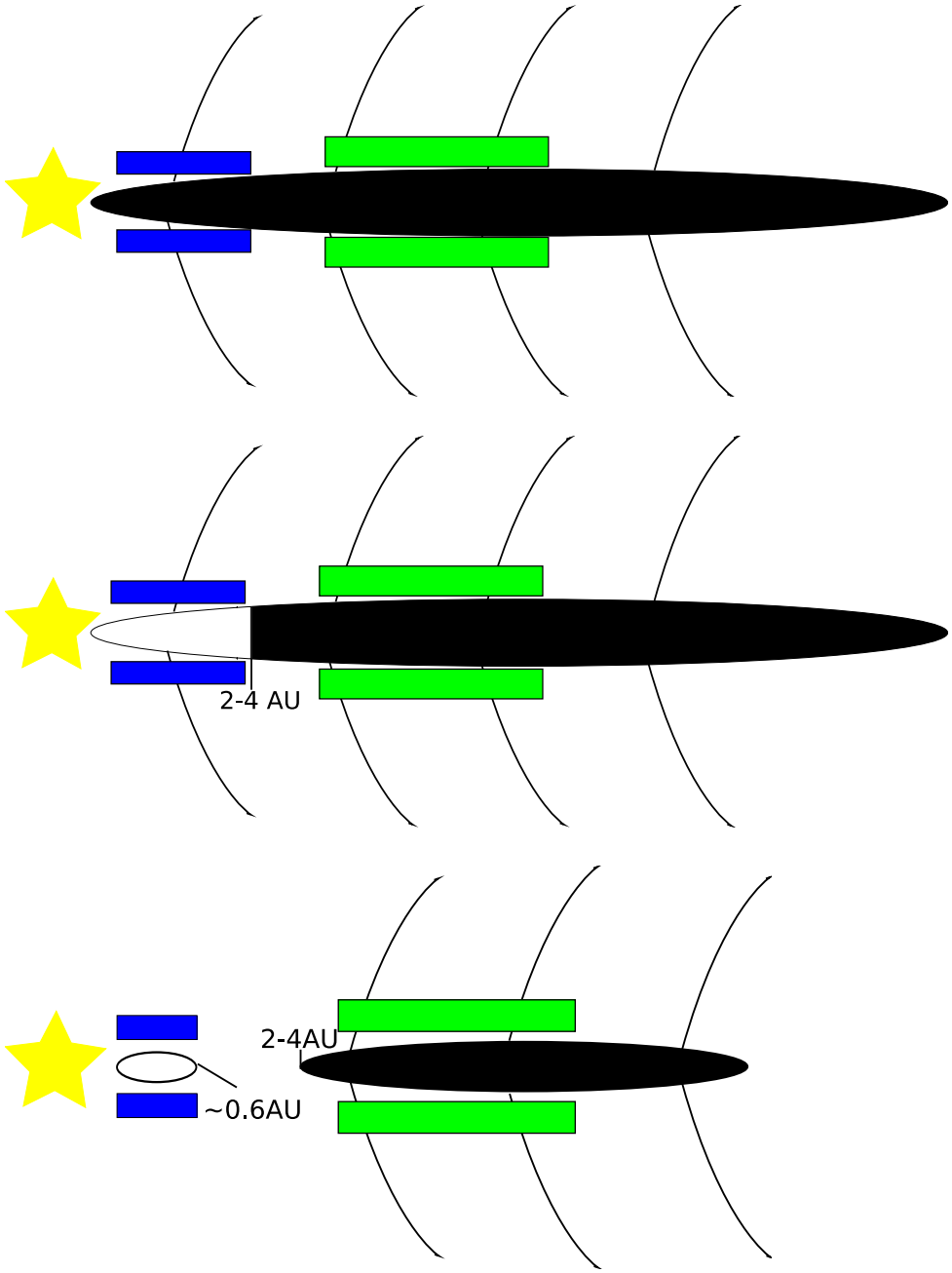

Figure 5.8: Schematic showing possible disc structures for TW Hya. The blue region represents the OI emitting gas, and the green represents NeII emitting gas. The top disc represents a primordial gas and dust structure. The middle disc shows an inner opacity drop in the dust disc due to grain growth or a small gap due the presence of a small planet; however the gap in the gas disc is small compared to the photoevaportive flow scale. The bottom disc shows a large gap in the gas disc, either carved out by photoevaporation of the presence of a massive planet/binary companion.
A black filled disc indicates it is optically thick to the line emission, whereas a white disc represents that it is optically thin to line emission.

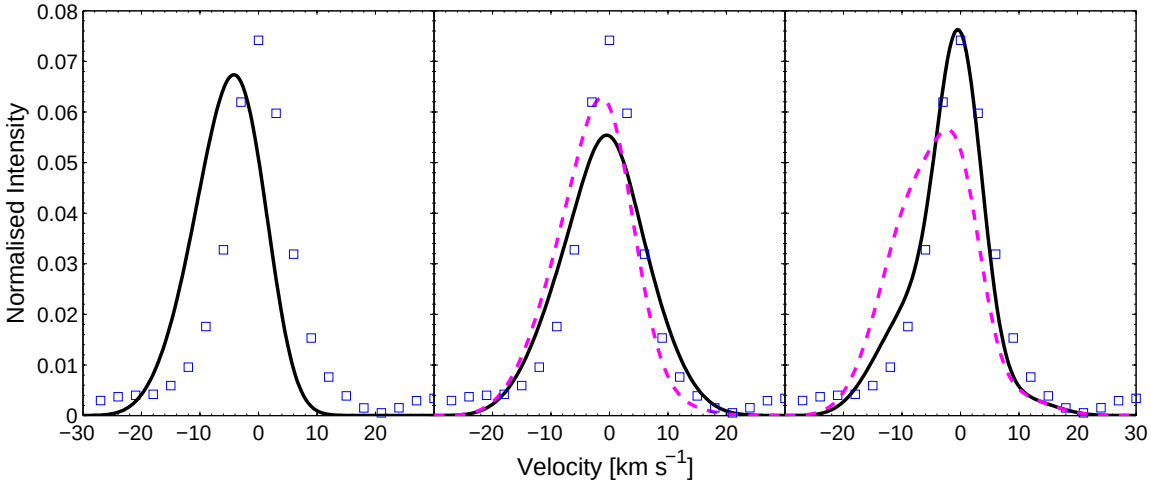

Figure 5.9: Comparisons of theoretical OI 6300Å line profiles to the observed emission, the blue points represent the median OI 6300Å profile (Pascucci et al. 2011) and the lines represent the theoretical profiles. The left-hand panel shows a theoretical profile for a primordial disc. The centre panel shows a primordial gas disc with an opacity hole at 2AU (dashed) and 4AU (solid). The right-hand panel shows a gap in the primordial disc from 0.6AU to 2AU (dashed) and 4AU (solid).

I have performed no calculations with an inner gas disc. However, a first approximation comes from starting with the primordial flow structure and making the inner hole optically thin in the line as before, along with removing the flow and disc from within the gas disc's gap. This is a reasonable starting point since in this case I expect the OI to come mostly from the bound inner gas disc, which is fairly accurately described in the primordial disc calculation.

In Figure 5.9 I show these estimated line profiles compared with the observed profile and note the other observed optical lines have an identical morphology in both the observations and models.

This clearly demonstrates that while a line centred on the stellar velocity can be accounted for by any of the 'transition' disc models, the models that do this by 'seeing' both sides of the wind are too broad to match the observed line. In fact the line is close to being explained by thermal and Keplerian broadening alone, without any kinematic broadening in the wind. This is shown in the case of the simple model used as an attempt to replicate the emission from a disc with a large gap in the gas disc. As mentioned earlier the OI emission arises from two components: the hot inner bound disc and the inner region of the flow. In the gap model the inner flow falls in this gap so that the bound hot inner disc is the only component remaining. Therefore, this naturally gives rise to a component that is only broadened by thermal and Keplerian components. Furthermore, this analysis shows that the opacity hole must extend to a radii greater than 2AU otherwise the OI emitting component would show up as a detectable blue-shift in the line profiles. The model with a gap between 0.6AU and 4AU is clearly the best fit, although it does not reproduce the line wings perfectly.

While this analysis is simplistic, it is clear that the optical lines cannot arise from a region of the disc that is photoevaporating. Therefore, either the flow is somehow suppressed at small radii or there is a large gap in the disc such that there is no flow arising from the inner disc. Resolved observations that determine the radial location of the NeII and optical lines should help unravel the reason why the NeII emission is emitted from within a photoevaporative flow and the optical lines are not. Should spatially resolved spectroscopy confirm this gap scenario, then observational confirmation of a massive companion

would determine whether this is a 'transition' disc that has been generated by planet formation, otherwise a photoevaporation origin is the remaining viable alternative.

5.6 Conclusions

In this Chapter I have calculated the line emission from gas within a photoevaporative wind and compared this with observations. The main findings are summarised below:

1. Line emission provides a useful diagnostic to probe a photoevaporative wind, which can be used to test the photoevaporation model.

2. The X-ray photoevaporation model provides a natural solution to the presence of a blue-shifted OI 6300Å line, observed by Hartigan et al.(1995). However, an FUV or EUV driven photoevaporative flow is incapable of reproducing this observation.

3. The NeII line provides an excellent tracer of the photoevaporative wind, although it is unable to place constrains on the mass-loss rates.

4. Line emission from 'transition' discs can be used to to probe the presence and structure of an inner gas disc.

5. The 'transition' object TW Hya shows direct evidence for photoevaporation in the NeII line, however there is no evidence in the optical lines for a photoevaporative flow. This indicates that the gas disc in TW Hya is not a standard primordial gas disc, and the dust's opacity gap is indicative of a gap in the gas disc.

6. The preliminary findings based on rough modelling of the OI line suggest that the inner disc of TW Hya is truncated at the same radius in both gas and dust.

In this Chapter I have discussed emission lines as a way of investigating photoevaporative flows. However, line emission is only a local probe of certain regions of the flow at specific density and temperature regimes. Therefore, in the next Chapter I will consider a global tracer for a photoevaporative flow.

6

Detecting the wind II: dust emission in edge-on discs

In the previous two Chapters the tests of the photoevaporation model have either relied on indirect statistical comparisons, or local tests of small scale regions of the photoevaporative flow. Whilst these tests have proved invaluable in gathering information about the presence of photoevaporation and its implications for disc evolution, it would be extremely useful if we had a large scale probe of the entire flow.

In Chapter 5 I showed that line emission from the gas in the flow was locally confined to regions with a specific density and temperature, which does not provide an overall picture of the global flow structure. However, we know protoplanetary discs also contain a large reservoir of small dust grains, which can be entrained in the photoevaporative flow. These, entrained dust grains could then be carried to large a radius, enabling the global flow morphology and structure to be traced by the dust grains. Obviously, this extra dust mass in the photoevaporative wind is going to have negligible impact on the SED of a young star, as the SED is dominated by the dust properties at and just above the disc's photosphere. However, in the case that the disc is edge-on, the central star is obscured by the optically thick inner dust disc, allowing low surface brightness imaging of scattered light from dust grains in the optically thin regions. Scattered light imaging of edge on discs has been used to infer properties of the disc's atmosphere (e.g. Watson et al. 2007) and the presence of in-falling rotating envelopes around young (Class I) stars (Stark et al. 2006). Therefore, it is certainly possible that dust entrained in a photoevaporative wind may also be a possible target for scattered light imaging. With a proposal of this type the main issue is the possibility of actually observing the faint emission from a tenuous photoevaporative wind above the disc's atmosphere, and this boils down to resolution and detection limits. Therefore, flows which are more luminous and occur on larger scales will be easier to detect and resolve with current facilities. The scale of any photoevporative flow clearly scales with mass through $R_g \propto M_*$ and as we go to larger mass the scale of the flow will become larger. In order to consider how the luminosity of dust in a photoevaporative region will vary with mass, I assume that the luminosity of such a region is dominated by scattered light (which it will

be since the region will be optically thin). So the luminosity of this region L_s will scale as the number of scattered photons, which is given by:

$$L_s \propto L_* P_s \tag{6.1}$$

where P_s is the photon scattering probability, which will scale as the size of the region over the photon mean free path ($R_g/\ell_{\rm mfp}$), where $\ell_{\rm mfp}$ is given by the density multiplied the scattering cross-section (or size of the dust grain squared). Now using $\dot{M}_w = n \times A \times c_s$, we see that the density is given by $n \propto \dot{M}_w R_g^{-2}$ and the luminosity of this region scales as:

$$L_s \propto L_* M_*^{-1} \dot{M}_w(M_*)\, \sigma(M_*) \tag{6.2}$$

Since the luminosity of pre-main sequence stars varies as a high power of stellar mass $L_* \propto M_*^{3-4}$ then the luminosity of these regions will also increase as a high power of stellar mass. Herbig Ae/Be stars are more luminous than their lower mass T Tauri counterparts and provide an opportunity to observe the expected large scale morphology in resolved images. As mention above such analysis will be only useful for discs observed at nearly edge-on inclinations. Several edge-on discs around young stars exhibit extended emission above and below their mid-plane at NIR wavelengths (e.g. Padgett et al. 1999 & Perrin et al. 2006) and some have been further imaged through AO systems providing excellent spatial resolution, as in the case of PDS 144N (Perrin et al. 2006). Therefore, edge-on discs around Herbig Ae/Be stars provide the perfect opportunity to detect a disc wind on a global scale, through light scattered by the dust grains that will inevitably be entrained by the wind.

In this Chapter I present a 'proof of concept' calculation to investigate the imprint of photoevaporation on the extended emission observed around edge-on Herbig Ae/Be stars. I will compare our model to current observations of edge-on discs, along with following the fate of crystalline grains in the wind as they are transported to large radii.

6.1 Model

Considering the force balance on a dust grain, it is easy to show that small dust particles are entrained in a photoevaporative wind, which carries them out to large distances. Takeuchi et al. (2005) showed that the drag force on a grain is approximately:

$$F_d \approx \frac{m_d \rho_w v_w^2}{\rho_d a} \tag{6.3}$$

where m_d, ρ_d and a are, respectively; the mass, the density and the radius of a dust grain (assumed to be spherical) and ρ_w and v_w are the density and velocity of the wind. At large radius ($z/R > 1$) the flow is approximately spherical, implying $\rho_w v_w$ falls off as $1/r^2$. Since gravity also falls off as $1/r^2$ and v_w increases monotonically with radius, then if a grain is still entrained when the centrifugal force falls away ($l \sim R_{\rm launch}$), it will be entrained permanently, allowing dust to be carried to very large distance from the star, since the drag force will dominate over gravity.

I build a simplified model to test the possibility of extended emission from dust grains due to a photoevaporative wind, and I choose a set of assumptions that allows us to place an upper limit on

this expected level of emission. Namely I assume that the entire dust population is able to reach the launching surface of the wind via some turbulent mechanism and ignore the effects of settling and grain growth. This simple model ignores the details of the bound regions of the disc and thus ignores any emission produced by this region, including *only* the wind itself and its contributions to emission. This simplification means the model will not be accurate near the mid-plane, where emission from dust in the disc's upper atmosphere dominates over the wind emission. Therefore, the model will be unable to reproduce the observed intensities and optical depths seen at several scale heights above and below the mid-plane in an edge-on disc; however, here we are interested in the extended emission, which in the absence of an in-falling envelope will be dominated by the photoevaporative wind.

The method for constructing scattered light images can be split into three separate parts: (i) hydrodynamic calculations of the photoevaporative wind; (ii) calculation of the dust profile distribution and crystallinity based on the hydrodynamic solution; (iii) radiative transfer modeling of the dust distribution.

6.1.1 Hydrodynamic photoevaporative wind

While the wind driving source for lower mass (T Tauri) stars is likely to be X-rays as described throughout this thesis, the wind driving source around intermediate mass stars has not yet been thoroughly investigated. X-ray photoevaporation may still occur to some degree; however, the lower L_X/L_{bol} ratio of Herbig Ae/Be compared to T Tauri stars (e.g. Albacate Colombo et al. 2007) and their higher EUV fluxes, may reduce the role of X-rays in driving the wind. I adopt here the EUV driven wind of Hollenbach et al (1994) and hydrodynamic solution of Font et al. (2004), which is a *simple* and *scalable* hydrodynamic solution, allowing us to consider a wide range of parameter space, something not possible with more complicated FUV models (Gorti & Hollenbach 2009) or X-ray models described in Chapter 3. The simplified EUV treatment is suitable for the purpose of this work which aims at being the first approach in studying the qualitative aspects of scattered light emission from a disc wind. To this end, I have repeated the calculation of Font et al. (2004) and Alexander (2008) and I refer the reader to these papers for a detailed description of the model setup, although the basics are summarised below.

6.1.2 Model Setup

As the mass-loss rates are not well known for Herbig Ae/Be stars, I have left the ionizing luminosity (which sets the mass-loss rates) for an EUV driven wind (Hollenbach et al. 1994) as a free parameter and consider the effect of changing mass-loss rates on the morphology, colour of the emission and crystallinity distribution in the winds. I consider an EUV wind from a primordial disc around a $2.5 M_{\odot}$ star with a range in ionizing luminosity from 10^{41} to 10^{45} s^{-1} in steps of 1 dex. These luminosities correspond to mass-loss rates in the range $10^{-10} - 10^{-8} M_{\odot} \mathrm{yr}^{-1}$ and are similar to values calculated by Alexander et al. (2004). In order to calculate the images, I compute scattered light images at 1.6, 2.1 & 3.8μm with band passes corresponding to the H, K' & L' bands. In order to consider the relative contributions of crystalline to amorphous dust I take the calculated crystallinity fractions in the disc of Dullemond et al. (2006) for an evolved Herbig Ae/Be star. I further assume that this disc crystallinity fraction is the same at the base of our photoevaporative wind, such that the crystallinity fraction along the streamline can be calculated by following the thermal evolution of the dust entrained on that streamline.

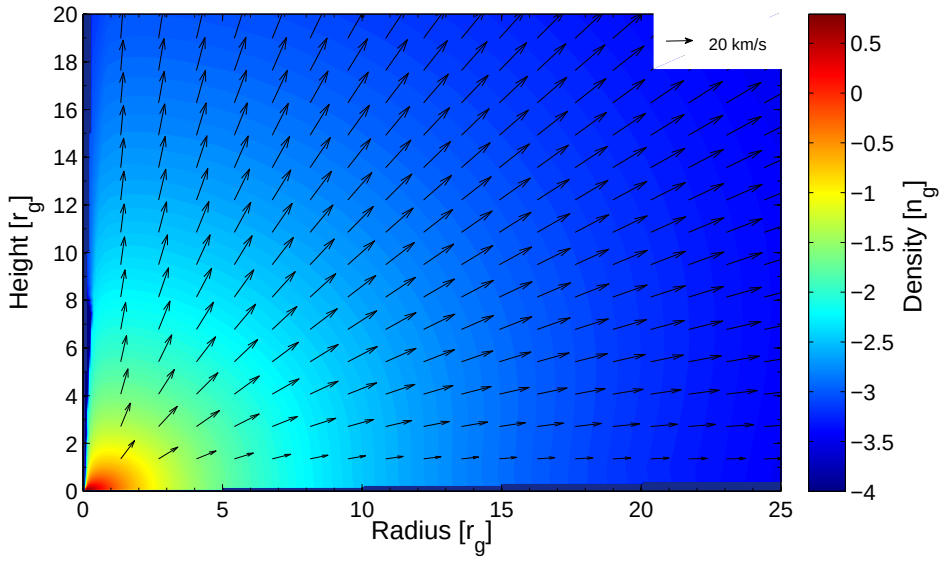

Figure 6.1: EUV wind structure: the colour-map shows the density, while the arrows show the direction and magnitude of the gas flow. Note that just after launch the flow is very close to being spherical.

Numerical EUV Photoevaporative Wind

In order to determine an accurate kinematic structure of the wind I must compute a numerical solution to the problem. I use the ZEUS2D code (Stone & Norman 1992a) and employ a spherical grid with $\theta = [0, \pi/2]$, the radial grid cells are logarithmically spaced, such that I have adequate resolution at small radius to resolve the onset of the flow. The calculation is an isothermal wind calculation with the sound speed set to $c_s = 10\text{km s}^{-1}$ and the radius scaled to the length scale r_g. I use a radial range of $r = [0.05, 40]r_g$ with $N_r = 240$ and $N_\theta = 50$. The number density at the base (i.e. the density along the $\theta = \pi/2$ axis) of the wind was calculated semi-analytically by Hollenbach et al. (1994) and scales as $R^{-3/2}$ for $R < R_g$ and as $R^{-5/2}$ outside R_g, as in Font et al. (2004) and Alexander et al. (2008) I use the smooth base density profile suggested by Font et al. (2004) that varies between the two power laws:

$$n(R) = n_g \left[\frac{2}{(R/R_g)^{15/2} + (R/R_g)^{25/2}} \right]^{1/5} \tag{6.4}$$

where n_g is the density at R_g which was determined through the numerical calculations of Hollenbach et al. (1994) to be:

$$n_g \approx 2.8 \times 10^4 \left(\frac{\Phi_*}{10^{41}\text{s}^{-1}} \right)^{1/2} \left(\frac{M_*}{1\text{M}_\odot} \right)^{-3/2} \text{cm}^{-3} \tag{6.5}$$

where Φ_* is the ionizing luminosity. I note that this hydrodynamic calculation does not include a cold bound 'disc' component, since as discussed above the base density structure of the wind is known a priori. This base density, along with Keplerian rotation is reset at every time-step and the model is allowed to evolve to a steady state, launching a wind from the grid's mid-plane (representing the disc's surface). As expected, I find excellent agreement with the results of the Font et al. (2004) and Alexander (2008) calculations. In Figure 6.1 I show a plot of the converged wind structure showing that the wind is approximately spherical once it has reached several scale heights, in agreement with our earlier discussion.

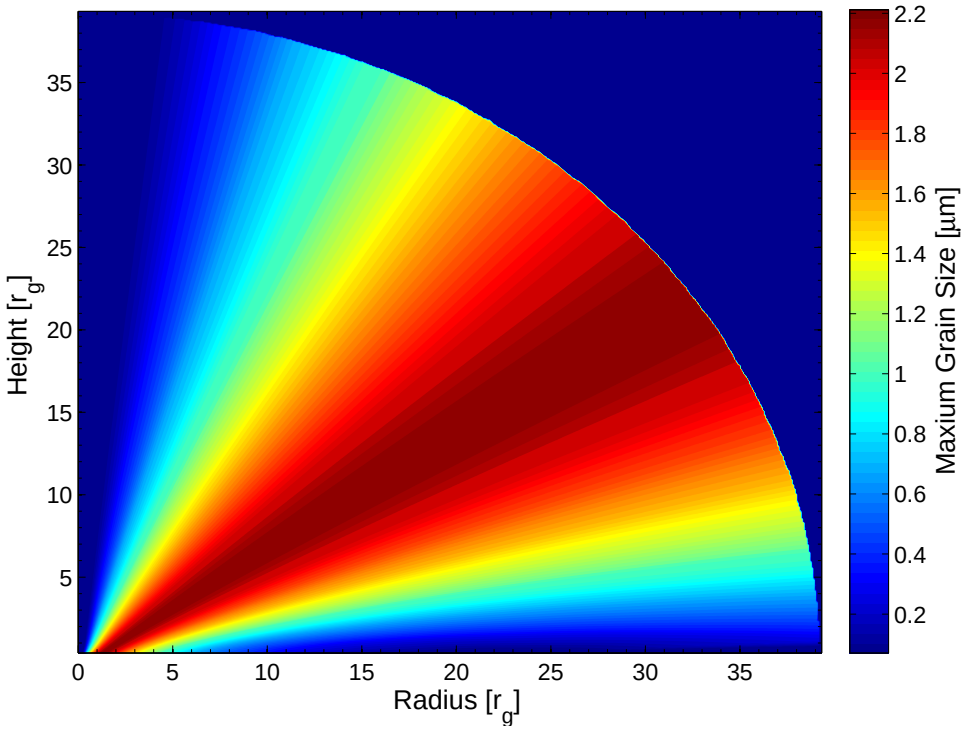

Figure 6.2: Colour map of the maximum size of entrained dust particles at a given position for $\Phi_* = 10^{43}\mathrm{s}^{-1}$, I note that most dust comes from within 1-5r_g.

6.1.3 Dust Distribution

In order to calculate the dust distribution in the wind, I must make some assumptions about the underlying dust distribution in the disc. I adopt a dust to gas mass ratio of 0.01, and a power law grain size distribution of index -3.5 (MRN), with grain sizes ranging from a_{min}=5$\times 10^{-3}\mu$m to a_{max}=1mm and I adopt spherical grains with a density of 1g cm^{-3}. Assuming that the dust is fully mixed within the disc up to the transition between the cold bound disc and the hot EUV heated flow, I then calculate streamlines from the base of the flow to the edge of the grid. For each streamline, I then compute the force balance between the drag force (calculated from Equation 1), gravity and the centrifugal force. I take the dust grain as entrained if the net force along the streamline is > 0. I then obtain the maximum grain size entrained along the entire streamline (making sure to check that each grain can be entrained the entire length of the streamline). In Figure 6.2 I show the obtained maximum grain size as a function of position in the flow for an ionizing luminosity of $\Phi_* = 10^{43}\mathrm{s}^{-1}$.

The dust density can then be computed from this maximum grain size under the assumption that the dust all comes from the same underlying population described above. In Figure 6.3 we show the obtained dust density, noting that the combination of a photoevaporative wind and a selective dust population naturally reproduces a 'wingnut' structure.

6.1.4 Radiative Transfer

I calculate the radiative transfer as a two step process: The temperature structure of the dust is calculated using a 3D grid calculated from the 2D dust density calculations, using a version modified of MOCASSINV2 to allow cell-to-cell variations of the grain size distribution; Then this temperature structure is used

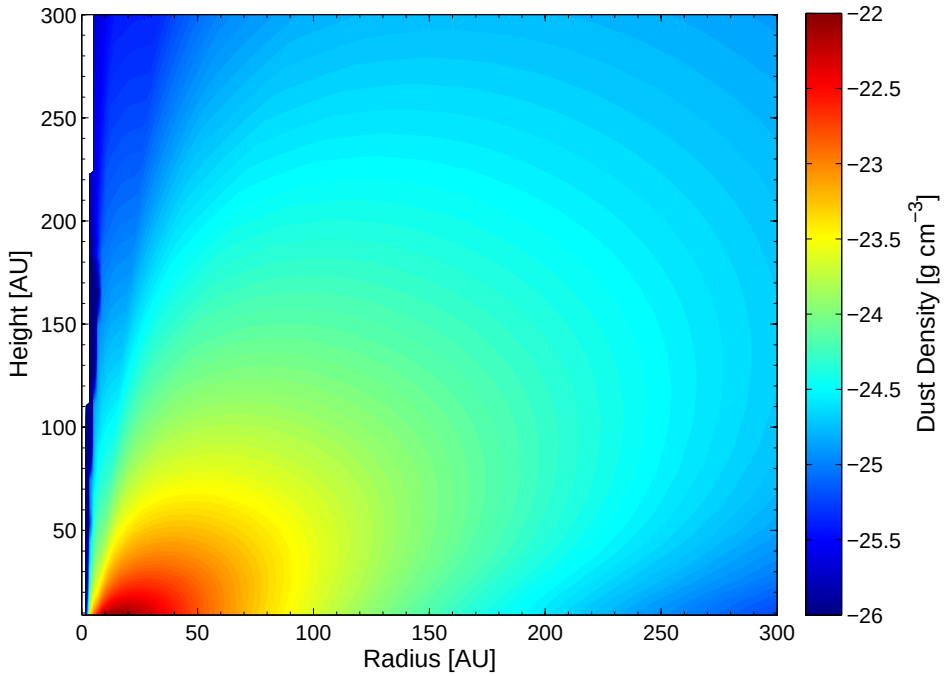

Figure 6.3: Dust mass density distribution in the wind model for the $\Phi_* = 10^{43}\mathrm{s}^{-1}$ calculation.

to determine synthetic scattered light images .

I interpolate the results from Section 6.1.3 onto a 3D Cartesian grid with resolution $N_X \times N_Y \times N_Z = 99 \times 99 \times 50$ assuming azimuthal symmetry, using the range in the x and y axis of [-32,32]r_g and in the z axis of [0,32]r_g. The input SED used to irradiate the wind is taken from the model set of Robitaille et al. (2006), Model Number:3011099, corresponding to a 2.51$M_\odot$ star with an effective temperature of 9480K and radius of 2.18$R_\odot$, surrounded by an optically thick disc extending into the dust destruction radius. The irradiating SED is placed at the origin of the Cartesian grid; this approximation is valid in this case where we are mainly interested in scattering of NIR photons on the much larger scale of the wind i.e. on a scale much greater than the scale the disc emission arises from.

In order to calculate images of the dust distribution, I have used the simple ray tracing driver for MOCASSIN, called MOCASSINTHINIMAGE. The standard Monte-Carlo radiative transfer techniques used to calculate scattered light images in MOCASSIN (i.e. by capturing scattered photons along the line of sight of interest) is inappropriate for use in this case. The wind structure is too optically thin to obtain a converged image with a computationally feasible number of energy packets, since most packets leave the grid without interacting with the distribution[1]. MOCASSINTHINIMAGE performs a ray tracing calculation throughout the grid in both scattered and thermal emission, under the assumption that the medium is optically thin (true of the wind always). I note again that since I have not explicitly included the dust in the 'bound' region of the disc we will not calculate scattered light emission from this region. I also assume the disc mid-plane is optically thick to all radiation, and hence only consider one hemisphere of the wind.

[1]It is important to emphasise that this is not the case for the temperature calculation discussed above, where an interaction is not required with a photon packet to include its contribution to the radiative energy density and hence temperature in that cell (see Lucy 1999; Ercolano et al 2003).

6.1.5 Calculations of Crystallinity Structure

The origin of crystalline dust grains detected in protoplanetary discs via infra-red (IR) spectroscopy (e.g. Bouwman et al. 2001) and directly within our own solar system (e.g. Wooden et al. 1999) is still a matter of discussion. The source of all dust in star formation - the ISM - is inferred to be entirely amorphous (e.g. Kemper et al. 2005). Spectroscopy of discs (van Boekel et al. 2005; Apai et al. 2005) indicates a non-negligible level of crystalline dust outside the crystalline radius, where grains are hot enough ($T > 800$K) to be thermally annealed and converted into crystalline grains (e.g. Fabian et al. 2000; Bockeleé-Morvan et al. 2002). This discovery has lead to the development of disc models with radial mixing to allow crystalline grains that formed in the hot inner disc to be transported to larger radii (e.g. Morfill & Voelk 1984; Gail 2001, 2002; Wehrstedt & Gail 2002; Bockelee-Morvan et al. 2002; Dullemond et al. 2006; Hughes & Armitage 2010). Another suggestion put forward by Shu et al. (1996), is that crystalline grains could be carried outwards by an x-wind. Given that the crystallization radius of <1-2AU is smaller than the minimum launch radius for a photoevaporative wind ($> 2AU$) around Herbig Ae/Be stars and lower mass stars, the photoevaporative wind cannot be the direct source of the crystalline grains at larger radii, but could work in combination with radial mixing to produce the observed enhancement. Furthermore, crystallinity around edge-on discs can be used to probe the source of the dust in the extended emission, since a disc origin will give rise to crystalline dust grains in the wind while an in-falling envelope will contain only amorphous grains.

In order to consider the structure of the dust grains in the wind, I have built a very simple dust crystallinity model. I assume that the grains are launched from a disc that is infinitesimally thin and has the crystalline structure calculated by Dullemond et al. (2006), for a Herbig star with a mass of $2.5M_{\odot}$ after 3.3Myr of evolution. Any dust that was amorphous and is heated to a temperature > 800K while entrained in the wind is then assumed to immediately become totally crystalline, as the crystallization time-scale is shorter than the flow time-scale (e.g. Dullemond et al. 2006). Any dust that starts off crystalline or becomes crystalline at any point in the flow is assumed to be crystalline for the remainder of the flow regardless of the temperature it reaches at any other stage (I find that no dust in the flow reaches a temperature exceeding the evaporation temperature, which would destroy crystalline dust grains). In order to calculate a radial profile of the fraction of dust in the wind that is crystalline/amorphous I must apply some cut off on the flow, since the total mass of the flow is a function of time since it switched on, rather than a converged quantity. Since much of the information on dust structure comes from the 10μm silicate feature, a temperature cut-off is most appropriate. Thus I calculate the mass-fraction of crystalline grains out to a temperature of 100K; as such this should provide a reasonable estimate of the observable crystallinity-fraction (anything colder is extremely unlikely to make much impact on the 10μm silicate feature). Furthermore, since each cylindrical radial region will be cut by many streamlines with different crystallinity fractions, in order to calculate an average crystallinity fraction we perform a number density weighted average out to the temperature cut-off.

6.2 Images

In Figure 6.4 I show calculated images of the 5 different models in the H, K' & L' bands; they all show a 'wingnut' morphology. The emission is strongest in the bluer bands with the H band being strongest and

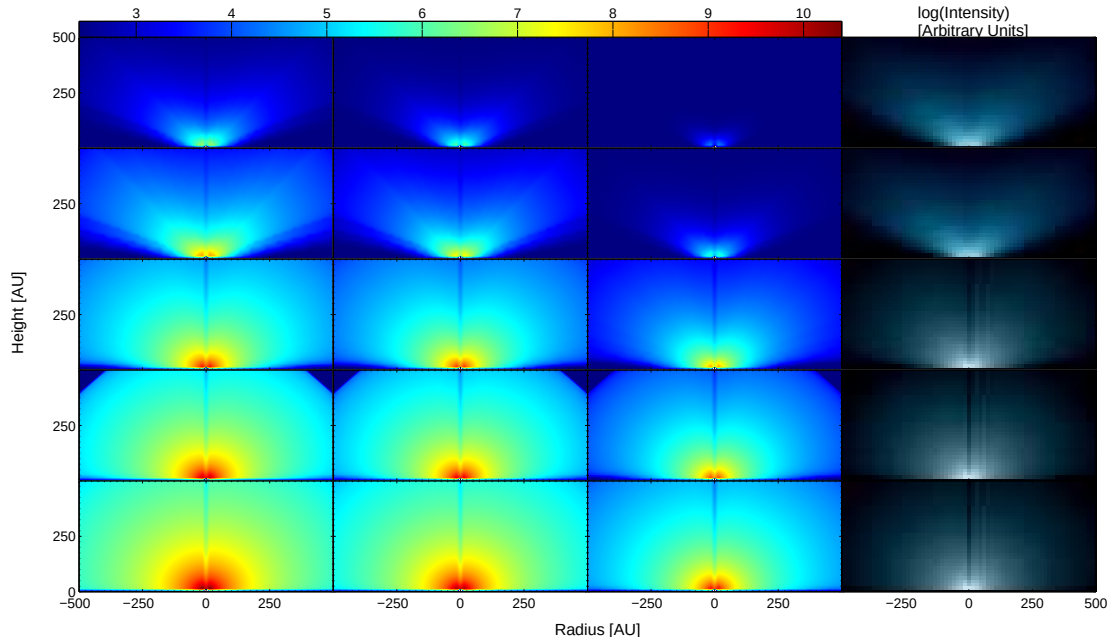

Figure 6.4: Synthetic images for disc models with irradiating fluxes $\Phi_* = 10^{41}, 10^{42}, 10^{43}, 10^{44}, 10^{45}$erg s^{-1}, the far left hand column shows the image in the H band, the next column displays the K' band and the next column the L' band. The far right column displays an RGB composite image (L',K' & H bands respectively). The images are individually scaled so that there is a 5dex spread between the brightest pixel and the darkest. All images assume the disc is edge-on (i.e. an inclination of 90^o), therefore I block out the star assuming it would be blocked out by the presence of an optically thick disc.

the L' being the weakest.

As the mass-loss rate increases the emission becomes more extended and reaches larger radii, since the density along a streamline falls to a given value at larger radius. I also find that all of the emission is scattered light from the central star and inner disc, many orders of magnitude above any thermal emission from the wind itself, in agreement with the assertion that the wind is optically thin. The fact that the emission is dominated by scattered light allows us to understand the evolution of the colour variation and emission morphology as the mass-loss rates change. For high mass-loss rates the emission morphology follows the gas density distribution of the wind (i.e. essentially spherical with a gap on axis in a region where the wind is negligible), while more pronounced 'wingnut' profiles are clearly visible for lower values of mass-loss rate. This arises from the fact that scattering at a given wavelength is dominated by dust grains of comparable sizes. Given that the bands we are interested in are in the range 1-5μm, then when there is large spatial variation in grains of this size, then a profile that differs markedly from the gas density would be expected (e.g. the wingnut). However, for large enough mass-loss rates, dust grains with sizes in the range 1-5μm can be entrained in the flow everywhere and the emission then simply follows the gas density distribution. I find that all of the synthetic images are dominated by blue light; this is somewhat expected since the smallest grains can always be entrained in the flow and outnumber the larger grains, thus dominating the opacity for an MRN size distribution as the one considered here. Furthermore, the negative slope with wavelength of the irradiating field, which in the 1-5μm range is dominated by emission from the disc, means that short wavelength photons are more abundant, contributing to the blue appearance of the synthetic images.

Table 6.1: Model Luminosities

$\log(\Phi_*)$ s^{-1}	log(Luminosity) erg s^{-1} Hz^{-1}		
	H	K'	L'
41	15.8	15.4	14.0
42	17.4	17.2	16.2
43	18.3	18.2	17.5
44	18.9	18.8	18.2
45	19.4	19.3	18.7

6.3 Crystallinity Profile

We have used the wind profiles and dust temperature information from the radiative transfer calculation (Section 6.1.4) to calculate crystallinity fractions in the wind. I have assessed the impact of the wind on the observable crystallinity fraction for discs, where the inner disc is both obscured (edge-on) and unobscured. In the unobscured case, to observe the disc's crystallinity fraction the wind will also make a contribution along the line of sight. I compare the disc's emission to the wind's emission at 10μm and find that at all radii the disc dominates over the wind, meaning that the observed crystallinity fraction for non edge-on discs is unaffected by the photoevaporative wind. However, when the disc is observed close to edge-on, the disc's contribution will be undetectable and the crystallinity fraction in the wind may be studied.

It is important to note at this point, that the radial distribution of the crystallinity fraction in a wind is likely to differ from the disc's 'native' distribution. In Figure 6.5 we show radial profiles of the crystallinity fraction obtained from a photoevaporative wind (solid black line) and compare it to the input crystallinity distribution of the disc (dashed blue line). The figure shows that at small radii < 2.5AU there is no crystallinity in the wind simply because there is no wind inside this radius to carry the dust grains to large heights. Between 2.5-200AU there is a falling crystallinity fraction; however, it is always in excess of the disc's underlying fraction, beyond outside 200AU it continues to fall, even though the crystallinity fraction in the disc has now risen above the level in the wind. The crystallinity fraction in the wind remains the same for all ionizing luminosities and is insensitive to the temperature cut-off described in Section 6.1.5 in the range 150-50K.

The observed wind crystallinity profile is a direct consequence of the streamline topology, which implies that the grains in the wind at any given cylindrical radius must have originated in the disc at a smaller radius and hence, in general, with a higher crystallinity fraction. The rise in the disc crystallinity at a radii $>$ 100AU is not translated into the wind population, since most of the dust in the wind is entrained inside $5r_g \approx 100$AU. The low wind rates at $>$ 100AU, coupled with the geometric dilution of the wind, mean that the crystallinity fraction in the wind continues to fall with radius. The insensitivity of the crystallinity fraction to the mass-loss rate is simply arises from the fact that the number of dust particles at a given point scales approximately as $n_{\rm dust} \propto \Phi_*^{1/2}$. This is the same scaling as the gas, since it is largely unaffected by the change in maximum grain size as crystalline and non-crystalline grains are entrained to the same extent.

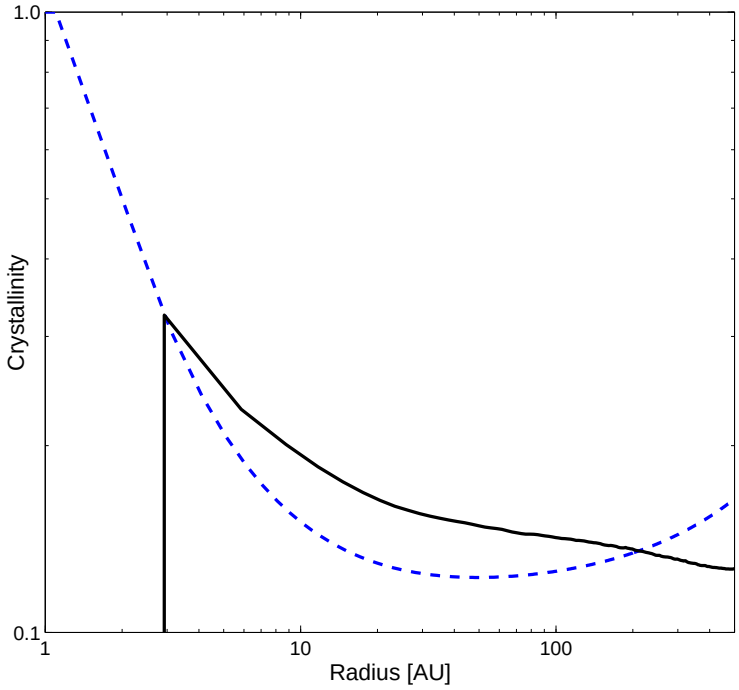

Figure 6.5: Cylindrical radial profiles of the wind crystallinity fraction (solid line) calculated as a number density weighted mean in the wind and the underlying disc distribution taken from Dullemond et al. (2006) for an evolved 3.3Myr 2.5$M_{\odot}$ Herbig star (dashed line).

6.4 Comparisons to Observed Edge-on Objects

There are several objects that show extended emission above and below the dark dust lane indicative of an optically thick disc. All the objects in the sample presented by Padgett et al. (1999), which includes the well known 'Butterfly Star', show extended scattered light emission above and below a dark dust lane. However, the objects in the Padgett et al. (1999) sample are all relatively low-mass (Class I) young stars, and the high fluxes detected in scattered light indicate that there is much more mass present than would be expected in a photoevaporative wind. Furthermore the observed structure is much more filamentary than our model predict. These observations clearly indicate that a photoevaporative wind is too weak to have produced the observed extended emission. Padgett et al. (1999) suggested that these objects are young (Class I) objects, with the extended emission arising from an in-falling envelope. Wolf et al. (2003) and Stark et al. (2006) have successfully reproduced these observations using detailed radiative transfer modelling that include the combination of a disc component, an in-falling envelope and an outflow cavity.

However, PDS 144N (Perrin et al. 2006) is a more promising candidate for a photoevaporative wind (shown in Figure 6.6) , with images showing a morphology very similar to the 'wingnut' shapes predicted for the lower mass-loss rates $\Phi_* \leq 10^{43}$erg s^{-1}. Furthermore adopting the $\Phi_* = 10^{43}$erg s^{-1}, which predicts a surface brightness of 0.01 Jy arcsec^{-2} in H at a radius and height of $(R = 100, z = 100)$AU, I can derive a distance to PDS 144N. By comparing the observed image to our predicted image I find a distance of 200-400pc, which is in the range of previous estimates[2]. As discussed in Perrin et al. (2006), it is

[2]Previous estimates range from 140 to 2000pc. Perrin et al. (2006) use a nearby A5 Herbig star (PDS 144S) to derive a distance of 1000pc, taking the system to be a wide binary. However, such a distance places the system 300pc above the

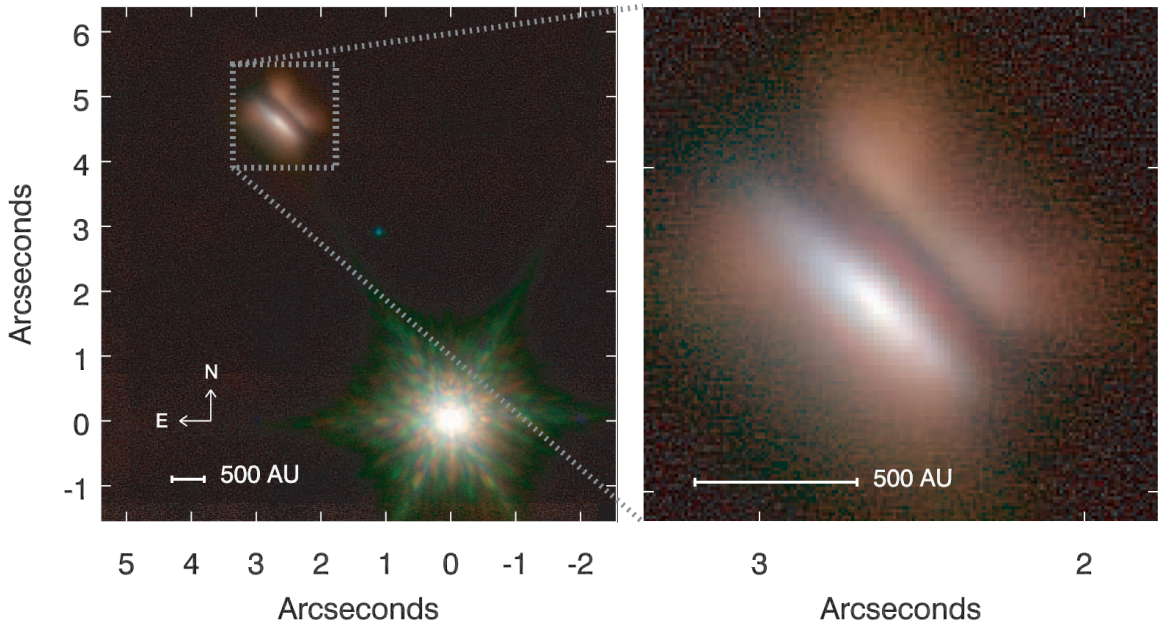

Figure 6.6: Three colour plot of PDS 144 where the H,K' and L' band are shown as blue, green and red respectively. The scale bar assumes a distance of 1000pc (Figure from Perrin et al. 2006).

highly unlikely that the morphology arises from foreground extinction, as the suggested explanation to the morphology of the Padgett et al. (1999) sample. Perrin et al. (2006) indeed discuss photoevaporation as a possible source for the extended emission. However, they oversimplify the photoevaporation model by just considering the radial scale r_g, ignoring the fact that, as discussed in Section 2, dust grains can be carried to very large distances in the wind, and that at several flow scale heights from the disc the streamlines are spherical. The models show that the use of r_g in discussing the characteristic scales of the flow in dust is a poor approximation, since, as shown in Figure 6.2, dust entrained at $\sim 1r_g$ can be easily carried to radii and heights of $> 20r_g$, where the maximum grain size increases with height. The reason for this morphology is streamlines at higher heights originate at smaller cylindrical radii where the gas density is high enough to entrain large grains, and this produces a dust density that varies on scales different to r_g as shown in Figure 6.3. Perrin et al. (2006) present models of the object in which they construct an in-falling envelope with a jet cavity surrounding an extended passive accretion disc. While their model (Figure 6 of Perrin et al. 2006) can also reproduce extended emission, it cannot reproduce the distinctive 'wingnut' morphology seen in the observations and in the model presented in this work (see the top panels of Figure 6.4).

However both the model presented by Perrin et al. (2006) and the ones presented in this work fail to reproduce one important aspect of the observations. The observed colour of PDS 144N is such that the extended regions of the emission become dominated by the redder scattered light. This is opposite to what is predicted by the Perrin et al. (2006) model which predicts a colour variation of red to blue with height and the blue band dominating the emission at large height. This is due to a dust population whose maximum grain size decreases with height (as you move from the disc population to the envelope - ISM like - population). On the contrary, the photoevaporation model *can* reproduce the sign of the observed

Galactic plane. This would require the ejection of the wide binary system from a dense cluster, or formation in situ, both of which are unlikely.

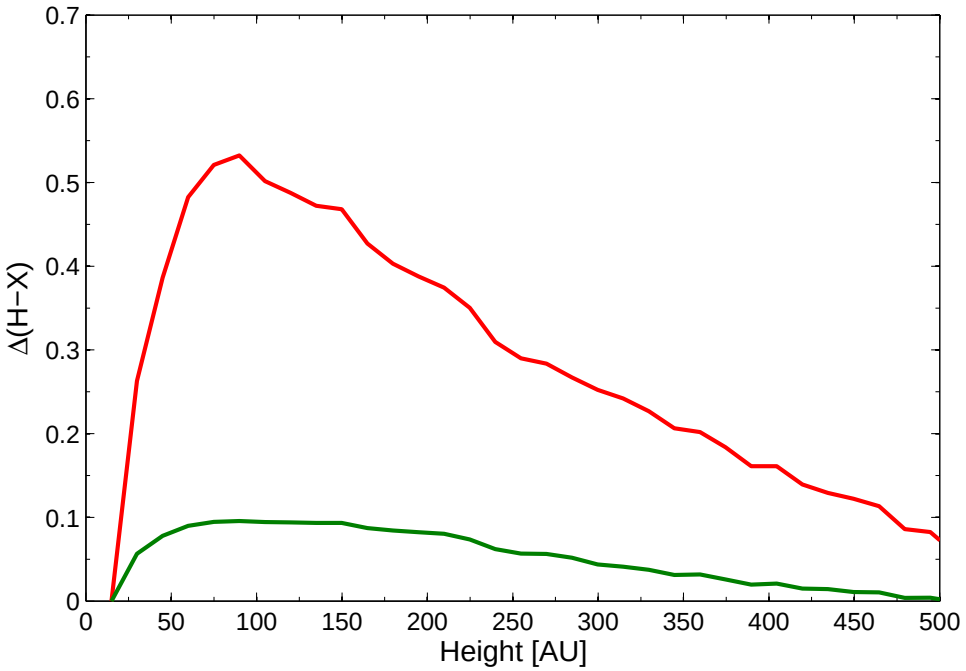

Figure 6.7: Change in colour (ΔH-X) as a function of height above the mid-plane, at a cylindrical radius of 100AU. Green line: X=K' band colour; red line: X=L' band colour. The model shown is the $\Phi_* = 10^{43}$ s^{-1} calculation.

colour variation i.e that the relative strength of the red light increases with height. This is demonstrated in Figure 6.7 where we plot the change in H-K' and H-L' for the $\Phi_* = 10^{43}$ s^{-1} model as a function of height above the mid-plane for the $\Phi_* = 10^{43}$ s^{-1}, where there is variations in the grain population at sizes of a few microns, which dominate the scattering opacity at NIR wavelengths. While our models predict that the colours become redder with height above the disc (due to the fact that larger grains are entrained at greater height, see Figure 6.2, and these scatter red light more efficiently), our models predict scattered blue light to remain dominant at large heights. As discussed in Section 6.2, in our model blue light dominates due to the spectral slope of the irradiating SED and the fact that small grains are present in the wind at all heights. I estimate using Figure 3 of Perrin et al. (2006) a change in H-L' (Δ(H-L')) of $>$1.5, at least three times larger than our simple model can predict. However, in order to allow the redder bands to dominate over the bluer bands one needs to (i) increase the available disc emission at the redder wavelengths so there is more original flux to scatter and/or (ii) remove the smaller grains which are currently dominating the scattered light; (iii) increase the optical depth to the star/disc so the extended region becomes optically thick, resulting in the reddening of photons as they pass through. Grain growth in the disc provides a natural solution to both (i) and (ii). Dullemond & Dominik (2005) have shown that the dust grains in a disc easily grow to $\sim 1\mu$m reducing the opacity of the disc at shorter wavelengths and resulting in a disc spectrum that falls less steeply or even rises to longer wavelengths in the 1-5μm range. Furthermore, the removal of small grains from the disc will also result in the removal of small grains from the wind, reducing the scattering efficiency at the shorter bluer radiation.

Future observations of the 10μm silicate feature may help disentangle the origin of the dust particles in the extended region around PDS 144N since an in-falling envelope would be entirely composed of amorphous ISM type grains, while, as shown by our models, a photoevaporative wind origin implies the

presence of crystalline silicate grains in the extended regions.

6.5 Conclusions

I have considered the fate of dust grains that can be entrained in a photoevaporative wind from the surface of a disc surrounding a Herbig Ae/Be star. For a median mass-loss rate of $\sim 10^{-9}\mathrm{M}_{\odot}\mathrm{yr}^{-1}$, I find that grains up to radii of several microns can be entrained in the wind. I also show that, once entrained in the wind, the dust grains will remain entrained and be carried out to very large radius ($> 10r_g$).

1. The combination of a photoevaporative wind structure and a variable dust grain population resulting from the variable drag force at the base of the wind, can naturally reproduce a 'wingnut' morphology of the dust density distribution in the wind.

2. The model is not applicable to the well known edge-on discs in the Padgett et al. (1999) sample, which are too young and optically thick to be explained with a photoevaporative origin, but are likely to arise from an in-falling envelope as shown in Wolf et al. (2003) and Stark et al. (2006).

3. Synthetic images show a wingnut morphology inferred from the dust density distributions, similar to observations of the edge-on disc around PDS 144N (Perrin et al. 2006). However, the synthetic images are dominated by emission from the smallest grains entrained in the flow, hence failing to reproduce the colour gradient of the observations, which show redder emission at larger heights above the disc. Grain growth in the disc, is a natural solution to the colour problem, and I estimate severely depleted abundance of grains with radii smaller than 1μm.

4. I find that crystallinity fraction will remain unchanged when the disc's photosphere can be observed since the observable mass in the wind is much less than the observable mass in the disc.

5. When the disc photosphere is obscured (i.e. for edge-on discs) the crystallinity fraction in the wind is significantly enhanced above the discs underlying crystallinity fraction.

   The observations of edge-on discs around more massive stars, could provide a new opportunity to study the structure of photoevaporative flows arising from the discs of forming stars. Where an observed 'wingnut' morphology and colour gradient are indicators of dust entrained in such a flow. Finally, I suggest that detection of crystalline grains in extended emission around an edge on disc is indicative of a photoevaporative wind and argues against an envelope origin for the extended emission.

7

Summary and Outlook

In this thesis I have considered photoevaporation from protoplanetary discs as a dispersal mechanism. This is motivated by the need to identify the dominant dispersal mechanism (if in fact there is a dominant one) for protoplanetary discs, as observations indicated that disc lifetimes are too short, and discs transition from a primordial to cleared state too rapidly to be explained by pure viscous effects. Currently the two ideas for disc dispersal are the removal of disc material to form planets or the removal of disc material in a photoevaporative wind. It is now observationally established that both these processes must be occurring for at least some forming young stars. The main question this thesis attempts to address is: Can photoevaporation provide a dominant dispersal mechanism around all young stars?

In order to study the photoevaporative flow, I have used a combination of simple scaling laws and numerical methods, and Chapters 2 & 3 outline the attempts to consider photoevaporation from real protoplanetary discs that are exposed to the full spectrum of ionizing radiation. This analysis has shown that it is likely to be the X-rays that are responsible for driving and setting the photoevaportive mass-loss rates, and that the mass-loss rates scale linearly with X-ray luminosity and do not explicitly depend on the mass of the central star. Furthermore, given the wind topologies that arise from primordial discs, this mass-loss rate is set at the X-ray wind's sonic surface, where the flow is close to being spherical. This condition places powerful constraints on the role of disc structure and the FUV flux on the derived mass-loss rates. Since in a spherical flow the temperature at the sonic surface is just given by the Parker wind result, which purely depends on stellar mass and position, then the sound speed at the sonic surface is fixed. A fixed temperature at a given radius also fixes the density in X-ray heating, thus the mass-flux is set at the sonic surface, irrespective of the underlying disc structure. Therefore, the underlying structure of a protoplanetary disc must adjust itself to feed the X-ray driven photoevaporative flow at the correct mass-loss rate, rather than the mass-loss rate adjusting itself to changes in the disc's structure.

Once the accretion rate through the disc has fallen below the mass-loss rate in the wind, photoevaporation opens a gap in the disc. This separates the disc into an inner and outer disc, where the inner disc

rapidly drains onto the central star exposing the outer disc to high energy radiation. The topology of the wind then changes and the outer disc is eroded to larger and larger radii, where this efficient clearing arises because mass-loss rate is approximately independent of the distance to the outer disc. Finally, at some point the mid-plane column of the disc drops to a point where a sufficient mass fraction of the disc is heated up and it is dynamically destroyed. Thus photoevaporation driven by the X-rays does provide a dispersal mechanism that is capable of clearing the entire disc in a suitable time-scale.

In Chapter 4 the photoevaporation model developed was used to follow the evolution of an entire population of viscously evolving discs, in order to asses whether photoevaporation can be a dominant dispersal mechanism. To do this I follow the evolution of simple 1D disc models that are under the action of viscosity and photoevaporation, where our currently uncertainty of the viscosity is parametrised over, based on observations. This analysis shows that the observed spread in X-ray luminosity is sufficient to reproduce the observed spread in current observables, e.g. accretion rate and disc lifetime, while reproducing the required overall evolution with theoretically sensible viscosity parameters. Furthermore, the model is able to account for a large fraction of so called 'transition' discs and the observed correlations between X-ray luminosity and disc evolution diagnostics.

In Chapters 5 & 6 I have derived direct observable consequences of a photoevaporative wind, in both gas and dust diagnostics. The gas line emission provides a powerful probe of the photoevaporative flow and currently offers the only direct evidence for photoevaporation occurring from discs. Furthermore, an X-ray driven photoevaporative wind provides the only explanation for the ~ 5 km s^{-1} component of the OI 6300Å line observed by Hartigan et al. (1995), and the other line emission currently compares favourably with available observations. Chapter 6 discusses the observable implications of the small dust particles that a photevaportive wind may entrain. I use higher mass Herbig Ae/Be stars as a test bed for this idea, where the dust in the wind could be imaged provided the disc is close to edge-on, giving rise to a 'wingnut' morphology. This analysis suggests that dust entrained in a photoevaporative flow may be the origin of the unexplained extended emission around the young Herbig star PDS 144N.

7.1 Outstanding Issues

While the model presented in this thesis has satisfied its original aim - to develop a dominant dispersal mechanism for all protoplanetery discs - there are still several issues that remain unresolved. Perhaps the biggest source of uncertainly is the value of the X-ray luminosity the disc actually sees. Accretion columns, magnetic disc winds and jets all provide a source of neutral attenuation along the line of sight between the star's corona and the outer disc. In the work presented here I have assumed that this neutral column has a negligible affect on the X-ray flux between the star and disc, and is valid up-to neutral columns in the range $10^{20} - 10^{21}$cm^{-2}. With neutral columns larger than this, the effective X-ray luminosity the disc will 'see' will be significantly lower that the values used in this work. While this will not affect the wind structure and derived mass-loss rates, a scaling between the observed X-ray luminosity function and the X-ray luminosity function seen by the disc may need to be included. Gorti et al. (2009) argue that this neutral column may in fact be a function of accretion rate with very large columns $\sim 10^{22}$ cm^{-2} at the earliest times, something that is suggestively indicated by the observations of Güdel et al. (2010). Therefore, while I have assumed that the X-ray luminosity is fixed on the time-scales of disc evolution (since the intrinsic X-ray luminosity of the star does not vary with time), the X-ray luminosity

that reaches the disc may vary over time, as the neutral column close to the star starts off at a large value but falls over time. Observationally it may appear that the affect of neutral columns close to the central star maybe important, with Guedel et al. (2010) estimating neutral columns in the jets/magnetic winds and accretion columns around young stars of $\lesssim 10^{23}$ cm^{-2}, thus modelling is required to asses how these neutral columns between the star and observer translate into neutral columns between the star and disc. Certainly if the majority of the neutral column does scale with accretion rate, then it may not be that big an issue, since photoevaporation only begins to become important for disc dispersal when the accretion rate to falls to values just above the photoevaporation rate (i.e. when the neutral columns may have fallen to values that allow the X-rays to fully reach the disc).

Therefore, while the model presented in this thesis provides the first starting point of the *maximum* effect of photoevaporation, it may need to be calibrated in order to account for the evolving neutral columns close to the star, simply by adjusting the X-ray luminosity the disc receives compared to the intrinsic X-ray luminosity as a function of time.

As alluded to in Chapter 3, the inclusion of an extra source of FUV heating is unlikely to affect the X-ray dominated flow in the inner region. This does not completely rule out an FUV driven flow underneath, that undergoes a sonic transition at very large radius $>$ 100AU. While this is unlikely to impinge greatly on the evolutionary models presented in this thesis, it may have an impact on the outer regions of the disc. While a full inclusion of FUV heating was not possible within the framework of the radiation-hydrodynamic algorithm presented here, it is in principle simple to do. A standalone FUV algorithm does already exist and is presented in Richling & Yorke (2000); a coupling of this algorithm with the X-ray algorithm (and possibly a better treatment of the dust temperatures) would be required. Also the possibility of such a flow will depend on the interaction of such an FUV flow with the outer disc and X-ray wind above and will require simulations with a larger dynamic range than those used here, out to a least several hundred AU. Until these calculations are performed the photoevaporation problem around T Tauri stars cannot claim to have been solved, although the theory and tests performed in this thesis show that the flow from the inner regions and hence the disc's evolution is likely to be controlled by the X-ray radiation field.

7.2 Implications and future direction

There are several interesting implications that photoevaporation may have on the protoplanetary disc. The radial size distribution of dust grains expected for protoplanetary discs implies that most of the mass resides in the largest particles. Such dust grains will not be entrained in the photoevaporative wind, therefore photoevaporation preferentially removes gas from the disc leading to an increase of the disc's dust to gas mass ratio. At high gas to dust mass ratios the streaming instability (e.g. Youdin & Johansen 2007) has been invoked as a possible route to planetesimal formation. However, the required dust to gas mass ratio is much higher $(0.03-0.1)$ than the value expected in the disc at formation (0.01). Photoevaporation has often been invoked (e.g. Throop & Bally 2005) as a leading candidate for increasing the dust to gas ratio, often without much explanation. In fact a zeroth order calculation only yields a 3/2 increase: if we assume that the disc evolves viscously until $\dot{M}_* = \dot{M}_w$ when the disc is instantaneously cleared, and further assume no dust mass is lost in the wind then the final disc gas mass is $2\dot{M}_*\tau_d$ (from Equation 1.21), but as no dust mass is lost in the wind then the final dust mass must be

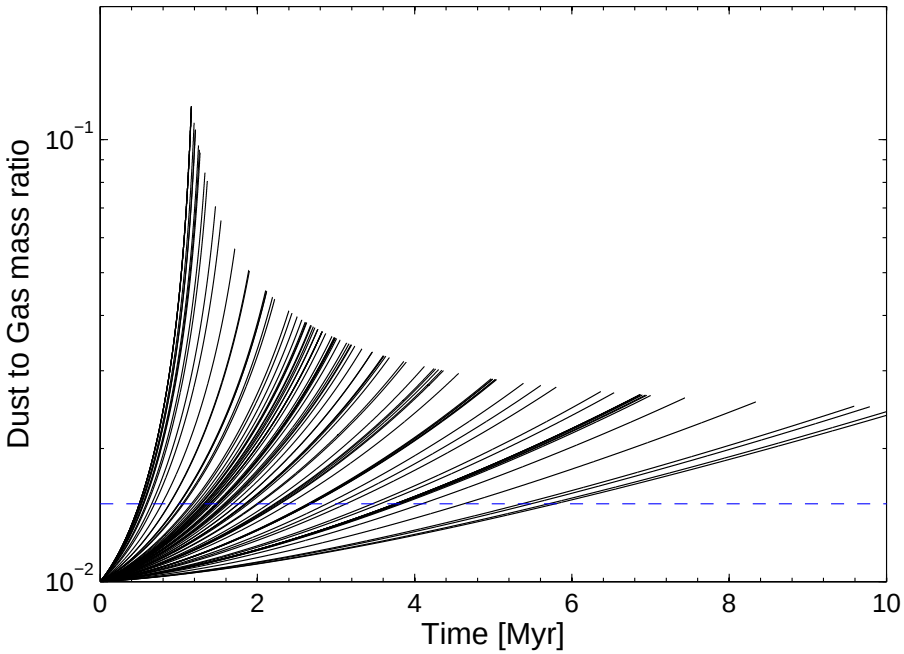

Figure 7.1: The Evolution of the global dust to gas ratio of individual discs with time (assumed to be 0.01 at $t = 0$), taken from the disc population calculated in Chapter 4 shown as black lines under the assumption of no dust mass lost in the wind and no migration. The blue line shows the value expected from a simple zeroth order calculation described in the text.

$3X_0\dot{M}_*\tau_d$ where X_0 is the initial dust to gas ratio. Therefore the final dust to gas ratio is $3/2X_0$.

A better but still simplistic calculation is shown in Figure 7.1 for the disc population shown calculated in Chapter 4. This shows that the global dust to gas mass ratio reaches values much higher than the value implied by a factor of $3/2$ increase. The origin of the rapid removal of gas material just before clearing is yet to be understood, but it certainly implies that this avenue of photoevaporation-triggered planetesimal formation is worth exploring. Furthermore, the high global dust to gas mass ratios imply that locally it may start to exceed unity. At this point the back reaction of the dust's angular momentum on the gas cannot be neglected, and may in fact suppress migration of dust particles. Therefore, any calculation that aims to follow the dust evolution may need to account for this effect. Certainly a two-dimensional calculation that incorporates dust migration, settling and photoevaporation may provide an interesting avenue of future research within the planet/planetismal formation field.

A

Numerical Fits to the Mass-loss Rates

In this appendix, I provide fits to the total mass-loss rates and mass-loss profiles ($\dot{\Sigma}_w$) obtained from the numerical calculations performed in Chapter 3. The fits are based on the results provided by an online 'function finder' service, provided at http://zunzun.com, and their functional form does *not* represent the results of an analytic calculation and should be treated in such a way. Furthermore, these fits were performed in such a way as to described the cumulative mass-loss rates accurately, which is important for the global viscous evolution. As such the fits are least accurate at small radius, should sensitivity at these radii become important, more accurate fits to this region can be provided upon request. The surface mass-loss profiles $\dot{\Sigma}_w$ given in Equations A.2 & A.5 are provided in normalised form and must be scaled so that $\int 2\pi R\dot{\Sigma}_w \mathrm{d}R$ yields the required total mass-loss rate, given in Equations A.1 & A.4.

A.1 Primordial Discs

The total mass-loss rate variation with X-ray luminosity is shown in Figure 3.4, where the solid line is described by:

$$\dot{M}_w = 6.25 \times 10^{-9} \left(\frac{M_*}{1\ \mathrm{M}_\odot} \right)^{-0.068} \left(\frac{L_X}{10^{30} \mathrm{erg\ s^{-1}}} \right)^{1.14} \mathrm{M}_\odot\ \mathrm{yr}^{-1} \tag{A.1}$$

The mass-loss profile, derived from the solid line in Figure 3.6 is described by:

$$\begin{aligned} \dot{\Sigma}_w(x > 0.7) \quad = \quad & 10^{(a_1 \log_{10}(x)^6 + b_1 \log_{10}(x)^5 + c_1 \log_{10}(x)^4 + d_1 \log_{10}(x)^3 + e_1 \log_{10}(x)^2 + f_1 \log_{10}(x) + g_1)} \\ & \times \left(\frac{6a_1 \log(x)^5}{x^2 \log(10)^7} + \frac{5b_1 \log(x)^4}{x^2 \log(10)^6} + \frac{4c_1 \log(x)^3}{x^2 \log(10)^5} \right. \\ & \left. + \frac{3d_1 \log(x)^2}{x^2 \log(10)^4} + \frac{2e_1 \log(x)}{x^2 \log(10)^3} + \frac{f_1}{x^2 \log(10)^2} \right) \times \exp\left[-\left(\frac{x}{100} \right)^{10} \right] \end{aligned} \tag{A.2}$$

where $a_1 = 0.15138$, $b_1 = -1.2182$, $c_1 = 3.4046$, $d_1 = -3.5717$, $e_1 = -0.32762$, $f_1 = 3.6064$, $g_1 = -2.4918$ and:

$$x = 0.85 \left(\frac{R}{\mathrm{AU}}\right) \left(\frac{M_*}{1\ \mathrm{M}_\odot}\right)^{-1} \tag{A.3}$$

where $\dot{\Sigma}_w(x < 0.7) = 0$. Logarithms of the form $\log(x)$ are taken taken using the natural base.

A.2 Discs with Inner holes

As described previously, the total mass-loss rate is approximately independent of inner hole radius, which is approximately given by:

$$\dot{M}_w = 4.8 \times 10^{-9} \left(\frac{M_*}{1\ \mathrm{M}_\odot}\right)^{-0.148} \left(\frac{L_X}{10^{30} \mathrm{erg\ s}^{-1}}\right)^{1.14} \mathrm{M}_\odot\ \mathrm{yr}^{-1} \tag{A.4}$$

The mass-loss profile, derived from the solid line in Figure 3.7 is described by:

$$\begin{aligned} \dot{\Sigma}_w(y) &= \left[\frac{a_2 b_2 \exp(b_2 y)}{R} + \frac{c_2 d_2 \exp(d_2 y)}{R} + \frac{e_2 f_2 \exp(f_2 y)}{R}\right] \\ &\quad \times \exp\left[-\left(\frac{y}{57}\right)^{10}\right] \end{aligned} \tag{A.5}$$

where $a_2 = -0.438226$, $b_2 = -0.10658387$, $c_2 = 0.5699464$, $d_2 = 0.010732277$, $e_2 = -0.131809597$, $f_2 = -1.32285709$ and:

$$y = 0.95\,(R - R_{\mathrm{hole}}) \left(\frac{M_*}{1\ \mathrm{M}_\odot}\right)^{-1} \tag{A.6}$$

where $\dot{\Sigma}_w(y < 0) = 0$.

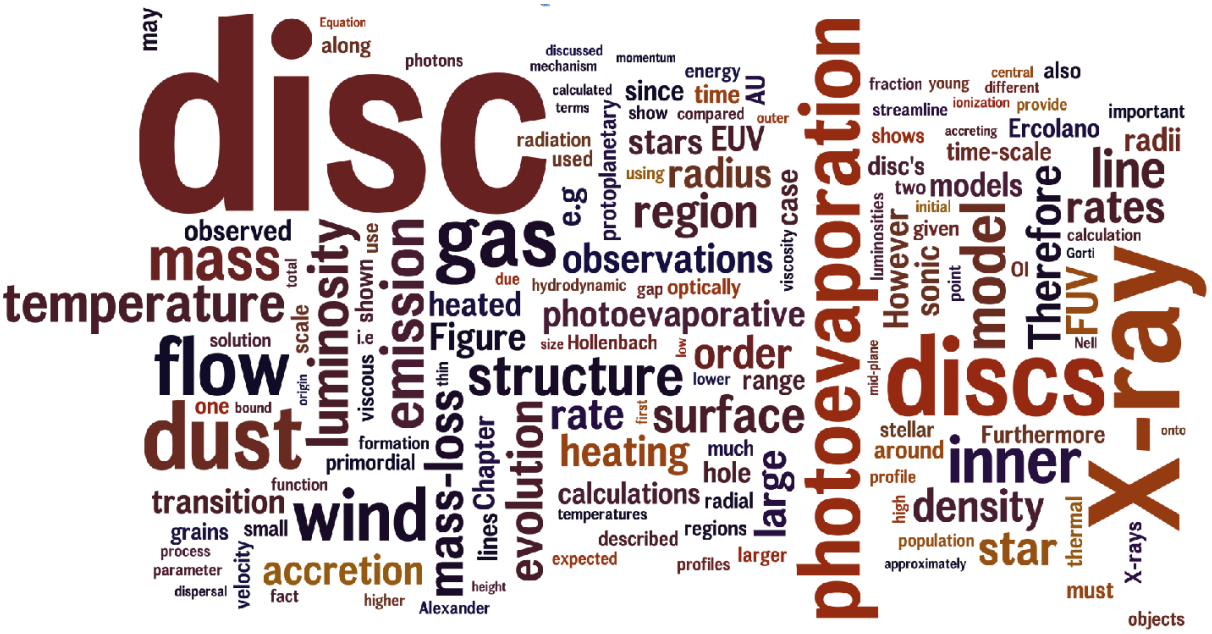
disc
photoevaporation
X-ray
discs
gas
mass
temperature
flow
dust
luminosity
emission
mass-loss
wind
accretion
evolution
structure
surface
rate
heating
inner
star
density
model
line
rates
region
observations
photoevaporative
radius
stars
EUV
Figure
heated
order
calculations
large
hole
Therefore
However
FUV
Furthermore
around
stellar
shows
Ercolano
time-scale
radii
important
also
may
along
Equation
photons
discussed
mechanism
momentum
energy
since
time
AU
calculated
terms
show
compared
outer
radiation
used
protoplanetary
e.g
using
viscosity
case
fraction
young
central
different
streamline
ionization
provide
disc's
two
models
initial
given
luminosities
sonic
point
OI
Gorti
calculation
Nell
mid-plane
onto
profile
high
population
approximately
thermal
X-rays
must
objects
observed
total
scale
solution
origin
one
bound
function
transition
grains
small
process
parameter
velocity
dispersal
fact
shown
use
viscous
i.e
formation
primordial
thin
Chapter
lines
height
higher
Alexander
due
hydrodynamic
gap
optically
size
Hollenbach
low
first
lower
range
much
radial
regions
larger
profiles
described
expected
temperatures

BIBLIOGRAPHY

A

Adams, F. C., & Shu, F. H. 1986, ApJ, 308, 836

Adams, F. C., Hollenbach, D., Laughlin, G., & Gorti, U. 2004, ApJ, 611, 360

Albacete Colombo, J. F., Flaccomio, E., Micela, G., Sciortino, S., & Damiani, F. 2007, A&A, 464, 211

Alexander, R. D., Clarke, C. J., & Pringle, J. E. 2004, MNRAS, 354, 71

Alexander, R. D., Clarke, C. J., & Pringle, J. E. 2005, MNRAS, 358, 283

Alexander, R. D., Clarke, C. J., & Pringle, J. E. 2006, MNRAS, 369, 216

Alexander, R. D., Clarke, C. J., & Pringle, J. E. 2006, MNRAS, 369, 229

Alexander, R. D., & Armitage, P. J. 2007, MNRAS, 375, 500

Alexander, R. D. 2008, MNRAS, 391, L64

Alexander R. D., Armitage P. J., 2009, ApJ, 704, 989

Andre P., Ward-Thompson D., Barsony M., 1993, ApJ, 406, 122

Andre P., Montmerle T., 1994, ApJ, 420, 837

Andrews S. M., Williams J. P., 2005, ApJ, 631, 1134

Andrews S. M., Williams J. P., 2007, ApJ, 671, 1800

Andrews S. M., Wilner D. J., Hughes A. M., Qi C., Dullemond C. P., 2010, ApJ, 723, 1241

Apai D., Pascucci I., Bouwman J., Natta A., Henning T., Dullemond C. P., 2005, Sci, 310, 834

Armitage, P. J., & Hansen, B. M. S. 1999, Nature, 402, 633

Armitage, P. J., Clarke, C. J., & Palla, F. 2003, MNRAS, 342, 1139

Armitage, P. J. 2010, Astrophysics of Planet Formation, by Philip J. Armitage, pp. 294. ISBN 978-0-521-88745-8 (hardback). Cambridge, UK: Cambridge University Press, 2010.,

Asplund, M., Grevesse, N., & Sauval, A. J. 2005, Cosmic Abundances as Records of Stellar Evolution and Nucleosynthesis, 336, 25

B

Balbus, S. A., & Hawley, J. F. 1991, ApJ, 376, 214

Ballesteros-Paredes, J., & Hartmann, L. 2007, RMXAA, 43, 123

Baraffe, I., Chabrier, G., & Gallardo, J. 2009, ApJ, 702, L27

Beckwith, K., Armitage, P. J., & Simon, J. B. 2011, arXiv:1105.1789

Brown, J. M., Blake, G. A., Qi, C., Dullemond, C. P., Wilner, D. J., & Williams, J. P. 2009, ApJ, 704, 496

Bruderer, S., Doty, S. D., & Benz, A. O. 2009, ApJS, 183, 179

Bockelée-Morvan, D., Gautier, D., Hersant, F., Huré, J.-M., & Robert, F. 2002, A&A, 384, 1107

Bouwman, J., Meeus, G., de Koter, A., Hony, S., Dominik, C., & Waters, L. B. F. M. 2001, A&A, 375, 950

Burkert A., Bodenheimer P., 2000, ApJ, 543, 822

C

Cabot, W., Canuto, V. M., Hubickyj, O., & Pollack, J. B. 1987, Icarus, 69, 423

Calvet N., D'Alessio P., Hartmann L., Wilner D., Walsh A., Sitko M., 2002, ApJ, 568, 1008

Calvet N., Muzerolle J., Briceño C., Hernández J., Hartmann L., Saucedo J. L., Gordon K. D., 2004, AJ, 128, 1294

Calvet, N., et al. 2005, ApJ, 630, L185

Cassen, P., & Moosman, A. 1981, Icarus, 48, 353

Calvet & D'alessio, 2011, Physical Processes in Circumstellar Disks Around Young Stars, Ed. Paulo Garcia, Chapter 2. Published by University of Chicago Press.

Chiang, E. I., & Goldreich, P. 1997, ApJ, 490, 368

Cieza, L. A., et al. 2010, ApJ, 712, 925

Clarke, C. J., Gendrin, A., & Sotomayor, M. 2001, MNRAS, 328, 485

Clarke, C. J. 2007, MNRAS, 376, 1350

Clarke, C. J. 2009, MNRAS, 396, 1066

Cohen, M. 1975, MNRAS, 173, 279

Currie, T., & Sicilia-Aguilar, A. 2011, ApJ, 732, 24

D

Drake, J. J., Ercolano, B., Flaccomio, E., & Micela, G. 2009, ApJ, 699, L35

Dullemond C. P., Dominik C., 2005, A&A, 434, 971

Dullemond C. P., Apai D., Walch S., 2006, ApJ, 640, L67

Dutrey A., Guilloteau S., Prato L., Simon M., Duvert G., Schuster K., Menard F., 1998, A&A, 338, L63

Duvert G., Guilloteau S., Ménard F., Simon M., Dutrey A., 2000, A&A, 355, 165

D'Alessio P., Canto J., Calvet N., Lizano S., 1998, ApJ, 500, 411

D'Alessio P., Calvet N., Hartmann L., Lizano S., Cantó J., 1999, ApJ, 527, 893

D'Alessio P., Calvet N., Hartmann L., 2001, ApJ, 553, 321

E

Edgar R., Clarke C., 2003, MNRAS, 338, 962

Edwards S., Hartigan P., Ghandour L., Andrulis C., 1994, AJ, 108, 1056

Ercolano, B., Barlow, M. J., Storey, P. J., & Liu, X.-W. 2003, MNRAS, 340, 1136

Ercolano, B., Barlow, M. J., & Storey, P. J. 2005, MNRAS, 362, 1038

Ercolano, B., & Storey, P. J. 2006, MNRAS, 372, 1875

Ercolano, B., Young, P. R., Drake, J. J., & Raymond, J. C. 2008, ApJS, 175, 534

Ercolano, B., Drake, J. J., Raymond, J. C., & Clarke, C. C. 2008, ApJ, 688, 398

Ercolano, B., Clarke, C. J., & Robitaille, T. P. 2009, MNRAS, 394, L141

Ercolano, B., Clarke, C. J., & Drake, J. J. 2009, ApJ, 699, 1639

Ercolano, B., & Clarke, C. J. 2010, MNRAS, 402, 2735

Ercolano, B., & Owen, J. E. 2010, MNRAS, 406, 1553

Ercolano, B., Clarke, C. J., & Hall, A. C. 2011, MNRAS, 410, 671

Ercolano, B., Bastian, N., Spezzi, L., & Owen, J. 2011, arXiv:1105.2406

Espaillat, C., et al. 2007, ApJ, 664, L111

Espaillat, C., et al. 2008, ApJ, 689, L145

Espaillat, C., et al. 2010, ApJ, 717, 441

F

Fabian, D., Jäger, C., Henning, T., Dorschner, J., & Mutschke, H. 2000, A&A, 364, 282

Feigelson, E. D., & Decampli, W. M. 1981, ApJ, 243, L89

Flaccomio, E., Micela, G., & Sciortino, S. 2003, A&A, 402, 277

Flaccomio, E., Stelzer, B., Sciortino, S., Micela, G., Pillitteri, I., & Testi, L. 2009, A&A, 505, 695

Flock, M., Dzyurkevich, N., Klahr, H., Turner, N. J., & Henning, T. 2011, arXiv:1104.4565

Font, A. S., McCarthy, I. G., Johnstone, D., & Ballantyne, D. R. 2004, ApJ, 607, 890

Furlan E., et al., 2006, ApJS, 165, 568

G

Gail, H.-P. 2001, A&A, 378, 192

Gail, H.-P. 2002, A&A, 390, 253

Gammie, C. F. 1996, ApJ, 457, 355

Glassgold, A. E., Najita, J., & Igea, J. 1997, ApJ, 480, 344

Glassgold, A. E., Najita, J., & Igea, J. 2004, ApJ, 615, 972

Glassgold, A. E., Najita, J. R., & Igea, J. 2007, ApJ, 656, 515

Güdel, M., et al. 2007, A&A, 468, 353

Güdel, M., et al. 2010, A&A, 519, A113

Guilloteau S., Dutrey A., 1998, A&A, 339, 467

Goldsmith P. F., Arquilla R., 1985, prpl.conf, 137

Goodman A. A., Benson P. J., Fuller G. A., Myers P. C., 1993, ApJ, 406, 528

Gorti, U., & Hollenbach, D. 2004, ApJ, 613, 424

Gorti, U., & Hollenbach, D. 2008, ApJ, 683, 287

Gorti, U., & Hollenbach, D. 2009, ApJ, 690, 1539

Gorti, U., Dullemond, C. P., & Hollenbach, D. 2009, ApJ, 705, 1237

Gorti, U., Hollenbach, D., Najita, J., & Pascucci, I. 2011, ApJ, 735, 90

Graves S. F., et al., 2010, MNRAS, 409, 1412

Gregory, S. G., Wood, K., & Jardine, M. 2007, MNRAS, 379, L35

H

Haisch K. E., Jr., Lada E. A., Piña R. K., Telesco C. M., Lada C. J., 2001, AJ, 121, 1512

Haisch, K. E., Jr., Lada, E. A., & Lada, C. J. 2001, ApJ, 553, L153

Hartigan P., Edwards S., Ghandour L., 1995, ApJ, 452, 736

Hartmann L., Calvet N., Gullbring E., D'Alessio P., 1998, ApJ, 495, 385

Hartmann, L. 2009, Accretion Processes in Star Formation: Second Edition, by Lee Hartmann. ISBN 978-0-521-53199-3. Published by Cambridge University Press, Cambridge, UK, 2009.,

Hayes, J. C., Norman, M. L., Fiedler, R. A., Bordner, J. O., Li, P. S., Clark, S. E., ud-Doula, A., & Mac Low, M.-M. 2006, ApJS, 165, 188

Hempelmann, A., Schmitt, J. H. M. M., Schultz, M., Ruediger, G., & Stepien, K. 1995, A&A, 294, 515

Herbig G. H., Bell K. R., 1988, cels.book,

Herbig, G. H. 1990, ApJ, 360, 639

Herczeg, G. J., Najita, J. R., Hillenbrand, L. A., & Pascucci, I. 2007, ApJ, 670, 509

Herczeg G. J., Hillenbrand L. A., 2007, AAS, 38, 852

Herczeg G. J., Hillenbrand L. A., 2008, ApJ, 681, 594

Hollenbach, D. J., & Tielens, A. G. G. M. 1997, ARA&A, 35, 179

Hollenbach, D., Johnstone, D., & Shu, F. 1993, Massive Stars: Their Lives in the Interstellar Medium, 35, 26

Hollenbach, D., Johnstone, D., Lizano, S., & Shu, F. 1994, ApJ, 428, 654

Hollenbach, D. J., Yorke, H. W., & Johnstone, D. 2000, Protostars and Planets IV, 401

Hollenbach, D., & Gorti, U. 2009, ApJ, 703, 1203

Hughes A. M., Wilner D. J., Kamp I., Hogerheijde M. R., 2008, ApJ, 681, 626

Hughes, A. M., et al. 2009, ApJ, 698, 131

Hughes, A. M., et al. 2010, arXiv:1007.3267

Hughes, A. L. H., & Armitage, P. J. 2010, ApJ, 719, 1633

I

Ingleby, L., Calvet, N., Hernández, J., Briceño, C., Espaillat, C., Miller, J., Bergin, E., & Hartmann, L. 2011, AJ, 141, 127

Imanishi, K., Koyama, K., & Tsuboi, Y. 2001, ApJ, 557, 747

J

Jeans J. H., 1902, RSPTA, 199, 1

Johnstone, D., Hollenbach, D., & Bally, J. 1998, ApJ, 499, 758

K

Kamp, I., & Dullemond, C. P. 2004, ApJ, 615, 991

Kamp, I., Tilling, I., Woitke, P., Thi, W.-F., & Hogerheijde, M. 2010, A&A, 510, A18

Kashyap, V., & Drake, J. J. 2000, Bulletin of the Astronomical Society of India, 28, 475

Kastner, J. H., Huenemoerder, D. P., Schulz, N. S., & Weintraub, D. A. 1999, ApJ, 525, 837

Kemper, F., Vriend, W. J., & Tielens, A. G. G. M. 2005, ApJ, 633, 534

Kennedy G. M., Kenyon S. J., 2009, ApJ, 695, 1210

Kenyon, S. J., & Hartmann, L. 1987, ApJ, 323, 714

Kenyon S. J., Hartmann L., 1995, ApJS, 101, 117

Kim, K. H., et al. 2009, ApJ, 700, 1017

Korycansky, D. G. 1992, ApJ, 399, 176

Kuiper R., Klahr H., Beuther H., Henning T., 2010, ApJ, 722, 1556

Kuiper R., Klahr H., Beuther H., Henning T., 2011, ApJ, 732, 20

Kraus, A. L., Ireland, M. J., Martinache, F., & Lloyd, J. P. 2009, American Institute of Physics Conference Series, 1094, 453

Krumholz M. R., Klein R. I., McKee C. F., 2007, ApJ, 656, 959

Krumholz M. R., Klein R. I., McKee C. F., Offner S. S. R., Cunningham A. J., 2009, Sci, 323, 754

L

Lada C. J., 1987, IAUS, 115, 1

Lahuis, F., van Dishoeck, E. F., Blake, G. A., Evans, N. J., II, Kessler-Silacci, J. E., & Pontoppidan, K. M. 2007, ApJ, 665, 492

Lamzin, S. A., Kravtsova, A. S., Romanova, M. M., & Batalha, C. 2004, Astronomy Letters, 30, 413

Landi, E., & Phillips, K. J. H. 2006, ApJS, 166, 421

Lin, D. N. C., & Papaloizou, J. 1980, MNRAS, 191, 37

Lin, D. N. C., & Papaloizou, J. 1979, MNRAS, 186, 799

Lin, D. N. C., & Papaloizou, J. 1979, MNRAS, 188, 191

Lin, D. N. C., & Pringle, J. E. 1987, MNRAS, 225, 607

Lin, D. N. C., & Pringle, J. E. 1990, ApJ, 358, 515

Lodato, G., & Rice, W. K. M. 2004, MNRAS, 351, 630

Lodato, G., & Rice, W. K. M. 2005, MNRAS, 358, 1489

Looper, D. L., et al. 2010, ApJ, 714, 45

Lucy, L. B. 1999, A&A, 344, 282

Luhman K. L., Allen P. R., Espaillat C., Hartmann L., Calvet N., 2010, ApJS, 186, 111

Lynden-Bell, D., & Pringle, J. E. 1974, MNRAS, 168, 603

M

Maggio, A., Flaccomio, E., Favata, F., Micela, G., Sciortino, S., Feigelson, E. D., & Getman, K. V. 2007, ApJ, 660, 1462

Mamajek, E. E. 2005, ApJ, 634, 1385

Mamajek, E. E. 2009, American Institute of Physics Conference Series, 1158, 3

Mathis J. S., Rumpl W., Nordsieck K. H., 1977, ApJ, 217, 425

Mayne, N. J., & Naylor, T. 2008, MNRAS, 386, 261

Meijerink, R., Glassgold, A. E., & Najita, J. R. 2008, ApJ, 676, 518

Mendoza V., E. E. 1966, ApJ, 143, 1010

Mendoza V., E. E. 1968, ApJ, 151, 977

Merín, B., et al. 2010, ApJ, 718, 1200

Mohanty, S., Jayawardhana, R., & Basri, G. 2005, ApJ, 626, 498

Morfill, G. E., & Voelk, H. J. 1984, ApJ, 287, 371

Muzerolle J., Hartmann L., Calvet N., 1998, AJ, 116, 455

Muzerolle J., Briceño C., Calvet N., Hartmann L., Hillenbrand L., Gullbring E., 2000, ApJ, 545, L141

Muzerolle J., Calvet N., Hartmann L., 2001, ApJ, 550, 944

Muzerolle J., Luhman K. L., Briceño C., Hartmann L., Calvet N., 2005, ApJ, 625, 906

Muzerolle J., Allen L. E., Megeath S. T., Hernández J., Gutermuth R. A., 2010, ApJ, 708, 1107

Myers P. C., Benson P. J., 1983, ApJ, 266, 309

N

Najita, J. R., et al. 2009, ApJ, 697, 957

Najita, J. R., Carr, J. S., Strom, S. E., Watson, D. M., Pascucci, I., Hollenbach, D., Gorti, U., & Keller, L. 2010, ApJ, 712, 274

Natta A., Meyer M. R., Beckwith S. V. W., 2000, ApJ, 534, 838

Natta A., Testi L., Muzerolle J., Randich S., Comerón F., Persi P., 2004, A&A, 424, 603

Neuhaeuser, R., Sterzik, M. F., Schmitt, J. H. M. M., Wichmann, R., & Krautter, J. 1995, A&A, 297, 391

P

Parker, E. N. 1958, ApJ, 128, 664

Pascucci, I., et al. 2007, ApJ, 663, 383

Pascucci I., Sterzik M., 2009, ApJ, 702, 724

Padgett, D. L., Brandner, W., Stapelfeldt, K. R., Strom, S. E., Terebey, S., & Koerner, D. 1999, AJ, 117, 1490

Palla, F., & Stahler, S. W. 2000, ApJ, 540, 255

Perez-Becker, D., & Chiang, E. 2011, ApJ, 735, 8

Perrin, M. D., Duchêne, G., Kalas, P., & Graham, J. R. 2006, ApJ, 645, 1272

Pontoppidan, K. M., Blake, G. A., van Dishoeck, E. F., Smette, A., Ireland, M. J., & Brown, J. 2008, ApJ, 684, 1323

Pringle, J. E. 1981, ARA&A, 19, 137

Preibisch, T., et al. 2005, ApJS, 160, 582

Proga, D., Stone, J. M., & Kallman, T. R. 2000, ApJ, 543, 686

Q

Qi C., et al., 2004, ApJ, 616, L11

R

Ratzka, T., Leinert, C., Henning, T., Bouwman, J., Dullemond, C. P., & Jaffe, W. 2007, A&A, 471, 173

Rice, W. K. M., Wood, K., Armitage, P. J., Whitney, B. A., & Bjorkman, J. E. 2003, MNRAS, 342, 79

Rice, W. K. M., Armitage, P. J., Wood, K., & Lodato, G. 2006, MNRAS, 373, 1619

Richling, S., & Yorke, H. W. 2000, ApJ, 539, 258

Robitaille, T. P., Whitney, B. A., Indebetouw, R., Wood, K., & Denzmore, P. 2006, ApJS, 167, 256

Ruden, S. P., & Lin, D. N. C. 1986, ApJ, 308, 883

Ruden, S. P., Papaloizou, J. C. B., & Lin, D. N. C. 1988, ApJ, 329, 739

Ruden, S. P. 1993, Planets Around Pulsars, 36, 197

Ruden, S. P. 2004, ApJ, 605, 880

Ryu, D., & Goodman, J. 1992, ApJ, 388, 438

S

Salyk, C., Blake, G. A., Boogert, A. C. A., & Brown, J. M. 2007, ApJ, 655, L105

Sanz-Forcada, J., Brickhouse, N. S., & Dupree, A. K. 2002, ApJ, 570, 799

Savage, B. D., & Sembach, K. R. 1996, ApJ, 470, 893

Schisano, E., Ercolano, B., G ”udel, M. 2010, MNRAS, 401, 1636

Shakura, N. I., & Sunyaev, R. A. 1973, A&A, 24, 337

Shang, H., Glassgold, A. E., Lin, W.-C., & Liu, C.-F. J. 2010, ApJ, 714, 1733

Shu, F. H., Johnstone, D., & Hollenbach, D. 1993, Icarus, 106, 92

Shu, F. H., Shang, H., & Lee, T. 1996, Science, 271, 1545

Skrutskie M. F., Dutkevitch D., Strom S. E., Edwards S., Strom K. M., Shure M. A., 1990, AJ, 99, 1187

Stark, D. P., Whitney, B. A., Stassun, K., & Wood, K. 2006, ApJ, 649, 900

Stelzer, B., & Neuhäuser, R. 2001, A&A, 377, 538

Strom K. M., Strom S. E., Edwards S., Cabrit S., Skrutskie M. F., 1989, AJ, 97, 1451

Stone, J. M., & Norman, M. L. 1992, ApJS, 80, 753

Stone, J. M., & Norman, M. L. 1992, ApJS, 80, 791

T

Takeuchi, T., & Lin, D. N. C. 2002, ApJ, 581, 1344

Takeuchi, T., Clarke, C. J., & Lin, D. N. C. 2005, ApJ, 627, 286

Tarter, C. B., Tucker, W. H., & Salpeter, E. E. 1969, ApJ, 156, 943

Throop, H. B., & Bally, J. 2005, ApJ, 623, L149

Tielens, A. G. G. M., & Hollenbach, D. 1985, ApJ, 291, 722

Tielens, A. G. G. M., & Hollenbach, D. 1985, ApJ, 291, 747

V

van Boekel, R., Min, M., Waters, L. B. F. M., de Koter, A., Dominik, C., van den Ancker, M. E., & Bouwman, J. 2005, A&A, 437, 189

van Boekel, R., Güdel, M., Henning, T., Lahuis, F., & Pantin, E. 2009, A&A, 497, 137

Verner, D. A., Yakovlev, D. G., Band, I. M., & Trzhaskovskaya, M. B. 1993, Atomic Data and Nuclear

Data Tables, 55, 233

Verner, D. A., & Yakovlev, D. G. 1995, A&AS, 109, 125

W

Walter, F. M., & Kuhi, L. V. 1984, ApJ, 284, 194

Watson, A. M., Stapelfeldt, K. R., Wood, K., & Ménard, F. 2007, Protostars and Planets V, 523

Wehrstedt, M., & Gail, H.-P. 2002, A&A, 385, 181

Weidenschilling, S. J. 1977, MNRAS, 180, 57

White, R. J., & Ghez, A. M. 2001, ApJ, 556, 265

White, R. J., & Hillenbrand, L. A. 2004, ApJ, 616, 998

Whitney, B. A., Wood, K., Bjorkman, J. E., & Wolff, M. J. 2003, ApJ, 591, 1049

Whitney, B. A., Wood, K., Bjorkman, J. E., & Cohen, M. 2003, ApJ, 598, 1079

Wolf, S., Padgett, D. L., & Stapelfeldt, K. R. 2003, ApJ, 588, 373

Woitke, P., Kamp, I., & Thi, W.-F. 2009, A&A, 501, 383

Wolfire M. G., Cassinelli J. P., 1986, ApJ, 310, 207

Wolfire M. G., Cassinelli J. P., 1987, ApJ, 319, 850

Wooden, D. H., Harker, D. E., Woodward, C. E., Butner, H. M., Koike, C., Witteborn, F. C., & McMurtry, C. W. 1999, ApJ, 517, 1034

Wyatt M. C., 2008, ARA&A, 46, 339

Y

Yasui, C., Kobayashi, N., Tokunaga, A. T., Saito, M., & Tokoku, C. 2009, ApJ, 705, 54

Yorke H. W., Bodenheimer P., 1999, ApJ, 525, 330

Yorke H. W., Sonnhalter C., 2002, ApJ, 569, 846

Youdin, A., & Johansen, A. 2007, ApJ, 662, 613

Z

Zinnecker H., Yorke H. W., 2007, ARA&A, 45, 481

Zuckerman B., Forveille T., Kastner J. H., 1995, Natur, 373, 494